EXPERIMENTAL AND NUMERICAL STUDY OF HEAT TRANSFER ON TURBINE BLADES

by

Graham Stuart Kennedy

Dissertation submitted in fulfilment of the academic requirements for the degree of Master of Science in Engineering in the School of Mechanical Engineering.

University of KwaZulu-Natal

Durban

2007

ABSTRACT

An experimental and numerical study of the aerodynamics and the associated heat transfer on turbine blades, has been carried out as part of the ongoing ***Armscor/Denel*** aircraft engine maintenance program. The experimental tests were performed using an existing continuous flow cascade test facility at the University of KwaZulu-Natal, Durban. These experimental results were used to validate the two-dimensional numerical results, generated using a commercially available Computational Fluid Dynamics (CFD) package, FLUENT.

The existing experimental turbine test facility utilises a continuous flow cascade technique where a cooled, instrumented blade is rapidly introduced to the hot-air stream exposing it to the cascade flow. This creates the heat transient required for measurement of the isothermal heat transfer coefficients, using thin-film heat flux gauges. A static pressure test blade is used in conjunction with a scanivalve system, to determine the blade mid-span pressure distribution.

This latest research effort requires validation of de Villiers' [2002] results, whilst improving the error discrepancies between the experimental and numerical analyses. Maintenance on the test rig has been performed, including the addition of a new pressure control system to ensure the correct cascade flow conditions and boundary conditions are obtained. Experimental pressure distribution measurements were performed, to validate previous work by de Villiers [2002] and to ensure the correct operation of the test rig. Experimental error was identified in de Villiers' [2002] suction surface pressure distribution, and new experimental pressure results were acquired.

Following the essential overhaul of critical rig components, experimental heat transfer tests were performed. The newly restored equipment produced new isothermal heat transfer coefficient results that validated the results of de Villiers' [2002].

Numerous CFD meshing techniques were investigated and implemented in FLUENT, to produce the numerical solution. The pressure correlation proved to be excellent with an average error of 3%. The varying cascade inlet turbulence intensity was identified as a major source of heat transfer error. Implementing this variance into FLUENT, a significant reduction in error was seen. The resulting average heat transfer error measured 12%, a major improvement from 29% error in 2002.

PREFACE

The author hereby states that this entire dissertation, unless specifically indicated to the contrary in the text, is his own original work, and has not been submitted in part or whole to any other University. This dissertation records the work carried out by the author in the School of Mechanical Engineering at the University of KwaZulu-Natal, Durban, from April 2003 to December 2004. This project was supervised by Prof. S. Govender and forms part of an ongoing study in the experimental and numerical field of turbine blade aerodynamics and heat transfer.

"We don't stop playing because we get old, we get old because we stop playing."

Unknown

ACKNOWLEDGEMENTS

The author wishes to express thanks to the following people:

Prof. S. Govender and Prof. J. Visser, for providing me with this excellent opportunity to perform research in the field of heat transfer and aerodynamics on turbine blades.

To the workshop staff of the School of Mechanical Engineering, for their advice and assistance with the maintenance of the experimental rig. A special thanks to Mr Michael Smith, for his invaluable expertise and help in many aspects of the experimental work. A further, special thanks, is also extended to Mr Colin Mandri, for being of great assistance with the data acquisition and electrical problems.

Mr D. de Kock and Mr M. Morris for their advice with the CFD work.

Mr Jacques de Villiers, for his advice with the project.

To my office colleagues, Krys, Vaughan and Justin, for providing me with times of laughter, support and advice. In stressful times, their company was always most welcome.

To my family, for their constant support and love. An enormous thanks is expressed to my parents, Bruce and Jenny, for providing me with my excellent educational opportunities. None of this would be possible without their support and love. To my brother and sister, for their interest and support in my work and constant laughter always.

Very special thanks to my girlfriend, Kerry. Her undivided love, support, encouragement, and laughter during my studies have been invaluable and are hugely appreciated. Your second opinions, continuous interest and knowledge provided immense guidance, thank you.

TABLE OF CONTENTS

NOMENCLATURE

$\frac{\Lambda^*}{\beta}$	calibration constant for the electrical analogue
α	thermal diffusivity
α_R	temperature coefficient of resistance
c	capacitance
c'	distributed electrical capacitance per unit length
d	thin-film gauge thickness
D	chord length
h	isothermal heat transfer coefficient
i	current
k	conductivity
k-ε	kinetic energy term (k) and kinetic energy dissipation rate (ε) in turbulence modelling
$k-\omega$	kinetic energy term (k) and specific kinetic energy dissipation rate (ε) in turbulence modelling
$\dot{m}$	mass flow
p_{op}	operating pressure
p	local (relative to p_{op}) gauge pressure
q	heat flux per unit area
$\dot{q}_s(t)$	heat flux rate per unit time
R	thin-film resistance
R	Specific gas constant
Re	Reynolds number
r'	distributed electrical resistance per unit length
ρ	density
T	temperature
t	time
θ	temperature change relative to ambient $(T - T_\infty)$
U	velocity
u_τ	friction velocity which is related to the shear stress and density by $\sqrt{\tau_0/\rho}$
μ	viscosity

V	voltage
y^+	non-dimensionalised distance from the wall
y	cell height perpendicular to the wall

Abbreviations

2-D	Two-Dimensional
CFD	Computational Fluid Dynamics
CUBRC	Calspan – University of Buffalo Research Centre, Inc
HP	High Pressure
I/O	Input/Output
LES	Large Eddy Simulations
LENS	Large Energy National Shock Tunnel
LP	Low Pressure
SA	Spalart-Allmaras
SKE	standard k-ε turbulence model
SSTKW	Shear-Stress Transport
TFG	Thin Film Gauges
RANS	Reynolds-Averaged Navier-Stokes equations
VI	Virtual Instrument (from LabVIEW)
VKI	von Karman Institute

Subscripts

0	reference or initial condition
1	thin film gauge material
2	substrate material
∞	ambient condition (space), or infinity (time)
in	inlet
out	outlet
op	operating
s	surface

Superscripts

'	For $T_0 = 298$ K
"	Corrected for $T_0 = 313$ K

CHAPTER 1

INTRODUCTION

The gas turbine engine has proven itself as a remarkable source of energy production and is fast becoming a reliable component of modern day living. Its uses are spreading from the more typical advanced aircraft propulsion units to commercial power generation and even drive systems in military vehicles. As a means of propulsion, the jet engine has allowed for travel around the globe in a matter of hours, providing major advantages in business and economic productivity. It is these demands and an aspiration for technological advancements that provides a continued need for improvements to gas turbine performance. These improvements can include increased service life, lower specific fuel consumption (SFC), better specific power output and increased efficiency. As described in Walsh and Fletcher[2004], these are some of the key parameters that define overall engine performance.

Related to these performance parameters, is the thermal efficiency, which helps the designer understand the variation of the performance parameters. Walsh and Fletcher [2004] define thermal efficiency as the rate of addition of kinetic energy to the air, divided by the rate of fuel energy supplied. Thermal efficiency increases as the turbine inlet temperature (TIT) and pressure ratio increase together (Walsh and Fletcher [2004]). With the SFC inversely proportional to the thermal efficiency, high fuel costs and /or weight, result in a classic desire for an increase in turbine inlet temperature (TIT) and pressure ratio. This fact is supported by Camci and Arts [1989].

A basic turbo-jet gas turbine engine layout is shown below in Figure 1-1.

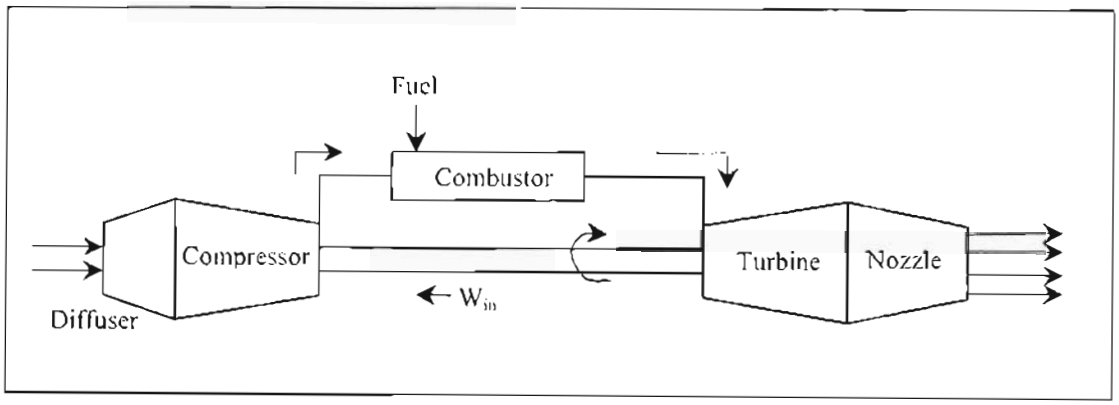

Figure 1-1: Basic schematic layout of a turbo-jet gas turbine engine
(Reproduced from de Villiers [2002])

The turbine has the task of extracting work from the high temperature, high energy, high pressure gas exiting the combustor. This work is used to drive the compressor and other components. Turbine inlet temperatures (TIT) of 1800 K, and a 25/1 pressure ratio are typical values in high performance jet engines (Camci and Arts [1989]). These high operating temperatures and pressures require the turbine blades to be cooled to within the material's thermal limitations of approximately 1300 K (Glezer et al [2001]). By cooling the blades, the blade metal temperature can be kept to a safe temperature and stress combination, within the material capability. At present this is done by cooling the blades using either internal convective and/or film cooling techniques which Glezer et al [2001] indicates; has permitted TIT's of 1700 K in the high-pressure turbine stage. However, these cooling techniques counteract the benefits of increasing the TIT, by utilising cooling air bled from the latter stages of the compressor, thereby reducing the overall cycle efficiency of the system. Ideally, as little cooling air as possible should be used, in order to optimise efficiency. Advanced high temperature resistant super alloys, such as nickel-based alloys with thermal coatings (**http://www.ueet.nasa.gov/parts.htm#turbine**), are now also used in turbine blades to permit higher operating temperatures, thereby reducing the mass flow of coolant required and improving the cycle efficiency.

Glezer et al [2001] found that even one percent coolant to mainstream mass flow ratio, can have significant effects on the performance and exit conditions of the high-pressure turbine stage. Walsh and Fletcher [2004] indicate penalties in isentropic efficiency ranging from 0.25-1.5% per 1% coolant to mainstream mass flow ratio, depending on coolant injection location. Coolant air-flow can incur a significant decrease in isentropic efficiency, since the turbine energy invested in compressing the cooling air, does not produce thrust power. Consequently, understanding the temperature distribution over the blade surface and establishing where the hot gas impacts the blade surface, allows for the cooling air to be more accurately directed. The heat transfer from the hot gas stream to the blade determines the temperature distribution. Designing a turbine blade for optimum heat transfer, will require the minimum necessary blade cooling air thereby maximising the engine efficiency. Stepka [1980] showed that the greatest improvements in blade life prediction can be achieved by improving the prediction of the external heat transfer coefficient. Hence the prediction of the heat transfer and its variation around the blade is of great practical significance.

The extensive research in turbine blade heat transfer distributions, presents further advantageous findings beyond that of the system thermal efficiency and specific thrust. Operation of a propulsion gas turbine engine is particularly expensive, where a majority of

the costs are due to maintenance. These costs would be considerably reduced if component life was increased and the service intervals were extended and accurately predicted (Tinga et al [2000]). Until now, a conservative approach to blade overhauls has had to be implemented by replacing blades more frequently than may have been necessary. Tinga et al [2000] presents a technique to predict turbine component life based on analysis of engine performance. The analysis tool consists of a sequence of software methods, which includes a Computational Fluid Dynamics (CFD) analysis to determine the heat transfer to the hot section components. This knowledge of the heat transfer distribution and mechanical blade properties, can be used to determine the thermal stresses and in turn, the blade life. Maya et al [1978], in a study of thermal fatigue life prediction, shows that the thermal stresses are due to the chordwise blade temperature distribution, proving to be six to seven times greater than the spanwise direction. Furthermore, knowing the heat loading on the blade, design recommendations can be made to extend the blade life, ultimately resulting in longer periods between costly replacements and providing cost effective maintenance.

During the late Nineteenth Century, axial flow turbines were developed with little knowledge of the fluid mechanics involved. The turbine efficiency was very poor, and in the early part of the Twentieth Century, the need for an aerodynamic approach to the design of turbines and compressors was realised. The first primitive cascade wind tunnels were therefore developed to provide aerodynamic test data for machines with higher efficiencies. Since then, extensive cascade and fully rotational rig tests have been performed resulting in current turbine cycle efficiencies now sitting at above 90% (Walsh and Fletcher [2004]).

Design of turbo machines involves the analysis of several variables such as, blade angles, Reynolds Numbers, free steam turbulence levels and many others. The design variables are so numerous that successful designs cannot result without careful analysis of these variables available from experimental testing. However, repetitive physical aerodynamic experimentation is costly and time consuming. These high costs persuaded early designers to generate performance correlations between the various variables, such as aspect ratio, stage loading, reaction, and axial velocity ratio (flow coefficient). For example, the Swindell or Smith chart shows contours of constant isentropic efficiency versus stage loading and axial velocity ratio, which designers can use as a comparator for different design options whilst optimising parameters and gaining judgement on the efficiency attainable for a particular design. Use of these correlation charts and formulae, allow designers to perform preliminary designs and analyses to optimise performance and costs. With the advent of computing power, modern Computational Fluid Dynamics (CFD) software codes are a desirable method of virtual testing. These provide another tool which designers can use to

predict the fluid flow and its associated variables, by solving numerically, the set of governing Navier Stokes equations. However, experimental verification of these CFD codes is still essential to ascertain their accuracy with reality.

Experimental aerodynamic cascade testing, together with the heat transfer coefficient distribution around the profile of the SMR-95 turbine blade, has been performed at the University of KwaZulu-Natal using a steady state, supersonic cascade rig. The rig makes it possible to simulate realistic engine conditions. This research effort forms part of an ongoing project, with work being performed by de Villiers [2002], Snedden [1995] and Stieger [1998]. Results trends show an improvement over previous years and the current effort requires validation of the previous results and more importantly, improved accuracy. This experimental work aims to serve as an experimental database against which CFD codes can be verified.

A numerical solution has been performed using a commercially available CFD package, FLUENT. The subsequent chapters in this thesis include a literature survey and theory pertaining to the research, followed by a description of the experimental equipment. The experimental results are then presented and discussed, before the CFD modelling and results are discussed. A conclusion and recommendations for further work are given in the final chapter.

CHAPTER 2

LITERATURE SURVEY

2.1 Overview

Research activity involving heat transfer measurements, is generally divided into two related categories: experimental measurements and numerical predictions. This current heat transfer research effort is no different. With this in mind, this literature review follows this trend. Experimental heat transfer measurements are reviewed, with particular interest in the experimental work performed on the supersonic cascade rig available at the University of KwaZulu-Natal, Durban. The previous work of Snedden [1995], Stieger [1998], and de Villiers [2002] provides useful literature and information pertaining to the history and progression of the heat transfer results. Experimental heat transfer measurements and their numerical CFD comparisons are presented, reporting some of the significant findings of past turbine blade heat transfer research.

Transient measurement of the heat transfer into a turbine blade requires a temperature gradient to be developed between the blade surface and the air stream. Rapidly exposing the surface of the blade to a hot air flow, generates a heat flux into the blade with a corresponding heat transfer coefficient. There are various methods of creating this temperature gradient, or rapid change in heat flux and this literature survey reviews some of the more common and more successful facilities used amongst the heat transfer community. In addition to the various testing facilities used for turbine blade heat transfer testing, there are numerous techniques of measuring the heat transfer coefficients. These, together with their respective researchers, will be discussed in the literature review.

Cascade facilities are a reliable means of turbine blade flow data. The techniques developed in cascade facilities often progress further to be implemented within full-stage rotating rigs. The economic benefit of cascade testing, although potentially costly (technique dependent), is considerable. Cascade testing, in comparison to full-scale rotational rigs, has significantly lower cost and time implications. Yet, the significant benefit of cascade testing is the fact that the complex 3-dimensional flow field in a turbine stage is simplified to a 2-dimensional flow field by the removal of spanwise variation of flow variables (total pressure, temperature, flow angle, and Mach number or velocity). This removal of additional variables allows insight into the variables being examined, such as incidence angle, turbulence

intensity, Reynolds number, and Mach number as investigated by Consigny and Richards [1982], without introducing elements that may complicate the analysis. Also, the testing of a few blades in cascade permits larger chords than the equivalent profile geometry in a full annulus for the same airflow use. Cascade tests have the promise of providing detailed measurements over blade surfaces as well as the incoming flow. This results in a clear interpretation of flow patterns and aids in characterisation of the flow phenomenon. With reliable experimental results available from cascade testing, CFD codes can be accurately validated. Furthermore, cascades boast an educational value to any junior engineer and a quicker understanding of turbine flow dynamics is achieved, as would otherwise not be achieved in fully rotational testing.

2.2 Experimental facilities

2.2.1 Light piston compression tunnels

The turbomachinery and propulsion department at the von Karman Institute in Belgium uses a short duration, isentropic compression tube cascade facility CT-2.

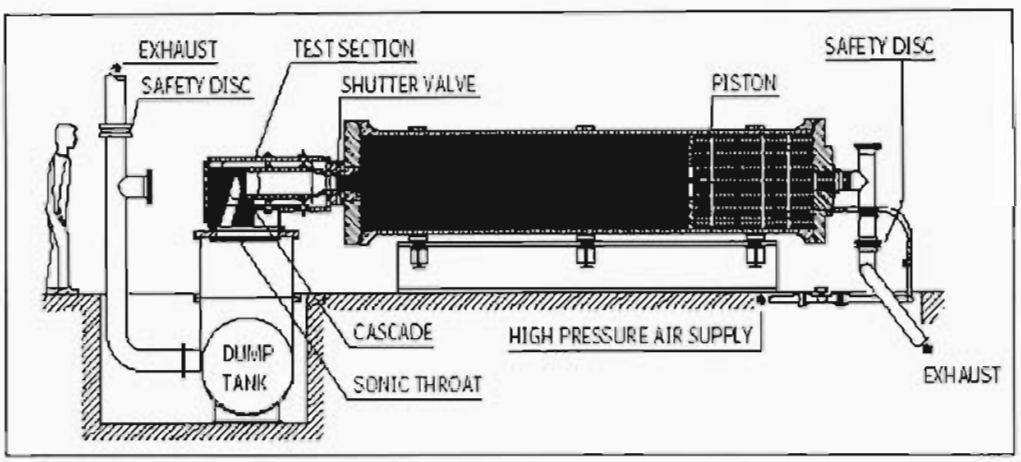

Figure 2-1: The CT-2 light piston, isentropic compression tube at the von Karman Institute (Reproduced from http://www.vki.ac.be/tu-dept/index.html)

With this experimental technique, and this facility in particular, compressed air is used to drive the lightweight piston forward within a 5m-long, 1m-diameter cylinder, nearly isentropically compressing the air in front of the piston. Once the compressed air reaches the appropriate pressure and temperature to generate the test conditions, a fast acting shutter valve is actuated that releases the heated, high-pressure air over the cascade blade model. This sudden exposure of the blade to heated gas creates the step change in flux into the blade. Steady free-stream flow conditions are maintained for 100 to 800 ms, and can be varied

between 300K and 600K and between 0.5 and 7 bar. A sonic cascade exit throat ensures constant mass flow and the 5 m^3 dump tank allows for downstream pressure adjustments with a range of 0.1-3 bar. Details of this facility and its principles of operation are described in Jones and Launder [1973] and Consigny and Richards [1982]. Consigny and Richards [1978] and [1982] conducted short-duration measurements of heat transfer to a gas turbine rotor blade using this facility. Measurements of heating to cooled gas turbine surfaces and measurements of heat transfer rate to a gas turbine rotor blade were conducted in these respective reports. At the same facility, Camci and Arts [1985] conducted an experimental heat transfer investigation around the film-cooled leading edge of the same rotor blade section as tested by Consigny and Richards [1982]. Camci and Arts [1989] followed with an experimental convective heat transfer investigation around the same film-cooled gas turbine blade.

The CT-2 facility is used to perform pressure, temperature, turbulence and heat transfer measurements. High-speed data acquisition records the relevant data and corresponding data may be matched with the use of Schlieren visualisations. The Schlieren flow visualisation technique uses a light source, dependent on the colour scheme required. This light source is focused through an adjustable slit and a parallel beam of light is passed through the cascade blade test section that is supported by transparent sidewalls. Positioning of various parabolic mirrors, focuses the image onto a knife-edge cut-off. Density gradients within the cascade flow field bend the light rays, which has the effect of producing lighter or darker areas on the screen according to the density differences. This allows flow visualisation where shocks and other flow phenomenon can be observed.

Ligrani et al [1982] conducted heat transfer research using this particular rig at the von Karman Institute. Significant reference is made to Ligrani et al [1982] in the subsequent sections on heat transfer measurement techniques. Oxford University utilises an isentropic light piston type test facility for intermediate short-duration tests, with test times on the order of 300ms to 1 s. Full-scale Reynolds and Mach numbers, and flow-to-wall temperature ratios are achieved during the test duration. The facility is well documented in Schultz et al [1973], [1977] and [1981]. Schultz and Jones [1973] conducted numerous short-duration heat transfer measurements on this particular rig.

2.2.2 Shock tube facilities

Test times on the order of 2 to 50 ms are achieved at Calspan – University of Buffalo Research Centre (CUBRC) and now Ohio State University. Experimental testing is

conducted using a short-duration shock-tube tunnel as the source of heated, pressurised air. Professor Dunn of the University, has pioneered the use of this particular short duration technique to obtain fundamental measurements on full stage rotating turbines (http://www4.nationalacademies.org). The shock tube technique is capable of operating in either blow down mode for aerodynamic measurements, or reflected shock mode when heat transfer measurements are required. The facility makes use of a 100-foot long shock tunnel attached to a 32 foot long by 9-foot diameter dump tank in which the turbine rig is mounted. The facility can be seen in Figure 2-2. The shock tube approach uses a shock wave to compress and heat the gas. This shock wave is produced by a rapid release of a high velocity driver gas of either hydrogen or helium. This high velocity driver gas compresses the test gas. In shock mode, the shock wave is reflected, creating a reservoir of high temperature, high-pressure gas. In both blow down and shock mode, the gas is expanded through a nozzle containing the test section. This year, the lab is preparing for an experimental program undertaking measurements on a fully cooled turbine stage.

Snedden [1995] outlines the operation and use of the above mentioned rigs in more depth. These two particular facilities are well developed and documented, the results having been instrumental in experimental cascade and fully rotational turbine measurements.

Figure 2-2: The former Calspan turbine test facility, now residing at the Gas Turbine Laboratory in Ohio, USA (Reproduced from http://gtl.eng.ohio-state.edu/ttf.html)

2.2.3 Continuously running facilities

The disadvantage in the large rig arrangements described above, is that large amounts of storage space are required to house the large test-gas compression and heating facilities. This is evident from Figure 2-2. The experimental research presented in this dissertation, was conducted on a continuously running cascade facility. This involves a cascade that is continuously exposed to heated air flow.

The cascade operates within a plenum under vacuum and the heated gas is generated by a compressor, driving a circulated flow within the chamber. This recirculation of flow, means that the large space requirements of the blow down and shock tunnel tube are not necessary. This technique, together with a heat transfer measurement system, has effectively been implemented in continuous projects of recent years. A full description of the experimental equipment and the operating procedures are given in Chapter 3 of this dissertation.

To generate the realistic engine wall to gas temperature ratios, the test blade is cooled within a cooling box supplied by cooling air. The test blade section instrumented with thin-film heat flux gauges, is rapidly ejected from the cooling box and into the hot gas stream by actuating a pneumatic ram. This test section is mounted upon an un-instrumented blade replica. Prior to taking measurements, the un-instrumented profile is within the cascade and then displaced by the instrumented section when pneumatically plunged. Doing this means that the flow is not disturbed and the flow characteristics around the blade surface are fully developed. The thin-film gauge method of measuring the heat flux is described in the subsequent section.

Graziani et al [1980] conducted heat transfer measurements on the endwall and airfoil surfaces using a large scale, low speed, open circuit cascade wind tunnel facility. This facility was used to measure the complex heat transfer pattern on the airfoil and endwall surfaces of a large scale (approximately ten times aircraft engine size) turbine blade rectilinear cascade. Two inlet boundary layer thicknesses were investigated. A thin endwall inlet boundary layer (approximately 2 percent airfoil span) was generated by shortening the inlet duct and installing a boundary layer bleed system upstream and parallel to the cascade inlet plane. Langston et al [1977] conducted early subsonic flow measurements in the same large scale, low speed, open circuit cascade wind tunnel facility as that which was used by Graziani et al [1980]. This study focused on flow visualisation in an effort to evaluate the three-dimensional nature of the cascade flow-field.

2.3 Thin-film gauges

Many heat transfer measuring techniques have been tried and implemented. Some of the most popular techniques are reviewed by de Villiers [2002]. This review focuses specifically on the thin-film heat flux gauge as a tool for heat flux measurement, since this is the technique implemented at the University of KwaZulu-Natal. Development work on thin-film heat flux gauges began in the 1950's. Initial use of the gauge involved measurements of surface temperature. Vidal [1956] was amongst one of the first to implement the thin-film gauge for heat flux measurement on short-duration facilities such as shock tubes.

The thin-film gauge is essentially a resistance thermometer. The gauge is a device consisting of a thin metal element having a very small heat capacity, attached to the surface of a good insulator. Applying a constant current to the gauge, a change in temperature will result in a corresponding voltage change. Proper calibration of the metal film means that the temperature history of the insulator surface can be determined. Applying existing theory for transient heat conduction and making assumptions about the material properties of the insulator, the heat flux to the insulator surface can be calculated.

Schultz and Jones [1973] present two methods of constructing thin-film gauges using vacuum deposition or hand painting. Ligrani et al [1982] describes the construction of thin-film gauges by hand painting platinum onto an insulator of machinable glass ceramic, Macor. This material provides for easy machining purposes and is the test blade insulator used at the University of KwaZulu-Natal. A copy of the thermal, machining and material properties are given in Appendix 1 of Snedden's dissertation [1995]. Gauges made from hand painting can be susceptible to irregularities in surface area, thickness and temperature coefficient of resistance. Snedden [1995] implemented a very cost effective technique of gauge construction. Thin strips of platinum, 1cm high and 1 mm wide, were painted on to the Macor substrate and fired in an oven separately. Extreme caution and attention to detail is required during the gauge construction. Snedden [1995] gives a full description of the gauge construction technique used.

Schultz and Jones [1973] indicate that the data from the thin-film gauges may be processed in two different ways. The voltage, proportional to the substrate surface temperature may be processed directly into digital form to numerically reconstruct the heat flux. Alternatively, the gauge voltage may be processed via an analogue circuit, its output recorded as a signal proportional to the heat flux into the substrate. The technique implemented at the University of KwaZulu-Natal is one developed by Ligrani et al [1982]. This system takes the gauge

voltage output and converts it, via an electrical analogue circuit, to a signal proportional to heat flux. The heat flux signal is recorded and used to numerically reconstruct the surface temperature. Plotting a heat flux versus temperature graph, a least squares straight line fit is extrapolated back to the original surface temperature.

This represents the heat flux (q) into the blade and using equation 2-1, the isothermal heat transfer coefficients (h) can be calculated.

$$q = h\left(T_{gas} - T_{wall}\right) \qquad (2\text{-}1)$$

Ligrani et al [1982] provides a full description of the principles of thin-film gauge operation presented by Schultz and Jones [1973], as well as the heat transfer theory, gauge construction, calibration, measurements and the associated electronics. The experimental heat transfer technique developed at the former University of Natal by Snedden [1995] makes use of this technique. The analogue circuit boards were built based on the design presented by Oldfield et al [1982] and much attention was focused on noise reduction in the data acquisition and analogue circuits. The boards were modified by Snedden [1995] to reduce noise.

Dunn [1995] highlights the use of three representative thin-film gauges, providing extensive descriptions on the method of construction, calibration, measurement and signal processing. The specific type of thin-film gauge used by various associations varies according to the test times and type of experimental facilities used. In the event of the University of KwaZulu-Natal rig playing any role in future heat transfer measurements, specifically in turbine internal cooling, review of the above outlined literature will be essential to the successful construction and implementation of accurate heat flux measurements.

Macor, the substrate material used for the thin-film gauges at the University of KwaZulu-Natal, is easily machinable. The use of this material is acceptable where stress levels in the component are low. However, Macor does not boast sufficient strength for it to be applicable in rotating rig equipment. Furthermore, it is difficult to construct complex blade geometry designs for internal cooling purposes. Doorly and Oldfield [1986] [1987] and Doorly [1987] developed a gauge consisting of thin-film gauges deposited on a vitreous enamel-coated metal to overcome this obstacle.

The extreme care and precision required in the complex manufacture of thin-film gauges, together with the calibrations needed and the extreme accuracy required for reliable heat transfer measurements; has led to the search for new types of gauges. Many of these new techniques have not encompassed the frequency response to be used in rotational turbine measurements. The thin-film gauge has thus proven itself as an invaluable experimental gauge and may not be replaced any time soon. Thin-film gauge accuracy is on the order of ± 5% of the reading, which is ahead of the slightly lagging predictive techniques used.

2.4 Published heat transfer work

There is an abundance of published experimental and numerical heat transfer measurements. Harasgama and Wedlake [1990] presented heat transfer measurements performed on a highly loaded nozzle guide vane. The measurements were performed in an annular cascade using an isentropic light piston rig. The influence of Reynolds number and Mach number on the heat transfer distribution was investigated and proved to be significant.

Brown and Burton [1978] measured experimentally, the effects of free-stream turbulence intensity and velocity distribution on heat transfer to curved surfaces. Local heat transfer was found to increase with increasing free-stream turbulence intensity for a laminar boundary layer region, however, remained unaffected in a wholly turbulent boundary layer. In addition, turbulence intensity, velocity distribution, and Reynolds number affected the onset position of transition from a laminar to turbulent boundary layer.

In a study aimed at revealing the local variations of heat transfer associated with regions of strong three-dimensional flow, Graziani et al [1980] used heater strips and thermocouples to determine the heat transfer on a blade in a steady state turbine cascade. Flow visualisations, static pressure and heat transfer measurements were performed at two different inlet boundary layer thicknesses. These measurements were conducted at a Reynolds number typical of gas turbine operation. The accuracy and spatial resolution of the experiments were sufficient to disclose important details pertaining to the flow field. Results showed that the passage secondary flows greatly influence the heat transfer to the endwall and suction surface of the airfoil. The airfoil pressure surface heat transfer, however, was unaffected by the secondary flows, exhibiting a heat transfer pattern suggestive of two-dimensional flow. The experimental mid-span Stanton numbers were compared to the predicted values of the numerical Boundary-Layer code STAN 5, developed by Crawford and Kays [1976] at Stanford University. Good agreement between the measured mid-span data and the predicted values was seen over a majority of the profile. The largest discrepancy was found on the

suction surface, downstream of the minimum pressure location. The measured heat transfer values prove to be lower in this region, thought to be due to flow convergence toward mid-span, causing the mid-span boundary layer to grow more rapidly. The convergence of the suction surface streamlines toward mid-span can be seen on the flow visualisation. The rapid flow convergence on the suction surface was shown to occur at the same location for both inlet boundary layer sizes. This region and the region downstream are associated with the three-dimensional passage vortex as it travels off the endwall up onto the suction surface.

STAN 5 is a numerical Boundary-Layer code used for the solution of the boundary layer equations. Boundary-layer codes use the calculated pressure and velocity gradient along the blade surface as input. The program is a development of the original developed by Patankar and Spalding [1967]. The program accommodates for the calculation of a large variety of two-dimensional flows, including laminar and turbulent flows with provision to predict transition. Turbulence modelling includes a Prandtl mixing-length scheme throughout the flow, or a turbulent kinetic energy (TKE) scheme, or an eddy diffusivity function. The mixing–length scheme is used in the sublayer region for the latter two models.

Schmidt and Patankar [1991] describe transition as a complex phenomenon influenced by Reynolds number, free-stream turbulence, pressure gradient, surface roughness and streamline curvature. The most dominant factor influencing boundary layer transition is the magnitude of free-stream turbulence (Schmidt and Patankar [1991]). Schmidt and Patankar [1991] conducted an analysis of the capability of $k-\varepsilon$ low-Reynolds-number (LRN) turbulence models to predict transition in boundary layers subjected to free-stream turbulence. Schmidt and Patankar [1991] investigated the sensitivity of transition to starting profiles of k and ε, the sensitivity to starting location as well as the response to free-stream turbulence. In the analysis, two representative models, namely Jones and Launder [1972, 1973], and Bremhorst [1981], were employed to assess the ability of $k-\varepsilon$ LRN turbulence models to predict accurate results. Jones and Launder [1972, 1973] first introduced these so-called "low-Reynolds number" functions into the $k-\varepsilon$ two-equation turbulence model. Patel et al [1985] reviews a variety of other models introducing similar functions as suggested by researchers. These functions provide a modifying influence on the $k-\varepsilon$ equations in the near-wall region, so that near-wall damping effects are simulated. The $k-\varepsilon$ LRN turbulence models predict transition through the transport of turbulent kinetic energy from the free-stream into the near-wall region and the subsequent response of the LRN functions in the equations. The results of the Schmidt and Patankar [1991] study show that the two models analysed, both predict transition lengths significantly shorter than

those found from experiment. Both models accurately predicted the aspects of boundary-layer transition, showing the onset of transition to move upstream with increasing turbulence intensity. However, for calculations started at low Reynolds number, transition was generally predicted at unrealistically early locations, which realised the limitations of the, then current, $k-\varepsilon$ models and the need for further development.

Consigny et al [1978] performed experimental measurements of heat transfer to cooled gas turbine surfaces. The measurements were undertaken in the VKI isentropic light piston tunnels CT1 and CT2, the latter of which is described in 2.2.1. The heat transfer measurements were obtained from the transient surface temperature of thin-film platinum resistance thermometer gauges. the same technique that is implemented at the University of KwaZulu-Natal rig. The study of interest demonstrated the effect of Mach number, Reynolds number, wall to recovery temperature ratio, surface curvature, and pressure gradient on the heat transfer measurements. For the high-pressure case tested (5.2 bar). a fully developed turbulent boundary layer was shown to exist, without flow relaminarisation. The results were compared to existing prediction techniques. Predictions using both the methods of Spalding and Chi [1964] and Bradshaw and Unsworth [1974], showed favourable comparisons with better prediction in trend and level obtained from the Bradshaw and Unsworth [1974] method. In the low-pressure case (1.2 bar), the boundary layer was found to undergo transition with relaminarisation. In comparing the prediction results, Spalding and Chi [1964], although ignoring pressure gradient effects, gave the best results. The Bradshaw and Unsworth [1974] method predicted pressure gradient flows well, yet gave errors of over 50% in the relaminarisation region.

Four years later, Consigny and Richards [1982] presented a useful paper presenting detailed heat transfer measurements on a gas turbine rotor blade. Under well controlled conditions, the same VKI short-duration isentropic light piston tunnel CT2 was utilised to vary the Mach number, inlet flow angle, Reynolds number, and flow turbulence level. Changing the total pressure varied the Reynolds number of the inlet flow, and adjusting the pressure in the exit dump tank regulated the cascade outlet Mach number. Blade surface pressure measurements along the midspan of the blade were taken using static pressure tappings. The heat transfer to the blade was, once again, measured using thin-film platinum resistive thermometer gauges. Consigny and Richards [1982] describe the fundamental flowfield characteristics using the heat transfer distribution. The high levels of heat transfer at the stagnation point, or leading edge, are no surprise to any turbine heat transfer researcher, and are as a result of the leading edge flow impingement. Either side of the leading edge the heat transfer falls rapidly corresponding to laminar heating. For a subsonic outlet Mach number (M_{2is}=0.62), transition

on the suction surface was noted to occur earlier for the maximum turbulence intensity test case (Tu=5.2%) than for smaller values of Tu. This agrees with the LRN predictions of Schmidt and Patankar [1991]. Consigny and Richards [1982] identify the onset of transition at this point due to the rapid increase in heat transfer. For Tu=0.8%, however, the heat transfer coefficients continue to diminish along the suction surface, considerably near the trailing edge, possibly signifying boundary layer separation at this point.

On the pressure surface a separation bubble, immediately downstream of the leading edge, results in low heat transfer levels with an expected high heating level thereafter, caused by turbulent reattachment of the boundary layer. The separation bubble and heat transfer jump was shown to nearly disappear at Tu=5.2%. An interest finding, which agrees with Brown and Burton [1978] and Graziani et al [1980], is that downstream of reattachment, the heat transfer in the turbulent boundary layer remains unaffected by any changes in turbulence intensity.

The influence of Reynolds number was also investigated which reported that transition also advances upstream with increasing levels in Reynolds number. A pressure surface separation bubble occurred for all test cases with turbulent reattachment of the boundary layer. For the lowest Reynolds number case, however, after reattachment the heat transfer decreases with distance indicative of relaminarisation, possibly due to the strong favourable pressure gradient.

A low Reynolds number version of the $k-\varepsilon$ two-equation turbulence model was used for the prediction of the heat transfer. The LRN corrections used were those of Jones and Launder [1972, 1973]. Prediction results show that the laminar heat transfer is not affected by the free-stream turbulence. On the suction side, the position of transition is not well predicted, repeatedly predicting transition too early, as reported by Schmidt and Patankar [1991]. Overall, the prediction of heat transfer in the transition region was not good. On the pressure surface, in the case of Tu=0.8%, the heat transfer is under predicted by 30%, yet for the case of Tu=5.2%, heat transfer appears to be satisfactorily predicted. This influence of Tu on heat transfer in the turbulent boundary layer region is interesting, since experiment showed negligible influence of Tu.

Camci and Arts [1985] and [1989] performed an experimental heat transfer investigation around the same film-cooled rotor blade section as tested by Consigny and Richards [1982]. Convective heat transfer to the blade in the absence and presence of film cooling was investigated. The studies discovered that, even in the absence of coolant emission, the

suction surface boundary layer was affected by the existence of the leading edge injection holes. The pressure surface boundary layer, however, was influenced by the favourable free-stream pressure gradient. The convective heat transfer distribution proved to be largely influenced by the coolant to free-stream temperature ratio. In addition, for low coolant to free-stream mass flow ratios, film cooling proved to be effective in reducing the heat transfer. However, for higher coolant to free-stream mass flow ratios, increases in local heat transfer were measured immediately downstream of the cooling holes.

Hodson [1985] investigated the boundary layer near the leading edge of a high-speed turbine blade. Cascade measurements were carried out with an array of surface-mounted, constant-temperature, hot-film anemometers. The measurements were interpreted with the aid of inviscid and viscous prediction codes. The effects of Reynolds number, compressibility, incidence, and free-stream turbulence on the boundary layer were presented in the study. Increasing the inlet free-stream turbulence intensity proved to significantly reduce the length of the leading edge separation bubbles.

Wang et al [1985] modified the two-dimensional, boundary-layer program, STAN5, to incorporate a LRN version of the $k-\varepsilon$ two-equation turbulence model, for the predictions of flow and heat transfer around turbine airfoils. Hylton et al [1983] indicated that in an initial study by Jones and Launder [1972], their LRN model did not satisfactorily predict the heat transfer over the C3X airfoil. This was attributed to the improper prescription of the initial and boundary conditions for turbulent kinetic energy (k) and its dissipation rate (ε) at the airfoil leading edge. Modified initial and boundary conditions were introduced in this study by Wang et al [1985], in conjunction with a two-zone model to treat the k and ε variables in the near wall region. Wang et al [1985] performed heat transfer predictions for a flat plate, the C3X airfoil of Hylton et al [1983] and the Turner airfoil of Turner [1971]. The results of interest in this research are those of the two airfoils. The predictions were compared to the experimental data of the C3X airfoil (Hylton et al [1983]) and the Turner airfoil (Turner [1971]). In the case of the C3X airfoil, the heat transfer is well predicted, especially the progressive increase in heat transfer with turbulence intensity on the pressure surface. The suction surface, however, is over predicted, believed to be as a result of streamline surface curvature. In addition, the leading edge heat transfer was over predicted. For the Turner airfoil, the heat transfer was well predicted except at the trailing edge. It was reported that the model of Wang et al [1985] did not over predict the leading edge heat transfer for the Turner airfoil, since the Reynolds number for this case was lower than that of the C3X airfoil. This resulted in slower flow explaining the enhanced performance of the

LRN model. Generally, the model demonstrated capability to predict heat transfer trends on both sides of the airfoil, yet it was suggested that prediction could be improved if a better velocity boundary-layer input was used for the Boundary-Layer code.

Nicholson et al [1984] utilised transient methods in the Oxford cascade tunnel to investigate the flow on two different blade profiles, intended to minimise heat transfer to their pressure surfaces. Effects of Reynolds number, free stream turbulence and Mach number on heat transfer were investigated. Two profiles were designed, each minimising the heat transfer to the pressure surface using different boundary layer control techniques. Design of the pressure surface boundary layer for the high stagger blade, was intended to reduce heat transfer by means of relaminarising. The low stagger blade was designed for the same effect by increasing the thickness of the turbulent boundary layer. The results showed that significant reductions in pressure surface heat transfer could be achieved by appropriate boundary layer optimisation, without aerodynamic losses.

Bellows and Mayle [1986] used heater strips and thermocouples to investigate the heat transfer downstream of a leading edge separation bubble. The test body had a cylindrical semicircular leading edge which smoothly joined two parallel flat surfaces. The test section was positioned such that flow symmetry was achieved around the top and bottom of the blade. Flow visualisations were performed as well as static pressure tapping measurements. Their experimental results disclose information about the flow characteristics and heat transfer associated with a leading edge separation bubble.

2.5 Published Heat Transfer Cascade Work at the University of KwaZulu-Natal rig

Research on turbine blade heat transfer distribution, specifically on the University of KwaZulu-Natal rig, dates back to 1995. Snedden [1995] developed and refined the high speed cascade facility originally designed by Van der Steege [1990]. Snedden [1995] implemented a new guillotine blade plunging technique, to rapidly plunge the cooled instrumented blade into the hot gas stream. Using thin-film heat flux gauges and the analogue boards developed by Oldfield et al [1982], Snedden recorded the heat flux into the blade. Snedden focused much effort on noise reduction and modified the boards for better performance. The method of gauge construction used and the heat transfer measurement and signal processing principles, were those developed by Schultz and Jones [1973] and Ligrani et al [1982].

Snedden [1995] conducted heat transfer measurements on the Atar 09K50 Nozzle Guide Vane (NGV). Uncertainty was shown to be 10%. Laminar flow areas revealed uncertainty of ± 10% but variance of as much as ± 20% in other areas was noted. In turbulent regions and at chord lengths greater than 70%, repeatability of ± 30% was observed. Snedden [1995] showed turbulent transition at approximately 50% of the suction surface; this appears to be where the greatest variance is seen due to the turbulent nature of the flow. It was suggested that perhaps the gauge substrate thickness at the trailing edge could be a source of error. This could assist in conduction effects between the pressure and suction surfaces. Use of a new High Turning Angle (HTA) SMR-95 blade then followed. This blade had a thicker trailing edge. It was chosen as an internally cooled rotor blade test case following the work done on the Atar 09K50 NGV test case, since the South African Air Force and the Russians re-engined an F1 and Cheetah with the SMR-95, the power plant of the Mig 29. The external heat transfer needed to be verified. This is the blade profile currently under investigation in this dissertation.

Snedden conducted further work on the University of Natal rig from 1995 – 1998. Snedden [1998] presents the results from measurements of the inlet flow angularity and velocity, as well as the turbulence intensity of the flow field in the SMR-95 cascade. Periodicity tests of the static inlet and outlet pressures were also conducted by Snedden [1998]. The results showed very poor periodicity for the inlet and outlet when using the two-piece suction side tailboard. Using the straight suction side wall tailboard, an improvement in periodicity was seen, with approximately 500 Pa variation at the exit plane.

Snedden [1998] conducted turbulence intensity experiments on the SMR-95 cascade inlet. Constant current hot-wire probes were used, which measured velocity as a change in voltage. The voltage changes as a function of the forced convection cooling experienced by the heated wire. Turbulence intensity tests at quarter span, mid-span and three-quarter span were measured across the inlet of the cascade. The tests were conducted at varying total pressure and drive shaft rpm and the turbulence intensity was varied by inserting turbulence generating rods at the inlet.

The results for no turbulence grid, drive shaft of 1500 rpm, and a total pressure of 0.4 bar, are displayed in Figure 2-3. These turbulence results, shown as percentages, show a strong influence from the inlet total temperature and pressure probes, mounted as shown at the inlet of the cascade. The level of turbulence either side of the instrumented blade is thus reason for concern. Figure 2-3 shows this where the rightmost passage mid-span turbulence level was only 1.3%, compared to the middle passage mid-span turbulence measurement of 5.3%.

At the test conditions of the current research (no turbulence grid, drive shaft speed of 2500 rpm, total pressure 0.4 bar), the turbulence intensity measurement is 3% at the leading edge mid-span. This result however, is suspect since the turbulence intensity measurements at 2500 rpm, lay in the fully saturated region of the hot wire probe calibration curve.

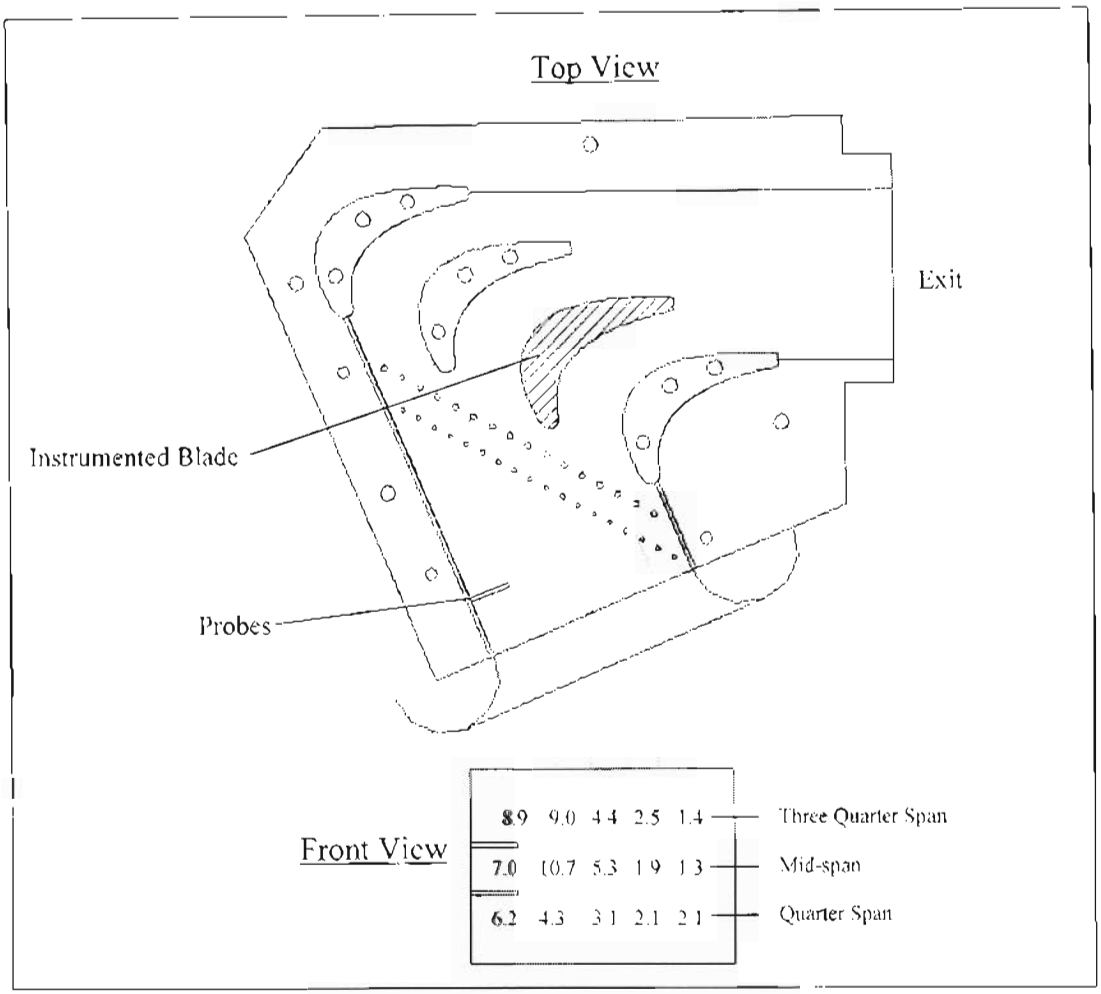

Figure 2-3: Turbulence intensities measured by Snedden [1998] at various leading edge measurement stations in the cascade inlet

Stieger [1998] performed flow visualisations and blade static pressure measurements to characterise the flow within the cascade. In addition, the technique for heat flux measurement developed by Snedden [1995], was used to provide validation of Snedden's [1995] results. The influence of Reynolds number, free stream turbulence intensity and the position of a boundary layer trip were varied to investigate the effects on the boundary layer flow. The heat transfer results validated Snedden's [1995] technique but contrasted the numerically computed predictions from a code used at CSIR. Although the experimental results did not agree well with predicted values, the techniques developed provided useful information regarding the flow phenomenon around the blade surface.

In 2002, de Villiers [2002] conducted upgrading and restoration of the rig and data acquisition systems. The pressure and heat transfer distribution around the blade was measured. The work of Snedden [1995], and Stieger [1998] was validated and the experimental results compared with the numerical prediction, generated using FLUENT. The new experimental pressure distribution correlated excellently with the prediction with all errors within 5%.

CFD heat transfer results generated by de Villiers [2002] did not match the experimental values measured by Snedden [1995] and Stieger [1998]. They did however; follow the trends of de Villiers' experimental values with an average error of approximately 29%.

2.6 Computational Fluid Dynamics (CFD) modelling

2.6.1 Choice of turbulence model

2.6.1.1 1-Equation (Spalart-Allmaras) model

The Spalart-Allmaras turbulence model is a 1-equation model and is mainly intended for aerospace/turbo-machinary applications. It has been shown to produce good results for boundary layers with adverse pressure gradients and separation, as well as supersonic/transonic flows over airfoils. From the known flow phenomenon of the SMR-95 and the above reasons, this model is suitable to implement and investigate. For the Spalart-Allmaras model, the option of vorticity/strain based production of the eddy viscosity was chosen. This option reduces the effect of rotation on turbulence. The Spalart-Allmaras model is capable of calculating the steep near-wall profiles as long as the mesh is sufficiently fine.

2.6.1.2 2-Equation ($k-\varepsilon$ and $k-\omega$) turbulence models

Various turbulence model options are available from the $k-\varepsilon$ model. These are the Standard (SKE), Realizable (RKE), and the Renormalization Group (RNG) models. The SKE is the most widely used turbulence model for industrial applications. It is a two-equation model and has been shown to perform poorly for flows with strong separation, large streamline curvature, and high pressure gradients. These phenomenons are known to occur

on the turbine blade profile being studied, so this model was discarded as an option. The RKE and RNG are improvements made to the SKE model and are more suitable.

The RKE and RNG $k-\varepsilon$ models have shown to be superior over the SKE $k-\varepsilon$. Between the RKE and RNG $k-\varepsilon$ models, the RKE is more likely to provide the best performance for flows with adverse pressure boundary layers and separation. Furthermore, initial studies suggest the RKE is superior for numerous validations of separated flows and secondary flows. Therefore, the RKE $k-\varepsilon$ model was chosen as a turbulence model to be used.

Two versions of the $k-\omega$ turbulence model are available. These are the Standard $k-\omega$, and the Shear-Stress Transport (SST) $k-\omega$ models. These models are generally implemented in the aerospace and turbo-machinery applications. The SST $k-\omega$ model was developed to incorporate the accurate capability of the Standard $k-\omega$ model in the near wall region, and the free-stream effectiveness of the $k-\varepsilon$ model in the far-field. This makes the SST $k-\omega$ model more accurate for a wider range of flows such as adverse pressure gradients, transonic shocks, and airfoils. The SST $k-\omega$ model was thus also considered for the numerical solution.

2.6.2 Near wall treatments for turbulent flows

It is in the near wall region where the solution variables have large gradients. Therefore it is very important to model the flow in this region accurately if any success in the prediction is expected. The near wall modelling technique affects the reliability of the solution significantly. The Spalart-Allmaras and $k-\omega$ models were designed to operate throughout the entire boundary layer given that the near wall mesh is fine enough. However, the $k-\varepsilon$ turbulence models are more reliable in regions further away from the walls, where the flow is generally turbulent. The boundary layer sublayer (see Figure 2-4) is a laminar region, therefore, near wall modelling is performed to make the $k-\varepsilon$ model more suitable to solving the viscous effects of the wall.

Generally there are two methods of modelling the near wall region, namely, the Wall Function approach, and the Near-Wall Model approach. The Wall Function method assumes fully developed, attached turbulent flow, and models the effect of the laminar sublayer on the turbulent boundary layer at the edge of the sublayer, at y+ around 30. The viscosity affected region of the viscous sublayer and buffer layers, are therefore not meshed and hence not

solved for, thereby saving the fine meshes required for the Near Wall Model. The subdivisions of the near-wall region are shown in Figure 2-4.

Semi-empirical formulae are used to link the viscosity affected region and the fully turbulent region. The Near-Wall Model approach solves for the entire region, from the turbulent core to the wall. This means that the enhanced near–wall formulation is valid throughout the near-wall regions. This is essential for modelling heat transfer accurately (particularly separated flow and developing boundary layer flow), since the boundary layer flow greatly affects the corresponding heat flux into the blade surface.

For enhanced near-wall modeling, the mesh is required to be fine enough in order to solve the viscous sublayer. It is thus recommended that for the enhanced wall treatment, the centroid of the wall-adjacent cell should be located within the viscous sublayer (y^+=1). The wall function approach requires the first cell centroid to be within the log-law layer (y^+=30–300). This shows that the wall modeling technique chosen, drastically affects the meshing technique used.

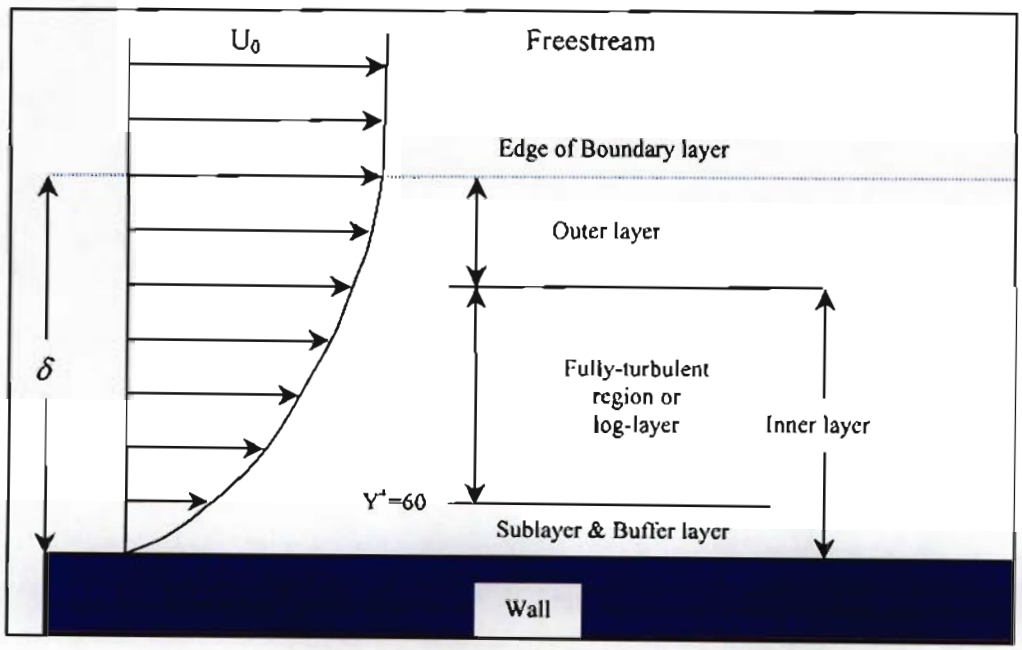

Figure 2-4: Subdivisions of the near-wall region

CHAPTER 3

EXPERIMENTAL EQUIPMENT

3.1 High-speed rig

The existing experimental turbine blade test facility at the University of KwaZulu-Natal, Durban, utilizes a continuous flow cascade technique whereby a four-blade cascade is continuously subjected to a hot-air stream. The rig has been used to perform the SMR-95 blade static pressure distribution measurements and isothermal heat transfer coefficient measurements. This continuous flow cascade technique offers significant reductions in cost compared to the more conventional light piston or blow down tunnels, which offer only short durations of flow. The rig has recently seen numerous new additions and alterations to equipment by the author, as well as extensive equipment maintenance in an effort to prepare the rig adequately for reliable experimental measurements.

The basic principle of operation behind the rig's continuous flow is shown in Figure 3-1, and consists of a large plenum, or chamber, that has a hydraulic motor attached externally at one end, driving a high-speed centrifugal compressor within.

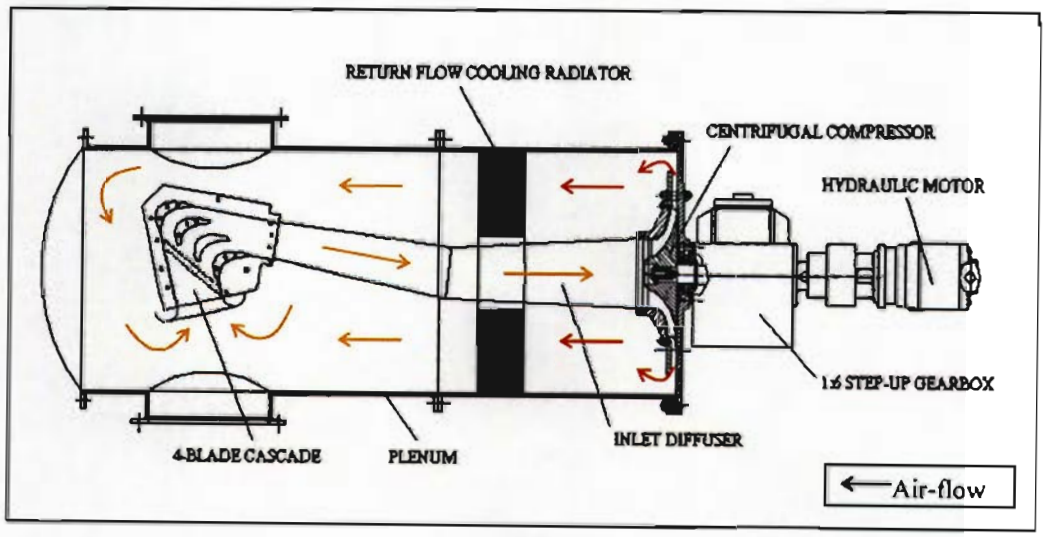

Figure 3-1: Supersonic rig layout, as seen from above (Reproduced from de Villiers [2002])

The eye of the compressor draws air through the inlet bell mouth of the cascade, into the cascade containing the instrumented blade and down the compressor inlet diffuser. Passing through the compressor, the air is compressed, raising the temperature of the gas stream and

directing the flow radially before being turned back in the axial direction. Here the flow passes through an annular radiator before entering the cascade inlet. The radiator serves to control the cascade temperature by manually controlling the flow of cooling water through the radiator. Temperatures are limited to $100°C$ due to the tolerance of equipment such as thermocouple leads, piping and seals. This system thus provides the re-circulating flow necessary for the experimental measurements.

The subsequent sections in this chapter will serve to describe briefly and explain the basic operation of the various items of equipment vital to the operation of the rig. A comprehensive rig starting procedure for experimental measurements is also included. Items of equipment that are specific to either the static pressure or heat transfer distribution measurements will be discussed later in their respective chapters.

3.2 Plenum

The plenum consists of a large 0.6 m diameter steel chamber of 1.55 m in length. A photograph illustrating the plenum together with associated equipment is shown in Figure 3-2.

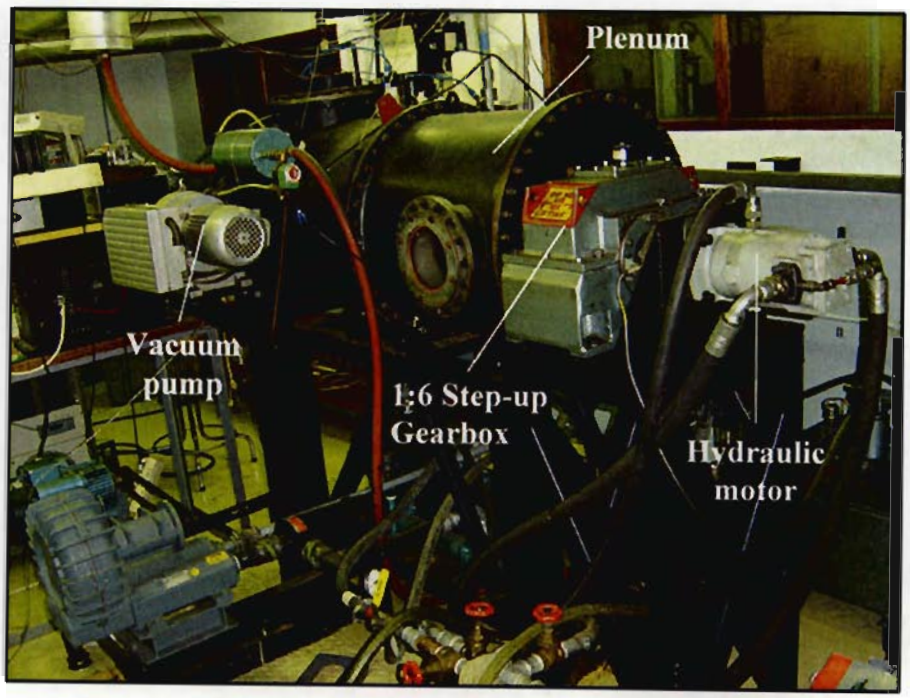

Figure 3-2: Plenum with associated equipment

During tests, the plenum operates at a vacuum where the pressure is reduced to 0.4 bar by the vacuum pump. The vacuum pump and hence the plenum pressure are controlled by the new digital pressure control system, installed and implemented by the author. This pressure

control system was built to replace the original, analogue control system implemented by Stieger [1998]. A more detailed explanation of the new control system operation is given in section 3-3. The previous system utilised a variable resistor to vary the set pressure, which proved to be very inaccurate, together with the fact that the controller invariably was not able to control the pressure correctly. This necessitated the building of a more modern and reliable pressure control system.

The ability to adjust and control the plenum pressure presents two advantages for the tests. Firstly, since the density of the air is directly proportional to the pressure through equation 3-1 as expressed by de Villiers, by lowering the pressure within the plenum, the density is lowered. This results in less work required to move the air through the cascade, consequently less power is needed to drive the compressor. Secondly, by controlling the plenum pressure, the Reynolds number based on chord length can be controlled. Equation 3-2 shows the relationship between the Reynolds number and density, where the Reynolds number is directly proportional to the density, which in turn is directly proportional to the pressure as shown in equation 3-1 below.

$$\rho = \frac{P}{RT} \tag{3-1}$$

where P = pressure at that point

R = 287 J/kg.K

T = temperature at that point

$$\mathrm{Re} = \frac{\rho D U}{\mu} \tag{3-2}$$

where D = blade chord length,

U = velocity at a point

μ = viscosity

The rear compressor section, end-wall of the plenum is flat and allows the compressor shaft to enter the plenum. Access to the plenum is found through the dished end plate held in position by 40 bolts and sealed by a fibrous gasket. Four Pyrex access windows provide visual access into the plenum. A further four access ports are used to carry various measurement leads and pipes from the plenum to the various measurement devices. Cover

plates are used to seal the portals effectively. Two of these are used during the pressure measurement tests to transmit the blade static pressure tapping piping to the scanivalve, which measures the static blade pressures. Another two cover plates are used during the heat transfer tests to transmit the heat flux gauge flying leads and the thermocouple cables respectively. Reliable sealing of all these ports is imperative in maintaining the vacuum pressure within the plenum.

3.3 Vacuum pump and pressure control circuitry

A Rietschle VCE 25 submerged oil vane type vacuum pump serves to provide the vacuum required within the plenum. The vacuum pump is continuously running, and the pressure is controlled by the control system, which activates a solenoid valve located on the suction pipe, connecting the pump to the plenum. The total plenum pressure is measured by a newly installed vacuum pressure transducer that is screwed directly into a blank flange on one of the plenum ports. This WIKA™ vacuum pressure transducer, outputs 4-20 mA and the corresponding voltage signal is sent to the newly installed controller that is mounted on the wall nearby. Locating the transducer directly within the plenum wall is advantageous since it prevents any measurement errors which may be caused by leaking or blocked silicon tubing, which was the technique previously used to connect the transducer to the plenum. The controller consists of a digital display where the pre-set pressure can be adjusted to the required operating pressure. Since the transducer measures vacuum pressure, the set value needs to be adjusted relative to the atmospheric pressure for each test. The cascade total inlet pressure is measured by a Kulite ITQ-1000 (0-100 mV) total pressure transducer (see section 3-6 and Figure 3-9) which is mounted on the wall. The Kulite total pressure transducer outputs 40.2 mV at a plenum pressure of 0.4 bar. Therefore, setting the controller pressure so that the Kulite transducer outputs 40.2 mV, means the set pressure is 0.4 bar. When the power supply to the controller is switched on, the controller relay contact closes. This contact, rated at 220 V, sends 220 V to a secondary relay that has been installed by the author. This has been done to protect the significantly more expensive controller relay. The signal passes through a 2:1 voltage transformer, supplying the solenoid valve with 110 V, thereby opening the solenoid valve and allowing air to be evacuated from the plenum by the vacuum pump. When the pre-set operating pressure of 0.4 bar absolute is reached, the controller sends a signal to close the solenoid valve. Due to the inevitable leakage from the plenum through the many seals, the pressure rises again, and the controller again sends a signal to open the solenoid valve for further air to be evacuated from the plenum.

A temperature display and controller was also installed and implemented by the author. This device provides a reading of the total cascade inlet temperature by receiving a signal from a stagnation total temperature probe, containing a K/J type thermometer located in the cascade inlet. The controller is, at present, not controlling any temperature; however it can be used for effective temperature control in the future. Both the temperature and the pressure displays/controllers have been neatly wired and housed within an electric 'yoke box'. Figure 3-3 illustrates the control box with the two displays neatly mounted within.

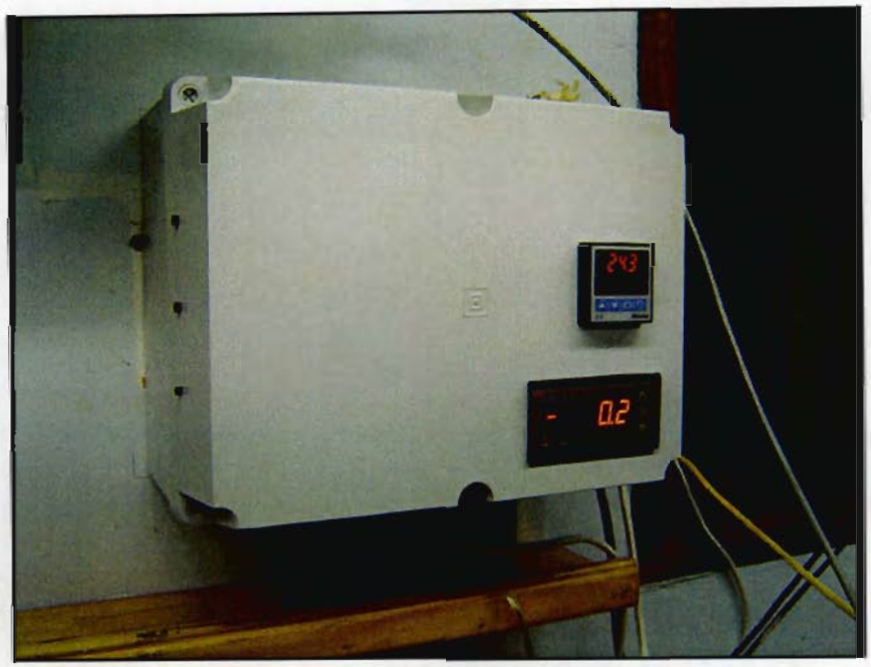

Figure 3-3: Box housing the pressure control system and cascade temperature display.

Since the plenum is designed to operate under vacuum, a pressure safety interlock has been installed which prevents the main hydraulic pump from starting unless a vacuum of 0.55 bar absolute is attained. This safety interlock, along with others to be discussed in subsequent sections, is linked to the safety electronic circuitry on the safety control box (Figure 3-5) and the main hydraulic pump. Details on the operation of the control circuitry are given in section 3.7.

3.4 Hydraulic pump and compressor

The centrifugal compressor located at the rear of the plenum generates the flow conditions as described earlier in section 3-1 and is driven by a 65kW hydraulic motor via a custom built 1:6 step-up gearbox. A Uchida hydraulic swash-plate pump, located in the adjacent lab, rotates the hydraulic motor at a maximum speed of 3000 rpm by supplying the motor

with hydraulic oil. The compressor can therefore rotate up to a maximum speed of 18000 rpm through the 1:6 step-up gearbox, and produce a design air mass flow of approximately 6 kg/s. By being able to control the hydraulic pressure supply to the motor using a speed switch that has a fine and coarse speed option, the cascade air velocity can be varied. Adjustment of the switch varies the flow-rate of the hydraulic oil from the pump by changing the angle of the swash-plate using a small DC motor found on the hydraulic pump.

At the point where the compressor shaft enters the plenum, the shaft is fitted with a mechanical carbon seal designed to completely seal the plenum from atmospheric pressure at a speed above 500 rpm. This, along with all other plenum seals, serves an important purpose in maintaining the vacuum at which the rig is designed to operate and to prevent damage to the compressor and mechanical seal. The safety circuitry on the main pump has separate individual interlocks for hydraulic oil level, oil temperature, main power, and sonic cascade. If the pump hydraulic oil level and the temperature are acceptable and the supersonic rig interlocks are all satisfied, the entire system will be fault free and the main pump can be started. It is important that the main pump is cooled and a pipe supplying cooling water to the pump is opened to allow for this cooling.

3.5 Gearbox lubrication

Gearbox lubrication is provided by an air motor, drawing oil from an oil sump containing an electrical immersion heater that heats the oil to a temperature above $40\,°C$.

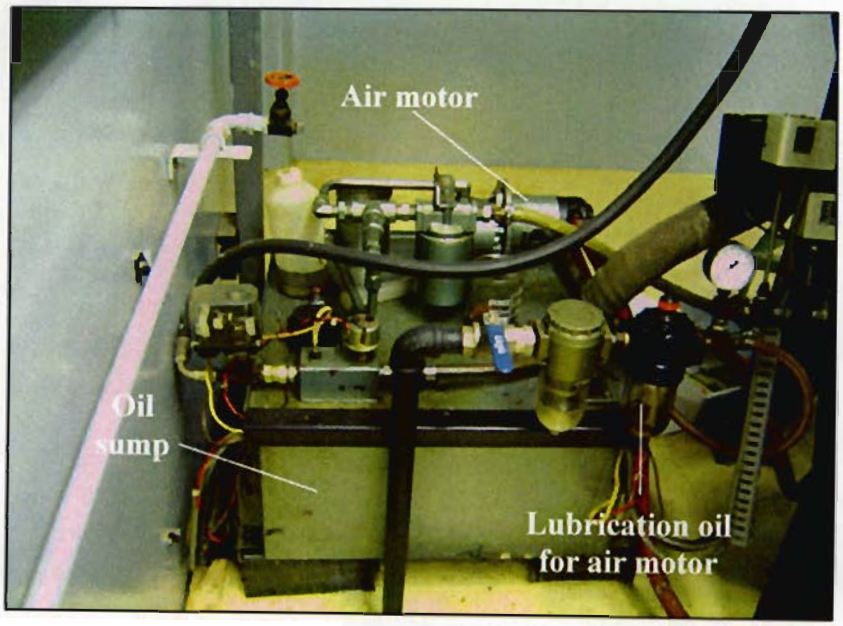

Figure 3-4: Air motor and lubricating oil sump

Compressed air, supplied from the workshop compressor at 6 bar, drives the air motor. This is advantageous in the event of a power failure since the motor will still be able to operate on stored air, providing lubricating oil to the gearbox and allowing the compressor to come to a safe stop. As for the vacuum pressure, safety interlocks are installed for the lubrication system that monitor the air pressure, oil flow rate and oil pressure. Satisfying each of these criteria results in the respective LED's changing from red to green. The lubricating oil flows from the oil sump through a water-cooling shell and tube heat exchanger and then into the gearbox. This prevents the oil from reaching too high a temperature in the event of high speeds operating on the gearbox.

3.6 The SMR-95 Cascade

The cascade utilized for the experimental testing consists of four blades all of the SMR-95 profile. This profile is that of a fully twisted, high turning angle rotor blade at a specific radius, the manufacturing co-ordinates of which may be found in Appendix 1. The original blade and aerothermal details at the selected radius are given in Table 3-1, followed by the scaled up test blade details in Table 3-2.

	Inlet	Outlet
Relative gas velocity [m/s]	410.46	613.72
Static pressure [kPa]	796.89	603.5
Static temperature [K]	1304.5	1216.1
Relative Mach No.	0.581	0.8997
Relative Reynolds No.	597713	756284
Relative flow angle	38.4°	28.6°
Chord [mm]	33.27	
Pitch [mm]	21.33	
$T_{wall}/T_{freestream}$	0.86	

Table 3-1: Original blade and aerothermal details (Reproduced from Snedden [1995])

The cascade consists of three aluminium blades located and bolted into position between two wire-cut end walls of 6mm plate. An appropriately positioned blade profile slot in the end walls provides for accommodation of the test blade which can be inserted through the slot for testing. The inlet of the cascade is a bell mouth, which aids to guide the air flow smoothly into the cascade whilst the cascade exit is a rectangular flange which fastens to

the diffuser, feeding the compressor eye. Figure 3-5 depicts the cascade layout as seen from above.

Blade chord [mm]	94.8
Pitch/Chord ratio	0.675
Camber angle	113°
Blade span [mm]	80
Leading edge diameter [mm]	10
Scale amplification	2.85

Table 3-2: Scaled up test blade details (Reproduced from Snedden [1995])

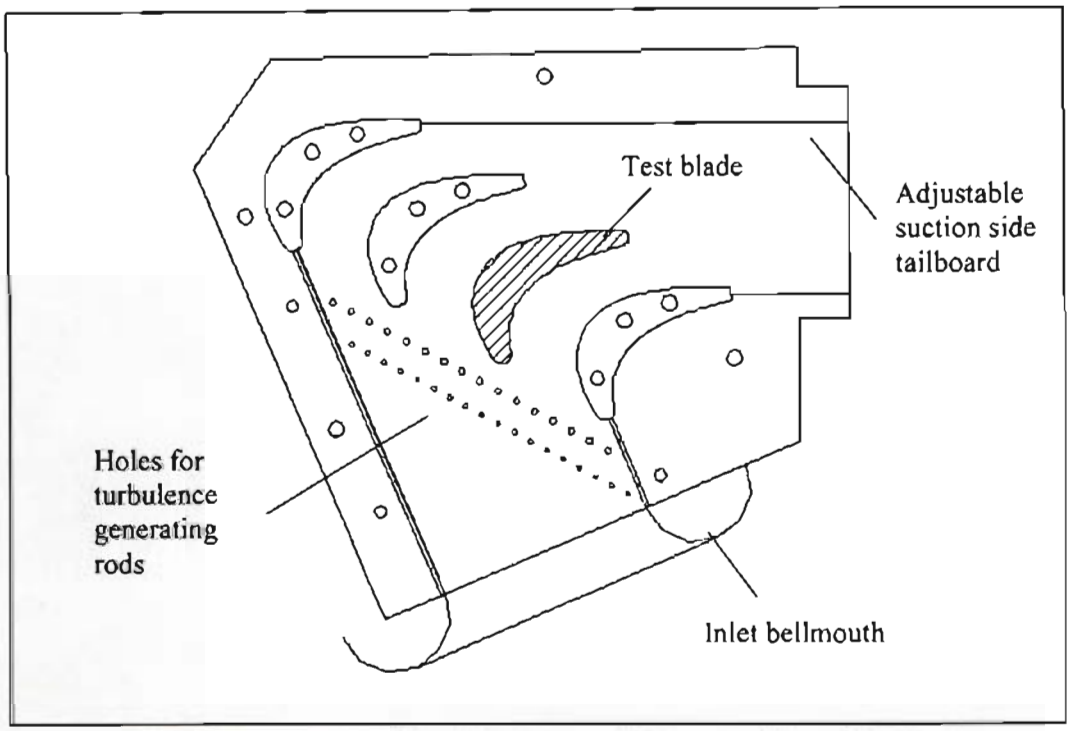

Figure 3-5: Top view of the SMR-95 cascade (Reproduced from de Villiers)

A total temperature K/J type thermocouple and total pressure Kiel type probe are located at the cascade inlet to measure the total inlet temperature and pressure respectively. Static inlet and exit pressure tappings are located at the inlet and exit respectively, to determine the pressure drop across the blade stack. These pressure tappings along with the Kiel probe, pass the measured pressure via silicon tubing on to the corresponding pressure transducer for measurement. A Kulite ITQ-1000 (0-100 mV) total pressure transducer measures the total cascade inlet pressure from the Kiel probe. Various turbulence intensity levels can be created by inserting turbulence generating rods into holes drilled just before the leading edge of the blades, however these are not utilized nor discussed in this thesis.

Snedden [1995] describes the turbulence intensities that can be achieved by inserting the rods in the cascade. Stieger [1998] presents heat transfer results for varying levels of inlet turbulence intensity. Figure 3-6, is a photograph taken from the inlet of the cascade, with the pressure test blade fastened into position.

Figure 3-6; Four-blade cascade viewed from the cascade bell mouth inlet

3.7 Control circuitry

A series of safety circuits housed in the safety control box, record and monitor certain aspects of the rig's performance to ensure no damage to equipment or persons is sustained. As briefly mentioned in earlier sections, the vacuum pressure, oil flow rate, oil pressure and air pressure are factors of the rig bound by safety interlocks. A compromise of any one of these interlocks during operation immediately shuts down the main hydraulic pump.

The operation of the gearbox lubrication system is extremely vital to avoid permanent damage to the custom built gearbox. Hence interlocks are installed to monitor the oil flow rate, oil pressure and air pressure supplied to the air motor. If the air pressure is sufficient, the air motor is activated resulting in the required oil flow and pressure and turning the three interlocks from red to green on the safety box control panel. The final interlock is the plenum vacuum pressure that is required to be less than 0.55 bar absolute, in order to start the main hydraulic pump. The Kulite ITQ-1000 (0-100 mV) absolute pressure transducer provides the signal to this pressure interlock safety circuit. Figure 3-7, illustrates the safety control box showing the various safety circuits with corresponding safety indicators.

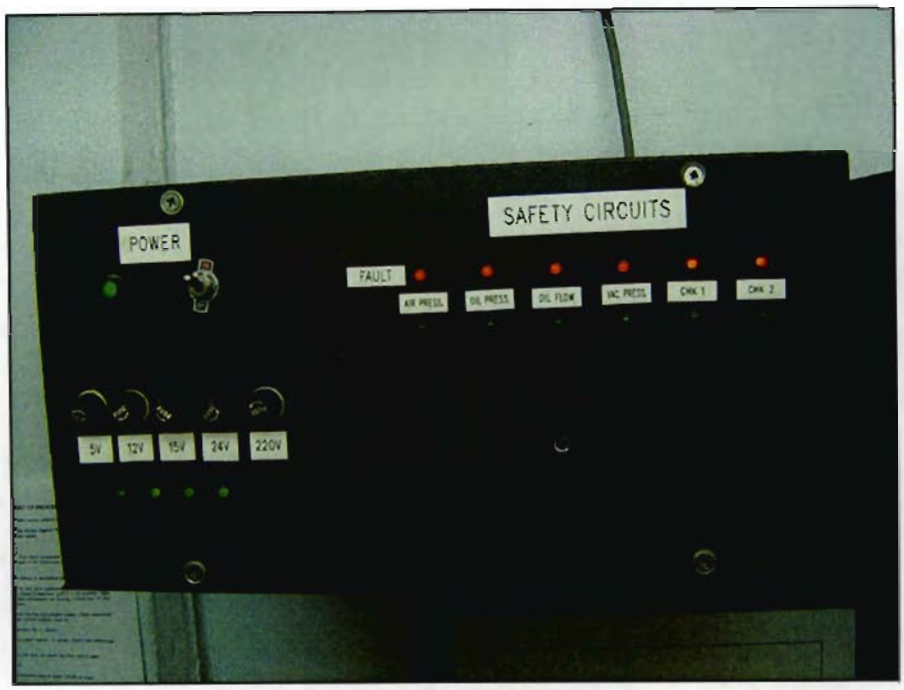

Figure 3-7: Safety control box

The safety circuitry of the rig is linked to the main hydraulic pump safety circuit and satisfying all the above safety criteria on the rig, as well as those mentioned for the pump in section 3-4, will deem the entire system fault free and illuminate a green light on the hydraulic pump control box. Only now can the main hydraulics be started.

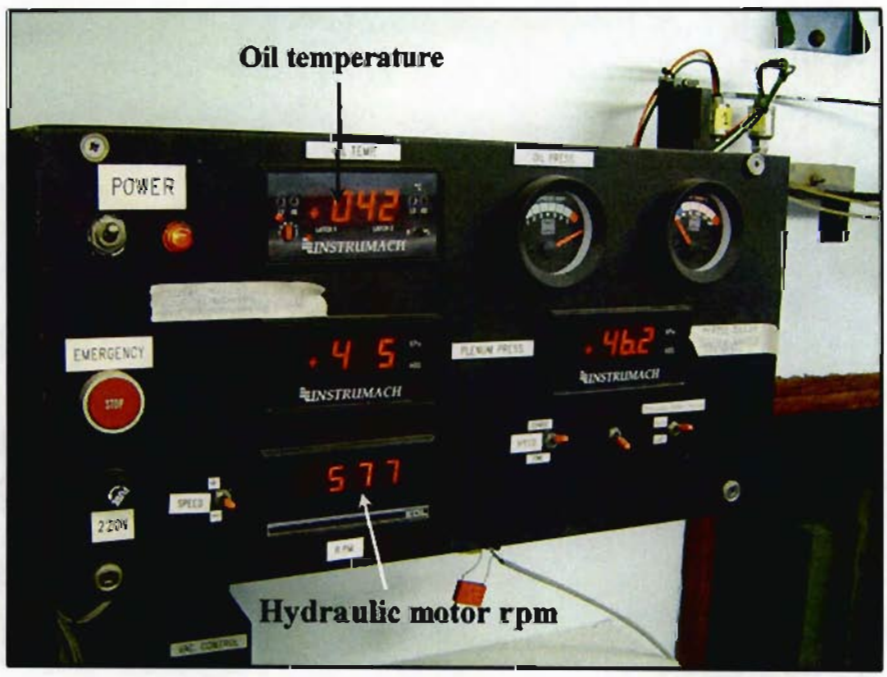

Figure 3-8: Display box

Adjacent to the safety control box is a display and control box housing various digital displays as well as the speed control for the hydraulic motor. The digital readings displayed are the lubricating oil temperature, hydraulic motor speed, total plenum and static inlet pressures. These old inaccurate pressure displays have been replaced with the more modern and accurate pressure control and display system. The speed of the hydraulic motor is monitored by a tachometer that provides a digital display. The motor speed is adjusted using the speed switch and a coarse and fine adjustment switch that can be toggled depending on speed requirements. All the above features of the display box are shown in Figure 3-8. Figure 3-9 illustrates the complete rig electronic monitoring and control circuitry.

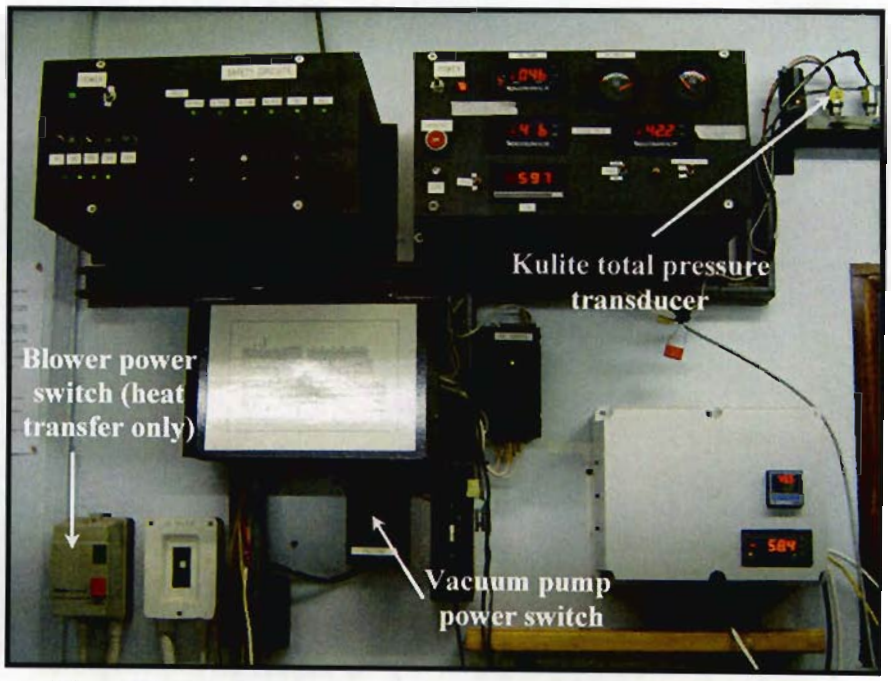

Figure 3-9: The complete rig electronic monitoring and control circuitry

3.8 Data acquisition

The supersonic rig data acquisition system consists of a Pentium 133 MHz computer installed with commercially available data acquisition and control software called LABVIEW. An Eagle Technologies PC30 PGL 12-bit A/D data acquisition card is used to acquire the data from both the static pressure measurements and heat transfer measurements. The card allows for an A/D acquisition rate of 100 kHz over sixteen single-ended analogue to digital input channels, or alternatively eight differential inputs and can be configured for unipolar (range 0-10V) or bipolar (range +/-5V) input.

The card is calibrated using the supplied calibration program "Cal30.exe" and adjusting variable resistors on the card. A PC30 U user interface card provides protection of the card from any sudden voltage spikes, which may happen to originate from any experiments. This card is located between the A/D card and the equipment acquiring the analogue signals. This protection card is much cheaper than the A/D card and so in the event of any large voltage spikes occurring, the protection card will take delivery of the damage, possibly resulting in a fuse needing replacing or replacement of the protection card, nevertheless, both proving much cheaper.

The analogue input mode was configured for differential input which reduces signal noise significantly as opposed to sampling through a single-ended channel. The acquisition software, LABVIEW, contains programs that perform the static pressure (see section 4.2.3) and heat transfer coefficient (see section 5.5) calculations automatically. This software also provides the ability to perform as a control system, in the case of the pressure measurements, where the pressure data is automatically acquired by reading the numerous voltages directly from the one pressure transducer.

3.9 Experimental rig operating procedure

The starting procedure of the experimental rig requires a good understanding and knowledge of all the associated equipment and their workings. Due to the ongoing research performed on the rig and numerous additions to equipment, it is difficult and time consuming to become completely familiar and confident with the operation. Documentation on the rig to date appears scattered, most likely due to experience and knowledge being lost as researchers come and go.

To help prevent any further difficulties with equipment and get future researchers familiar with the rig quickly, a comprehensive experimental rig starting procedure has been provided. This procedure expands on the one given by de Villiers and is given in Appendix 3. Included in Appendix 3 is a list of problems encountered with some of the rig components, followed by possible solutions to these problems.

CHAPTER 4
EXPERIMENTAL FLOW MEASUREMENTS

4.1 Introduction

Static pressure measurements on the SMR-95 turbine blade were performed in view of the fact that accurate measurement of the blade surface pressure distribution is essential for measurement of the corresponding heat transfer distribution. The difficulty associated with heat transfer measurements is coupled with the aerodynamics around the blade due to the high significance of the pressure distribution to the heat transfer predictions. If the required flow field is not achieved and accurately determined, the corresponding heat transfer coefficients will be incorrect. Performing the static pressure test provides information about the flow field around the blade that can be used as boundary condition inputs for the heat transfer tests as well as the CFD simulations. Previous results, generated by de Villiers [2002] and shown in Figure 4-1, illustrate an excellent correlation between the experimental and numerical static pressure distribution.

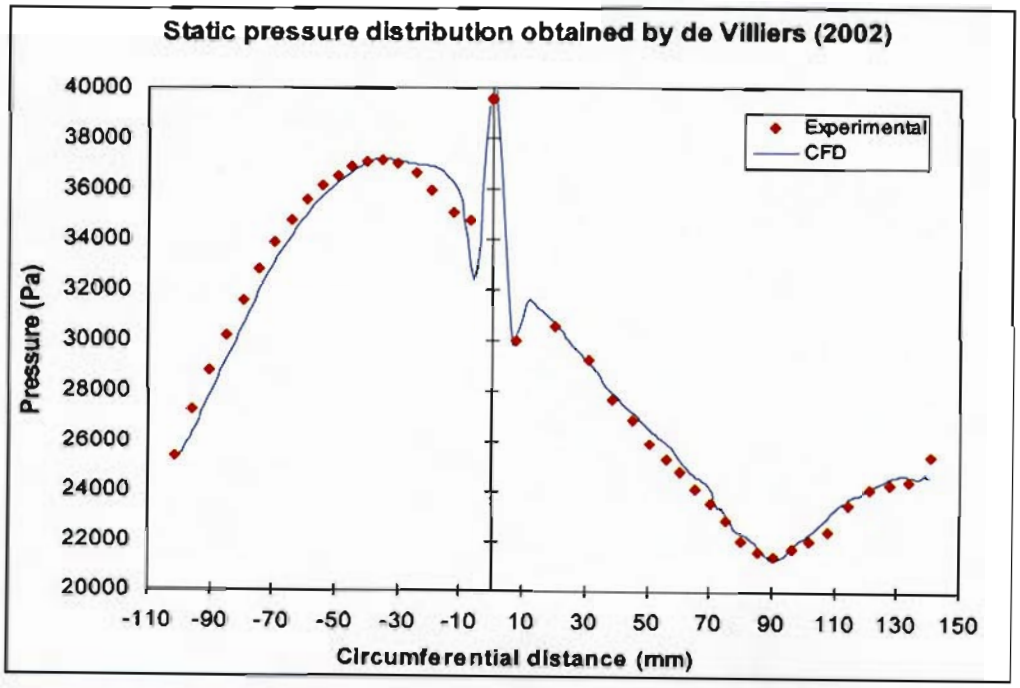

Figure 4-1: Previous experimental and numerical pressure distribution by de Villiers [2002]

However, close inspection of de Villiers' [2002] work showed possible hints of error on the suction side, which will be discussed later in section 4-4. For this reason, further experimentation in the pressure field was conducted, which not only provided an opportunity

to validate de Villiers' [2002] results, but also to gain experience in the operation of the experimental rig. Hence, the current flow conditions within the plenum could be determined which would prove vital in the ensuing heat transfer distribution.

The subsequent sections of this chapter will serve to explain the experimental equipment that is specific to the static pressure measurements. The experimental technique and setup will be discussed as well as the initial problems encountered with acquiring the pressure data. The experimental results obtained by the most recent University of KwaZulu-Natal researcher, Cassie [2007], will be shown and their corresponding flow phenomenon will be discussed.

4.2 Static pressure measurement equipment

4.2.1 Test blade

The static pressure measurement test blade consists of 42 static pressure tappings of 0.5 mm diameter, drilled perpendicularly to the blade surface along the midspan. The pressure surface possesses 20 tappings whilst the suction surface has 22. Larger holes on the side of the blade, corresponding to the tapping positions, are drilled down to the midspan of the blade and serve to channel the static pressures being measured, via small pipes and silicon tubing, to the pressure measurement equipment. The distribution and position of the pressure tappings, together with the side holes, are shown in Figure 4-2.

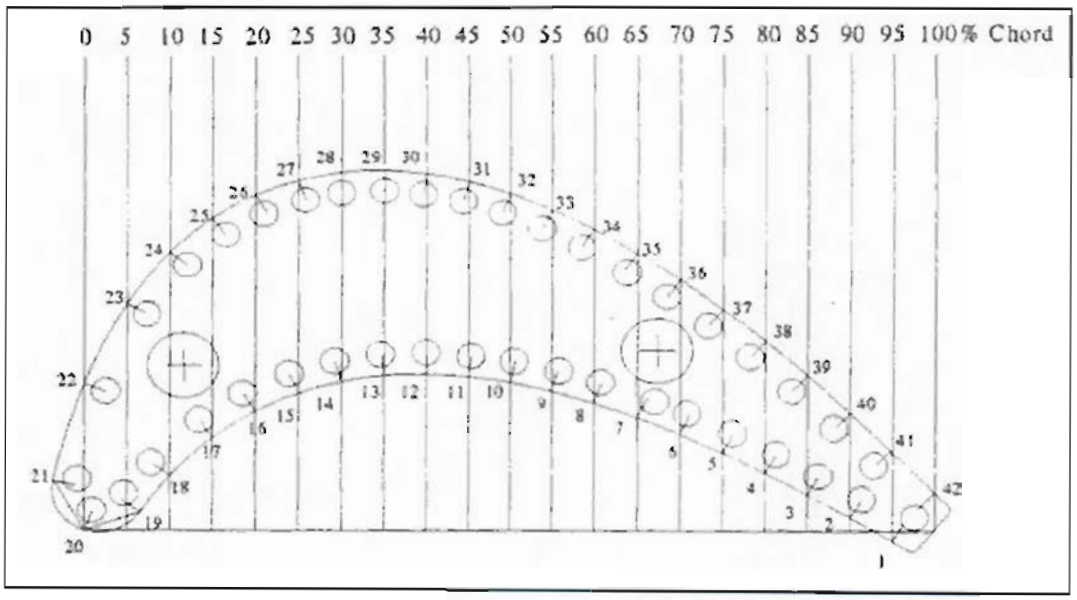

Figure 4-2: Scaled SMR-95 turbine blade with the static pressure tapping positions shown (Reproduced from Snedden [1995])

The static pressure test blade with the pipes for the attachment of the silicon tubing, and the 0.5 mm pressure tappings, can be seen in Figures 4-3 and 4-4 respectively.

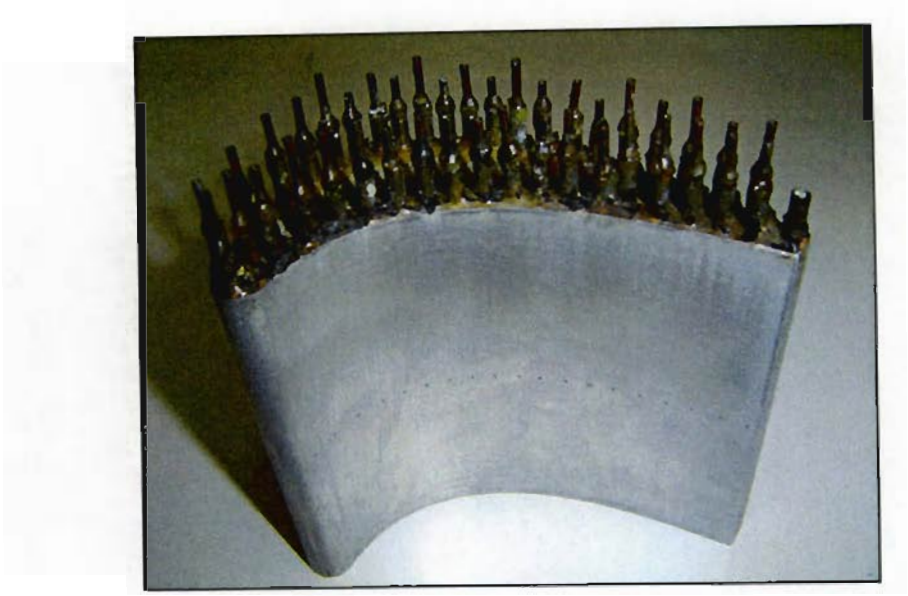

Figure 4-3: Pressure test blade with pipes for attachment of silicon tubing

Figure 4-4: Pressure blade with 0.5 mm pressure tappings drilled perpendicularly to the mid-span surface

The positions of the tappings, expressed as a circumferential distance from the leading edge, are given in Table 4-1. The final two tappings on the trailing edge of the blade are connected to the same port due to obvious space restrictions, and the static pressure for the suction and

pressure surfaces at this point, are assumed to be equal. The total circumferential distances around the suction and pressure surfaces are 144 mm and 103.5 mm respectively.

Tapping Number	Circumferential Position (mm)	Tapping Number	Circumferential Position (mm)	Tapping Number	Circumferential Position (mm)
1	-101.5	15	-30.4	29	65.7
2	-96	16	-24.6	30	70.5
3	-90.5	17	-19.4	31	75.4
4	-85.1	18	-12.7	32	80.4
5	-79.5	19	-7.1	33	85.6
6	-74.4	20	0	34	90.8
7	-69.4	21	7.7	35	96.5
8	-64.2	22	20	36	102.3
9	-59.2	23	31	37	108.3
10	-54.4	24	39	38	114.5
11	-49.6	25	45.4	39	120.9
12	-45	26	50.8	40	127.4
13	-40	27	56.1	41	133.9
14	-35.5	28	60.7	42	141

Table 4-1: Static pressure tapping positions expressed as a circumferential distance from the leading edge (Reproduced from de Villiers [2002])

In preparation for the static pressure measurements, the blade is fastened into the blade profile slot of the cascade. Silicon tubing is then connected from the blade pressure tappings to the inside of the plenum portal cover plates. This tubing continues on the outside of the cover plates to the measuring equipment, which is discussed shortly in section 4.2.2.

4.2.2 Scanivalve

The scanivalve, an ingenious pressure-measuring device, is used to aid the measurement of the multiple static pressure measurements. This device, working in conjunction with programmed software, allows for the pressure measurements to be taken automatically and rapidly. The scanivalve consists of two 1 pole – 24 throw fluid switch wafers and a solenoid drive with binary position wafer. Each wafer consists of 24 ports onto which the silicon tubes from the test blade pressure tappings are attached. A common port on the rotor is connected to a pressure transducer. A solenoid drive rotates the central rotor and hence switches the common port to each of the 24 ports on the stator in turn, allowing for 24 static pressure measurements to be made by a single pressure transducer. A port on the cover of the wafer receives a balance pressure, equal to or greater than the average pressures being measured, which acts as a pneumatic rotor thrust bearing and enhances sealing in the wafer. The total cascade inlet pressure, measured by the Kiel total pressure probe, was used as this balance pressure.

Switching 24V across the coil of the solenoid drive, steps the central rotor and common port to a new position and pressure tapping. The pressure transducer, via the common port, can then read the static pressure. A control wafer has a ratchet system to ensure that the rotor is switched to the correct position, and a binary position wafer allows for the position of the rotor to be recorded. Once the pressure is recorded, the scanivalve, with a signal from the software, steps again so that a new pressure may be recorded. This process allows for the automatic recording of pressure and its corresponding position on the wafer, and hence the blade.

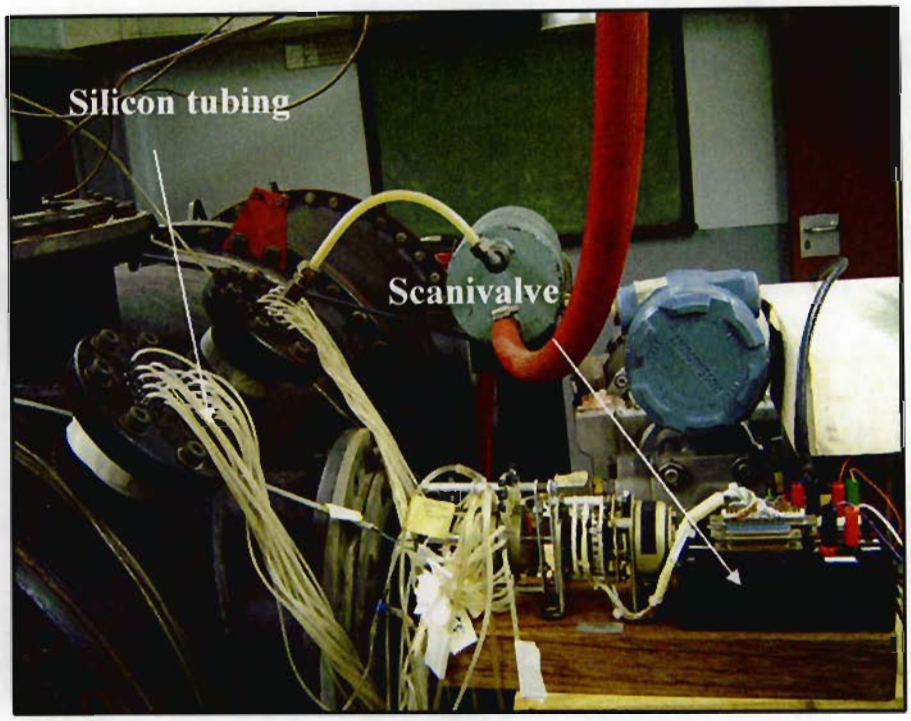

Figure 4-5: Scanivalve with attached silicon tubing

4.2.3 Scanivalve control circuit

A program, written using commercially available software, LABVIEW, and implemented by de Villiers, is responsible for the controlled stepping of the scanivalve rotor, the digital reading of the position of the rotor, and the reading of the voltages from the pressure transducer. The program also converts the transducer voltages into meaningful static pressure values through the use of programmed transducer calibration data (see section 4.2.5). The program written by de Villiers in LABVIEW, provides numerous selections corresponding to the necessary scanivalve function that is to be performed. LABVIEW is an object orientated programming tool. The program and its sub-programs include Virtual Instruments (VI's), developed by the Eagle Technologies engineers, to provide an interface between LABVIEW and the PC30 PGL card. "Go Home" is used to ensure that the

scanivalve is in the correct starting position before a test is run; this ensures that the pressures will be measured in the correct order. The "Step Once" option is used to step the rotor and check if the system is operating correctly. "Perform Measurement" is used to perform the pressure measurements, by stepping the scanivalve, reading the transducer voltage and converting it to a pressure value, reading the binary position of the rotor and then finally recording the data. A copy of the program and its components, as well as a comprehensive explanation of how the LABVIEW program works, can be found in Appendix 2 of de Villiers' [2002] dissertation.

The solenoid is stepped by supplying a signal of 5 V (for 100 ms) from one of the PC30 PGL digital output ports. This entails writing a binary true state (1) to the digital line. The 5 V is passed through a 15 kΩ resistor and into the base of a transistor. The transistor is turned on when the base is saturated by the 5 V signal and the collector is connected to the coil of a 24 V relay, which switches the 24 V supply across the coil of the solenoid drive and steps the rotor to the next position. The outputs of the binary position wafer, which are binary counts of 2^0 to 2^4 representing the binary position of the rotor, are connected to digital input ports of the PC30 PGL card. This allows the software program to read and record the rotor position. Each binary output is also grounded through a 120 Ω resistor and LED, which provides a physical backup binary display of the rotor position, which can be viewed on the scanivalve circuitry box. Further details pertaining the wiring of the control circuitry can be found in Stieger's dissertation [1998].

4.2.4 Rosemount differential pressure transducer

The static pressure measurements were measured using a Rosemount differential pressure transducer. The transducer is supplied with a voltage input, and outputs a current (4-20 mA) that is proportional to the differential pressure being measured. The measurable differential pressure range is 0–186.45 kPa with an accuracy of $\pm$ 0.2% of calibrated span, where the combined effects of repeatability, hysteresis and independent linearity are taken into account.

The common port on the rotor of the scanivalve is connected to the Low Pressure (LP) port of the transducer, while the total cascade inlet pressure, measured by the total pressure Kiel type probe, is connected to the High Pressure (HP) port. This means that the LP port receives the blade static pressure being measured, and the transducer output current is hence proportional to the difference between the total inlet pressure, and the measured static pressure. Monitoring the total inlet pressure allows for the static pressure to be calculated using equation 4-1.

$$P_{static} = P_{total\ inlet} - P_{differential} \quad (4\text{-}1)$$

In order for the pressure data to be acquired by the PC30 PGL card, the 4-20 mA transducer outputs need to be converted to a voltage, which is done by passing the output current through a 470 Ω resistor housed within the scanivalve circuitry box. The corresponding output voltage range of the transducer is 1.88 V – 9.4 V. The measured voltage is then supplied to the PC30U protection card via a differential analogue input channel, and consequently to the data acquisition card, where the data is recorded and processed by the program discussed in de Villiers' [2002] dissertation. For the purpose of calculating the static blade pressures, using equation 4-1 above, the data acquisition monitors the total inlet pressure by receiving a 0-100 mV signal from the Kulite pressure transducer. This signal is connected to one of the differential analogue input channels as well. Recording of this total inlet pressure (connected to the transducer HP port) and the differential pressure, therefore, allows the user to calculate the static pressure by simply applying equation 4-1, and the programmed transducer calibration constants (see section 4.2.5).

4.2.5 Calibration of the Rosemount differential pressure transducer

In order for the pressure transducer outputs to provide meaningful pressure data to the data acquisition, calibration curves for the Rosemount transducer had to be plotted to determine the relationship between the measured differential pressure and the current signal output, converted to a voltage via a 470 Ω resistor. Although the transducer was used by de Villiers [2002], and calibration data for the transducer existed, recalibrating would ensure the acquired data would be reliable.

On the transducer casing, are two screws used for calibrating the transducer, one for the span adjustment and another for zero adjustment. To simulate 0 kPa differential pressure, the two HP and LP ports were left open to the atmosphere. A voltmeter was use to monitor the output of the transducer whilst the zero adjustment screw was turned, until a voltage reading of 1.88 V was observed, corresponding to zero differential pressure. The maximum differential pressure never exceeds 0.4 bar, therefore the maximum range of the transducer was set to this pressure. Programming the newly installed pressure controller to a set value of 0.6 bar vacuum, this pressure was applied to the LP port, whilst the HP port was left open to the atmosphere, simulating a 0.4 bar differential pressure. Now the span screw was adjusted until a maximum output reading of 9.4 V was observed on the voltmeter. Adjustment of the span screw, however, affected the zero adjustment. Consequently the

process needs to be repeated until the appropriate voltage range corresponds to the pressure range.

To determine the transducer voltage response over the entire pressure range, the plenum vacuum pressure was applied to the LP port and the HP port left open. The vacuum pressure was also applied to a U-tube manometer. The vacuum pump was started, and the resultant voltage change from the transducer was acquired by Waveview software via channel 1. A stopwatch was started at the same time as the data acquisition and the height of the mercury in the manometer was monitored and recorded every 20 seconds. After 220 seconds, the acquired data from Waveview was exported to a text file, and the voltages corresponding to the 20 second intervals were extracted. The manometer mercury height readings were converted into pressure values using equation 4-2.

$$\Delta P = \rho g h \qquad (4\text{-}2)$$

Where: ρ = density of mercury (13 600 kg/m^3)

g = gravity

h = difference in height of mercury in tubes

These pressures are matched with the voltages corresponding to the same time intervals. A calibration curve was plotted and may be found in Figure A2-1, together with the calibration data in Table A2-1, of Appendix 2. Finding the straight line equation of the calibration curve yields the gradient (dP/dV) and y-intercept (P_0) for the characteristic curve. These are the calibration constants that are programmed into LABVIEW and used to calculate the differential pressure, and consequently the blade static pressure. The differential pressure can be calculated by the LABVIEW program by multiplying the sampled voltage with the gradient (dP/dV), then adding the y-intercept (P_0) as shown in equation 4-3 and Figure A2-1 in Appendix 2.

$$\text{Differential Pressure} = \left(\frac{dP}{dV} \times Voltage \right) + P_0 \qquad (4\text{-}3)$$

Where:

$$\frac{dP}{dV} = 5457 \ \frac{Pa}{V}$$

$$P_0 = -10170 \text{ Pa}$$

4.2.6 Calibration of the Kulite total pressure transducer

Calibration of the Kulite transducer was also done using the manometer and Waveview acquisition software. The voltage output of the Kulite transducer (0-100 mV) was sampled directly through channel 3 on the PC30 PGL card. Once again the voltages were matched with the corresponding mercury height readings and a curve of the points was plotted. Since the Kulite transducer measures total pressure, the calibration curve was drawn as the total pressure against the voltage. These calibration constants barely changed from those calculated by de Villiers [2002] and were left unchanged. The calibration curve and data may be found in Figure A2-2 and Table A2-2 of Appendix 2 respectively.

4.3 Experimental static pressure measurements

4.3.1 Setup of the static pressure measurement equipment

Before the static pressure measurements can be conducted, the associated equipment needs to be setup and connected. This entails installing and connecting all the above mentioned items of equipment. The first requirement is to fasten the test blade in the cascade as described in section 4.2.1. It is recommended that the 0.5 mm surface pressure tappings and associated piping, be blown out with compressed air to remove any blockages and foreign matter that may cause discrepancies in pressure measurements. Connection of each pressure tapping to the outside of the plenum is made via silicon tubing, which extends from the blade, to the connections on the inside of the access port cover plate. From here, the pressures are transmitted via silicon tubing to the respective scanivalve connection ports. The cascade static inlet, static exit, and cascade total inlet pressures are also connected to the exterior via silicon tubing to appropriately labelled pipes in the plenum. The thermocouple signal for the total inlet temperature is carried via a thermocouple lead, to the temperature display that is mounted in the pressure control box. This concludes the connection of all internal wiring and piping within the plenum.

To ensure the correct flow conditions are achieved within the plenum, all objects or piping potentially interfering with the flow must be checked. The compressor inlet diffuser must be inserted fully into the compressor housing. This can be checked visually through the rear Pyrex access window. Any piping or wiring must be kept well clear of the cascade bell mouth inlet to prevent it being sucked into the cascade during testing and hence disturbing the flow. This is a warning to future researchers, and like the author initially experienced, failure to conduct these checks can result in erroneous results which are time consuming.

Figure 4-6 illustrates the fitment location of the compressor inlet diffuser, showing where possible flow recirculation could occur if a good seal is not achieved.

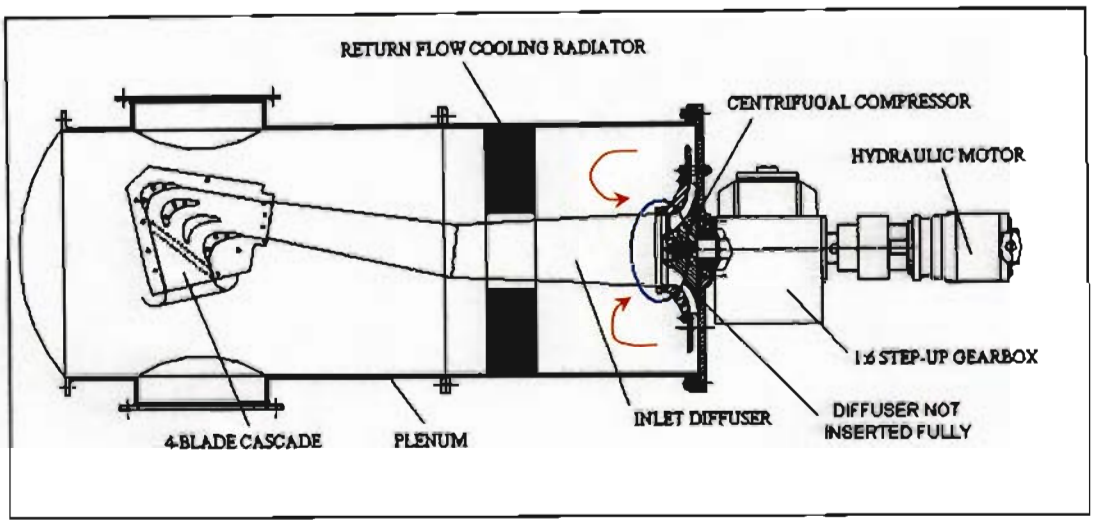

Figure 4-6: Figure indicating the fitment location of the compressor inlet diffuser

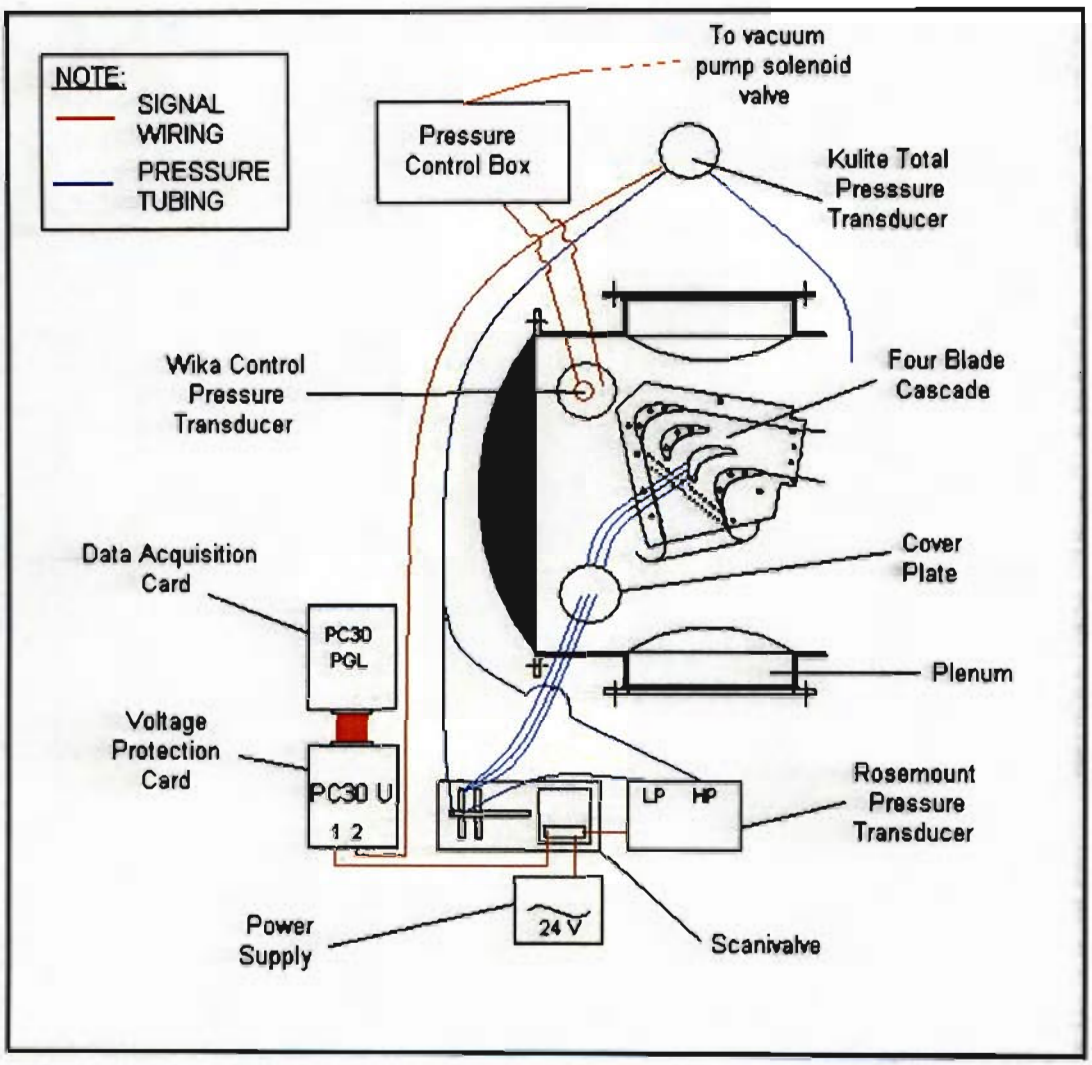

Figure 4-7: Basic connection setup for the pressure measurement equipment and instrumentation

Sealing of the plenum can now commence and the external equipment be connected. Shown in Figure 4-7, is the basic connection setup for the pressure measurement equipment, including pressure transducers, scanivalve, and data acquisition connections. Figure 4-8 illustrates a photograph of the pressure measurement equipment that has been setup.

The author wishes to inform future researchers of ensuring that the silicon tubing between the scanivalve and blade tappings are not in any way twisted (especially at the scanivalve connection points) thereby recording erroneous pressure readings.

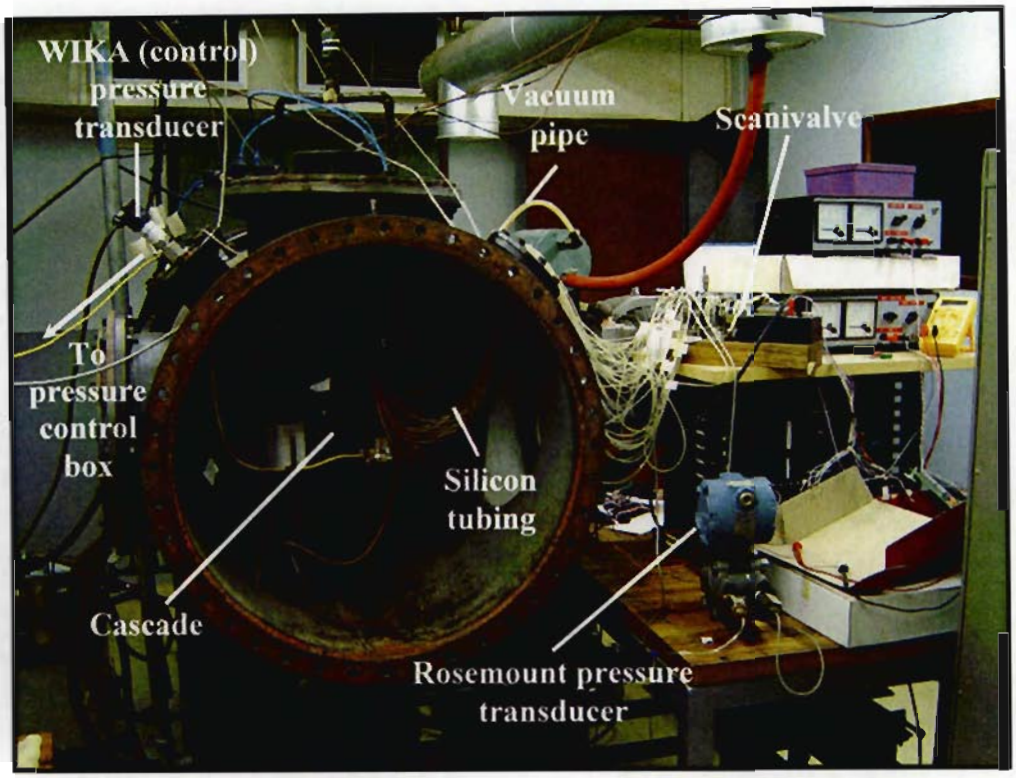

Figure 4-8: Photograph of the experimental pressure measurement equipment

The scanivalve is powered by a 24 V external power supply. The Rosemount pressure transducer is connected to the scanivalve circuitry box and the 24 V also provides power to the transducer. The common scanivalve rotor port is connected to the LP port of the transducer, whilst the total inlet pressure is connected to the HP port of the transducer and the balance pressure port of the scanivalve wafer, as described in section 4.2.4. The digital input wires, transmitting the scanivalve's binary position, are connected to the PC 30U digital channels, configured for digital input. The PC 30U digital output port, configured for digital output, is wired to the scanivalve and steps 5 V to the scanivalve for steeping of the rotor. The differential pressure signals from the Rosemount transducer are connected to the differential analogue input channel 1, whilst the total inlet pressure signal from the Kulite transducer is connected directly to the differential analogue input channel 2.

4.3.2 Problems encountered with starting the rig

Initial testing of the data acquisition system showed that the scanivalve was not being stepped and the rotor binary position was not being recorded. Furthermore, the voltage signals from the transducers were inaccurate.

Voltages into the analogue ports were simulated by voltage sources and the corresponding LABVIEW recording was checked. The values were not accurate indicating a serious error with the analogue input ports. The question was whether the error lay with the data acquisition card or the PC 30U voltage protection card. Bypassing the protection card revealed the correct voltages were being recorded by LABVIEW. The protection card appeared to be faulty.

To investigate the digital port problems, the digital inputs and outputs were reconfigured to other ports. After trial and error, some of the ports worked whilst others did not. This meant that only a portion of the scanivalve binary position was recorded and the program could not control the pressure measurement process adequately. Consultation with an electronics expert revealed that the protection card had possibly been short circuited. An attempt was made to fix the card by replacing a "Pico" fuse on the board. This proved not to solve the problem. At the start of the project, the card was found to be resting on a metal surface; this no doubt was the reason for the card being short circuited. A new card was purchased, and to prevent the same problem reoccurring, the card was housed within an insulated box. Following the purchase and installation of the new card, the digital control ports and analogue input ports worked correctly.

4.3.3 Performing static pressure measurement test

The pressure measurement test is begun by following the start-up procedure outlined in Appendix 3. Upon attaining the required base test conditions (see Table 4-2 in section 4.4.1), such as total inlet temperature of $100^{0}C$, total inlet pressure of 40 000 Pa, and compressor motor speed of 2500 rpm, the data acquisition system is started. The LABVIEW program "Pressure Measurement" is run and the acquired data is subsequently exported into a spreadsheet format. Since the acquired data represents the differential pressure relative to the total inlet pressure, subtracting the data from the total inlet pressure, equals the static pressure distribution corresponding to the position recorded. Plotting graphs of these static pressure values against the known circumferential blade distances (see Table

4-1) of the respective tappings, provides a picture of how the flow is behaving over the surface of the blade. The results of the experimental flow tests are illustrated and discussed in the subsequent section.

4.4 Experimental pressure distribution results

4.4.1 Overview

As discussed earlier in section 4-1, determining the static pressure distribution is vital to accurate heat transfer measurement. The pressure distribution can also help greatly and prove to be a useful tool with the analysis of the heat transfer, indicating corresponding flow and heat transfer phenomenon. In an attempt to validate the heat transfer work conducted by Snedden [1998], de Villiers [2002] produced an excellent correlation between the numerical and experimental pressure distribution. However, in view of the fact that only one pressure transducer was available; the suction and pressure surface data had to be measured separately, which involved changing over from one scanivalve wafer to the other. It was noted in de Villiers' [2002] work that during this change over period, the compressor speed had risen resulting in a higher inlet Mach number. This increase in inlet Mach number, although only slight, is shown by de Villiers [2002] to cause a significant reduction in static pressure. This gave good reason to conduct experimental pressure tests and would serve as a good foundation to becoming familiar with the workings of the rig and also to verify the flow conditions produced within the plenum.

Total inlet pressure [Pa]	40 000
Compressor motor speed [RPM]	2500
Turbulence intensity [%]	3
Total inlet temperature	100°C
Mach number at cascade inlet	0.441
Mach number at cascade exit	0.771
Reynolds number based on blade chord length at cascade inlet	2.78×10^8
Reynolds number based on blade chord length at cascade exit	2.47×10^8

Table 4-2: Base testing conditions used by de Villiers (2002)

The results obtained by de Villiers [2002], are shown to have been conducted at the operating conditions given in Table 4-2. To validate these results and attempt to attain more accurate results, the same test conditions were chosen for the testing. The Reynolds numbers

indicated by de Villiers [2002] in Table 4-2 appeared to be high in comparison to previous tests on the rig. These values were re-calculated and are indicated in Table 4-3, the operating conditions for the current experimental tests.

Total inlet pressure [Pa]	40 000
Compressor motor speed [RPM]	2500
Turbulence intensity [%]	3
Total inlet temperature	100°C
Mach number at cascade inlet	0.40
Mach number at cascade exit	0.63
Reynolds number based on blade chord length at cascade inlet	2.57×10^5
Reynolds number based on blade chord length at cascade exit	3.46×10^5

Table 4-3: Base testing conditions used for current research testing (2004)

4.4.2 Results

Amongst the numerous experimental pressure tests conducted by the author, was the identification and elimination of possible causes of error. As discussed earlier these causes include blocked pressure tappings and/or silicon tubing, insufficient sealing of the diffuser inlet, and obstructions within the inlet bellmouth to name a few. Following rectification of these checks, pressure distribution results of some fidelity were achieved. These are shown in Figure 4-9, and compared to the results generated by de Villiers [2002] and Snedden [1998] in 2002 and 1998 respectively.

The results from all three experiments showed excellent trend agreement. The static pressure distribution results from the previous year's yield an interesting progression and provides for discussion and possible conclusions to be drawn. On the suction surface, the author's results follow Snedden's results more closely than those of de Villiers [2002]. The measured pressure values measure slightly higher than Snedden's with an almost exact match in trend. de Villiers' [2002] suction surface results measure consistently lower than those of Snedden and the author. This difference in readings becomes more evident from 80mm suction surface length. This was of particular interest to the author.

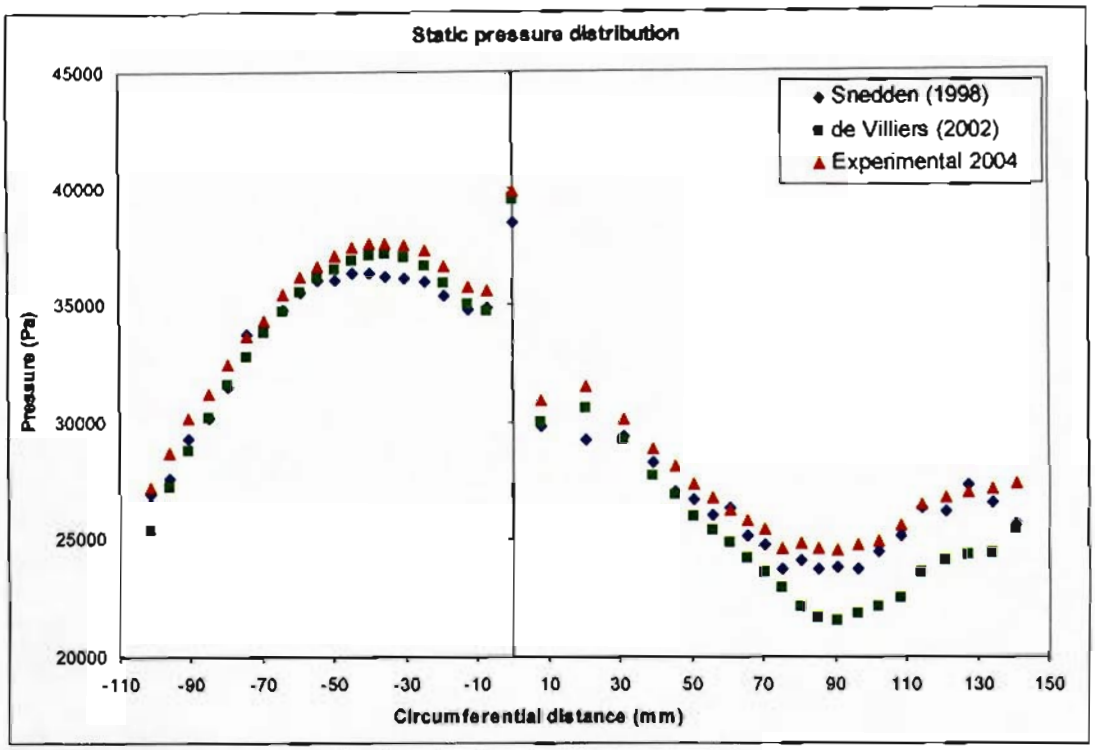

Figure 4-9: Static pressure distribution plot showing progression of results from 1998 – 2004

On the pressure surface, all three experimental plots show good agreement with each other and follow each other closely. However, Snedden's results show a discrepancy between 20 and 50mm circumferential distance, where the values lie approximately 1000 Pa beneath the values measured by de Villiers [2002] and the author. This is also true for the leading edge pressure measurement. The test conditions used by Snedden and de Villiers [2002] were collected and analysed. Since it appears that the flow conditions of the rig have changed very slightly in the past years, it was justified to perform a thorough analysis of the flow phenomenon within the cascade in order to establish the possible cause of any differences. Simply using the pressure data; namely the total, static inlet and static exit pressure, much information can be extracted about the flow in the cascade. High speed flow equations were used to perform these calculations. Table 4-4 contains the progressive testing data for the tests performed on the rig over the past few years.

The results of the author correlate more favourably with Snedden's results, especially on the suction surface. However, Table 4-4 shows that Snedden's pressure conditions were not the same as the author's, and Snedden's static inlet and exit pressures of 34531 Pa and 27 720 Pa respectively, were both lower. de Villiers' [2002] static inlet and exit pressures of 35 086 Pa and 27 500 Pa respectively are similar to those of Snedden's and yet de Villiers' [2002] results show a large discrepancy toward the suction surface trailing edge in comparison to the results of the author and Snedden. This further supports the original hypothesis that de

Villiers [2002] suction surface pressure distribution was recorded at too high a velocity, and needed further investigation.

Variable	Snedden (1998)	de Villiers (2002)	2004
Total Pressure (Pa)	39177.50	39452.00	39985.80
Total Temperature (K)	368.15	374.00	373.00
Inlet Static Pressure (Pa)	34531.61	35086.00	35830.00
Exit Static Pressure (Pa)	27720.89	27500.00	30500.00
Inlet Mach No.	0.43	0.44	0.40
Exit Mach No.	0.72	0.77	0.63
Inlet Static Temperature (K)	355.11	361.68	361.49
Exit Static Temperature (K)	333.50	337.36	345.23
Inlet Velocity (m/s)	162.01	157.51	152.23
Exit Velocity (m/s)	264.09	271.58	236.43
Total Density (kg/m^3)	0.37	0.37	0.37
Inlet Density (kg/m^3)	0.36	0.37	0.37
Exit Density (kg/m^3)	0.29	0.28	0.31
Inlet Reynolds No.	2.63E+05	2.62E+05	2.57E+05
Exit Reynolds No.	3.63E+05	3.66E+05	3.46E+05

Table 4-4: Table of flow data recorded on the rig from 1998 to 2004

Note: The Mach and Reynolds numbers have been calculated from the respective experimental measurements.

It must be noted how the suction surface data is seemingly heavily influenced by slight adjustments in flow pressure, whereas the pressure surface data remains relatively constant. Similar findings where the pressure surface remained unchanged and the suction surface was susceptible to changes in flow, were found in studies by Brown and Burton [1978], Graziani et. al. [1980], and Consigny and Richards [1982]. Further reasoning may be due to the suction side tailboard setting in the cascade which is far from ideal. Snedden conducted periodicity pressure tests on the cascade at the exit, which presented disappointing results. Ideally the cascade needs to be redesigned to include more blade rows that will avoid the influence of the suction side tailboard. Generally it is good cascade testing practice to achieve good periodicity in a pitchwise direction and good uniformity of the flow in a spanwise direction. It is written in Gostelow [1984] that good periodicity at subsonic speeds, dictates the use of a sufficient number of blades. Good periodicity has generally been specified with a minimum number of seven blades.

Table 4-4 was studied to determine the cause of the rig conditions changing over the past six years. Clearly the static inlet and exit pressures are the factors which have changed, thus affecting the corresponding velocities. As with the rig utilised in these tests, many cascade

tunnels cool the air using a heat exchanger downstream of the compressor. The tendency of water vapour to condense is assisted by the cooling of the air within the plenum following a test. This can lead to moisture build up in the plenum causing severe corrosion problems in the long run. Unfortunately, on completion of the final pressure measurements, slight evidence of moisture was seen within the plenum. The source of the moisture was found to be from the annular cooling radiator which was leaking slightly, due to corrosion. The problem of moisture and water vapour within the system during testing is not acceptable. Air and water vapour possess different properties and suggest two phase flow was most likely to have been possible. With this in mind, albeit that the author's results appear to support the pressure distribution of previous research, the results cannot be regarded reliable and conclusive. The above fact could possibly explain any changes in flow conditions. The annular cooling radiator has therefore since been replaced and the plenum walls have been renovated with a fresh coat of anti-corrosive paint, along with the cascade having been sanded clean of rust particles.

In addition, the corrosion of the radiator cooling fins could cause fusion between the fins and restrict the flow to some extent. This flow restriction could, as in the case of inadequate insertion of the diffuser inlet, reduce the mass flow into the cascade and reduce the velocity, increasing the pressure profile slightly. This suggestion was not supported by any experimental flow data and was therefore only passed as a possible cause of measurement error.

One other possible cause for the changing operating conditions, is the installation of the new and accurate pressure control system. The existing Kulite transducer measures the cascade total inlet pressure, whilst the plenum pressure is controlled using the signal received from the new *WIKA*™ pressure transducer. This new system controls the plenum pressure more accurately, thereby measuring static inlet and exit pressures that are slightly different to previous measurements.

4.4.3 Newly generated experimental pressure distribution

Due to the possibility of two-phase flow during the author's pressure measurements, further validation was required to conclude the pressure distribution. With the radiator replaced, and the plenum cleaned of corrosion evidence, new experimental pressure measurements have been performed without the effect of any water vapour. This was safely performed by Cassie [2007]. The 2007 experimental pressure distribution is shown in Figure 4-10.

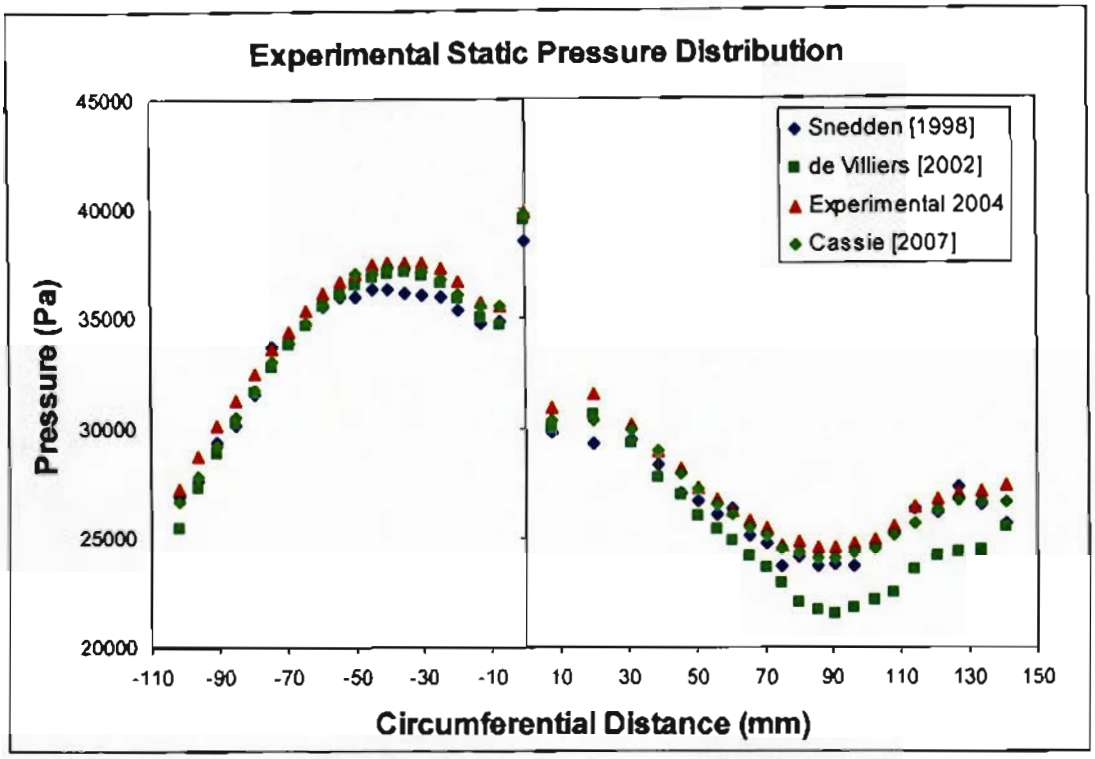

Figure 4-10: Static pressure distribution plot showing progression of results from 1998 – 2007

The new results show excellent agreement with the trends of previous tests and follow the results of Snedden and the author very closely over the entire blade surface. In fact, on the suction surface, a majority of the measured values are equal to the values measured by either the author or Snedden. On the pressure surface in the region from 10 – 50 mm circumferential distance, the new results deviate slightly from those of Snedden and follow the results of the author and de Villiers [2002] more closely. On the remainder of the pressure surface towards the trailing edge the new results can be seen to fall within the boundaries of all the results generated by Snedden, de Villiers [2002] and the author.

4.4.4 Conclusions and discussion of experimental flow

The original hypothesis that de Villiers' [2002] suction surface static pressure profile was too low seems to have been validated. The new pressure profile generated, follows the previous trends excellently. The suction surface data is shown to be most heavily influenced by any slight changes in the cascade flow conditions. This is predominantly seen from 80 mm suction surface length, toward the trailing edge.

The latest static pressure distribution generated by Cassie [2007] appears to be very satisfying. The reliable state of the rig has allowed for the measurement of reliable pressure

results. The pressure distribution plots from 1998 until now, do an excellent job in demonstrating the utmost importance of reliably generating and measuring the flow conditions within a cascade. Doing this accurately is hugely important for the input boundary conditions required in the CFD analysis. This is covered in the chapter 6 where the CFD solution is detailed. The final static pressure distribution is given in Figure 4-11.

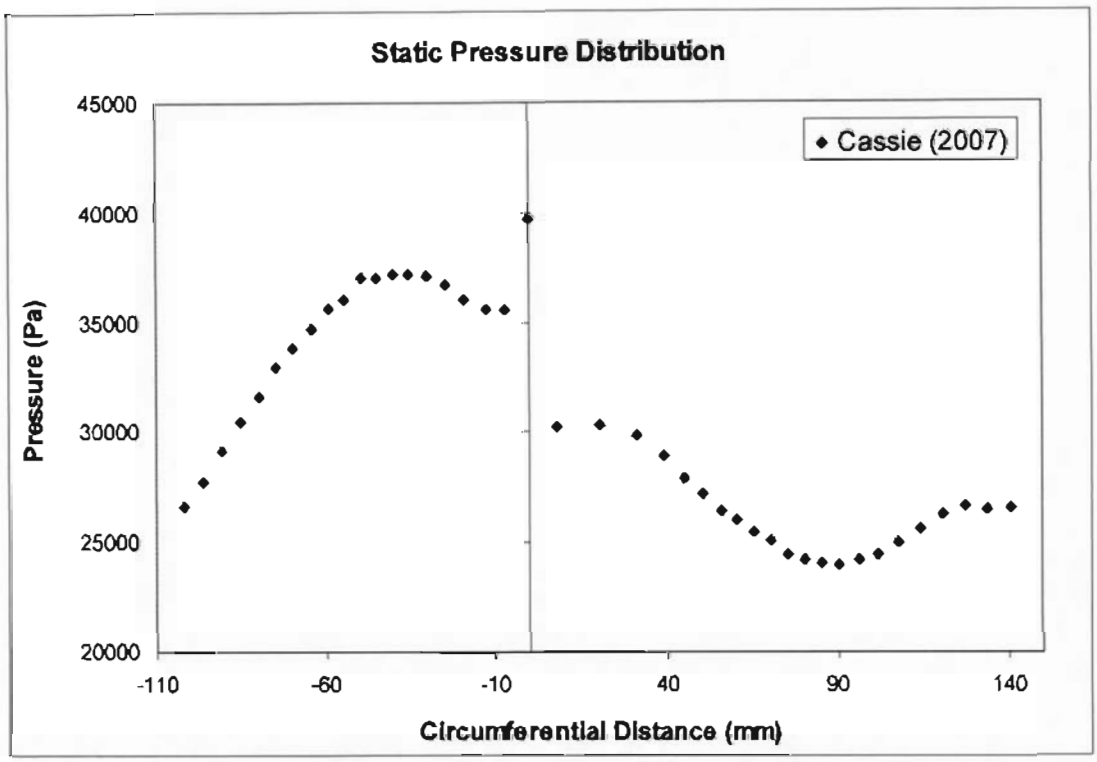

Figure 4-11: Final experimental static pressure distribution (Cassie [2007])

The old age of the rig, specifically the hydraulic drive pump, causes the flow speed to vary constantly. This problem was obviously encountered by de Villiers [2002] during the suction surface measurements. Careful monitoring of the compressor speed is required immediately prior to the pressure testing. The flow speed determines the inlet and exit static pressures, which, as discussed numerous times already, is the primary factor in the flow conditions. These pressures affect all variables in the cascade and require high accuracy and reliability, in order for repeatable results to be produced. Included in the recommendations for future work, is a suggestion for more reliable and accurate speed control. It must be remembered that measurement of turbine blade heat transfer is worthless for validation purposes, without detailed flow within the cascade.

In analysing the flow around the blade, the experimental results indicate the highest pressure to occur at the leading edge. Here the flow impinges at right angles to the blade surface and

the velocity is close to zero. The surface Mach number plot, generated from Cassie's [2007] experimental results using high speed flow equations, is shown in Figure 4-12.

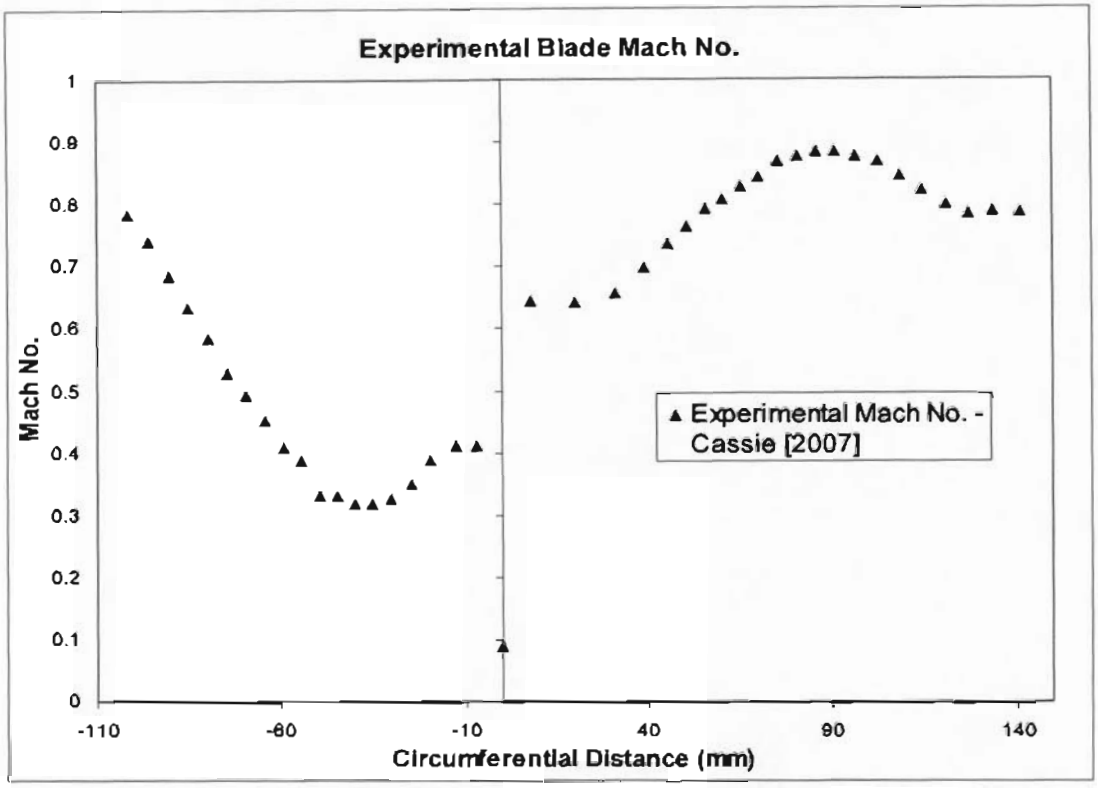

Figure 4-12: Experimental Mach number plot from Cassie's [2007] results

The flow then accelerates rapidly around the circular radius of the leading edge, corresponding to the sharp decrease in static pressure on both the pressure and suction surfaces. Here, the boundary layer develops under the influence of a favourable pressure gradient. It is known from industry that this blade profile has a separation bubble at the pressure surface leading edge. The leading edge pressure decrease must eventually reach a minimum, with the flow velocity reaching a maximum when $dp/dx = 0$ (corresponding to 7 mm pressure curve length). At this point, the flow faces an adverse pressure gradient ($dp/dx > 0$), and decelerates until the velocity gradient (perpendicular to the blade surface) at the surface becomes zero. Here, separation of the flow occurs, since the fluid near the surface lacks sufficient momentum to overcome the pressure gradient and continued downstream movement is impossible. Boundary layer separation must occur since the oncoming fluid also prohibits flow back upstream.

The low resolution of the experimental pressure tappings does not permit an accurate analysis of the flow phenomenon in this region. A more detailed and complete analysis can be done once the CFD solution is generated and can be used for comparison. The CFD solution will also provide a higher resolution of the pressure profile. The heat transfer

results will also be a very useful tool in describing the flow characteristics. Downstream of these points, the flow is seen to accelerate under the influence of the favourable pressure gradient. See chapter 6 for a complete discussion of the blade flow phenomenon, where final flow conclusions can be made and compared.

Sources of error with the experimental measurements are no doubt due to the experimental equipment available to the user. The flow speed is difficult to maintain and can cause variance in the flow conditions within the cascade. The measurement of the inlet and outlet static pressures are perhaps the most important sources of error. Snedden [1998] shows that the pressure and turbulence intensity vary significantly at the inlet. Cascade testing generally requires good periodicity and this can be achieved by increasing the size of the cascade and inserting more blade rows. This way the affect of the suction side tailboard will be eliminated.

CHAPTER 5

EXPERIMENTAL HEAT TRANSFER MEASUREMENTS

5.1 Introduction

Completion of the experimental flow measurements validated the blade static pressure distribution. This proved to be a valuable exercise since it was realised how small adjustments can significantly affect the cascade flow conditions. Furthermore, not only were the flow characteristics within the cascade determined, which showed to have changed slightly, but valuable experience and knowledge of the rig operating procedure was gained.

Measurement of the SMR-95 blade heat transfer coefficients could now commence. The flow conditions for the heat transfer measurements are the same as for the pressure measurements (see Table 4-3). The cascade is however, assembled with the heat transfer test blade stack that is instrumented with thin-film gauges. In order to generate a heat flux into the test blade, a temperature gradient between the hot gas-stream and the blade wall needs to be developed. To simulate realistic engine conditions, a blade wall to gas-stream ratio of approximately 0.8 is used.

The test blade is cooled in an insulated cooling box and plunged into the hot gas-stream by means of a pneumatic ram. This produces a rapid change in the blade wall temperature and consequently a voltage change in the thin-film heat flux gauges. The voltage change is converted, by the heat transfer analogue cards, into a current proportional to the heat flux. These cards have been built, based on the design by Oldfield et al [1982], and modified by Snedden [1995]. Appendix A5 of Snedden's dissertation [1995] gives a full description of the heat transfer analogue boards.

For the heat flux data to be recorded by the data acquisition system, the current needs to be converted to a voltage. The analogue cards perform the conversion and amplify and filter the voltage of high frequency noise by means of a 0.01 Hz – 100 kHz band pass filter. The cards, therefore, act as an initial noise filter before the voltage is processed by the data acquisition card. Measuring the heat flux directly in this manner presents a major advantage. To determine the heat transfer coefficients, both the heat flux and blade wall temperature need to be known. Therefore, to numerically reconstruct the blade wall temperature, an integration equation is used, which is inherently noise reducing. This means that only the

electronic noise is recorded. In a process where electronic noise can be crucial to accuracy, this technique is superior to direct measurement of the wall temperature. Direct measurement of the wall temperature requires a differential equation to calculate the heat flux and the electronic noise would thus be amplified numerically.

The final voltage from the analogue cards, which is proportional to the heat flux, is acquired by the data acquisition card and associated software. A software program written in LABVIEW by Snedden [1995], performs the necessary calculations for the processing of the heat transfer coefficients (see section 5.5).

The following sections serve to introduce the equipment that is specific to the heat transfer measurements. The calibration of the thin-film sensors is discussed and the experimental procedure is presented. Problems encountered during the tests are also presented. Following are the experimental results and associated discussions.

5.2 Heat transfer test blade stack

The heat transfer test blade consists of two sections: an aluminium un-instrumented blade ("dummy" blade), and an instrumented section made of a Macor substrate. The two sections are joined together to form one continuous blade profile. Figure 5-1 below illustrates the basic configuration of the test blade.

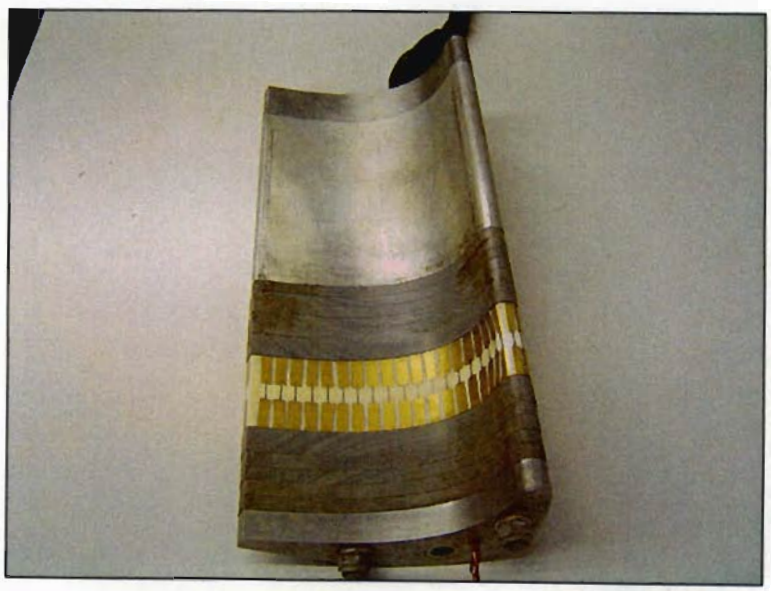

Figure 5-1: Configuration of the heat transfer test blade

This configuration allows for the aluminium dummy blade to be positioned within the cascade, where the hot-gas flow becomes fully developed over the profile. Meanwhile, the instrumented blade is connected above the aluminium blade and is positioned within the cooling box, where it is cooled before the test. By doing this, when the blade is plunged, the flow is not disturbed by the sudden introduction of the test blade. The two sections of the blade are insulated from one another by vesconite spacers. This prevents any heat conduction from the aluminium blade to the instrumented Macor section.

The test blade consists of 48 thin-film gauges hand-painted onto the Macor substrate. Shown below in Table 5-1 are the thin-film gauge sensor positions.

Sensor Number	Circumferential Position (mm)	Sensor Number	Circumferential Position (mm)	Sensor Number	Circumferential Position (mm)
LE 1	0.3	17	79.5	33	81.9
2	3.5	18	84.5	34	76.2
3	6.9	19	88.7	35	70.8
4	13	20	94.4	36	66
5	18.1	21	99.7	37	60.4
6	23.1	22	105.4	38	55
7	28.3	23	110.5	39	49
8	33	24	115.4	40	44.5
9	37.8	25	121	41	38.9
10	43.1	26	126.6	42	33.5
11	48.3	27	131.5	43	28.2
12	53.3	28	136.5	44	22.7
13	58.4	29	107	45	17.3
14	64.3	30	98.2	46	12
15	69.4	31	92.8	47	6.7
16	74.6	32	87.6	48	3.7

Table 5-1: Thin-film gauge heat flux sensor positions

The gauges consist of thin strips of platinum paint, positioned across the mid-span of the test blade. To transmit the gauge signal, gold painted leads are used. Gold is used since it has a very low resistance relative to that of the platinum gauge. It can therefore be assumed that the voltage drop only occurs across the platinum gauge. On one side of the gauge, the gold leads are painted to the edge of the blade, where they independently make contact with pins, which plug into holes in the Macor blade. These pins are used for connection onto the flying leads to transmit the heat gauge signals. The other side of the gauge sees the gold leads painted to the edge, where they are joined together forming a common ground. This common ground connects via a pin as well. These pins within the Macor test blade, allow the flying leads to be conveniently passed through internal passages of the blade and transmit

the signals to the analogue boards. The signals are finally supplied to the analogue cards by means of 25 pin D-type pin connectors. Figure 5-2 below illustrates the gauges.

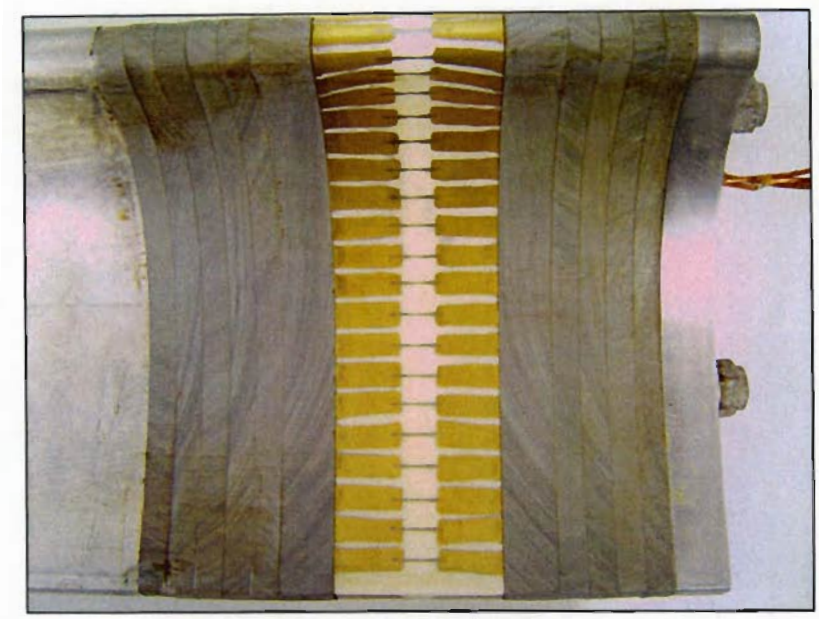

Figure 5-2: Thin-film gauges

The 48 sensors are divided into six groups of eight, eight sensors per D-type connector. The D-type connectors are numbered "P1" to "P6". P1 measures sensors 1 to 8 whilst P2 measures the next eight sensors (sensors 9 – 16). This pattern is repeated around the blade until the pressure surface leading edge sensor 48. The sensors are grouped into eight because there are only eight differential channels available on the data acquisition card. For this reason, only eight sensors, or one D-type connector, can be measured per test.

The aluminium dummy blade, Macor test blade, and Tufnell spacers are all tie-bolted together to form a sandwich of profiled sections, thereby making up the entire blade section. Furthermore, there are four K-type thermocouples embedded within the Macor section to measure the internal blade temperature before testing.

Macor provides all the necessary properties for the measurement of transient heat transfer. Importantly, it is well documented and has a high specific heat capacity and low thermal conductivity, which allows 1-Dimensional heat transfer theory to be applied. The material properties of Macor are found in Appendix 1 of Snedden's dissertation [1995]. A full description of the thin-film gauge manufacturing technique is also given in Snedden [1995].

5.3 Sliding mechanism and pneumatic ram

In order to facilitate the technique of plunging, or sliding the test blade into the cascade, the entire blade stack is attached at its bottom, to a sliding plate. This sliding plate, slides on linear bearings and nitrided rods. The sliding mechanism is fixed to the underside of the cascade and is positioned to allow the displaced dummy blade to slide out of the cascade. At the end of the sliding mechanism, two 6 mm FESTO shock absorbers are positioned to absorb the impact of the blade stack after plunging. Figure 5-3 illustrates the blade stack fastened onto the sliding mechanism.

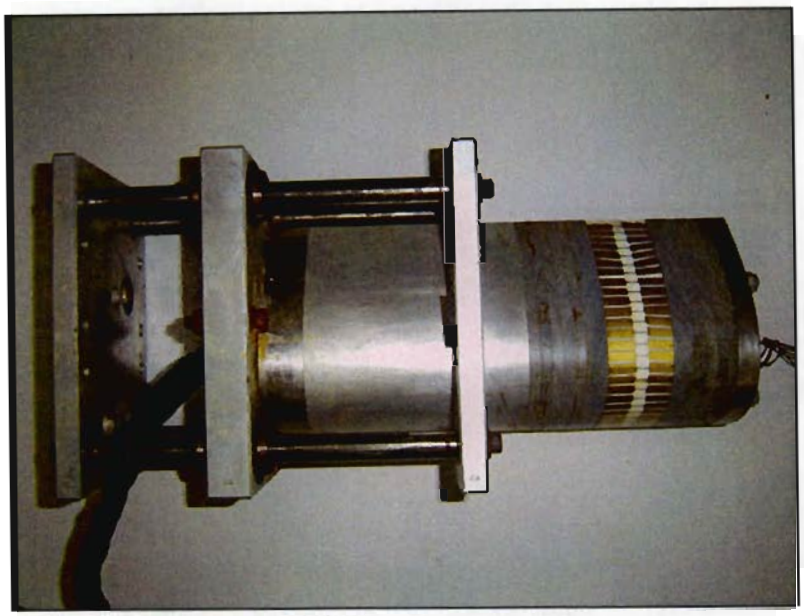

Figure 5-3: Blade stack fastened onto the sliding mechanism

A FESTO DSG-20-100-PPV-A pneumatic ram is screwed into the top end of the blade stack. This ram is end cushioned, which together with the shock absorbers; soften the blade stack impact at the end of plunging. The blade stack has been measured to take 200 ms from actuation till rest. The pneumatic ram is fired, or retracted by controlling the compressed air in the ram cylinder. Two ports on the cylinder are independently connected to two solenoid valves. The valves are supplied with compressed air at 6 bar, supplied from the same air-line that supplies the air motor. The alternate opening and closing of the valves is controlled by a switch on the data acquisition console. This switch controls which valve fills or dumps the compressed air in the cylinder, and hence which direction the ram is fired; ultimately retracting or plunging the blade.

5.4 Cooling circuit and cooling box

To achieve the realistic engine blade-wall to gas temperature ratio of 0.8, the test blade is initially chilled within the insulated cooling box. Figure 5-4 shows the cooling box open from the top, housing the blade within.

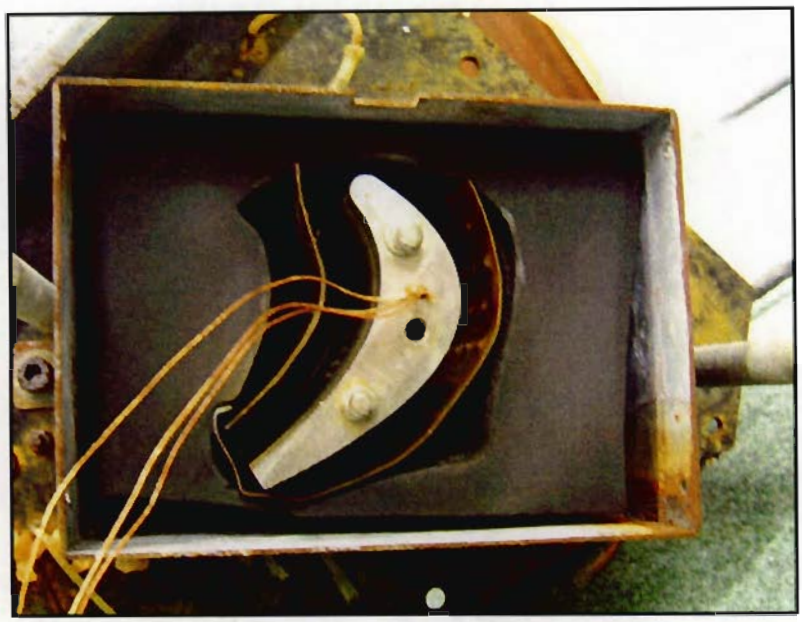

Figure 5-4: Cooling box with associated components

The cooling box is made from steel and is fastened on top of the cascade, positioned over the test blade. The cooling box contains layers of high temperature insulation, which lines the walls of the box and is cut to allow the blade and pneumatic ram to operate and move freely through the section. A lid covers the box and contains holes for cooling air pipes and the pneumatic ram. A new cooling box has been designed by the author. This box is smaller and fits easily on top of the cascade, without interfering with any pressure tappings. New high density, high temperature (resistant to $100^{\circ}C$), polyurethane foam has replaced the old oil saturated foam.

An Effepizeta belt-driven blower sucks air at $100^{0}C$ through a drain pipe at the bottom of the plenum. This air passes through a shell and tube water heat exchanger before entering the blower. Passing through the blower, the air is then blown through a second shell and tube water heat exchanger before it enters the plenum and is blown into the cooling box via two pipes. A perforated copper plate surrounds the test blade, which facilitates an impingement cooling process on the blade surface. The cooling box is not completely sealed

to ensure that the cool air does not pass into the cascade through the profile cut in the cascade end wall. The air entering the cooling box has been measured at $20^0 C$.

During the conducting of the tests, the current system nevertheless proved to be very difficult to maintain. These problems are described in subsequent sections. Details are given in section A4.2 of Appendix 4.

5.5 LABVIEW heat transfer analysis program software

The isothermal heat flux into the blade is calculated by plotting the heat flux against the wall temperature, as described by Ligrani et al [1982] and is presented in Appendix 1 of de Villiers' dissertation [2002]. Therefore a software program was developed in LABVIEW by Snedden [1995]. This program was developed to reconstruct the blade wall temperature using the voltage data acquired from the analogue cards. This voltage is proportional to the heat flux into the blade.

LABVIEW is designed for data acquisition and processing purposes. The program language is very user friendly, providing a graphical user interface (GUI) to work with. The programming structure is object orientated where virtual instruments (VI's) are literally wired together to form a virtual data acquisition and processing system. The specific heat transfer program written by Snedden [1995] is called ISOTEMP1 and the details pertaining to the design can be found in Appendix 4 of Snedden's dissertation [1995].

The heat flux voltage signal from the analogue cards, is acquired using WAVEVIEW software supplied by the manufacturers of the data acquisition card, Eagle Technologies. The data is saved and uploaded into LABVIEW in a text format. The ISOTEMP1 program then follows the following task process:

1. Reads the heat flux voltage data in text format
2. Calculates the acquisition rate from the first acquisition time step
3. Separates each channel voltage and saves it to a new file
4. Filters and trims the voltage data as per user instruction and saves the pertinent data

5. Converts the voltage to a heat flux according to calibration information entered by the user
6. Reconstructs the wall temperature history from the heat flux data
7. Saves the data and presents the final heat transfer coefficient results

To avoid any errors occurring in the LABVIEW program, the data acquired in WAVEVIEW must be of the correct format. There cannot be any headings or descriptions within the data text file. Furthermore, the channel columns must not have spaces and delimiters must be used to separate each channel. These settings for the data file must be predefined in WAVEVIEW before the data is saved.

Uploading the saved data text file into LABVIEW also requires a specific method to avoid any errors within the program. The "Raw Data Filename" text box must be left blank and the directory path name for the data to be saved in must be specified. Thereafter, the program will prompt which file must be read for analysis. Further details into the use of the program can be found in subsequent sections of this chapter.

5.6 Calibration of the thin-film gauges

As mentioned in Chapter 2, the thin-film gauge is essentially a resistance thermometer. The resistance of each gauge varies as a function of its temperature. For this reason each gauge needs to be calibrated to determine its individual resistance-to-temperature characteristic. The gauge resistance and hence calibration constant, is strongly dependent on its length and thickness of the paint. The thin-film heat flux gauge calibration constants represent the "Resistance/Temperature constant alphaR" value in the test data form of the LABVIEW program "ISOTEMP".

The gauges were all calibrated by Snedden in 1995, and lost documentation necessitated recalibration by de Villiers in 2002. de Villiers [2002] states that the variance of the calibration constants significantly affected the heat transfer coefficient results. Initial monitoring of the gauge resistances at ambient temperature indicated that the calibration constants had changed drastically. Therefore, to validate and ensure optimum accuracy, the gauges were recalibrated. Furthermore, it is highly recommended that the gauges be recalibrated as often as possible between testing. The tight tolerance between the cascade

end-wall and the thin film gauges upon blade plunging, can cause slight scratching of the gauges. Repeated plunges can result in the gauges becoming slightly thinner, and thus more sensitive.

The calibration of the gauges involves varying the temperature of the gauges in a well controlled temperature environment, and monitoring the resistance change. Ligrani et al [1982] discusses the use of a heated oil bath to calibrate the gauges in. This is the preferred apparatus for calibration purposes. However, at the University of KwaZulu-Natal, an industrial convection oven is available and was utilised for the calibration of the gauges.

The blade stack was placed in the oven and the sensor leads and all thermocouple wiring was passed through the lining of the oven door. The blade was left to stand for a significant length of time to allow the ambient temperature of the oven to settle for the first measurement. Two thermocouples were used to monitor the air temperature close to the surface of the blade. These are essential for accurate measurement and ultimately calibration constants. The oven controller displays the oven temperature. However, the controller thermocouple is positioned in front of the convection fan, resulting in a slightly inaccurate temperature reading. The four K-type thermocouples within the blade were also used to monitor the internal blade temperature.

de Villiers [2002] describes how problems arose when the oven could not control the temperature and keep it constant for a long enough period of time. This meant that the temperature varied as the resistances were measured. de Villiers [2002] measured the temperature of the oven air at the start and end of each D-type connector measurement, and then averaged the temperatures. These temperatures were used as the final values for the calibration plots. This appears to be unreliable and inaccurate and a new method was devised. This involved simply reading the temperature from each of the two thermocouples before each and every sensor resistance measurement. The average of the two thermocouple readings was then used as the temperature for the corresponding sensor resistance. This meant that any variance in the oven temperature was excluded as a source of error. The exact temperature at the time of measurement is known.

A spreadsheet for the calibration process was made. This had provision for the two thermocouple temperatures and their corresponding average temperature and sensor resistance. The temperature and corresponding resistances for all of the sensors were measured at ambient temperature. The temperature was measured using a FLUKE 52 K/J thermometer. The sensor resistances were measured using a digital multimeter, by

measuring the resistance between the corresponding pin pairs on the D-type connectors. These values were recorded on the spreadsheet before the oven controller was set to a higher temperature for the next measurement. Leaving the blade in the oven for an extended period of time allowed for the blade to reach a constant temperature throughout the entire blade. This would reduce error in the calibration calculations. The measurement of temperature and resistance was repeated for all the sensors for five widely spaced temperatures. The results of the individual sensor resistance changes to temperature were plotted and their gradients calculated. The calibration data and calibration constants (alphaR values) for all the sensors can be seen in Appendix 5. Excellent linearity was seen in the plots. A typical thin-film sensor calibration plot is shown in Figure 5-5.

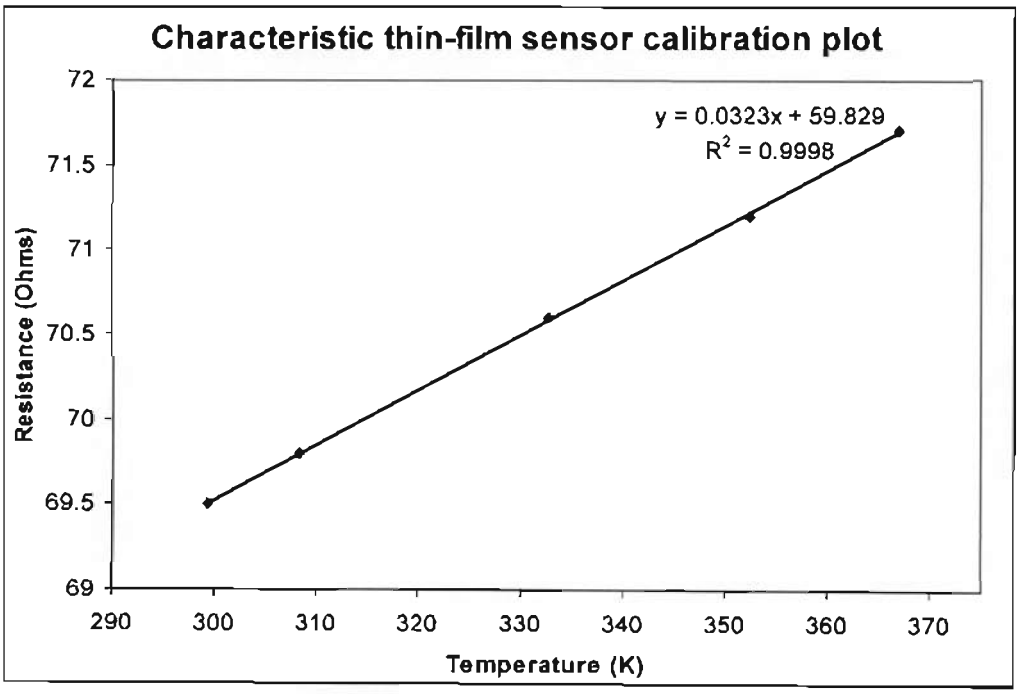

Figure 5-5: Typical thin-film sensor calibration plot

From the graph, the gradient $\Delta R / \Delta T$ can be calculated, as well as the y-intercept. Since the blade wall to free-stream temperature ratio is approximately 0.8 in order to simulate realistic engine conditions, the blade is plunged into the 373 K air stream at 313 K. This means that T_0, or the initial blade temperature, in equation A-13 presented by Ligrani et al [1982], is 313 K. With these values known, the resistance R_0 corresponding to a temperature of 313 K can be calculated for each individual sensor. The calibration constants for each sensor are then calculated by dividing their respective gradients by their individual R_0 values. The R_0 values for each sensor are very helpful since they indicate at what resistance each sensor measures 313 K, the initial blade plunging temperature. Since the thermocouples embedded in the Macor do not give an accurate measure of the blade surface temperature, these resistance values indicate to the operator of the rig, when to plunge the blade.

Snedden [1998] calculated the calibration constants using a T_0 value of 298 K since this was the initial blade temperature used by Ligrani et al [1982]. Since the blade was being plunged at 313 K, the calibration constants for the sensors would be inaccurate and could possibly affect the results. de Villiers [2002] identified this error and rectified it by using the correct T_0 value of 313 K. de Villiers' [2002] heat transfer distribution differed to that of Snedden's [1998]. An actual measurement of the associated error is given in section 5.10.1.

5.7 Assembling the cascade

The cascade needs to be assembled with the heat transfer blade stack and the associated equipment. This assembly is performed outside the plenum due to space restrictions within. The blade stack is firstly fastened to the sliding plate on the slider mechanism. Using extreme caution not to scratch the sensor surfaces, the blade is then inserted through the blade profile slot in the cascade end-wall. This slot has an extremely tight tolerance and caution against scratching the sensors must be exercised throughout the assembly. The sliding mechanism is then fastened to the underside of the cascade. Fastening the sliding mechanism too tight on any one side, pulls the blade to one side and causes the blade to jam. Tightening various bolts will allow the blade to slide freely.

Following this, the cooling box is fastened to the top of the cascade. The blade must be free to move past the insulating foam and perforated copper plate within the cooling box. The pneumatic ram is inserted through the cooling box lid and screwed into the top of the blade. The lid and pneumatic ram are then securely fastened to ensure no vibration occurs during plunging. The cooling pipes from the blower are connected to the inlets on the cooling box lid and the pneumatic ram air pipes connected onto the pneumatic cylinder. Figure 5-6 illustrates the cascade fully assembled within the plenum.

Following assembly, the cascade is fastened to the compressor inlet diffuser. The heat flux sensor flying leads are pulled through a specially made port cover and sealed with silicon gel. The blade internal thermocouple leads pass through another port cover and also sealed. Finally the static pressure tappings are connected to their respective pipes for measurement; and the total inlet temperature thermocouple is connected to the temperature display.

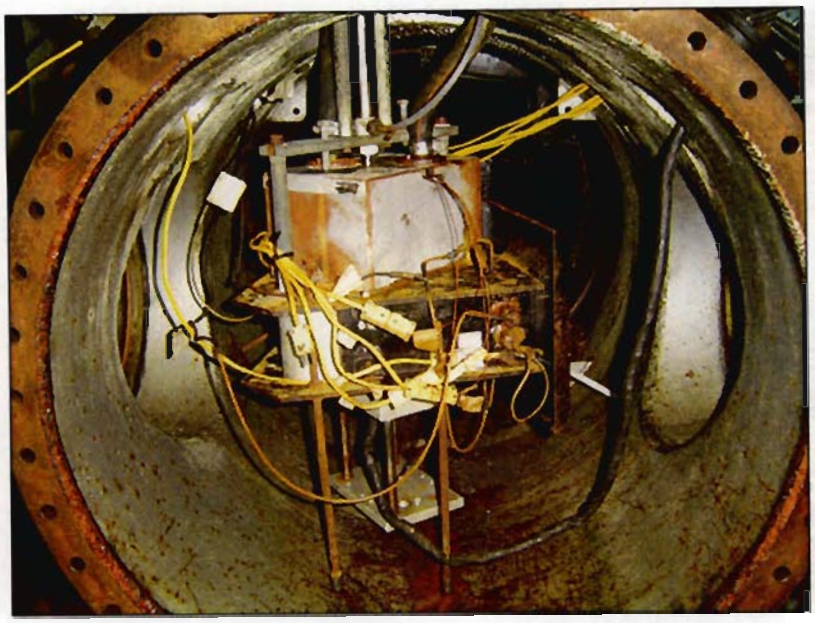

Figure 5-6: Fully assembled cascade within the plenum

5.8 Checking the pneumatic ram and cooling system

Before sealing the plenum, a check was performed to ensure the plunging mechanism functioned correctly. This requires air pressure and hence the compressed air supply needs to be opened, as well as the valve on the pneumatic air line. The pneumatic ram switch was actuated. The blade plunged the first time, however, it was seen to decelerate and jerk toward the end of its travel. It was initially thought that the bearings on the slider mechanism were worn and the slightly rusted nitrided rods had caused them to partially cease. Lubricating oil was applied to investigate its affects. No improvement in the plunging speed was seen. This plunging speed must be rapid to ensure that the blade is rapidly subjected to the hot cascade gas-stream and a transient heat transfer measurement can be undertaken.

Careful inspection of the entire working mechanism revealed that a small screw on the solenoid valve was blocking an airway that may be preventing the air being released from the pneumatic cylinder during plunging. This screw was removed and the blade plunge occurred very rapidly. The cause of the problem was that the air was not allowed to escape from the pneumatic cylinder and was simply being compressed by the ram, which prevented a free moving blade plunge.

The cooling system was also checked before the plenum was sealed. The belt-driven blower was started up and its initial operation was monitored. The blower had, of course, not been operated during the pressure tests and had therefore been standing for some length of time. The blower was working without complication until it suddenly ceased and the motor

switched off. This required immediate attention to the rotary components of the blower and the attached motor. Details of the problem and the maintenance to the blower and associated equipment, are given in section A4.2 of Appendix 4.

When connected to the cooling box inlets on the lid, significant flow of the cooling air could be felt entering the cascade from the cooling box through the cascade end-wall. This strongly suggested that the blower must be turned off immediately prior to plunging. This will prevent flow and temperature disturbances with the cascade flow and hence reducing erroneous heat transfer measurements.

5.9 Experimental procedure

The heat transfer experimental procedure is similar to that of the pressure measurements. However, extreme attention to detail is required during the experiments. This is given that there can only be eight sensor measurements per test run; the tests therefore have to be run six times to acquire all 48 sensor responses. In order to be accurate, all these tests need to be carried out at the same cascade conditions. In addition, there are numerous extra tasks and measurements which need to be taken care of immediately before the plunging of the blade.

5.9.1 Recording the heat transfer data

Outlined below, are some of the pertinent procedures that must be followed during the heat transfer testing. A spreadsheet, "Measured Experimental Data", was made which has provision for the recording of the specific data. The initial sensor resistance and voltage is required for input into the LABVIEW software program and this spreadsheet is used to record these values as well as the compressor rpm, total inlet temperature and the static inlet and outlet pressures. It is important to record all of these variables in order to determine the repeatability of the flow conditions for the various tests. Since the experimental heat transfer measurements are divided into six sections, it is imperative to ensure that the flow conditions for each of the tests are as similar as possible to each other. In addition, the spreadsheet also displays the resistance for each sensor that corresponds to a wall temperature of 40^{0}C (313 K). Having this form at hand and checking the sensor resistances, it can be determined when the blade plunge must be performed. This spreadsheet is presented in Appendix 6.

The speed of the compressor must be raised to the maximum of 3000 rpm, and the radiator cooling water should be left closed so the total inlet temperature is raised as quickly as possible. This is necessary since the gradual heat penetration into the cooling box, increases

the temperature of the blade. This can cause the initial blade plunging temperature of 40°C (313 K) to be exceeded. The cooling water supplying the heat exchangers for the blade cooling air, is opened fully throughout the test to keep the blade as cool as possible.

The rig should be kept running at high speed until the cascade total inlet temperature approaches 100°C. The speed can then be reduced to the required test speed of 2500 rpm and the radiator water valve manually adjusted to maintain the total inlet temperature at 100°C. By this time the initial blade temperature should be close to 40°C. The temperature of the blade wall is determined by monitoring the sensor resistances and comparing the values to the resistances corresponding to 40°C on the "Measured Experimental Data" spreadsheet. As soon as the sensor resistances correspond to a temperature of 40°C, the initial resistance of each sensor is recorded on the "Measured Experimental Data" spreadsheet. These resistances are valuable to calculate the initial blade wall temperature. The D-type plug of the eight sensors to be measured is then connected to the analogue cards. The initial voltage of each sensor is then measured. This is done using a selector box that is wired to a voltmeter. The eight initial voltages can thus be measured as quickly as possible. These voltages must all be recorded on the "Measured Experimental Data" spreadsheet. These measurements all need to be carried out as quickly as possible to ensure the cascade and initial blade conditions do not change during the process. Other parameters such as the compressor speed, total inlet temperature, and static inlet and outlet pressures, must also be noted and recorded. The blower must then be switched off and the WAVEVIEW acquisition system started, followed by the plunging of the blade into the hot stream.

5.9.2 Voltage trace analysis in LABVIEW

The measured heat flux voltage data is read by the LABVIEW software. The program calculates the data acquisition rate using the first acquired time step. The filters within the software have high and low frequency specifications. Should these specifications not be met, an error message will be received when LABVIEW attempts to separate the voltage channels. The message received from the filtering VI is shown in figure 5-7.

This error message was discovered in the early stages of heat transfer testing when the sampling frequency was too small. This was the case because the sampling frequency was set to the frequency required per channel. It must be noted that the sampling frequency applies to all eight channels being sampled. The WAVEVIEW sampling frequency must thus be set at eight times that of the frequency required per channel.

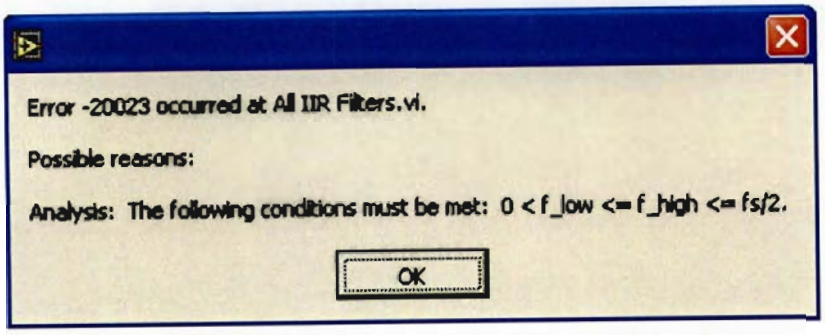

Figure 5-7: Error message received from LABVIEW filter VI

Ligrani et al [1982] discusses how the data acquisition system at the von Karman Institute is capable of sampling all 48 channels at a maximum sampling rate of 500 kHz. This equates to approximately 10 kHz per channel. Furthermore, de Villiers [2002] suggests that a higher frequency than previously used on the rig, be used to sample the heat flux raw data. The author agrees since this will greatly improve the resolution of the heat flux plot, which will produce more data sample points in the region of the heat flux plot immediately after the sudden step change. Ligrani et al [1982] shows that the voltage trace is only 300 ms long. Also, only 150 ms of the trace was used, where the plot is steady. A higher sampling frequency is therefore likely to provide for a more accurate analysis.

5.9.3 LABVIEW software analysis

de Villiers [2002] reports that the most effective LABVIEW filter is the Chebyshev II filter. However, de Villiers [2002] implemented an additional noise filter, the Median filter. This filter was inserted into the program before the data passed through the other LABVIEW filters. It therefore serves as a first line of software filtering, and removes the large voltage spikes previously encountered.

The first stage in the raw data analysis is to adjust the heat flux voltage signal. This involves signal processing where the noise levels are reduced as much as possible. This provides for a smoother signal for the heat flux calculation and ultimately, a better reconstruction of the blade wall temperature can be produced. After the Median filter filters the voltage signal and removes the large voltage spikes, filtering is performed by the Chebyshev II filter. At this stage the low and high frequency cut-off can be adjusted to produce as smooth a signal is possible. In addition, the length of the data sample can be adjusted to only include the essential data points immediately after the initial voltage spike. As reported by de Villiers [2002], the most effective filter cut-off frequency ranged between approximately 70 and 100 Hz. Signal processing is performed for each channel voltage and the program saves the new

voltage trace, to be used in the subsequent heat flux conversion and wall temperature reconstruction.

The acquired voltage traces, when viewed in LABVIEW, showed the characteristic step in voltage followed by the gradual increase in voltage. Following signal processing and filtering, a relatively smooth signal could be produced from most of the eight channels. However, noise was very evident in some of the channel voltage traces. This is certainly a major influence in discarded and inaccurate results, as is reported by de Villiers [2002] and Snedden [1995]. Figures 5-8a and 5-8b below, respectively illustrate a voltage trace before signal processing and a voltage trace after signal processing. Note in Figure 5-8b, the red plot represents the unfiltered trace whilst the yellow plot is the new filtered trace.

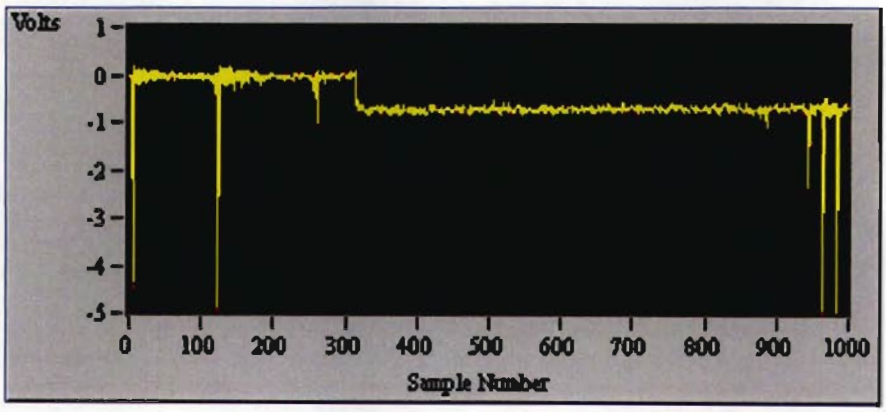

Figure 5-8a: Voltage trace before signal processing

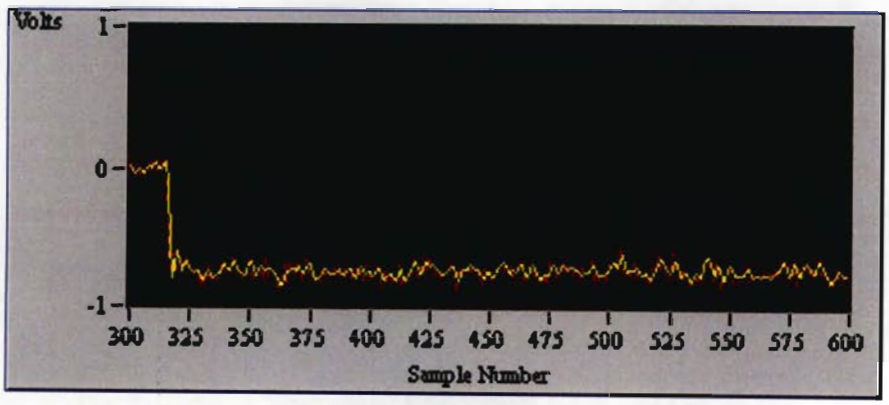

Figure 5-8b: Voltage trace having undergone signal processing

Following the signal processing of all eight sensors, the heat flux calculation is carried out. This requires calibration data input into LABVIEW. The calibration data for the substrate material, individual sensors, and analogue cards are entered into a specific program window, which is shown below in Figure 5-9.

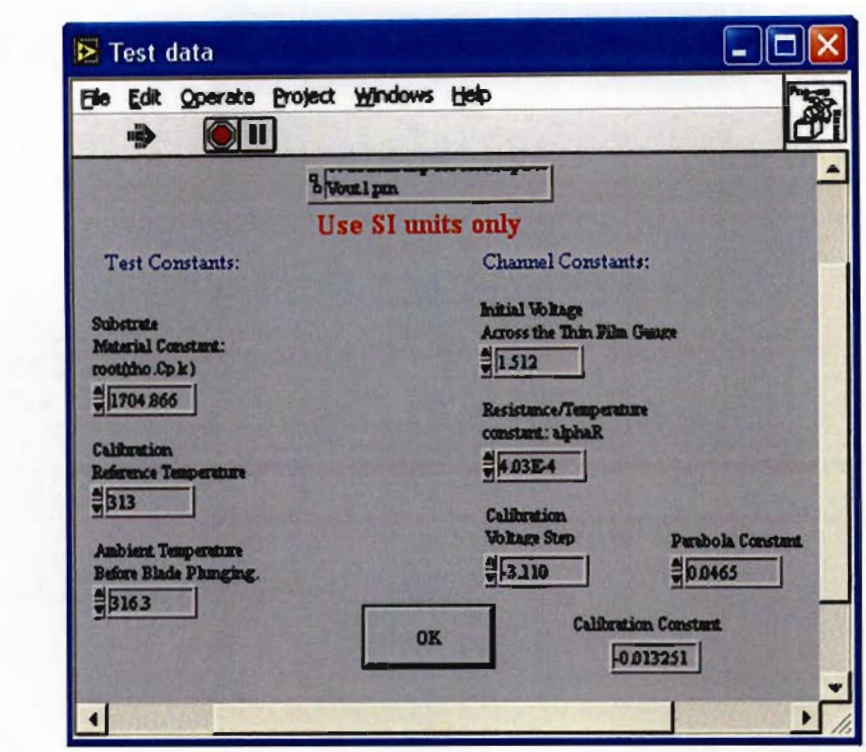

Figure 5-9: Calibration data input window

Referring to Figure 5-9, it can be seen that the window is divided into two columns. The "Test Constants" column refers to the data that is specific to the particular test under analysis. The substrate material constant for Macor (see Appendix 1 of de Villiers' dissertation [2002]) is constant for all the tests since the material is the same for all tests. The sensors have been calibrated to an initial calibration reference temperature of 40^0C (313 K) and hence this value is also constant for each test. The ambient temperature value however, needs to be changed since the ambient temperature around the blade before plunging varies. This is as a result of the impingement cooling process taking place within the cooling box. The initial sensor resistances recorded before the test, are useful to calculate this particular ambient temperature value.

The "Channel Constants" column refers to the particular sensor, or channel being analysed. Therefore the initial voltage and sensor calibration constant (alphaR) needs to be changed according the specific sensor. The final three calibration constants are constants taken from the calibration of the heat flux analogue cards. The "Calibration Constant" is calculated from the "Calibration Voltage Step" and the "Parabola Constant" (see Snedden [1995]. The individual card calibration constants could not be located by de Villiers [2002]. However, after inspecting Snedden's dissertation [1995], de Villiers [2002] discovered that the calibration step response for all the boards were very similar, i.e. range of 3.097-3.131 V,

with an average of 3.110 V. Hence the value of 3.110 V for the Calibration Step Voltage was used to calculate the Calibration constant.

The final results window in LABVIEW produces plots of the heat flux, wall temperature change with time, as well as the heat flux versus wall temperature. These plots can be seen in Figure 5-10.

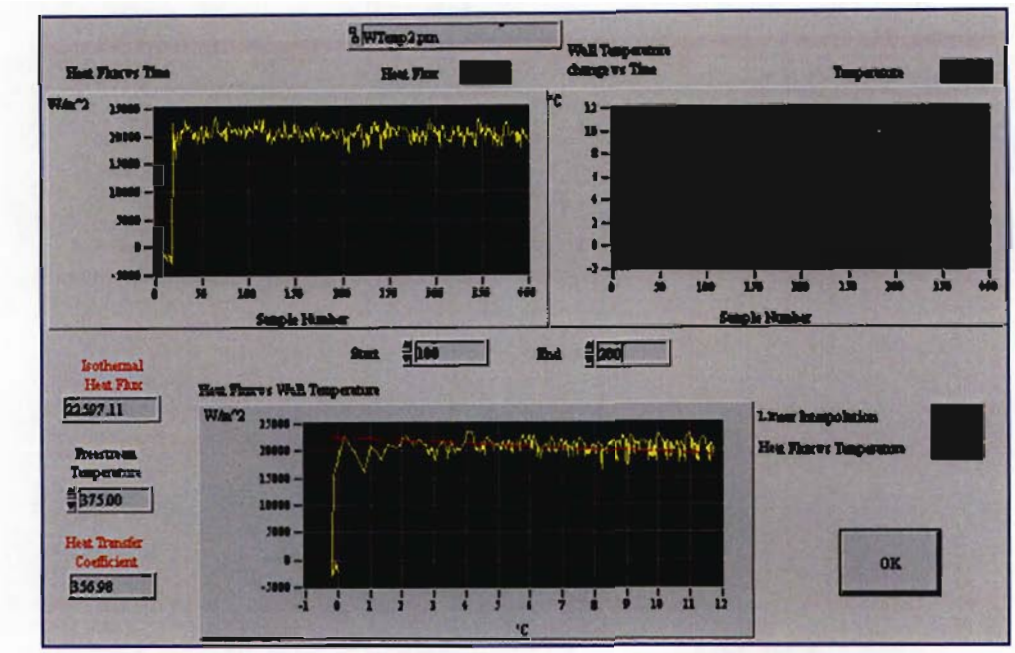

Figure 5-10: Final results window, showing the various plots for the heat transfer coefficient calculation

Comparison of these plots with the ones of Ligrani et al [1982] shows great similarity. Since only the initial portion of data, following the voltage step is relevant for the calculation, the beginning and end of the data set can be stipulated. This is done by entering the relevant numbers in the text boxes. The isothermal heat flux is then calculated by projecting a best fit line through the relevant data section of the heat flux versus temperature plot. The y-intercept of this line corresponds to the isothermal heat flux. The isothermal heat transfer coefficient can now be calculated by dividing the heat flux by the difference between the free stream and blade wall temperatures.

This process is repeated for all eight sensors on each D-type connector. For the analysis of each sensor, the heat transfer coefficient is recorded and plotted against the corresponding circumferential sensor position.

5.10 Isothermal heat transfer results

Previous experimental heat transfer results presented by Snedden [1998] and de Villiers [2002] are shown in Figure 5-11.

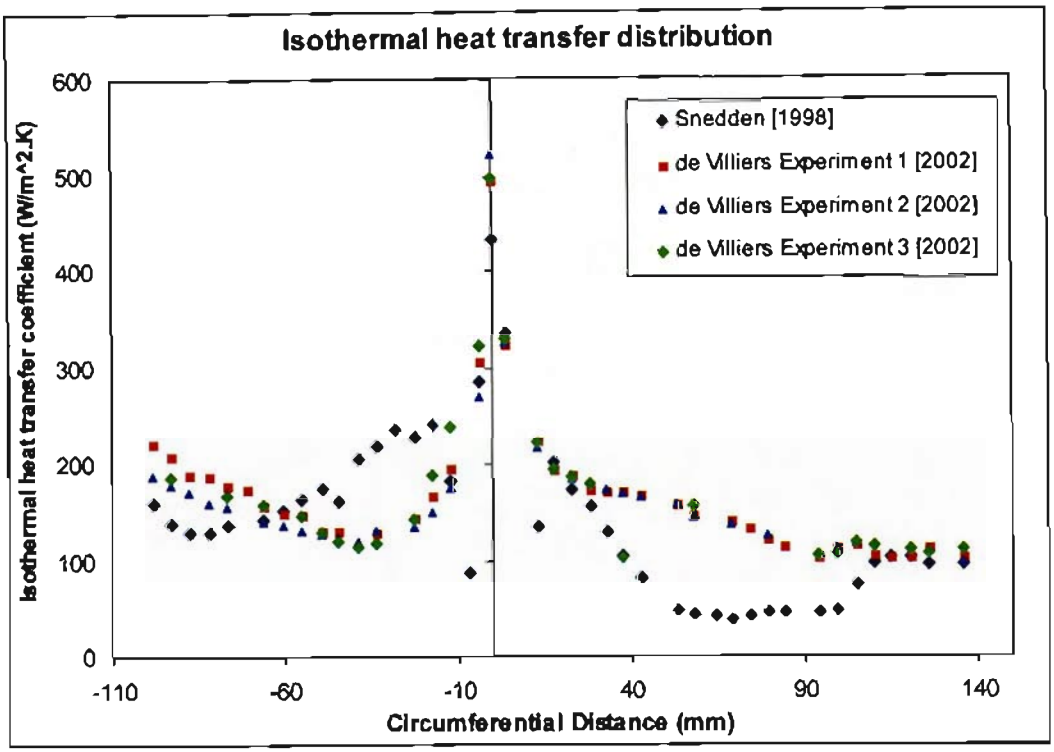

Figure 5-11: Comparison of previous experimental heat transfer results

de Villiers [2002] conducted three full sets of heat transfer coefficient data. Comparison of these results with those of Snedden's shows that significant discrepancies exist between the data sets of the two respective researchers. It must be noted that the trend of Stieger's [1998] data is similar to that of Snedden's (see Stieger [1998] Figures 6.3a, b and c). However, there appears to be no significant match in the trends of Snedden's and de Villiers' [2002] results. A possible explanation (as mentioned in section 5-6) is the fact that Snedden calculated the thin-film calibration constants using an initial blade temperature of 298K instead of 313K as is used in the experiments. de Villiers [2002] states that this could significantly affect the results. To quantify the effect of miscalculating the calibration constants, an attempt has been made to measure the percentage error.

5.10.1 Quantifying errors in the calibration constants

The absence of Snedden's [1998] measured experimental heat transfer data, such as initial gauge voltage and initial gauge resistance, makes it difficult or impossible, to recalculate the heat transfer coefficients for the corrected calibration constants using the LABVIEW heat

transfer analysing program, ISOTEMP1. However, the theoretical expression for the surface heat flux (equation 5-1 reproduced below) in Appendix 1 of de Villiers' dissertation [2002] can be used

$$\dot{q}_s = \frac{V_{out}}{V_0}\frac{\sqrt{\rho C k}}{\alpha_R}\frac{A^*}{\beta}(1+\alpha_R(T_\infty - T_0)) \qquad 5\text{-}1$$

to calculate the correct heat transfer coefficients, in terms of the incorrect coefficients. In calculating the corrected heat transfer coefficients, it can be seen that with the exception of the calibration constant α_R and initial blade temperature T_0, all other values would not change from the data measured by Snedden [1998]. The voltages V_{out} and V_0, the substrate thermal product $\sqrt{\rho C k}$ and the electrical analogue board calibration constant $\frac{A^*}{\beta}$ all remain as they were measured in the tests conducted by Snedden [1998]. These values would only change for the individual sensors.

Only the first 24 of Snedden's thin-film calibration constants were acquired, those spanning almost the entire blade suction surface. These were used to determine the surface heat flux $\dot{q}_s$ in terms of the substrate thermal product, electrical analogue board calibration constant, and the voltages. This is represented by q' in table A7.1 of Appendix 7. The corresponding heat transfer coefficient, shown as h', was then calculated using equation 2-1 for an initial blade temperature of T_0 = 298 K. New calibration constants where then calculated for an initial blade temperature of 313 K, using the available calibration data from Snedden [1998]. These too were used to calculate the surface heat flux (q") and corresponding heat transfer coefficient (h") in terms of the constants, for an initial blade temperature of T_0 = 313 K. The calculation procedure can be seen in Appendix 7.

An interesting result is observed, which reveals that the calibration constants change insignificantly. The measured heat flux remains constant and the blade plunge temperature T_0 changes from 298 K to 313 K. This, as the spreadsheet in Appendix 7 illustrates, results in the corrected heat transfer coefficients being a factor of 1.25 times the incorrect coefficients.

i.e. h" = 1.25 * h'

Where: h" = heat transfer coefficient corrected for T_0 = 313 K

h' = incorrect heat transfer coefficient for T_0 = 298 K

The above results imply that there is a consistent 20% error in the experimental results of Snedden [1998], as a result of the miscalculation. Figure 5-12 illustrates Snedden's corrected heat transfer distribution results in comparison to the incorrect results and to those of de Villiers [2002].

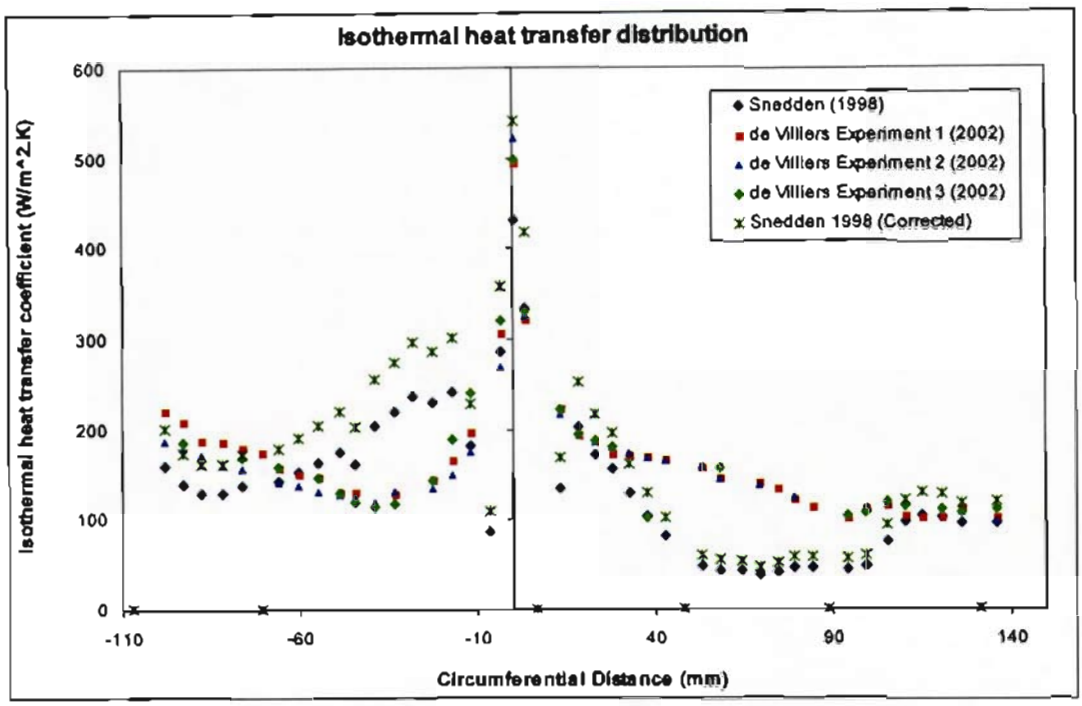

Figure 5-12: Plot of Snedden's (1998) corrected heat transfer coefficient distribution

Snedden's adjusted results are consistently 1.25 times the previous results indicating that there is no change in the heat transfer distribution trend, but only magnitude. There continues to be notable differences between the data sets of Snedden and de Villiers [2002]. The leading edge heat transfer coefficient of Snedden's results now appears closer to those measured by de Villiers [2002]. The high level of heat transfer in this region is characterised by the hot high-speed gas impinging on the leading edge. On either side of the leading edge, all measurements show a rapid decline in heat transfer corresponding to the rapidly accelerating laminar boundary layer under the influence of the favourable pressure gradient. On the pressure surface, the thin-film gauge at approximately 7 mm surface length was broken during de Villiers' [2002] tests and there is no data to be compared to that of Snedden's in this region. The very low level of heat transfer measured by Snedden at this point is suspected to be a laminar separation bubble. The variation in pressure near the leading edge, a consequence of the change in surface curvature, as Mayle [1991] states, is always found on turbine airfoils. Without film-cooling, laminar separation bubbles often occur in this region as is known to occur for this particular blade. This will be detailed further in Chapter 6 after comparisons with the CFD predictions.

On the pressure surface the heat transfer levels measured by Snedden show a steady decline from 17 mm to approximately 85 mm pressure surface length, rising slightly thereafter toward the trailing edge. This decline is indicative of a relaminarising boundary layer forming under the influence of the highly favourable pressure gradient. This trend is contrary to the pressure surface results of de Villiers [2002]. The heat transfer distribution measured by de Villiers [2002] shows a sharp decline in heat transfer from 12 mm until approximately 40 mm pressure surface length. This, as is the case with Snedden's results, could be associated with relaminarisation of the boundary layer. Mayle [1991] states that if the flow separates near the leading edge on the pressure side and reattaches turbulent, it will always transition back to laminar. Hodson [1984] showed this to happen on the suction surface. From 40 mm pressure surface length until the trailing edge, de Villiers' results [2002] show a contrasting steady incline in heat transfer. This could be explained by possible prolonged transition causing a gradual rise in heat transfer.

On the suction surface both the results of Snedden and de Villiers [2002] show a decline in the heat transfer coefficients along the blade surface until approximately 95 mm suction surface length. Snedden's results are significantly lower than those of de Villiers' [2002] over a majority of the suction surface. At 95 mm suction surface length all the measurements show a slight rise in the heat transfer level. From 110 mm suction surface length to the trailing edge, the best agreement between Snedden's and de Villiers' [2002] data is seen. A complete analysis of the pressure distribution, heat transfer distribution and the associated flow phenomena will provide further details along with comparisons to the CFD predictions in Chapter 6.

5.10.2 Current Experimental Heat Transfer Tests

Experimental heat transfer measurements conducted in 2004 were concluded as being unreliable due to the condition of the supersonic cascade rig during tests. Water leaks from the radiator prior to its repair, had caused significant rust build-up on the inside plenum walls as well as associated equipment such as the cascade and piping. These conditions are not ideal for accurate heat transfer measurement testing.

The rust within the plenum and the system itself has since been removed by Cassie [2007]. A galvanised paint coating has been applied to the plenum walls to prevent/inhibit corrosion in the future, and the cascade has been stripped and sanded clean. This has allowed Cassie [2007], to continue with experimental heat transfer testing. Preparations by Cassie [2007] are

currently being made for heat transfer tests to be performed. Accurate measurement of the blade surface pressure distribution is essential for determining reliable heat transfer distribution results. In Figure 4-10, the compared static pressure distributions of Snedden [1998], de Villiers [2002], the author's 2004 results, and Cassie's [2007] results show that the 2007 results have excellent agreement with the previous results. The largest discrepancy is between de Villiers' [2002] results toward the suction surface trailing edge; however, this is believed to be due to de Villiers' [2002] suction surface results being recorded at too high a velocity. Figure 4-10 shows that from the results of Snedden [1998], the author in 2004 and Cassie [2007], a reliable and validated pressure distribution has most certainly been established. It follows that with reliable flow conditions now setup, reliable heat transfer measurements can be expected which could serve to add value to and possibly validate the heat transfer distributions of Snedden [1998] and de Villiers [2002].

Judging from the similar pressure distributions, it is likely that heat transfer results in 2006 will follow closely to either one of the previous results by Snedden [1998] or de Villiers [2002]. The experimental heat transfer distributions of Snedden [1998] and de Villiers [2002] will be used to compare with the CFD heat transfer distribution generated in FLUENT. This will indicate the ability of the software to predict the heat transfer measurements and will also provide for analysis of the flow-field that was not captured in the experimental results.

5.11 Discussion of experimental heat transfer testing

Snedden's [1998] experimental heat transfer distribution has been adjusted for the miscalculated thin-film calibration constants. This exercise has indicated that the error, that was initially assumed to be significant, is now measured at 20%. This error is constant over the entire blade surface and the corrected heat transfer distribution shows no change in trend to the previous solution. This therefore results in no major matches in the solutions of de Villiers [2002] and Snedden. The trailing edges of the blade and leading edge are the regions with the best agreement between the two solutions. CFD solutions in Chapter 6 to follow will provide some answers to the experimental heat transfer distribution. However, further heat transfer testing is required to validate either of the experimental results to date.

With regard to experimental testing, the testing process must be conducted quickly and smoothly since the heat transfer test blade heats up gradually within the cooling box. In the event of the test blade exceeding the initial blade plunge temperature of 313 K, the entire experimental procedure needs to be repeated in order to achieve the desired blade wall free-

stream temperature ratio of 0.85. Test times, ideally, should be kept to a minimum to avoid this effect.

Furthermore, the ability to control the compressor speed has been made difficult by vibration on the hydraulic pump. The compressor speed, on occasion, varied randomly. The vibrations gradually rotate the power screw that is responsible for controlling the angle of the swash-plate. However, it was considered that perhaps there are further implications for the varying compressor speed. The hydraulic pump is an old system, which has been in use at the department for many years. The technology is old and non-routine service maintenance on the pump accelerates the pump's deterioration in condition and performance, clearly evident from the events of a ruptured seal (see section A4.3 of Appendix 4) and poor constant speed characteristics.

The deteriorating condition of these various rig components, makes the experimental procedure that much more difficult. An experimental procedure has been drawn up, and is included in Appendix 3, to facilitate, organise, and speed up the heat transfer measurement process. Measuring the heat flux into the test blade requires monitoring, control and measurement of numerous variables. The cascade flow conditions must be maintained at the required base test conditions of 2500 rpm and $100^{\circ}C$. This involves monitoring, and manually controlling, the compressor speed and radiator cooling water flow rate. The test blade surface temperature needs to be monitored by measuring the heat flux sensor resistances. At the initial blade plunging temperature, the sensor resistances and voltages need to be measured extremely rapidly, to minimise variances of all the variables above. These large numbers of tasks, followed, of course, by the blade plunging, make it difficult to achieve significant accuracy, especially for six repetitive tests. The time taken in measuring the initial sensor values, can be sufficient to allow for the flow conditions and blade temperatures to change slightly. With a new data acquisition board, exhibiting more differential channels, and LABVIEW available as a control and data acquisition system; incorporating the automatic acquisition of the heat flux sensor initial voltages and resistances into the ISOTEMP1 program, would help to significantly minimise errors.

No conclusive results with regard to the heat transfer or flow phenomenon are discussed in this chapter. The small sensor resolution reduces the scope of a detailed discussion. The CFD analysis in Chapter 6 provides a more detailed analysis of both the pressure and heat transfer distributions, where the new experimental data, the experimental data of de Villiers [2002], and the CFD solution can be discussed and compared.

CHAPTER 6

COMPUTATIONAL FLUID DYNAMICS (CFD) MODEL

6.1 Introduction

The numerical static pressure and heat transfer coefficient distributions, for the SMR-95 turbine blade, have been generated using a commercially available software package, FLUENT. As discussed earlier in section 4-1, the heat transfer measurements are coupled with the aerodynamic flow characteristics due to the high significance of the pressure distribution on the heat transfer predictions. Therefore, both the pressure and heat transfer coefficient distributions have been considered simultaneously, in order to analyse the accuracy of the specific modelling technique.

de Villiers [2002] also made use of FLUENT to generate the numerical solution, achieving an excellent correlation with the experimental pressure distribution, where all differences lay within 5%. The heat transfer coefficient prediction differed from the experimental measurements by an average of 29% over the blade surface. de Villiers [2002] attempted numerous different meshing techniques, of which the final model consisted of an unstructured quad pave mesh applied to the cascade. de Villiers [2002] found the $k-\varepsilon$ turbulence model to exhibit superior performance over the other turbulence models. This particular model was used to produce de Villiers' [2002] final numerical solution. Figures 6-1 and 6-2 on the following page, illustrate the experimental and numerical comparisons for de Villiers' [2002] pressure and heat transfer coefficient distributions, respectively.

Literature within de Villiers' dissertation [2002] provided useful information regarding the meshing techniques and turbulence models that were used to produce the previous (2002) numerical solution. Since the software and cascade geometry were the same, this provided a useful base with which to become familiar with the use of FLUENT and its associated solid modeller, GAMBIT. However, this proved most useful in allowing the author to identify possible sources of error within the CFD techniques employed by de Villiers [2002].

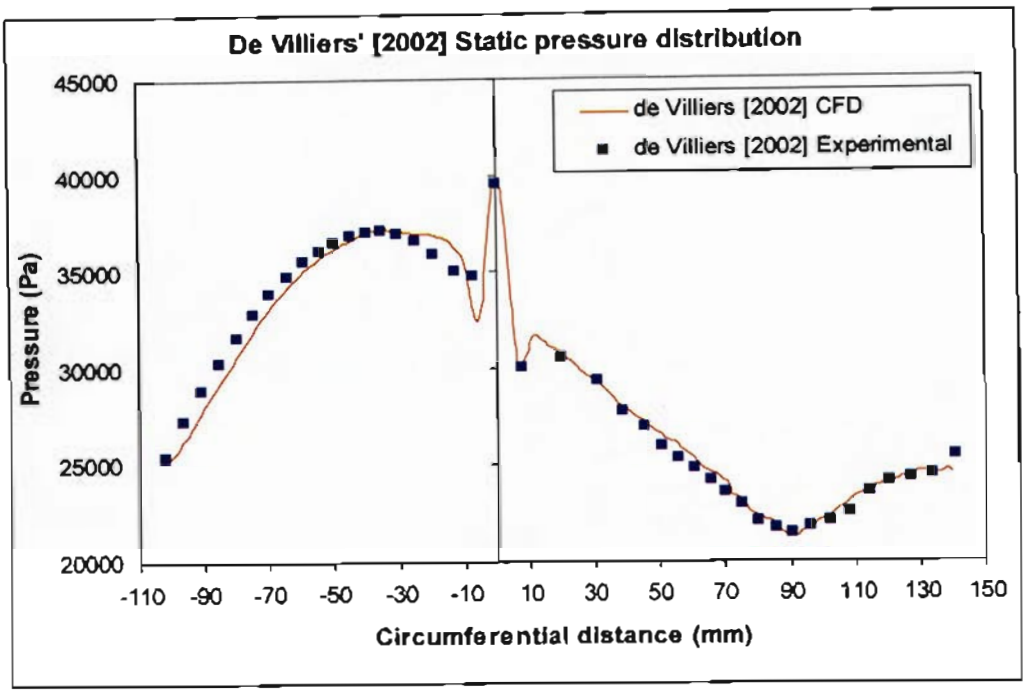

Figure 6-1: Previous experimental and numerical pressure distribution by de Villiers [2002]

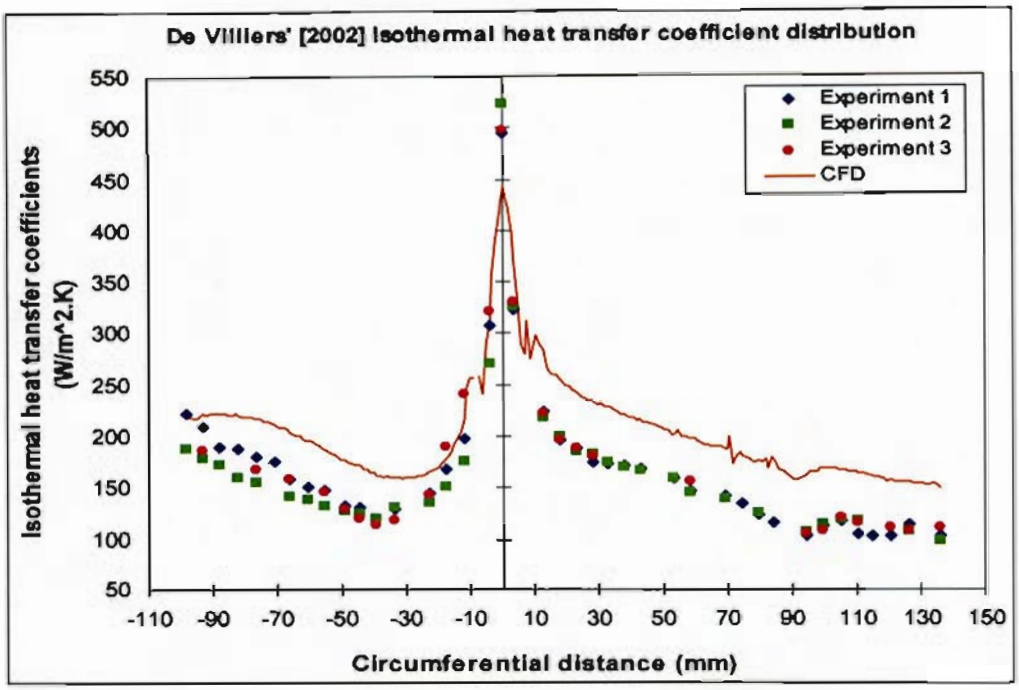

Figure 6-2: Previous experimental and numerical isothermal heat transfer distribution by de Villiers [2002]

Examining the pressure distribution of de Villiers [2002] in Figure 6-1, it can be seen that the experimental and numerical plots correspond very well with each other. The magnitude and position of most of the maximum and minimum pressure values, agree excellently. The suction surface and leading edge values are predicted perfectly, whilst the pressure surface

appears to be slightly under predicted by FLUENT. The heat transfer coefficient distribution in Figure 6-2, shows a large over prediction by FLUENT, with an average error of approximately 29%. The leading edge heat transfer coefficient is, however, under predicted by the CFD model, but the general trend has been calculated well for the entire blade surface.

6.2 Examination of the flow phenomenon from previous results

Examining the static pressure and heat transfer distribution simultaneously, assists in the interpretation of the blade flow phenomenon. The maximum pressure at the leading edge corresponds with the expected high level of heat flux as the high temperature, high speed gas, impinges on the blade leading edge, causing the stagnation point at the leading edge. Around both sides of the leading edge, the flow accelerates rapidly under the influence of a favourable pressure gradient. This is seen to correspond with the rapid decay in heat flux around the leading edge, due to the accelerating laminar boundary layer flow.

Following the rapid acceleration around the leading edge and the corresponding rapid heat flux decay, the CFD prediction shows a spike at 7 mm pressure surface, in both the pressure and heat transfer coefficient plots. The low resolution of the experimental results, does not permit an accurate and complete validation of these profiles, however, the trends appear to agree with the CFD prediction. As discussed in Chapter 4 and 5, this particular blade profile is known to exhibit a separation bubble on the pressure surface, at 7 mm surface length. The development of the separation bubble is explained in section 4.4.6. The separation bubble is aided by the flow passing over a step change in surface curvature between the leading edge radius and the remainder of the blade profile. The boundary layer separation point is the location for which $(du/dy)_{surface} = 0$. This location can be seen by the small plateau, or levelling of the pressure, at 7 mm pressure surface in Figure 6-1. The lower level of heat transfer in this region further validates the existence of this separation bubble, where the boundary layer flow separates and 'flows over' the small region of recirculation, thereby reducing the heat flux into the blade. The velocity profile associated with separation is shown in Figure 6-3 below.

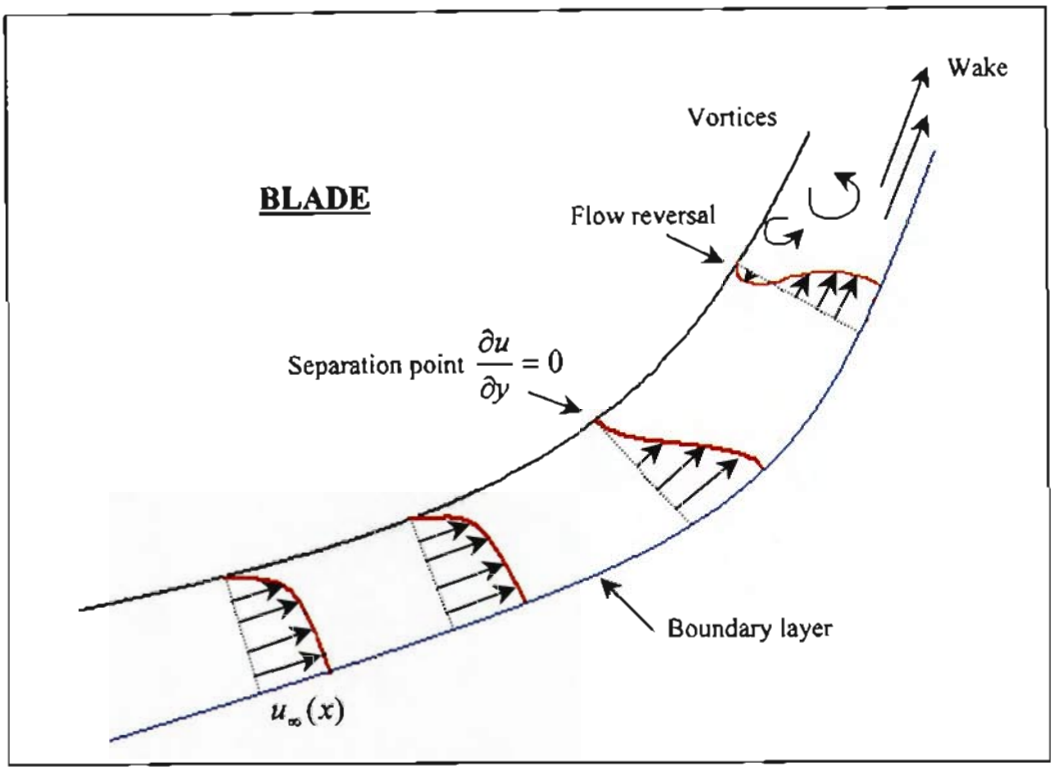

Figure 6-3: Velocity profile associated with separated flow

Following separation of the boundary layer, a wake is formed in the downstream region and the flow is highly irregular and characterised by vortex formation. This transition from laminar to turbulent flow causes a sudden spike in the local heat transfer coefficients, which can be seen in Figure 6-2. This spike in the heat transfer plot, is indicative of turbulent boundary layer reattachment. Following this, the further rapid decay in heat flux on the pressure surface indicates the relaminarisation of the boundary layer. The heat flux then gradually increases along the pressure surface as the boundary layer velocity increases and the boundary layer thins due to the relaminarisation.

On the suction surface, a similar spike in pressure and heat transfer is seen at approximately 7 mm suction surface length. Analysing the CFD velocity vectors, de Villiers [2002] reports no indication of separation in this region. It is unfortunate that the heat flux sensor at this point is broken, so no experimental result is available for the heat flux. Further CFD investigation into the flow variance will be required. Following this flow variance at 7 mm surface length, the pressure and heat transfer decrease steadily until 90 mm suction surface length. This is characteristic of an accelerating laminar boundary layer flow under the influence of the favourable pressure gradient. At 90 mm suction surface length, a plateau in the pressure plot is seen, together with a small increase in heat transfer coefficient. de Villiers [2002] makes no mention of the flow phenomenon in this region. However, Stieger

[1998] achieved similar results and reports this as being due to transition from a laminar to a turbulent boundary layer. The gradual decrease in heat transfer thereafter, could be explained by possible relaminarising of the boundary layer. Further CFD investigation could help explain this.

The preceding examination of the boundary layer flow phenomenon is essential in the analysis of the heat transfer rates. The convective heat transfer rates depend strongly on the type of boundary layer flow present. Therefore, analysing the heat transfer distribution can be a useful tool in making conclusions about the blade flow phenomenon and the associated heat loading.

6.3 Analysis of de Villiers' CFD modelling

Although the CFD results presented by de Villiers [2002], show excellent agreement with the experimental pressure distribution, and the heat transfer distribution trend is followed accurately; in analysing the results, numerous factors were found to be inconsistent with the GAMBIT and FLUENT modelling guidelines.

Generation and meshing of the cascade geometry is of extreme importance. A poor quality grid mesh will cause inaccurate results and/or slow convergence. Perfectly square cells, with minimal local variations in cell size produce a high quality mesh. GAMBIT measures the cell skewness by monitoring the cell corner angles, and these skewness values can be checked in the software. The least skew the cells, the faster the convergence and the more accurate the results are likely to be. In the case of quadrilateral/square cells, the skewness should not exceed 0.8. Ideally cells should be orthogonal to their neighbours.

In addition to cell skewness, local variations in cell size are important. The adjacent cells should not have a size ratio exceeding 1.2. de Villiers' [2002] cell growth rate in the boundary layer, was set to 1.35, resulting in large variations in cell size. These are visible in Figure 6-4 where the cells quickly become significantly larger. The edge mesh distribution, and hence the mesh density distribution, can be controlled by grading or spacing the cells appropriately. de Villiers [2002] used an unstructured quad pave mesh, applied to the cascade, for his final mesh. This technique, without correct and suitable cell spacing, can lead to large cell variations and large cell growth rates. This outcome can cause the mesh to be unreliable in producing accurate results.

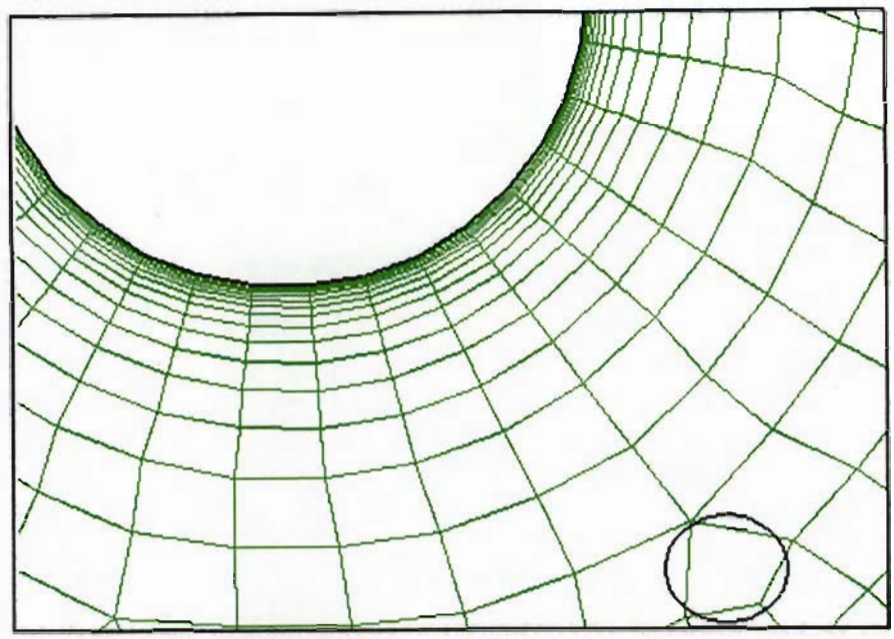

Figure 6-4: A close up of de Villiers' mesh (Reproduced from de Villiers [2002])

de Villiers [2002] reports that many of the models produced, had difficulty in converging. This is as a result of a poor mesh. Convergence of a model is extremely vital, and results cannot be justified if the solution has not converged. Therefore, considering the above errors and their corresponding solutions, the construction and development of new meshing techniques was required to produce results of higher quality and accuracy, which could be reliable.

The subsequent sections of this chapter, will introduce the various models that have been developed, immediately followed by the results pertaining to the respective models.

6.4 Development of GAMBIT meshes with corresponding FLUENT results

6.4.1 Reproduction of de Villiers' mesh (Grid 1)

In the initial stages of the CFD modelling, experimental results were not yet available from the author. de Villiers' [2002] results were therefore used to begin the CFD analysis and to become familiar with the software. The first mesh created, was a recreation of de Villiers' [2002] final mesh. This would provide validation of de Villiers [2002] work.

The blade geometry was created by importing the blade profile coordinates into GAMBIT. The blade surface was then created by sub-dividing the blade into smaller edges. If the blade is constructed from one complete edge, the curvature function in GAMBIT does not follow

the true profile of the blade. These smaller edges can then be connected to from the completed blade face, which will represent the true blade profile, thereby minimising alterations in flow. This blade construction technique was implemented for all of the models produced. The boundary layer attached to the blade surface, had a first row size of a=0.01, a growth factor b/a=1.35, with 15 rows. This produced a boundary layer thickness of 3.45 mm. The blade edge was meshed with a mesh size of 1 whilst the remainder of the cascade had an edge mesh size of 3.5. These values alone, indicate the extreme cell size variation that will occur in the mesh. The resulting mesh is shown in Figure 6-5, and a close up of the mesh surrounding the test blade is shown in Figure 6-6. The large cell size variations are encircled in Figure 6-6.

Analysing the reconstruction of de Villiers' [2002] mesh, the mesh consists of approximately 22 500 cells, with a worst cell skewness of 0.67. Although not particularly skew, skew cells can be responsible for convergence difficulties. Once the meshing process is complete, boundary and continuum types can be specified. Since the static inlet and exit pressures are known from the experimental results, the cascade inlet and outlet are set as a pressure inlet and pressure outlet, respectively. In addition, the blade suction and pressure surfaces are defined so that the corresponding blade pressure and heat flux data can later be extracted from the final FLUENT solution. The final mesh is then exported into FLUENT for solving.

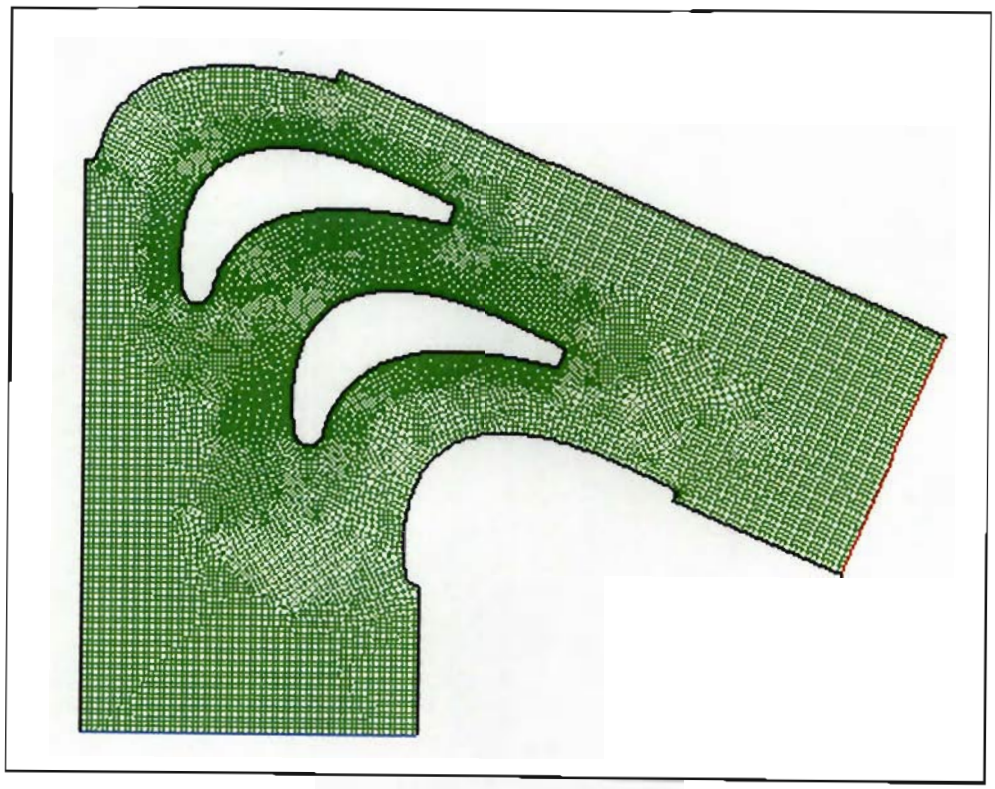

Figure 6-5: Reconstruction of de Villiers' [2002] mesh

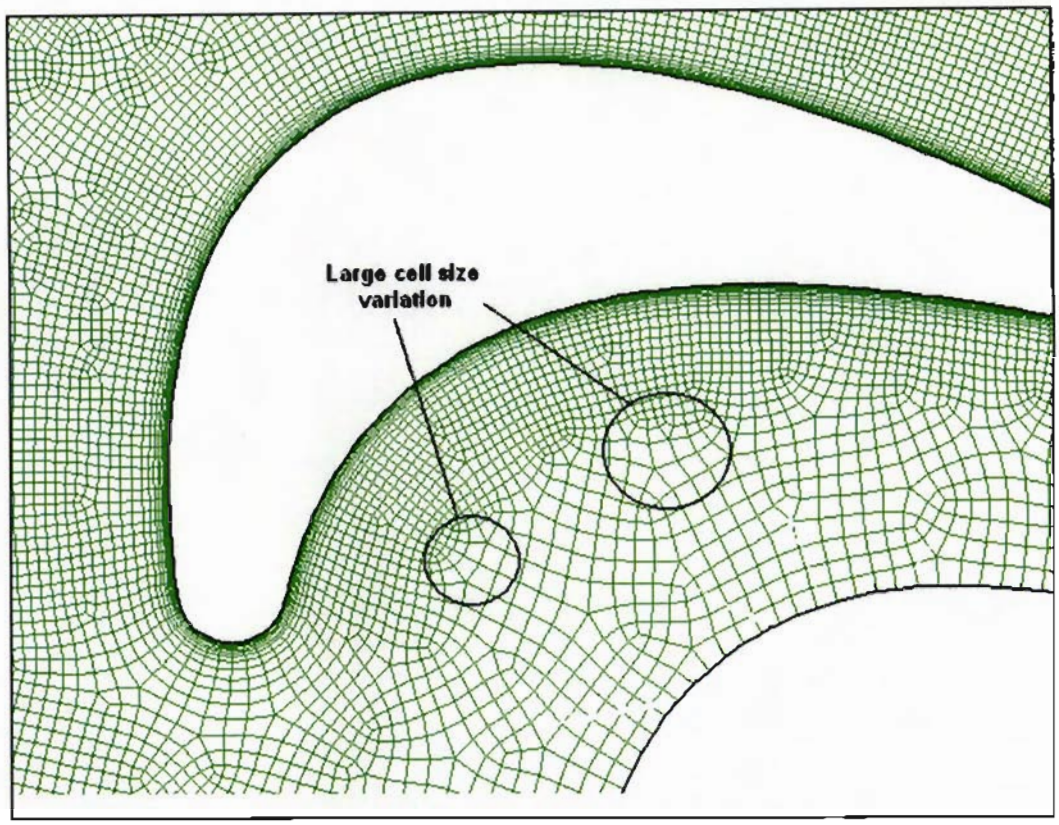

Figure 6-6: Close up the cell formation around the test blade of de Villiers' [2002] mesh

6.4.1.1 Setting up the FLUENT model

Before beginning the numerical solution, various settings have to be specified in FLUENT. The following description of the FLUENT model set up, applies to all the models that were implemented. As described in section 2.5.1, there are two different solvers. The solver most appropriate (for reasons explained in section 2.5.1) for this solution is the coupled implicit solver. In addition, various viscous models are available. Due to the turbulent nature of the flow, a turbulence model is required; and the Realizable $k-\varepsilon$ (RKE), (SST) $k-\omega$, and Spalart Allmaras (SA) turbulence models are appropriate for this solution (see section 2.5.2).

The fluid flow in the cascade is a high speed compressible flow. Therefore the material selection in FLUENT is very important. The density of the operating fluid must be set to 'ideal gas', which is the appropriate density relation for compressible flows. The energy equations are thus automatically enabled, which, with the coupled solver setting, are simultaneously solved with the transport equations.

The 'ideal gas' in FLUENT is defined as:

$$\rho = \frac{p_{op} + p}{RT} \tag{6-1}$$

Where: p_{op}= operating pressure

p = gauge pressure

R = 287 Pa.m^3/kg.K (Specific gas constant)

T = temperature

Setting the operating pressure in FLUENT is important. From equation 6-1 above, it can be seen that the density is determined by the value of the operating pressure. The relationship between the operating pressure, gauge pressure, and absolute pressure is defined by FLUENT in equation 6-2 as:

$$p_{abs} = p_{op} + p_{gauge} \tag{6-2}$$

The criteria used to determine the operating pressure are based on the Mach number regime, and the density relationship used. Table 6-1 below, illustrates the appropriate operating pressure settings.

Density relationship	**Mach No. regime**	**Operating pressure**
Ideal gas law	M>0.1	0 or ≈Mean flow pressure
Ideal gas law	M<0.1	≈Mean flow pressure

Table 6-1: Recommended settings for operating pressure

(Reproduced from FLUENT 6.1 online manual)

The cascade flow has M>0.1 and hence the operating pressure was set to 0 Pa. Using equation 6-2, zero operating pressure indicates that all pressures specified, and extracted from FLUENT, are gauge pressures.

The final set up of the FLUENT model is the input of the boundary conditions. These conditions significantly affect the solution. The solver requires an initial estimate with which to begin the simulation. Hence, one of the boundary conditions is used to initialise the solution. An incorrect boundary condition will therefore make the solution incorrect from the very beginning.

The cascade inlet and outlet boundaries are set as a pressure inlet and outlet respectively, since the static inlet and outlet pressure values have been measured during the experimental tests. Table 4-4 of the experimental results section, illustrates how the inlet and outlet pressure values significantly affect the entire flow field. These pressures drive the flow and hence their inputs must be accurate and reliable. The cascade inlet and outlet boundary conditions are illustrated below in Table 6-2 and Table 6-3 respectively.

Parameter	Value
Gauge Total Pressure (Pa)	39 986
Supersonic/Initial Gauge Pressure (Pa)	35 830
Total Temperature (K)	373
Direction Specification Method	Normal to Boundary
Turbulence Specification Method	Intensity and Hydraulic Diameter
Turbulence Intensity (%)	3
Hydraulic Diameter (mm)	119.24

Table 6-2: Pressure inlet boundary conditions

The turbulence intensity is set at 3 %, corresponding to a cascade inlet with no turbulence generating rods. This turbulence intensity is however, challenged in later sections due to the varying turbulence intensities at the inlet caused by the pressure and temperature probes (see section 2.5). The initial gauge pressure corresponds to the static inlet pressure measured in the experimental testing. The gauge pressures indicated in Tables 6-2 and 6-3, are the values recorded during the author's experimental testing.

Parameter	Value
Gauge Pressure (Pa)	30500
Backflow Total Temperature (K)	350
Direction Specification Method	Normal to Boundary
Turbulence Specification Method	Intensity and Hydraulic Diameter
Turbulence Intensity (%)	3
Hydraulic Diameter (mm)	91.894

Table 6-3: Pressure outlet boundary conditions

6.4.1.2 FLUENT results for de Villiers' mesh (Grid 1)

To provide validation of de Villiers' [2002] results, the Realizable $k-\varepsilon$ (RKE) model was also applied to de Villiers' [2002] mesh. As mentioned previously, experimental results were not yet available from the author. Hence, de Villiers' [2002] experimental results were used as an experimental comparison and the boundary conditions in FLUENT had to be adjusted, corresponding to the previously measured pressures. The initial gauge pressure was set at 35 000 Pa, and the outlet gauge pressure set at 27 500 Pa. The CFD pressure distribution results for the RKE model applied to de Villiers' [2002] mesh are shown in Figure 6-7, and are compared to the experimental results generated by de Villiers [2002].

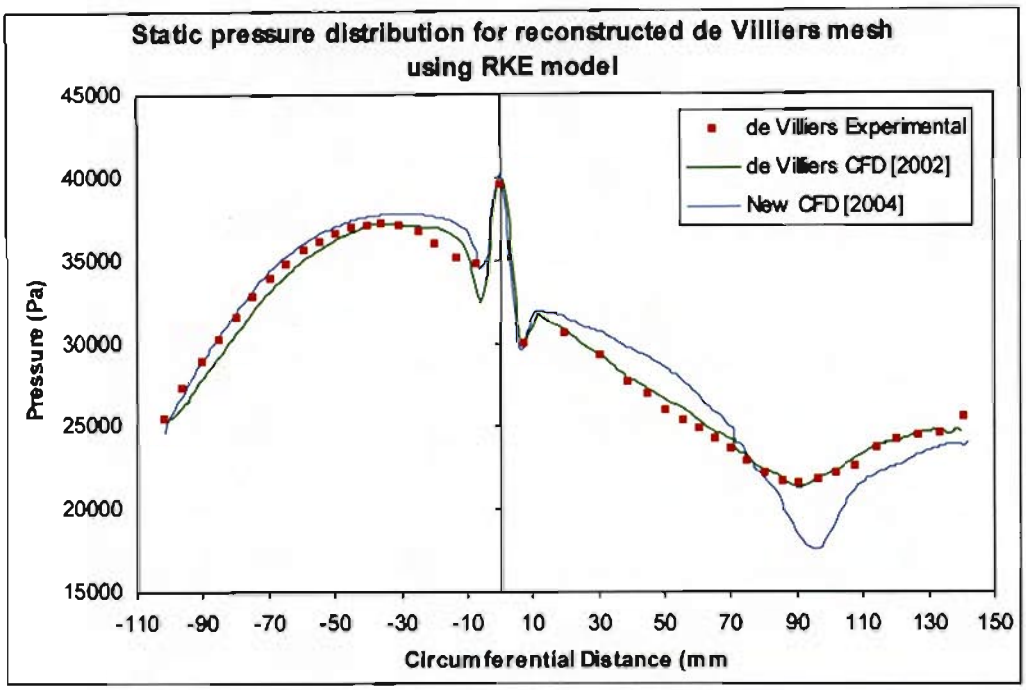

Figure 6-7: Pressure distribution results for reconstructed de Villiers [2002] mesh using RKE model

The pressure results show a surprising result. The same mesh and same boundary conditions were used in this model as were used by de Villiers [2002]. The pressure surface results prove to be more accurate than de Villiers [2002] CFD results, and the pressure at 7 mm surface length is more accurately predicted. The leading edge values correspond well. However, the suction surface results do not agree well with de Villiers' [2002] CFD solution. It must be noted, that de Villiers' [2002] experimental suction surface results were considered unreliable, since the compressor speed was too high. The experimental results in Chapter 4 illustrate how susceptible the suction surface results are to small fluctuations in flow conditions.

Investigation of the CFD work in de Villiers' dissertation [2002], de Villiers states the following for one particular model: "The solution never converged, however the contour plot seemed to follow the general trends so the results were extracted and plotted in Figure 6-16." This prompted further investigation into the convergence of de Villiers' [2002] CFD solution. For a solution to converge, the overall mass, momentum, energy, and species balances must be achieved. FLUENT recommends that the scaled energy and continuity residuals must decrease to 1×10^{-5}. In addition, the net overall heat and mass imbalance should be less than 1% of the smallest flux through a domain boundary.

In an attempt to regenerate de Villiers' results [2002], the solution was extracted from FLUENT when the solution appeared similar to the experimental results of de Villiers [2002]. The CFD solution never matched that of de Villiers' CFD results [2002], and the closest solution was achieved at residuals in the region of 1×10^{-3}, and a net mass flow imbalance of 0.28 kg/s (5%). This indicates that the solution is not converged, and the unconverged results are shown in Figure 6-8. Following this investigation, the results are closer to the experimental, but it is still unknown how de Villiers [2002] achieved the CFD solution.

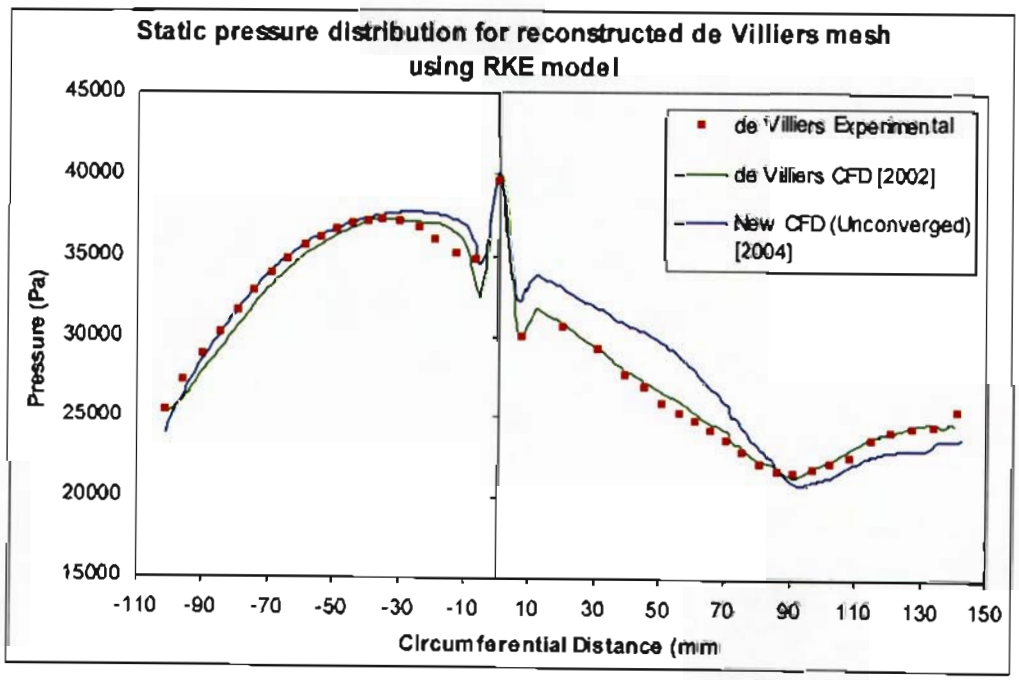

Figure 6-8: Unconverged pressure distribution results for reconstructed de Villiers' [2002] mesh using RKE model

The CFD isothermal heat transfer coefficient distribution results for the RKE model applied to de Villiers' [2002] mesh are shown in Figure 6-9, and are compared to the experimental results generated by de Villiers [2002].

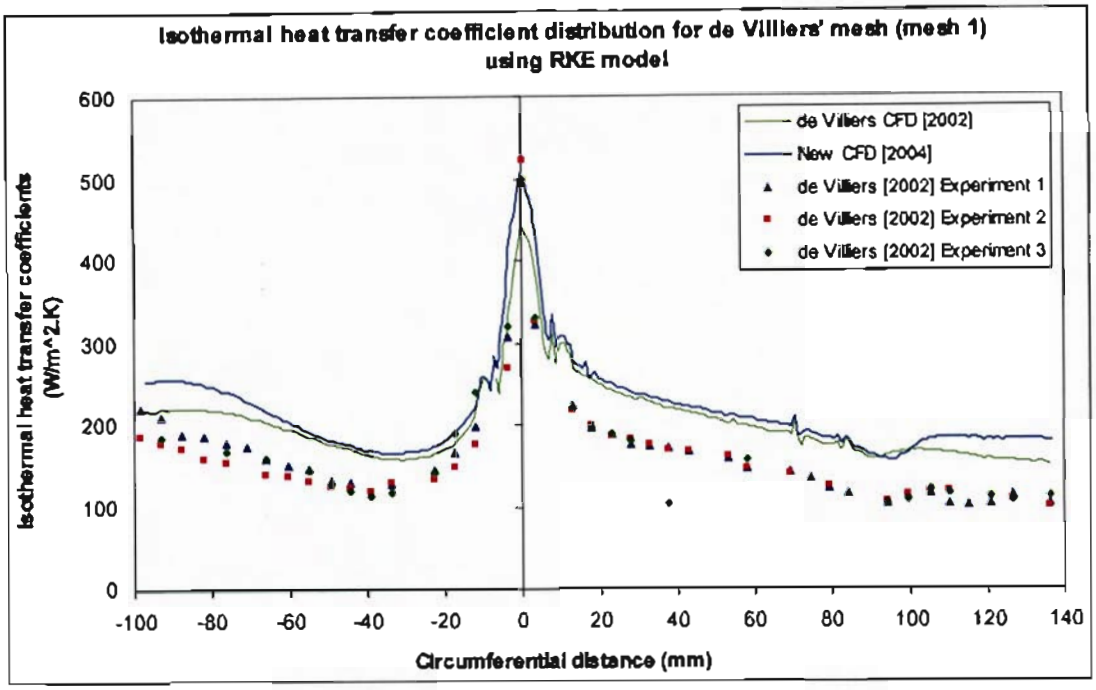

Figure 6-9: Isothermal heat transfer coefficient for reconstructed de Villiers [2002] mesh, using RKE model

The new CFD isothermal heat transfer coefficient results show good similarity with de Villiers' [2002] CFD solution, and also over predict the experimental values. At the leading edge however, the new CFD results predict the heat transfer coefficient perfectly, unlike that of de Villiers [2002]. It appears that de Villiers' [2002] heat transfer solution is fully converged.

6.4.2 Decomposed mesh (a = 0.01) (Grid 2)

The previous results showed some large inconsistencies with the pressure results, and the heat transfer coefficients are over predicted. This encouraged the need for a higher quality mesh. de Villiers [2002] constructed an unstructured quad pave mesh (Grid 1), which had large cell size variations. An attempt was therefore made, to divide the cascade flow region into smaller regions, which could be meshed with a mapped scheme and provide more mesh spacing control. This allows the complex cascade geometry to be manipulated into smaller, simpler, almost square sub-divisions. A mapped mesh scheme provides control of the mesh,

where the edge nodes are mapped to the opposite side of the region and the resulting mesh consists of almost square cells.

In order to resolve the near wall boundary layer characteristics, the wall adjacent cell's centroid must be located within the viscous sub layer ($y^+=1$). de Villiers' [2002] boundary layer first row size was a=0.01 mm. This was sufficiently fine to produce y^+ values less than or close to 1 for a majority of the blade surface. This first row size was hence used, yet a smaller cell growth rate of 1.1 was used. Note this is smaller than the value of 1.35 used by de Villiers [2002], and the recommended limit of 1.2. A boundary layer mesh thickness of 2.7 mm was achieved by applying 35 rows to the boundary layer mesh.

This new decomposed mesh technique was extensively investigated whilst the author's experimental measurements were being performed. This would allow the mesh to be implemented and the CFD results compared with the new experimental results. Due to the complex nature of the cascade geometry, the decomposition proved to be difficult, and minimising cell skewness was complex. The resulting decomposed geometry is shown in figure 6-10. A close up of the mesh surrounding the blade surface is shown in Figure 6-11.

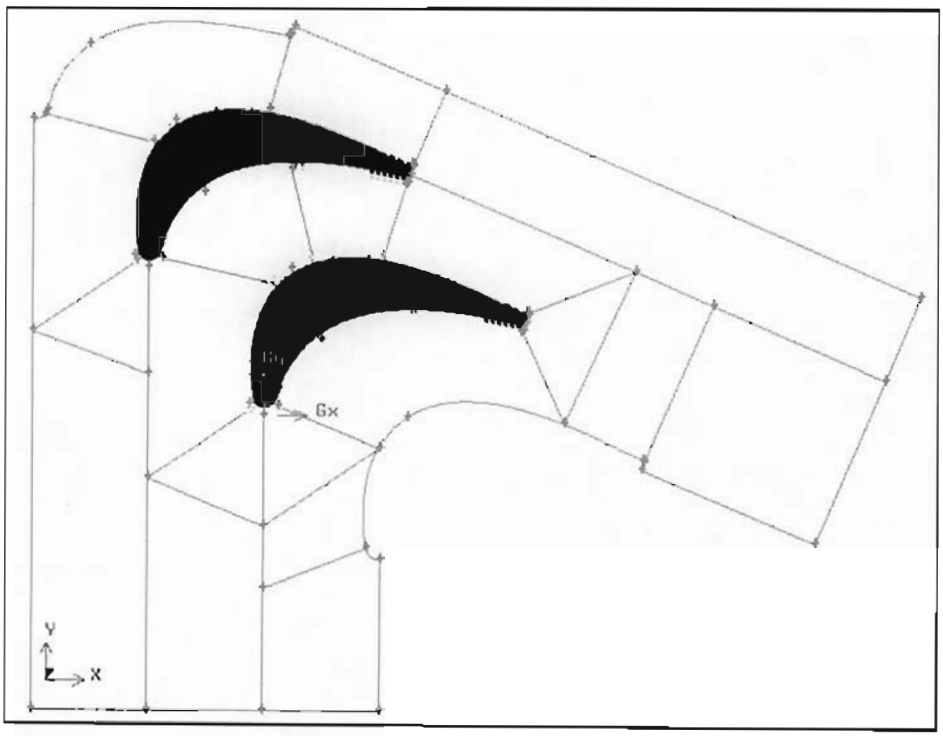

Figure 6-10: Decomposed cascade geometry

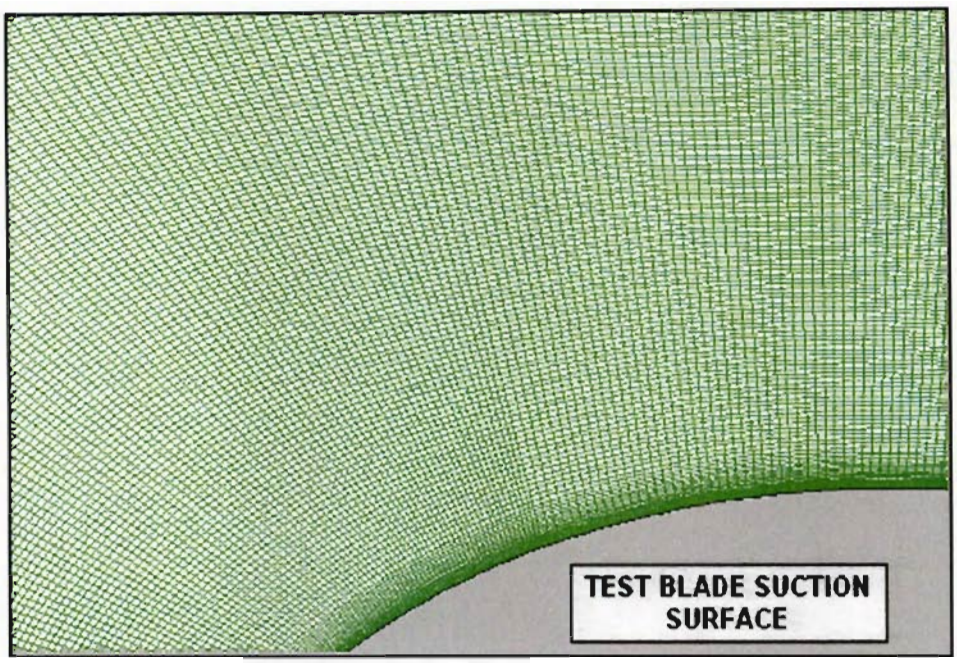

Figure 6-11: Square mesh projecting from test blade suction surface

The near perfect square cells of the decomposed mesh technique can be seen clearly in Figure 6-11. The cell size variation is extremely minimal and most appropriate. However, some complex geometry areas of the cascade make it extremely difficult to generate cells that are not skew. Although a large majority of the mesh consisted of near perfect square cells, the complex regions produced a small percentage of cells with a skewness of 0.7. These cells could cause difficulty in convergence of the model. Figure 6-12 illustrates skewed cells in a complex geometry region.

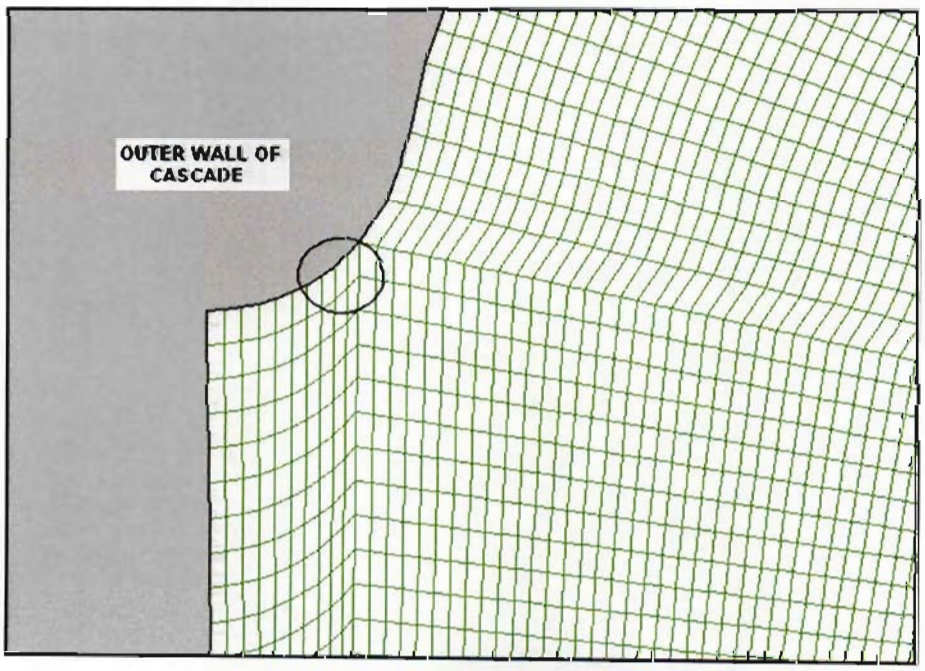

Figure 6-12: Skewed elements in complex geometry region

The mesh was extremely fine, consisting of 270 000 cells, and with the exception of a small number of skew cells, was very suitable. The mesh was exported into FLUENT where the various turbulence models were implemented. The CFD results are compared with the experimental results of Snedden [1998], de Villiers [2002] and Cassie [2007].

6.4.2.1 FLUENT results for decomposed mesh (Grid 2)

The Realizable $k-\varepsilon$ (RKE), SSTKW, and Spalart Allmaras (SA) turbulence models were all applied to grid 2. The skew cells within the mesh could be a probable cause of problems with the convergence, as the SA and SSTKW models had difficulty in converging fully. These results are not shown since they are unreliable. The RKE model came close to fully converging and the results are plotted in Figure 6-13.

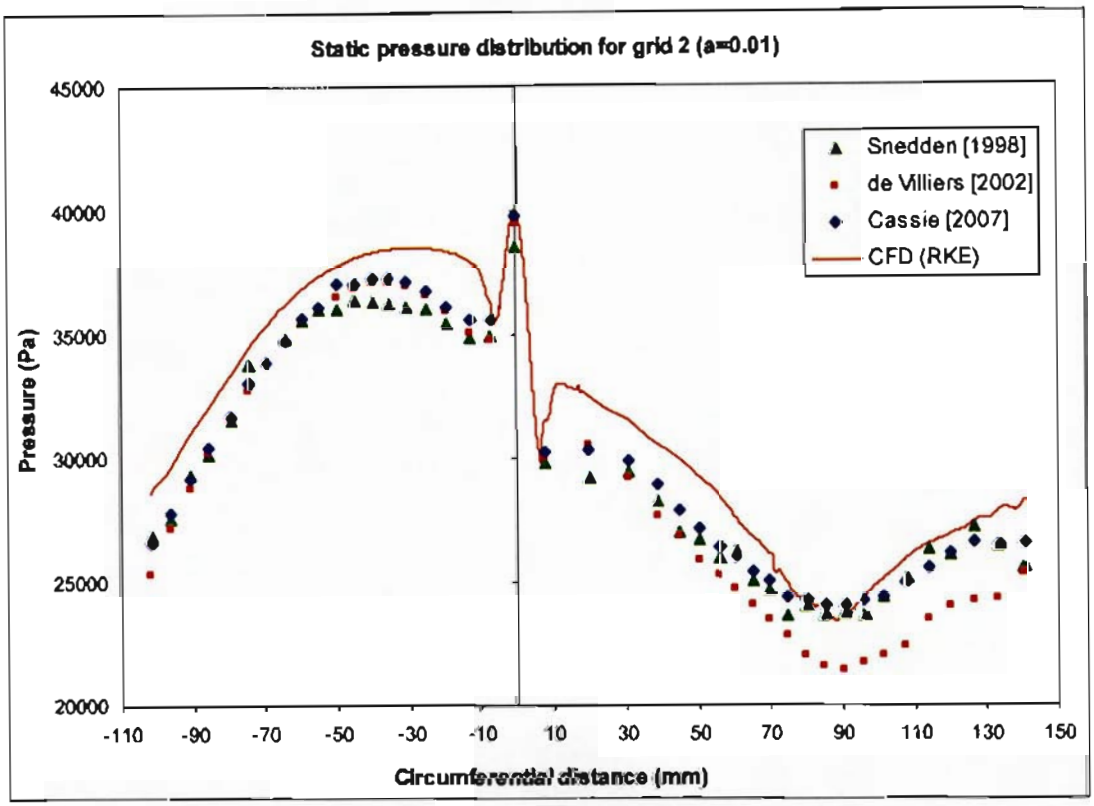

Figure 6-13: Pressure distribution results for the decomposed mesh (Grid 2) (a=0.01)

The CFD pressure distribution over predicted the pressure for a majority of the blade surface. The pressure surface is consistently over predicted with 2-5% error, but the pressure at 7 mm pressure surface length is well predicted. The leading edge pressure corresponds well with the results of de Villiers [2002] and Cassie [2007]. On the suction surface, the pressure at 7 mm surface length is well calculated however, thereafter and moving toward the trailing edge, the pressure is over predicted with approximately 3-5% error until 80 mm surface

length. From 80 mm suction surface length, to the trailing edge, the error is small. The pressure distribution results, show a remarkable improvement over the previous results obtained with de Villiers' [2002] mesh. However, the convergence difficulties of the other turbulence models justify the development of a new mesh. Figure 6-14, illustrates the blade wall Y-plus distribution. To resolve the near wall boundary layer characteristics, all values should lie below one. This is generally the case, however, in regions where the boundary layer is thin, on the pressure surface trailing edge and at 80 mm suction surface length, the values can be decreased further. This can be done by reducing the first row size "a".

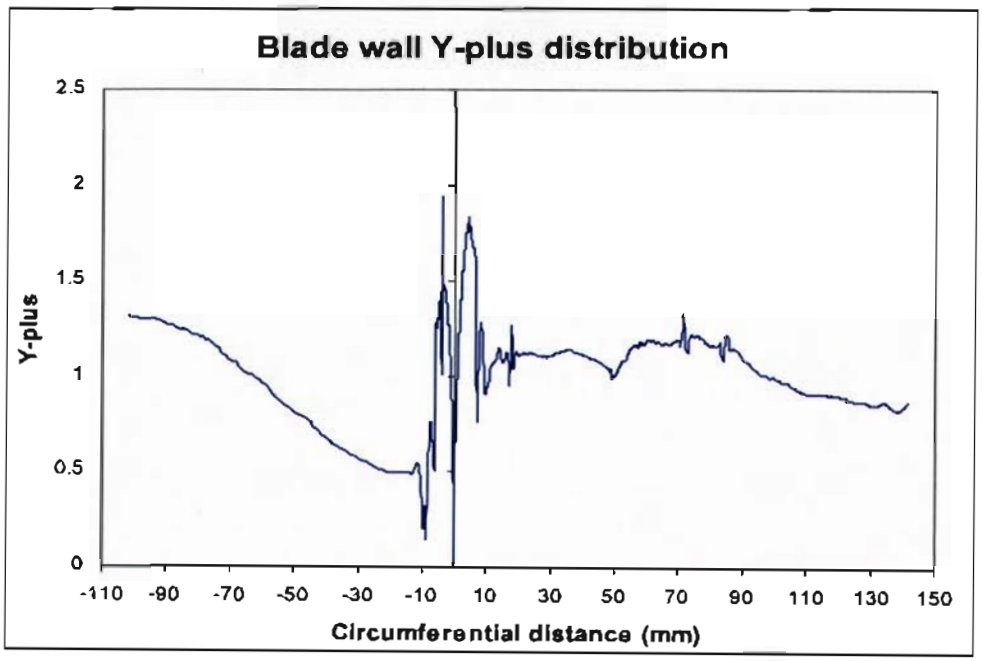

Figure 6-14: Blade wall Y-plus distribution for grid 2 (a=0.01 mm)

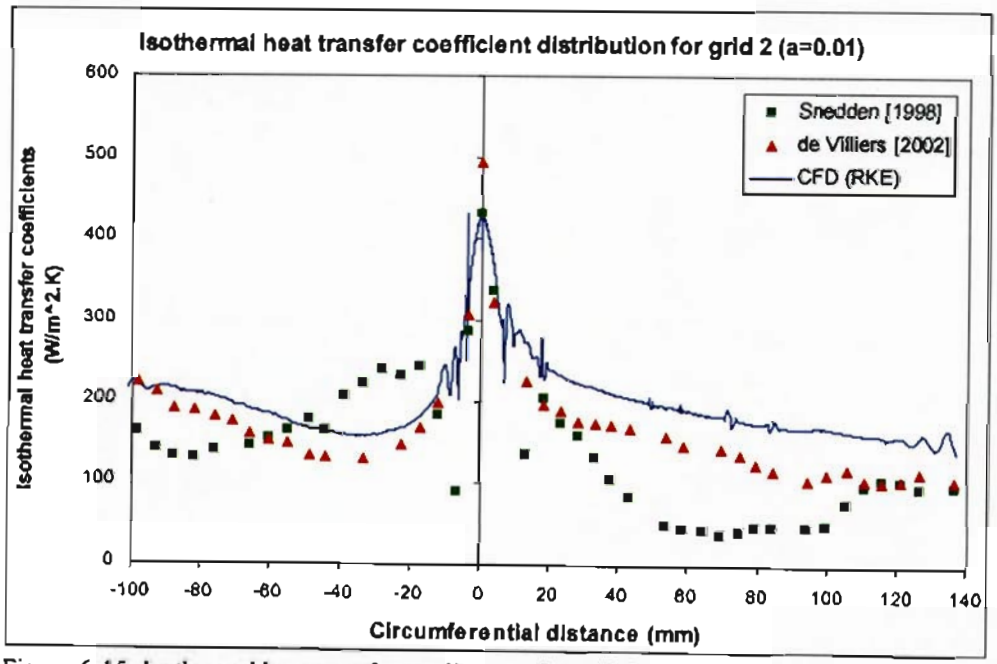

Figure 6-15: Isothermal heat transfer coefficients for grid 2 (a=0.01 mm), using RKE model

The CFD isothermal heat transfer distribution in Figure 6-15, shows similar results to the previous CFD mesh and the CFD of de Villiers [2002]. Due to the very close similarity between the three sets of data measured by de Villiers [2002], only Experiment 1 is used for comparison purposes to prevent crowding the graph. Snedden's original experimental heat transfer coefficient results plot is included here. The CFD solution does not agree well with Snedden's experimental results, showing contrasting trends throughout a majority of the blade profile. The leading edge and two adjacent coefficients however, show good agreement with the CFD solution. Increasing Snedden's results by the factor of 1.25 for correction of the calibration constants, would still not show good agreement. The trends of the CFD solution agree very favourably with the experimental results of de Villiers [2002]. A consistent over-prediction of approximately 20% is seen over most of the blade surface. The leading edge heat transfer coefficient is largely under-predicted whilst some coefficients in the region of the leading edge correspond with the experimental values. Improved convergence, and ultimately improved accuracy, in both the pressure and heat transfer distribution required a new mesh.

6.4.3 Decomposed mesh (a=0.001) (Grid 3)

The Y-plus values of the previous model indicate that the boundary layer size should be decreased further, to properly resolve the boundary layer. Nevertheless, the more cells within the boundary layer, the more accurately the solver can solve for the characteristic near-wall gradients of the region.

Since the cascade mesh density is determined by the blade wall edge mesh, reducing the boundary layer first row size, and refining the blade wall edge mesh, refines the cascade mesh and helps produce more square cells. At the same time, a finer boundary layer will be implemented. Hence, a new boundary layer with a first row size a=0.001mm was applied. The cell growth rate was once again set to 1.1 and 60 rows were constructed to produce a boundary layer mesh thickness of 3 mm. A close up of the resulting mesh is shown in Figure 6-16.

The resulting refined mesh, helped reduce the skewness of the cells positioned in the complex regions of the cascade geometry. Although still not perfect, a reduction in the percentage of cell skewness would certainly help with the convergence difficulties encountered with the previous meshes. The mesh was exported to FLUENT for solving.

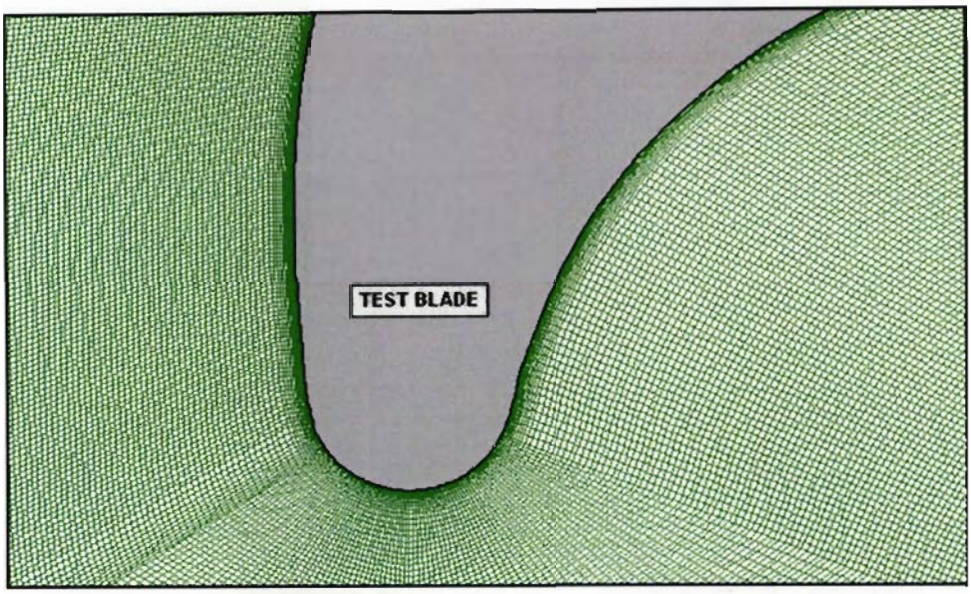

Figure 6-16: Close of the extremely fine decomposed mesh (Grid 3) surrounding the test blade

6.4.3.1 FLUENT results for decomposed mesh (Grid 3)

Refining the mesh in grid 2 above, proved to be successful since both the SA and RKE turbulence models now converged. The SSTKW model did still not converge however. Convergence times, nevertheless, were significantly reduced by the new mesh. The results are displayed in Figure 6-17.

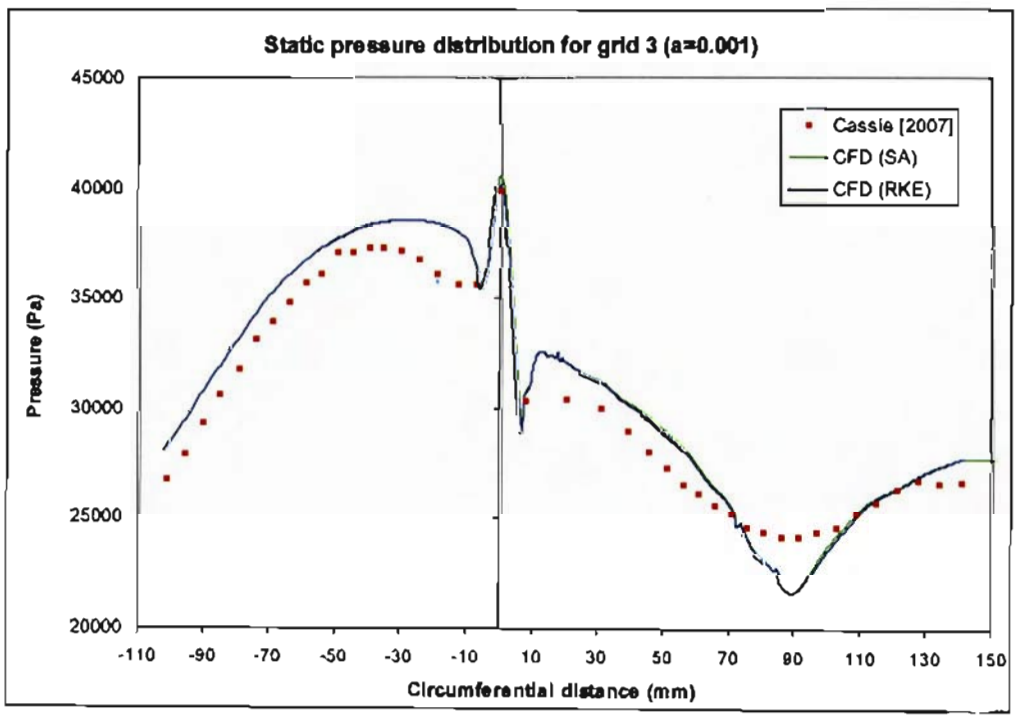

Figure 6-17: Pressure distribution results for the decomposed mesh (Grid 3) (a=0.001)

The CFD static pressure distribution results for grid 3, are very similar to those generated by the RKE model for grid 2. In Figure 6-17, it can be seen that the SA and RKE turbulence models produce almost the exact same pressure distribution. The SA model slightly over predicts the leading edge pressure. The majority of the pressure surface is once again over predicted by 2-5%. The pressure from 10 mm to 30 mm pressure surface length, once again, sees a slightly larger discrepancy than the rest of the pressure surface. Possible reasons could be due to the higher turbulence levels in this region, following the pressure surface separation bubble, where the turbulence models are having difficulty resolving the flow field. Examining the blade wall Y-plus values in Figure 6-18, the plot indicates the region of the thicker boundary layer, where the wall-adjacent cell Y-plus values are small. Since the plot is representative of the first cell Y-plus value, lower Y-plus values are indicative of a thicker boundary layer.

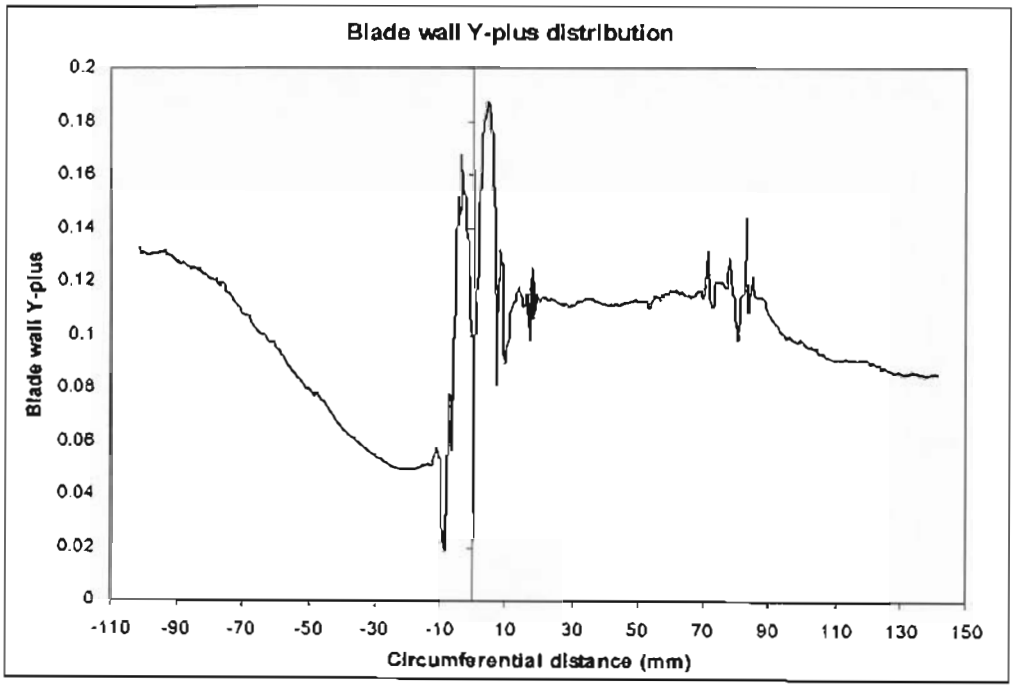

Figure 6-18: Blade wall Y-plus for grid 3 (a=0.001 mm)

On the suction surface, the pressure at 7 mm surface length is once again well predicted. From this point on, to 70 mm surface length, the CFD over predicts slightly with a maximum error of approximately 5%. At approximately 85 mm suction surface length, the Y-plus plot indicates that the boundary layer thickness suddenly increases. As shown and discussed later in section 6.7, this is caused by a change in velocity gradient seen at the blade throat. Here the CFD pressure plot deviates from the experimental pressure distribution. The experimental pressure plot shows a large pressure plateau from 75 to 100 mm suction surface length, whereas the CFD plot continues to drop, only recovering at 90 mm before rejoining

the experimental values at approximately 108 mm surface length. At 90 mm suction surface length, the error is 9%. Good agreement between the CFD and experimental values is seen for the remainder of the blade profile.

To look further at the success of the model, the heat transfer coefficient results must be analysed. These are plotted in Figure 6-19. The SA turbulence model performs better than the RKE model, with less error over a majority of the suction and pressure surfaces. Furthermore, the SA model predicts the leading edge heat transfer coefficient more accurately and also predicts the experimental heat transfer coefficient at 3.5 mm. Both turbulence models predict the pressure surface heat transfer distribution well, in particular, the region from 0 - 20 mm pressure surface.

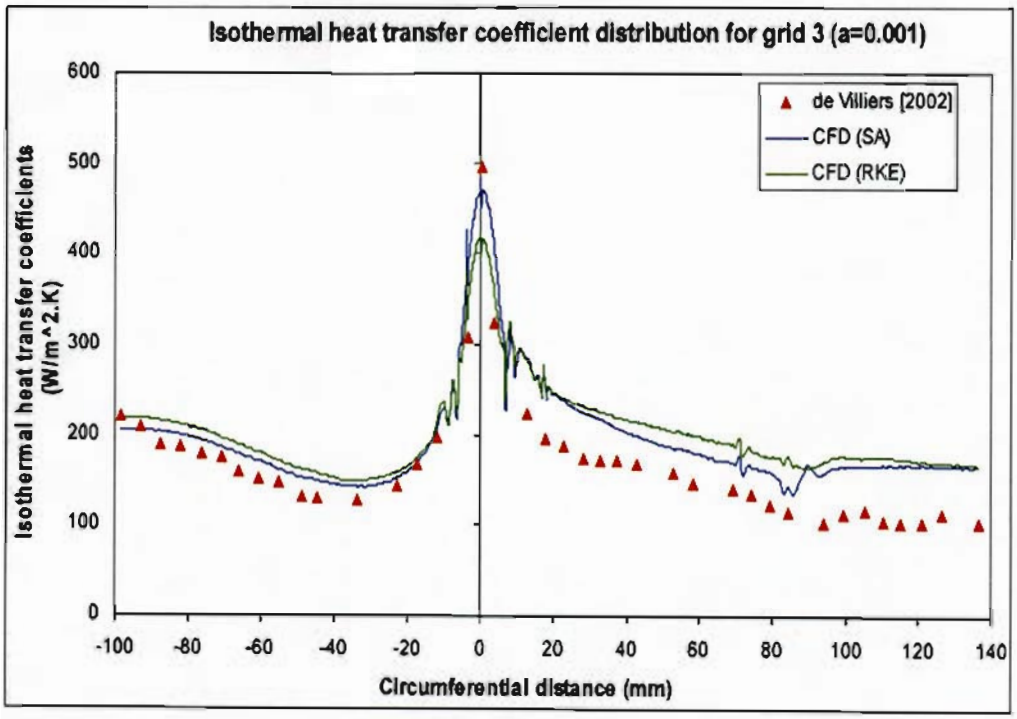

Figure 6-19: Isothermal heat transfer coefficient distribution for grid 3 (a=0.001 mm)

In the case of the SA model, the error on the pressure surface has been reduced to 10% over prediction. Both models respond equally to the spike in heat transfer coefficient at 7 mm pressure surface, associated with the turbulence after the separation bubble. The flow reversal within the leading edge separation bubble, can be seen from the velocity vector display from FLUENT, in Figure 6-20 on the following page.

A very large spike in heat transfer coefficient is seen at approximately 7 mm suction surface length. This response, together with the pressure distribution and Y-plus plot, can help

determine the flow phenomenon in this region. Looking at the wall Y-plus plot in Figure 6-18, the sharp increase of Y-plus values along the suction surface, from the leading edge, indicates the laminar boundary layer flow accelerating around the blade leading edge. This boundary layer thins as the velocity increases. The Y-plus plot then shows a very rapid decrease in Y-plus values, indication of a sudden boundary layer thickening. This spike in Y-plus values together with the spike in heat transfer could be associated with transition from laminar to turbulent flow. However, sudden transition is only likely in the presence of high turbulence (>10%) or high surface roughness. This cascade turbulence intensity is low, of the order 3%; and the blade is smooth polished MACOR. The heat transfer spikes at approximately 10 mm suction surface length are, like the pressure surface, reminiscent of a separation bubble. No separation point or flow reversal is seen at this point in the velocity vector plot. Yet, heat transfer is a function of velocity gradient at the wall. For separation, that gradient reaches zero. With the change in surface curvature from leading edge radius to suction surface proper, there will be a change in pressure distribution. Figure 6-17 shows as steep an adverse pressure gradient on the suction surface as the pressure surface downstream of the leading edge, but the suction surface static pressure values in that gradient are lower than those of the pressure surface values. This shows that the velocities are higher there than on the pressure surface, so the momentum forces overcome the pressure forces and the flow stays attached. This change in velocity manifests as a heat transfer spike.

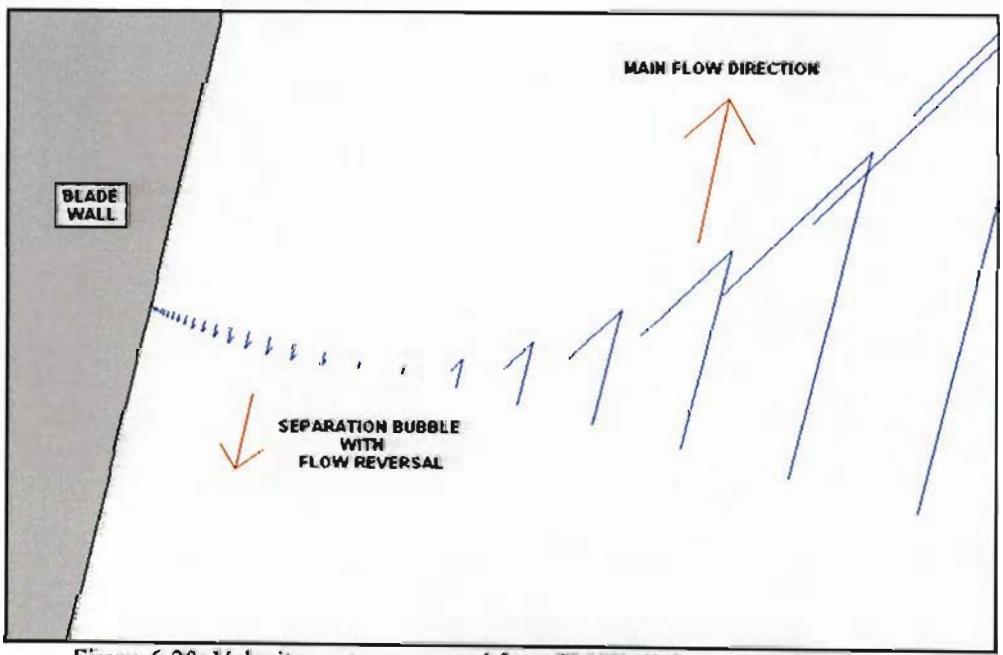

Figure 6-20: Velocity vectors exported from FLUENT, indicating flow reversal within the leading edge separation bubble at 7 mm pressure surface length

The heat transfer, thereafter, then decreases gradually, indicative of an accelerating, relaminarising boundary layer under the influence of a positive pressure gradient. The Y-

plus plot indicates how the boundary layer thickness remains fairly constant in this region (20-70 mm suction surface).

The SA turbulence model predicts a further spike in heat transfer, at 87 mm suction surface length. This corresponds with the decrease in wall Y-plus values at this point. It appears that transition occurs and the boundary layer thickens at this point, with an increase in heat transfer due to turbulence. This coincides with the throat of the passage. The boundary layer thickening can in fact be seen from the FLUENT Mach number contour plot, shown in Figure 6-33. This spike in the CFD plot, cannot be seen in the experimental heat transfer plot, due to the large spatial resolution of the experimental thin-film gauge sensors. However, the experimental plot indicates a slight dip in the heat transfer at 80 mm suction surface, corresponding to the dip in the CFD plot, immediately prior to the spike in heat transfer. The trend of the CFD and experimental plots then correlate where both the heat transfer plots level out towards the trailing edge of the suction surface. In this region, the CFD solution is largely over predicted, with errors measuring as much as 50%. The results discussed above, certainly indicate that the SA turbulence model performed superiorly over the RKE model. The SA model accuracy and the prediction of flow variances were superior across the entire blade surface. Clearly, marked improvements in the heat transfer results are being made in the development of the meshing technique. In an effort to further improve the results, the skew cells within the mesh would have to be eliminated.

6.4.4 A new decomposed mesh (Grid 4)

Numerous attempts were made to improve the mesh within the decomposed region, and eliminate the small number of skewed cells, in order to hopefully improve convergence times, as well as the solution accuracy. The previous mesh showed the significant improvement in convergence when skewed cells are eliminated. However, with the decomposed mesh, improving the cell skewness in one region or face, only worsened the skewness in other faces. The problem was solved by identifying the small areas where the skew cells existed and applying a smoothly graded, unstructured mesh to the appropriate areas.

A close up of the new decomposed mapped mesh, consisting of a combination of mapped and smoothly graded unstructured regions, is shown in Figure 6-21. Additional pictures of the mesh can be found in Appendix 8.

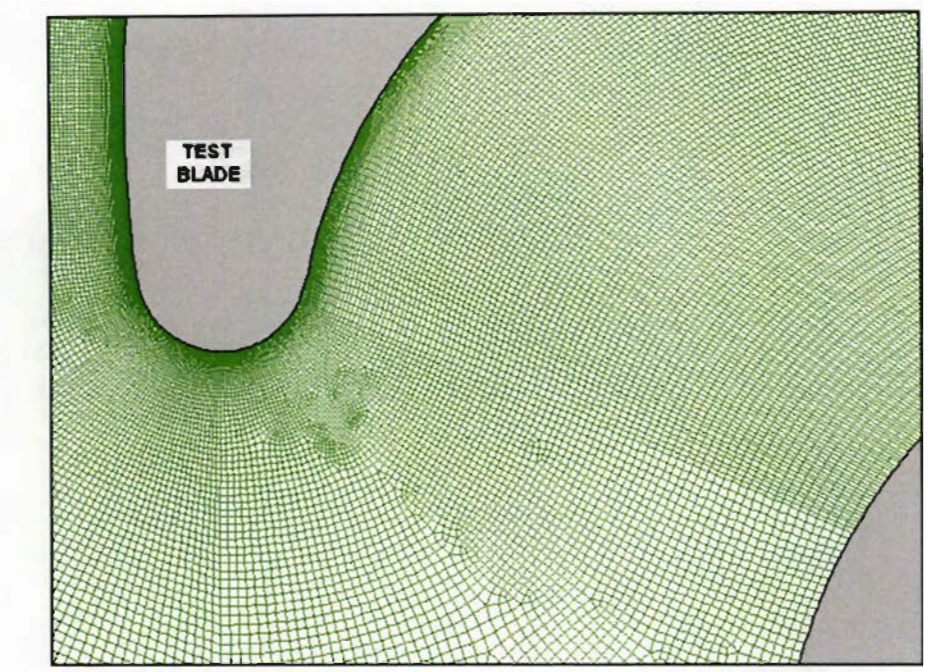

Figure 6-21: Close up of new decomposed mesh (Grid 4) surrounding the test blade

The same boundary layer mesh as in grid 3, was implemented for the grid 4. This boundary layer mesh showed a large number of cells within the viscous sublayer. Sixty rows were applied to the boundary layer mesh with a growth rate of 1.1. This, with appropriate edge grading, constructed perfect square cells at the edge of the boundary layer mesh. The mapped mesh scheme provided excellent control of the mesh density, maintaining a uniform near perfect square mesh distribution.

The mesh was remarkably successful, consisting of 157 000 cells with a worst cell skewness of only 0.52. This major reduction in cell skewness, improves convergence time and can improve solution accuracy too.

6.4.4.1 FLUENT results for the new decomposed mesh (Grid 4)

Exporting the mesh into FLUENT, the simulations were carried out and the corresponding results are displayed in Figure 6-22.

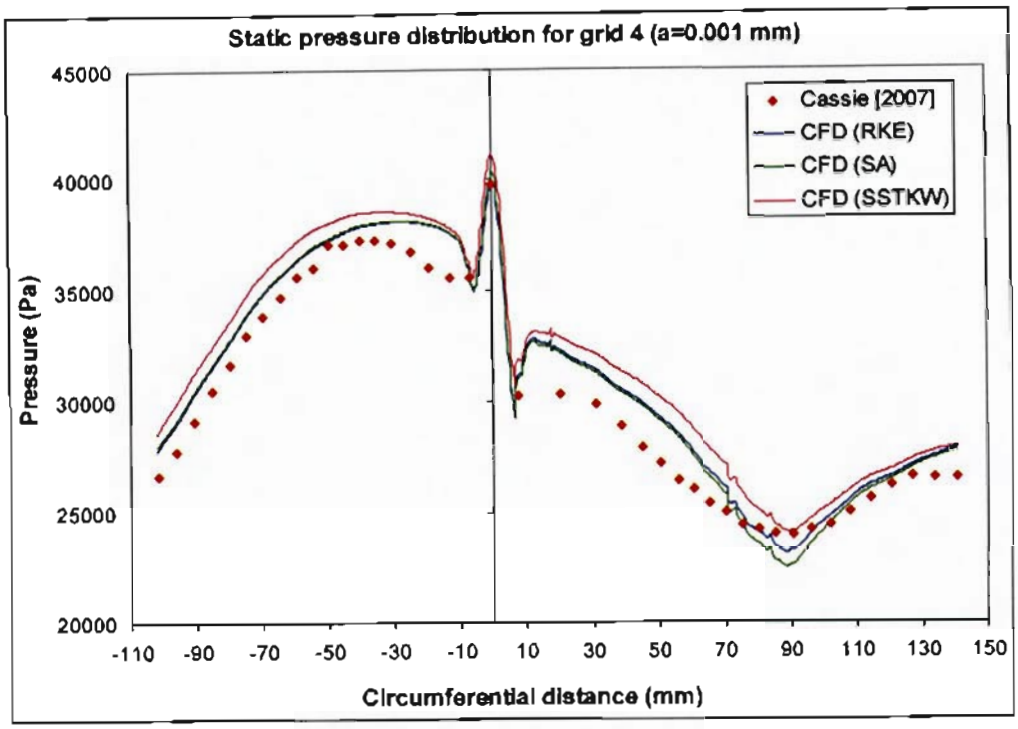

Figure 6-22: Static pressure distribution results for the decomposed mesh (Grid 4) (a=0.001)

Once again the SA and RKE turbulence models converged, noticeably much faster than the previous meshes. The SSTKW continuity residual, once again, did not quite achieve convergence to 1×10^{-5}. The solution was however, extracted when the continuity residual was at 5×10^{-5}.

The new pressure results show almost identical trends to the previous grid. However, in the case of the RKE and SA turbulence models, the margin of error at the change in pressure gradient (approximately 75 mm suction surface length) has been considerably reduced from 9%. The RKE model gives an error of 3% at this point, whilst the SA model gives an error of 6%. The remainder of the pressure profile remains identical to that of the previous solution.

The SSTKW solution is plotted for the first time, and the results show a general over prediction by the CFD model. The SSTKW solution produces a pressure profile that lies above the RKE and SA models for a majority of the blade surface, following the trends closely. It is interesting to note how the pressure at 90 mm suction surface length is now accurately predicted by the SSTKW model, which did not quite converge. This distribution is similar to the earlier unconverged pressure distribution. The isothermal heat transfer coefficient results below, present the accuracy of the flow modelling.

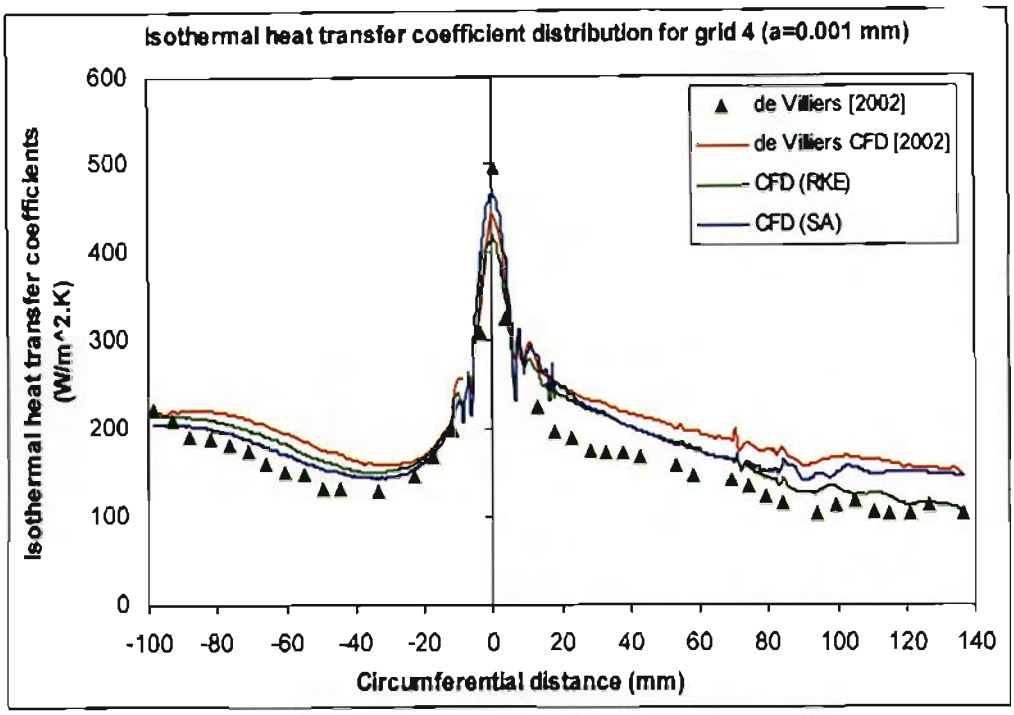

Figure 6-23: Isothermal heat transfer coefficient distribution for grid 4 (a=0.001 mm)

de Villiers' CFD [2002] results have been included in the plot, to illustrate the improvement in CFD results. The heat transfer results for the SSTKW model produced particularly erroneous results. The CFD plot over predicted the experimental values with an error of 100%, over the entire blade profile. The SSTKW model has shown very poor performance, mainly due to the extreme difficulty in convergence. The plot has not been included in Figure 6-23. The new decomposed mesh shows a slight improvement in the CFD heat transfer solution for the SA and RKE models. Once again, no new distribution trends are established.

However, the RKE model predicts the trailing edge of the suction surface very well, for the first time. At the suction surface trailing edge, the RKE CFD plot, intersects a majority of the experimental heat transfer coefficients. Comparing the previous RKE results for grid 3, it can be seen that for the new grid 4, the RKE model now follows the SA solution and at 75 mm suction surface length follows the experimental values more closely. Otherwise, the SA turbulence model performs better over the rest of the blade, predicting the leading edge and entire pressure surface more accurately.

With the above static pressure and isothermal heat transfer coefficient distributions, plots of the associated errors are shown in Figures 6-24 and 6-25 respectively.

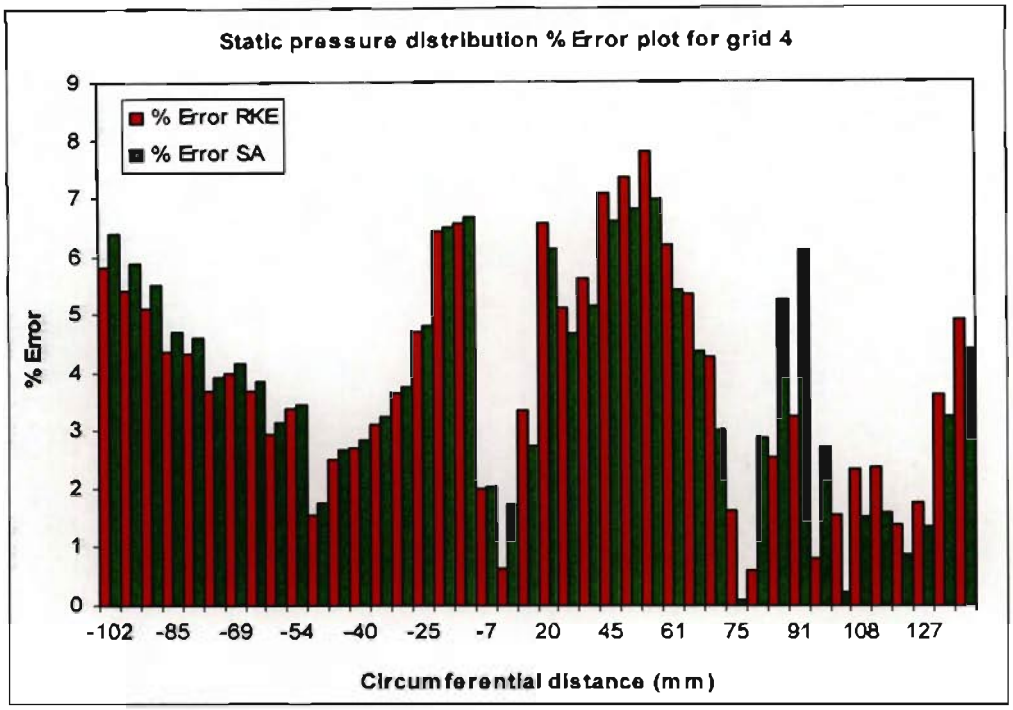

Figure 6-24: Plot of static pressure distribution percentage error for grid 4

The average pressure distribution error for the RKE model is 3.8%, and 3.9% for the SA model.

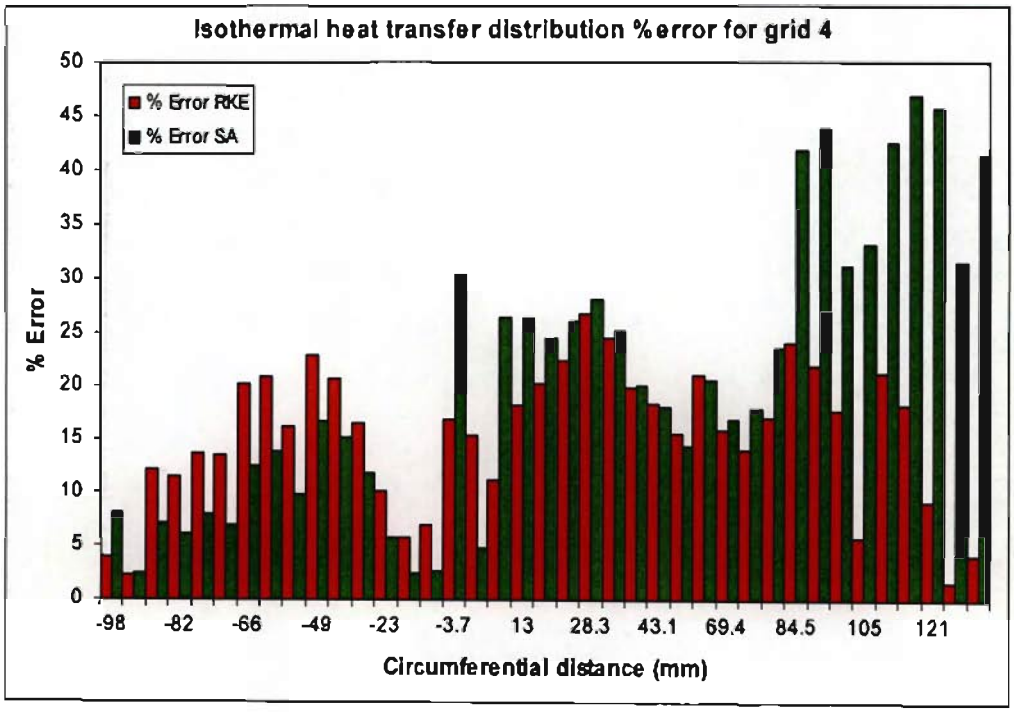

Figure 6-25: Plot of isothermal heat transfer distribution percentage error for grid 4

The average isothermal heat transfer distribution error for the RKE model is 15%, and 20% for the SA model. Clearly, in the heat transfer error plots, the pressure surface is more accurately predicted. In general the region of 20-100 mm suction surface is not predicted well. The large trailing edge error associated with the SA model heat transfer solution, is very evident in Figure 6-25. With much effort and time allocated to the meshing techniques, an improvement in the CFD results has been achieved, which can be seen in Figure 6-23, by comparing the previous CFD results of de Villiers [2002]. However, significant errors still exist. A search for alternative sources of error was most definitely required.

6.5 Varying turbulence intensities

As illustrated in Figure 2-2 of the literature survey in Chapter 2, Snedden [1998] showed how the turbulence intensities vary significantly at the cascade inlet. The CFD models were all carried out with a turbulence intensity of 3%. Yet the inlet pressure and temperature probes clearly have a large effect on the downstream turbulence intensity. The turbulence intensities at the leading edge, mid-passage, of the pressure and suction passages were measured at 1.2% and 5.3% respectively. In addition, the measured test blade leading edge turbulence intensity of 3% at 2500 rpm, can be regarded as suspect. This is due to the fact that the hot wire probe results lay in the fully saturated region of the calibration curve. Dunn [2001] discusses how 'knobs are turned' during a CFD process to ascertain their effect on the results. The cascade turbulence intensities were thus varied to determine the effect on the results.

The range of turbulence intensities used in the CFD simulations, were chosen from the turbulence intensity measurements performed by Snedden [1998]. Although Snedden [1998] only shows the variance in the cascade inlet turbulence intensity for 1500 rpm, these values provide a guideline as to how the turbulence is varying, and hence what values to use in the simulation. Figure 2-2 indicates that the turbulence intensities at mid-span, at the leading edge of the pressure and suction surface passages, are 1.2% and 5.3% respectively. Hence, simulations were carried out at these two inlet turbulence intensities. The simulation at 1.2% was used to plot the pressure surface results, and the simulation at 5.3% was used to plot the suction surface results. The corresponding static pressure distribution is shown in Figure 6-26.

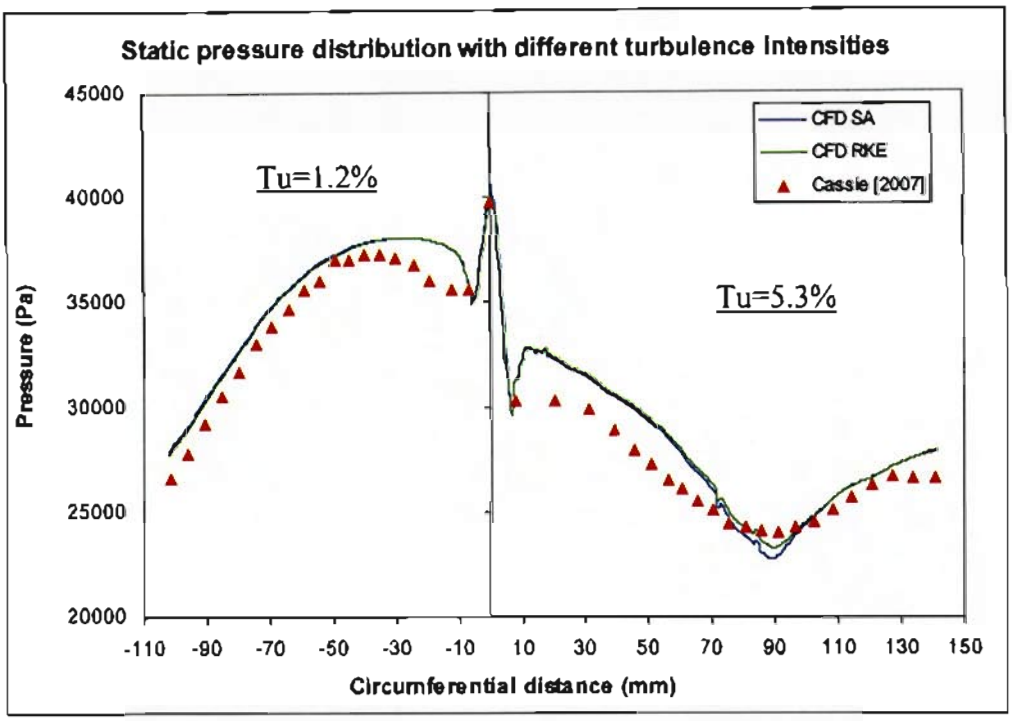

Figure 6-26: Static pressure distribution with different pressure and suction surface turbulence intensities

The static pressure distribution in Figure 6-26, indicates no change in the pressure results due to the differing turbulence intensities. The RKE and SA models produce the exact same results as for the 3% turbulence intensity case of grid 4 previously. Once again, the RKE model predicts the pressure slightly more accurately at 90 mm suction surface.

However, the heat transfer distribution in Figure 6-27, shows how the turbulence intensity has significantly affected the results. On the pressure surface, a slight improvement in both the RKE and SA models results is seen. The RKE solution almost matches the SA solution, and the maximum pressure surface error is now only approximately 12%. Error at the pressure surface trailing edge has been reduced to 5%. In the region of 0-20 mm pressure surface, the heat transfer prediction is very good, with many of the experimentally measured coefficients being intersected by the CFD plot. The leading edge experimental heat transfer coefficient is, however, largely under predicted by both the SA and RKE CFD plots. The turbulence intensity of 1.2% on the pressure surface has significantly reduced the error. This is good substantiation of the problem with the varying inlet turbulence intensities.

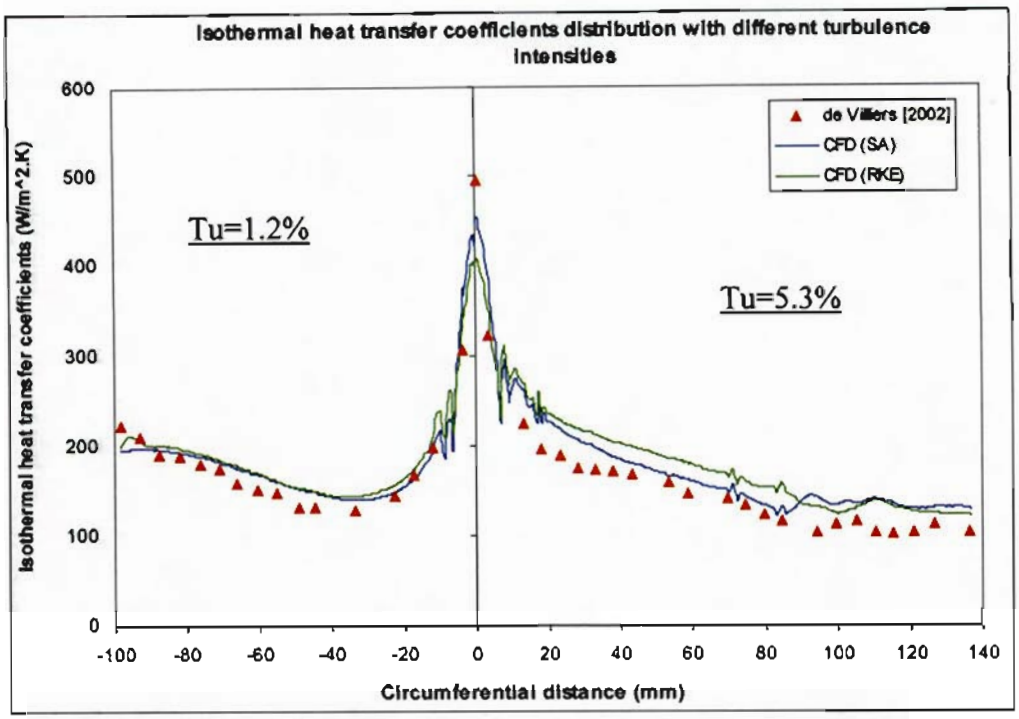

Figure 6-27: Isothermal heat transfer coefficient distribution with different pressure and suction surface turbulence intensities

On the suction surface, with the turbulence intensity at 5.3%, the SA model produces significantly more accurate results than in previous solutions. Error in the region from 20 mm to 90 mm suction surface length, has been significantly reduced, with a majority of the errors in the region of 4 - 15%. A slight increase in the experimental heat transfer coefficients is predicted by the SA turbulence model at approximately 90 mm surface length. The error thereafter is higher than on the rest of the blade surface. The RKE model shows significant improvement too, although not predicting as accurately as the SA solution from 20 – 90 mm suction surface length.

At the leading edge, the SA model, once again, predicts the leading edge heat transfer coefficient more accurately then the RKE model. The RKE model continues to over predict the heat transfer from 20-90 mm suction surface, by the same margin. The percentage errors between the experimental and numerical heat transfer measurements are displayed in Figure 6-28.

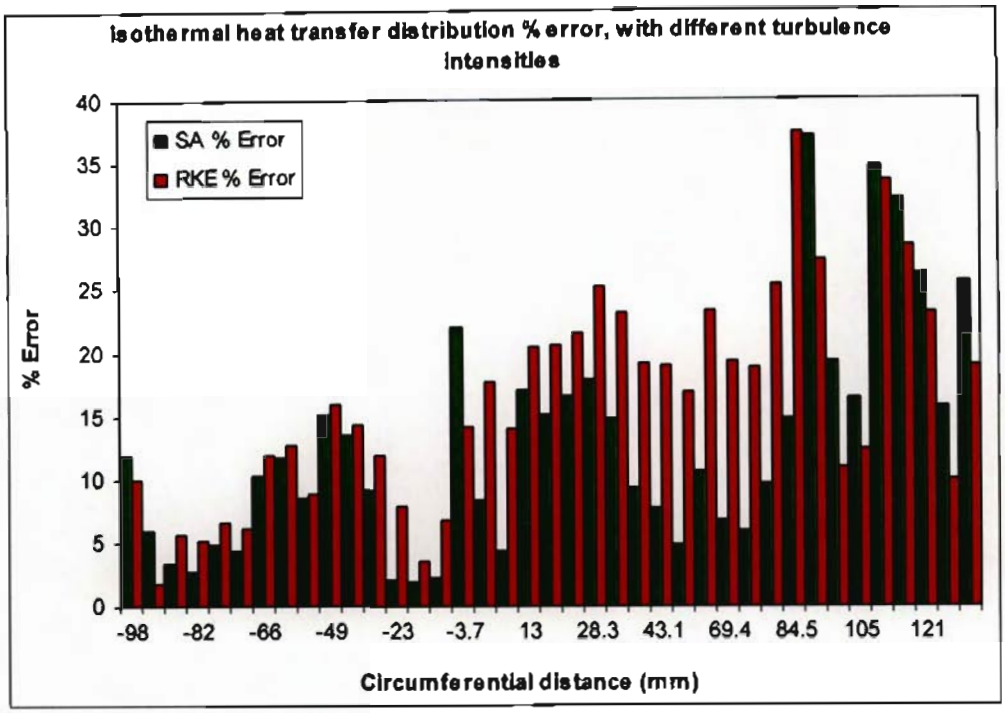

Figure 6-28: Plot of isothermal heat transfer distribution percentage error, with different pressure and suction surface turbulence intensities

The effect of implying different turbulence intensities on the pressure and suction surfaces has proved to be successful. The results certainly confirm the problem with the cascade's varying inlet turbulence intensity, produced by the temperature and pressure probes. Figure 6-28 illustrates how the error is distributed. Clearly, the pressure surface has been more accurately predicted, with an average error of 8% for both the SA and RKE models, respectively. This is a remarkable improvement over the average pressure surface error of 25% recorded by de Villiers [2002].

On the suction surface, average errors of 16% and 22% were recorded by the SA and RKE turbulence models, respectively. These figures too, show a remarkable improvement over the previous average suction surface error of 33% recorded by de Villiers [2002]. In general the SA model predicted the heat transfer distribution more accurately over the entire blade surface.

It must be noted, that this technique of sub-dividing the results from simulations at different turbulence intensities, may not be the most accurate method. However, it does provide insight and justification into what the actual turbulence intensity values within the cascade are. This highlights one of the sources of error within the CFD results over the past years. In order to make the model more accurate, it was planned to apply a user defined function (UDF) to the FLUENT model cascade inlet. This equation describes the variance of the

turbulence intensity across the inlet, and would accurately vary the turbulence intensity across the pressure inlet of the model. However, the low resolution of the experimental turbulence intensity measurements by Snedden [1998], does not permit this concept.

6.6 Additional mesh geometries attempted

Two additional mesh geometries were attempted for the CFD analysis. These, however, proved to be unsuitable for an accurate analysis of the cascade flow conditions. Results were initially generated for these geometries, however, their incompatibility was soon realised and the concepts were abandoned. The results for these meshes are therefore not included, yet a brief description of their original purpose is included, for aid in any further CFD research on the SMR-95 cascade.

6.6.1 Plenum geometry

The CFD results presented in this chapter, have been solved for the cascade geometry only. This is most appropriate since the boundary static pressure conditions of the cascade have been measured experimentally. However, modelling the cascade only, implies that the plenum flow conditions are not solved for. Therefore, it is unknown how the plenum geometry influences the flow conditions entering the cascade bell mouth inlet. For this reason, the cascade geometry was extended to include the entire plenum geometry in GAMBIT, which incorporated the section from the annular radiator. The radiator wall was thus created as the pressure inlet, and the cascade outlet remained as the pressure outlet.

The rather simple geometry of the plenum, together with the lack of large pressure gradients, permitted the use of a much coarser quad pave mesh in comparison to the cascade mesh. The cascade walls were therefore created with a 2.5 mm wall thickness, which allows for the walls to be graded differently on either side, thereby creating the different density meshes. Appropriate grading at the cascade bell mouth inlet, provided a smooth transition from the larger cells of the plenum, to the finer mesh of the cascade. Figure 6-29 below illustrates the plenum mesh created.

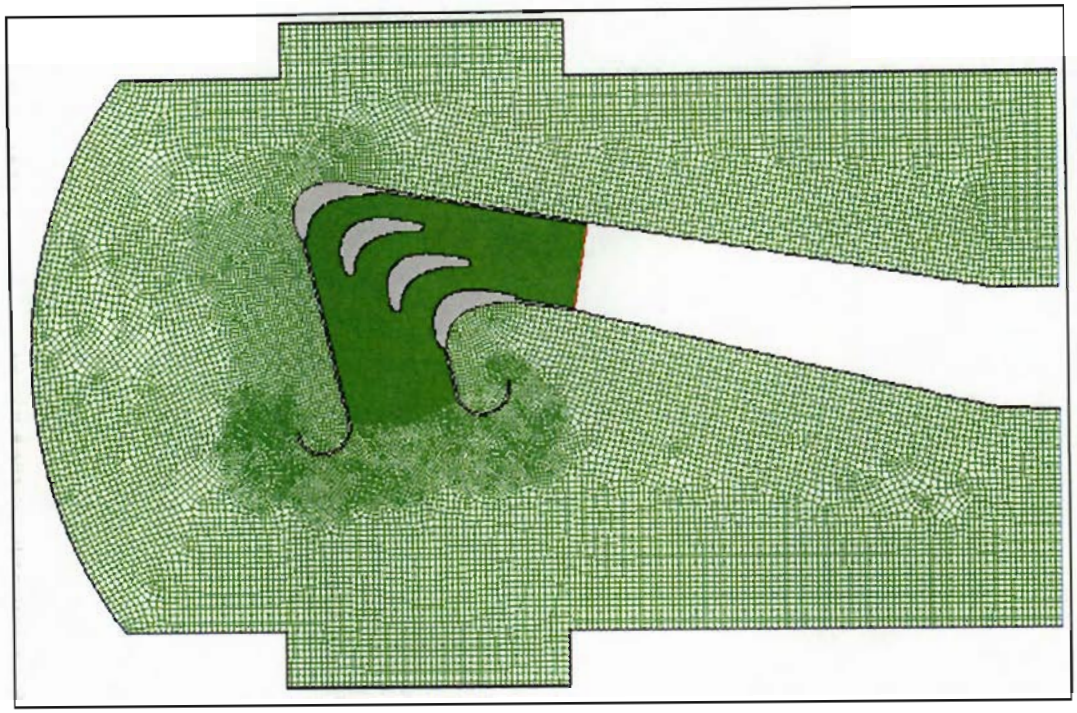

Figure 6-29: Plenum mesh geometry

This geometry, however, is not suitable for an accurate analysis. The problem lies with the fact that the pressure inlet conditions are not known at the radiator wall. Experimental measurement at this point would consider the model appropriate. Since the flow results have been shown to be largely influenced by the only small changes in flow conditions, the plenum model was abandoned since large and suspect assumptions would have to be made for the pressure inlet at the radiator wall.

6.6.2 Periodic geometry

FLUENT provides the ability to calculate streamwise periodic flow. This type of flow can be modelled when the flow pattern repeats itself over some length L, with a constant pressure drop across each repeated boundary. The model geometry must vary in a repeated manner along the direction of flow, creating a periodic, fully-developed flow, which repeats itself in successive cycles. With repeatable geometry configurations, such as the cascade with a repeated blade stack row, a fraction of the geometry can thus be created, modelled, and simply repeated to generate the entire cascade flow region. This allows for a much finer mesh, since the geometry size and hence the number of cells is considerably reduced. Figure 6-30 below, illustrates the configuration of this periodic mesh. The flow regime includes half of the two flow passages on either side of the test blade, where the outer boundaries are periodic boundaries. These boundaries are defined within GAMBIT, and allow the flow to pass through them thereby creating repeated flow conditions.

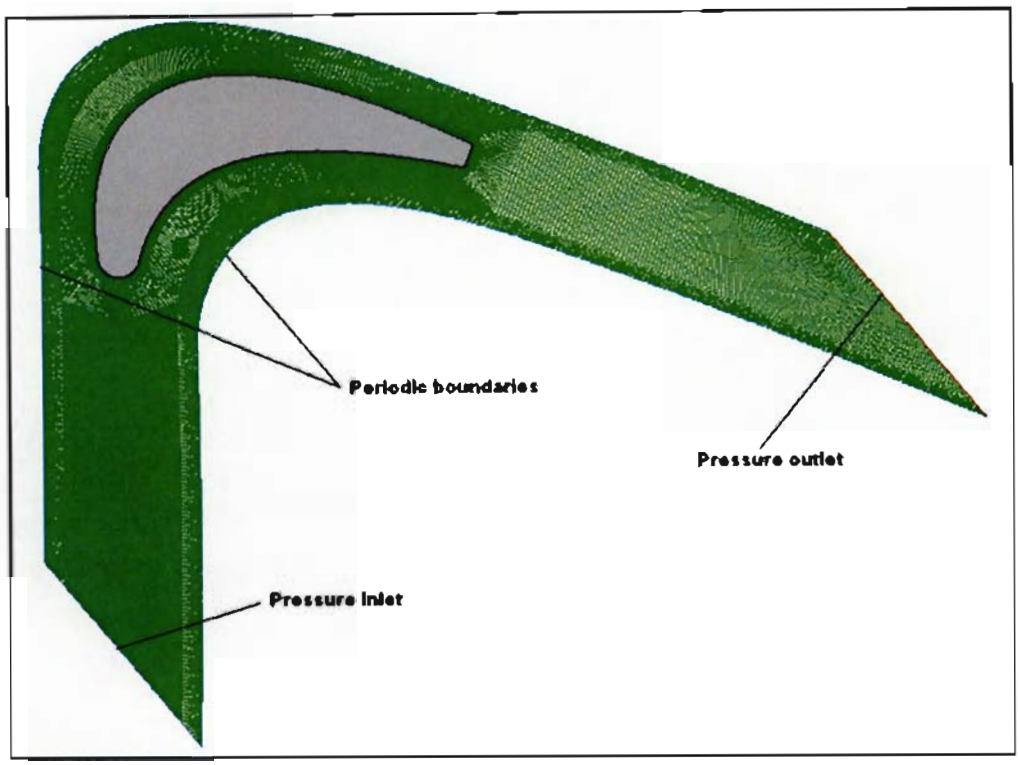

Figure 6-30: Periodic mesh geometry

This geometry too, although highly advantageous in reducing simulation times and reducing mesh sizes, is also not compatible with the SMR-95 cascade. The cascade flow conditions have to be periodic, or repeatable across the periodic flow boundaries. Snedden [1998] shows the periodicity results for the cascade inlet and exit, which revealed poor periodicity within the cascade. Gostelow [1984] recommends at least seven blades are to be used within a turbine cascade in order to achieve good periodicity. This meshing concept unfortunately, therefore also had to be abandoned. New designs of the cascade may permit the use of this type of meshing technique in the future.

6.7 Discussion

The CFD results presented in this chapter have proven to be very successful. Although the SSTKW turbulence model exhibited difficulty in convergence, leading to inaccurate results, the SA and RKE models produced similar results with significant reduction in error compared to the previous solution by de Villiers [2002]. Discrepancies found in de Villiers' [2002] pressure solution, prompted investigation into the convergence of de Villiers' [2002] model. It appears that de Villiers' [2002] static pressure solution is plotted from an unconverged solution.

Development of the meshing technique revealed the significant importance of a high quality mesh. The final solution was generated using a combination of a structured mapped mesh,

and an unstructured pave mesh in highly skewed regions, with a boundary layer fine enough to resolve both the velocity and thermal boundary layers. The SA and RKE turbulence models captured the boundary layer flow phenomenon of the SMR-95 blade, and the results match the experimental static pressure and isothermal heat transfer distribution trends very well. Simultaneously analysing the static pressure, heat transfer, and blade wall Y-plus distributions, allowed for an analysis of the boundary layer flow phenomenon. This is a vital factor of any convective heat transfer problem, since the steep near-wall velocity and thermal gradients determine the heat transfer characteristics through the blade surface. Stieger [1998] shows the effect that the Reynolds number and free-stream turbulence intensity have on the transition process. The isothermal heat transfer coefficient distribution shows a high degree of sensitivity to the transition from laminar to turbulent flow.

Figure 6-31 shows a comparative plot of the experimental and CFD (SA) Mach number distributions.

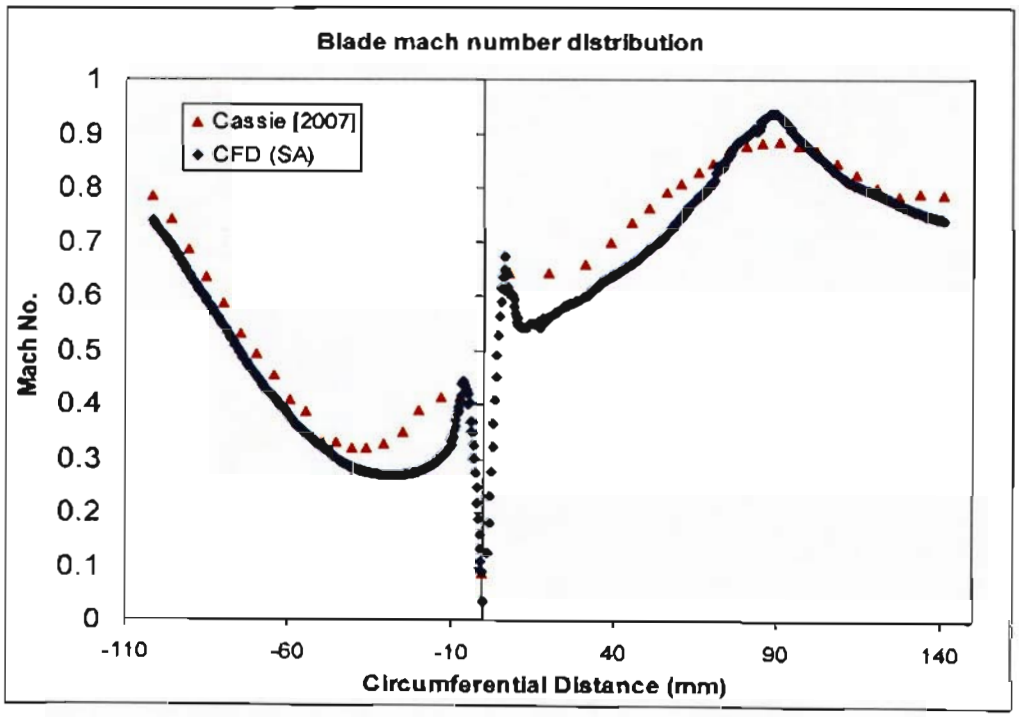

Figure 6-31: Cassie [2007] Experimental and CFD Mach number distributions

Figure 6-32, 6-33 and 6-34 show contour plots of the predicted bulk flowfield Mach number and pressure distribution respectively. Figure 6-35 shows the blade wall Y-plus distribution. These figures will be used in ensuing discussion regarding the blade surface flow phenomena.

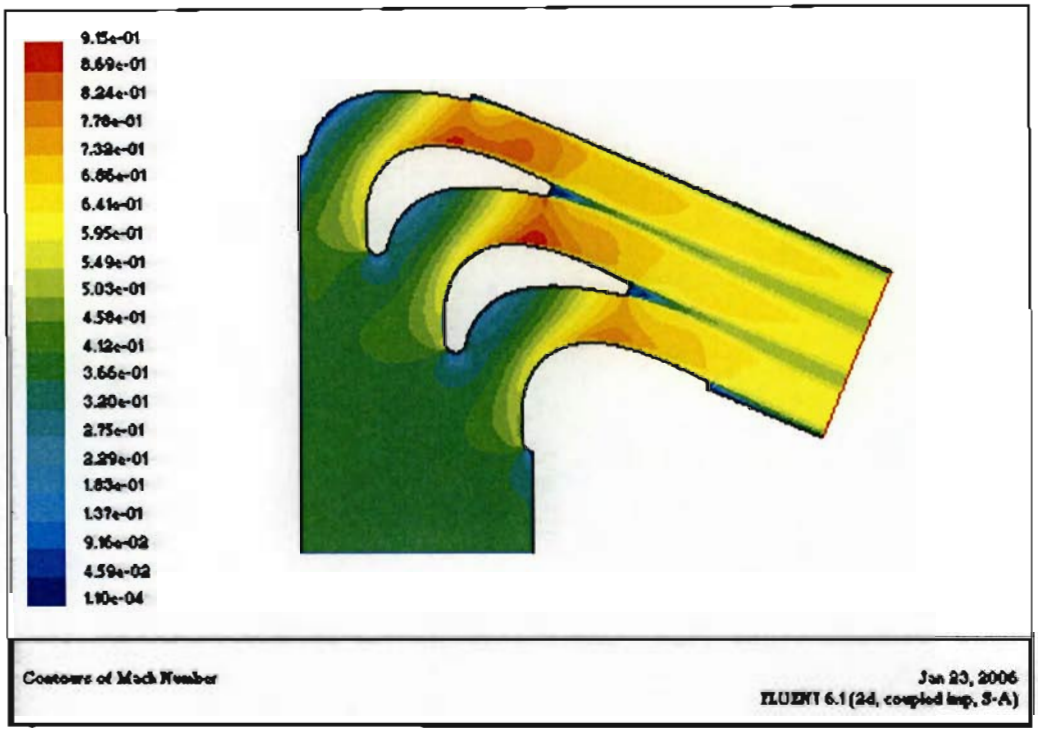

Figure 6-32: Contour plot of predicted bulk flowfield Mach number distribution

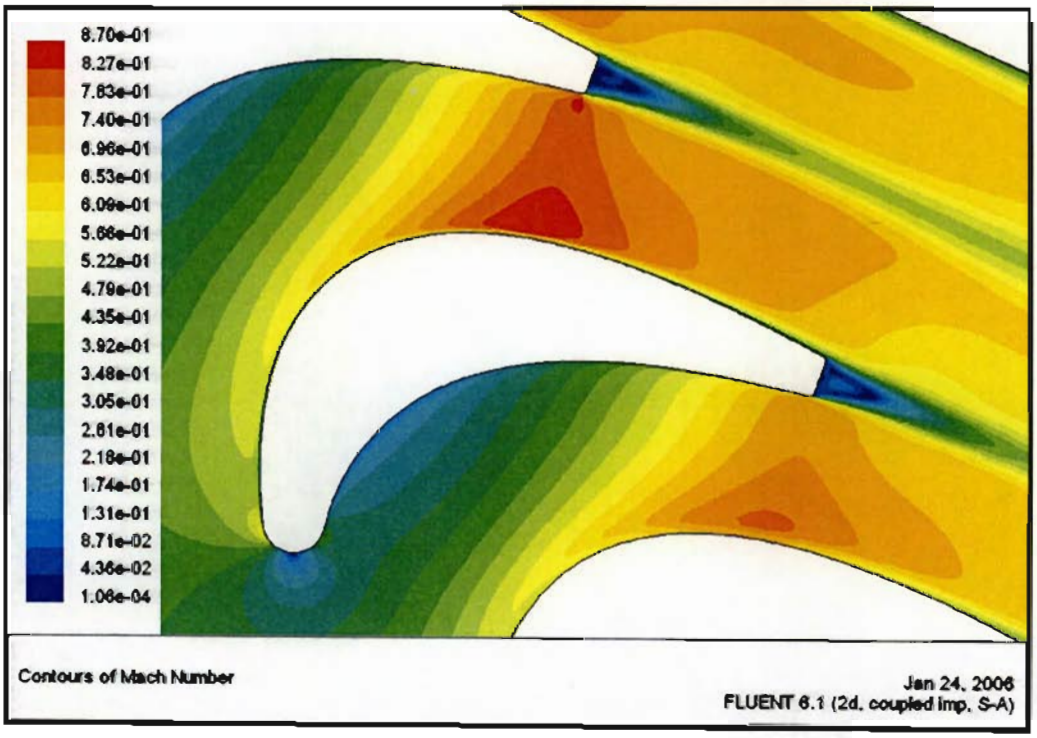

Figure 6-33: Close up of the Mach number contour plot surrounding the test blade

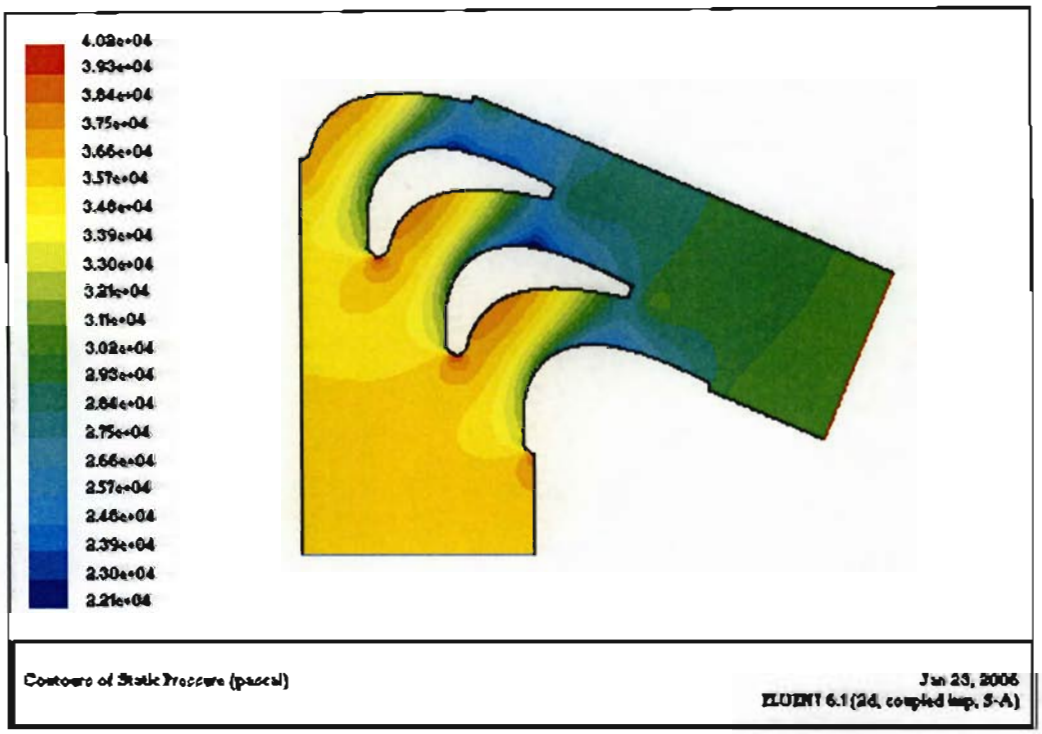

Figure 6-34: Contour plot of predicted bulk flowfield pressure distribution

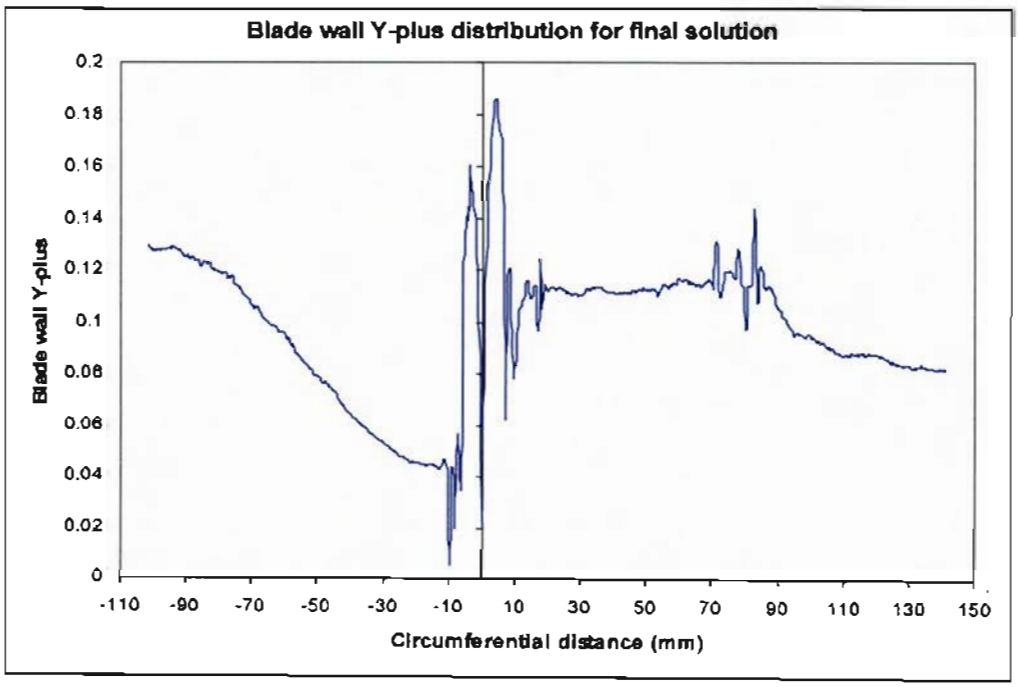

Figure 6-35: Blade wall Y-plus distribution for the final solution

To summarise the flow phenomenon, the high levels of static pressure and heat transfer at the leading edge, are characterised by the region of leading edge flow impingement. This region is very critical from a heat transfer point of view. The stagnation point is often the

point of maximum heat transfer on the blade surface since the boundary layer here is very thin (Larsson [1998]). Figure 6-31 shows the very low Mach number in this region. The leading edge is also susceptible to changes in turbulence intensity. Eddies within the inlet hot-gas stream can penetrate to the blade surface thereby increasing the heat transfer to the blade. Consigny and Richards [1982] show how the increase in turbulence intensity can increase the heat transfer in this region. Radomsky et. al. [1998] states that free-stream turbulence levels greater than 10% can increase heat transfer at the leading edge by 50%. The leading edge is also where the pressure and suction surface boundary layers develop. Therefore any disturbances are convected downstream and can have an affect on the heat transfer.

Downstream of the leading edge, on the pressure surface, the laminar boundary layer flow accelerates rapidly under the influence of a favourable pressure gradient. At 7 mm pressure surface length, the blade profile suddenly undergoes a step change in curvature, from the leading edge radius to the pressure surface profile. From published experimental work, this has been shown to almost always produce a boundary layer separation bubble. This step change in surface curvature causes a variation in the pressure gradient near the leading edge. This causes the accelerating laminar boundary layer flow to reach a maximum velocity (dp/dx=0) at 7 mm pressure surface length, and faces an adverse pressure gradient (dp/dx>0). As shown by Kundu and Cohen [2004], the boundary layer equation at the wall becomes:

$$\mu\left(\frac{\partial^2 u}{\partial y^2}\right)_{wall} = \frac{\partial p}{\partial x} \qquad (6\text{-}1)$$

In an accelerating boundary layer, as is the case from the leading edge, dp/dx<0, therefore

$$\left(\frac{\partial^2 u}{\partial y^2}\right)_{wall} < 0 \quad \text{(accelerating)} \qquad (6\text{-}2)$$

In contrast, for a decelerating boundary layer, dp/dx>0, therefore

$$\left(\frac{\partial^2 u}{\partial y^2}\right)_{wall} > 0 \quad \text{(decelerating)} \qquad (6\text{-}3)$$

It shows that the curvature of the boundary layer profile changes sign and therefore must exhibit an inflection point (point of changing curvature) where $\partial^2 u / \partial y^2 = 0$. This point of inflection can in fact be seen in Figure 6-3 and Figure 6-35.

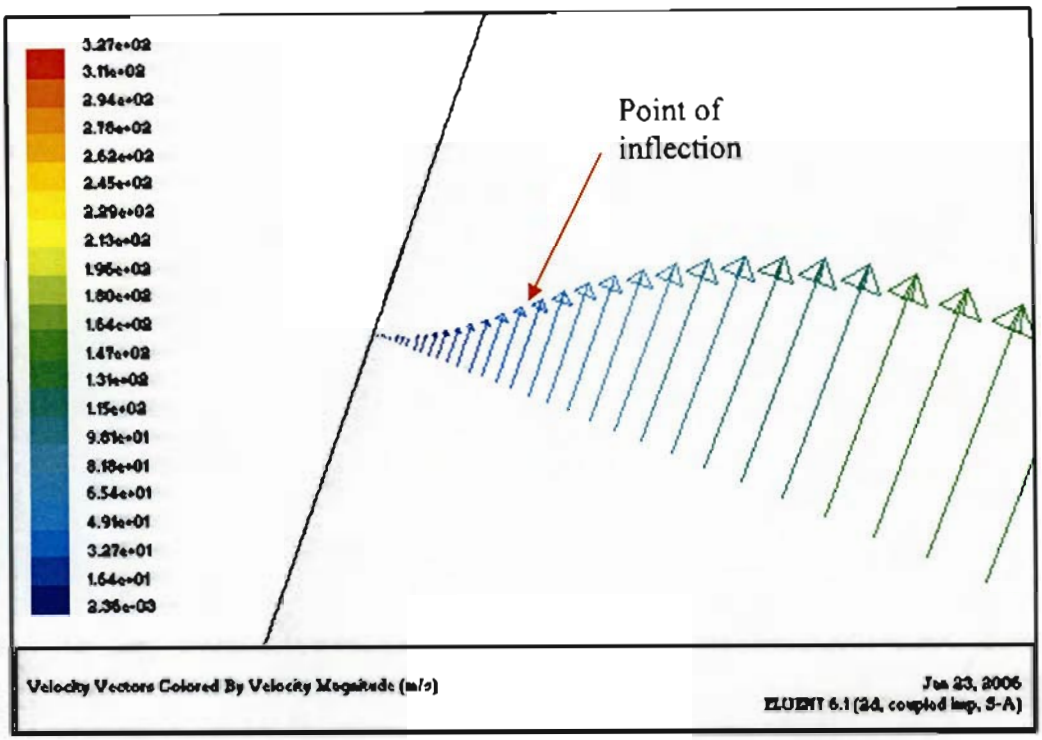

Figure 6-36: CFD velocity vector plot indicating the change in curvature of the boundary layer

The flow now decelerates until the velocity gradient at the surface becomes zero. Separation of the laminar boundary layer now occurs, since the laminar flow does not generate sufficient momentum transfer to overcome the velocity gradient. Flows with higher levels of turbulence however, can exhibit sufficient energy to overcome the adverse pressure gradient and either prevent or shorten the separation bubble. This is shown by Consigny and Richards [1982] by the near disappearance of the laminar bubble at a higher turbulence intensity. Bellows and Mayle [1986] also suggest that the bubble is shorter at higher Reynolds numbers. The separation bubble results in a very low level of heat transfer. This separated shear layer is very unstable, inducing transition from laminar to turbulent flow. The point of separation and transition can also be seen in the Y-plus distribution plot in Figure 6-35. The cell wall Y-plus values decrease rapidly at the onset of separation, and then decrease further at approximately 10 mm, as the transition process thickens the boundary layer.

The now turbulent flow reattaches, resulting in a separation bubble, exhibiting a small region of flow reversal that has been indicated in figure 6-20. In the laminar region of this bubble, there is a low level of heat transfer, resulting in the local minimum heat transfer coefficient. The turbulent reattachment is seen in Figure 6-35, where the Y-plus values suddenly increase. The turbulent boundary layer is thick at this point and the heat transfer decay is therefore seen to be rapid. The Y-plus plot indicates that the boundary layer thins from this point on, with a corresponding slight increase in heat transfer along the blade pressure

surface. This is indicative of the boundary layer relaminarising under the influence of a favourable pressure gradient. Mayle [1991] states that the flow will always transition back to laminar after turbulent reattachment in this region.

On the suction surface, following the rapid acceleration of the laminar boundary layer from the leading edge (seen from Mach number plot in Figure 6-31), a spike in heat transfer is visible at approximately 7 mm suction surface length. This corresponds with the rapid decrease in Y-plus values, indicative of a sudden thickening of the boundary layer. As described in section 6.4.3.1, the change in surface curvature in this region from leading edge radius to suction surface proper, induces a pressure and hence velocity gradient, manifesting a spike in heat transfer. Following the spike in heat transfer, the heat transfer distribution decreases rapidly, indicating relaminarising of the boundary layer, due to the favourable pressure gradient. The erratic heat transfer distribution stabilises at 20 mm suction surface length, and continues to decrease steadily under the influence of a favourable pressure gradient. Figure 6-35 indicates that the boundary layer thickness remains constant from 20 - 70 mm suction surface length. Due to the favourable pressure gradient, the flow accelerates from 20 mm suction surface length until 90 mm, visible in the plot of Mach number in Figure 6-31 and also the contour plots of Mach number in Figures 6-32 and 6-33. Figure 6-33 shows clearly the red contour of maximum Mach number. At 90 mm suction surface length, the maximum velocity point and corresponding with the blade throat passage, the flow undergoes a change in the velocity gradient. As shown in equation 6-3 this is associated with the adverse pressure gradient ($dp/dx>0$) in the pressure distribution. The boundary layer thickens in the decelerating stream, visible from the Y-plus plot in Figure 6-35 as well as the Mach number contour plot in Figure 6-33. This thickening causes a very slight decrease in heat transfer coefficient from 100 mm suction surface length to the trailing edge.

A good correlation between the experimental and numerical pressure measurements has been achieved by FLUENT. Average errors of 3.8% and 3.9% were achieved by the RKE and SA models respectively. The areas of maximum pressure error occur in regions of higher turbulence, such as downstream of the pressure surface separation bubble. Another area exhibiting error with the pressure results is the area from 20 – 70 mm suction surface length. The CFD pressure results are fully converged and can be regarded as very reliable. In two-dimensions, it is unlikely that the pressure solution will be significantly improved upon with the use of the available FLUENT solvers.

The FLUENT, isothermal heat transfer coefficient distribution, differs from the experimental values with an average error of 12% and 16% for the SA and RKE turbulence models, respectively. These errors show a remarkable improvement in the previous average error of approximately 29%, achieved by de Villiers in 2002. The large decrease in the error can be associated by the significant improvement in mesh technique and quality, accompanied by the investigation of the cascade inlet turbulence intensity variance. Varying the turbulence intensities according to the experimental values recorded by Snedden [1998], proved to significantly affect the results and minimise error. As discovered by Snedden [1998], this variance in turbulence intensity across the cascade inlet is cause for concern.

It is believed that a three-dimensional (3-D) CFD solution will be effective in providing a more accurate solution. Modelling in 3-D allows for the cascade inlet pressure and temperature probes to be included in the geometry, thereby providing an accurate representation of the varying turbulence intensity caused by the probes. The experimental and numerical pressure, and isothermal heat transfer coefficients, show how the suction surface results are significantly affected by small variations in flow conditions. This influence is amplified by the existence of the suction side tailboard. Design of a new cascade, with additional blades to improve periodicity will present advantages for further research development. However, a 3-D CFD model will prove to be most advantageous in solving for the secondary flows associated with complex geometries and end wall boundary layers. Graziani et al [1980] presents numerous conclusions with regard to the major influence which the secondary passage flows have on the suction surface heat transfer distribution. Furthermore, Graziani et al [1980], concludes that the blade pressure surface heat transfer is not affected by the secondary flows. This provides a good explanation as to why the pressure surface heat transfer distribution is more accurately modelled. Any practical turbine heat transfer measurement or prediction, must account for the effect of the complex three-dimensional flow field, which arises from turbine blade secondary flows.

CHAPTER 7

CONCLUSION AND RECOMMENDATIONS FOR FUTURE WORK

The project required the determination of the isothermal heat transfer coefficient distribution, with a high degree of accuracy. This required validation of the numerical two-dimensional solution generated in FLUENT, using experimentally measured values. The measurement of turbine blade heat transfer is, however, worthless as a means of validating predictions without properly resolving the associated cascade aerodynamics.

de Villiers [2002] produced a seemingly excellent correlation between the experimental and numerical pressure solutions. However, investigation into de Villiers' [2002] experimental technique revealed that the suction surface pressure distribution was recorded at too high a cascade velocity. This significantly affected the suction surface results. Therefore, new experimental pressure results were necessary to provide reliable prediction validation. Initial experimental work required maintenance on the rig as well as the repair of a mechanical seal malfunction. A digital pressure control system was designed and implemented by the author to replace the previous old and inaccurate analogue system. This new pressure control system, provided highly accurate and reliable means with which to control the pressure within the plenum. This allowed for the cascade inlet and outlet static pressures to be accurately measured. These values are vital to solution accuracy, since they are the boundary condition inputs into the numerical solver.

After significant electronic analysis, the data acquisition voltage protection card was found to be faulty, and a new card was purchased. Numerous pressure measurement experiments were conducted, utilising a scanivalve system to automatically record the pressures, whilst paying particular attention to the cascade flow conditions. The flow conditions and pressure results within the cascade, especially on the suction surface, were seen to vary considerably due to various small complications such as the loose compressor diffuser. The pressure distribution was also shown to vary due to the mere presence of the silicon tubing at the cascade inlet. Following the subsequent rectification of these problems, a new experimental pressure distribution was recorded. The original hypothesis that de Villiers' [2002] suction side pressure distribution was too low was validated. However, the rusted condition of the

rig and the possibility of two-phase flow deemed the results inconclusive. Cassie [2007] conducted further static pressure testing on the same rig, subsequent to improvements being made to the condition. The new experimental pressure tests provided good results very similar to the previous results of Snedden [1998], further validating the possible use of a higher flow speed on de Villiers' [2002] suction surface. This latest pressure distribution and its agreement with past results, suggests that the flow regime has been correctly setup. This is positive for future experimental heat transfer testing considering the link between the aerodynamics and heat transfer.

With regard to the experimental heat transfer measurements, the corroded condition of the rig during the testing stages concluded the author's results unreliable. Comparisons of experimental heat transfer results generated by Snedden [1998] and de Villiers [2002] were made. These two trends did not agree well and the error associated with the calibration constants used by Snedden [1998] was quantified. These errors proved to be significant and were calculated to be at a level of 20%. This error was shown to be constant over the entire blade surface, changing only the magnitude of Snedden's heat transfer coefficient measurements and not the trend. Correcting the error in Snedden's [1998] calibration constants brought the experimental heat transfer results of Snedden [1998] and de Villiers [2002] very close at the leading edge and the suction and pressure surface trailing edges. However large differences between the two data sets were still seen on the remainder of the blade surface. Validation of these experimental heat transfer results will be welcoming in order to conclude the distribution.

It is recommended that further increases in the acquisition frequency of the heat transfer data is required, for the acquisition of highly accurate heat flux data. Ideally, a data acquisition system, much like the one described by Ligrani et al [1982], is necessary. This system is capable of measuring all 48 heat flux sensor responses at a high frequency, in one experiment. This system would prevent the necessity of conducting six tests in order to generate a complete blade heat transfer distribution. Besides considerably reducing testing times, the heat flux data traces from all the thin-film gauges, would be acquired simultaneously thereby preventing any variance of the boundary conditions associated with the individual tests. The Eagle Technologies catalogue [2004] presents an extra low noise, high accuracy, 14-bit, 400 kHz analogue input board. This board, the PCI-703, exhibits 32 differential input channels, which would allow the entire blade heat transfer to be acquired in two tests. The author recommends this board as a possible consideration for future data acquisition advancements. In addition to this new board, it has been identified that modifying the LABVIEW program, ISOTEMP1, for additional data acquisition will be

advantageous. Automatically acquiring the initial sensor voltages and resistances will minimise errors.

It is recommended that the cooling system, used to pre-cool the heat transfer blade, should be modified. The blower draws air through the bottom of the plenum, and in doing so, suffers the risk of any leaking water entering the cooling system. Any water within the cooling system, as experienced in this research effort, causes numerous serious complications. Perhaps the most severe, is that the water is pumped through the cooling system and onto the thin-film heat flux gauges. This could possibly cause electrical short circuiting, inducing damage to a valuable and expensive piece of equipment. In addition, the water causes a corrosive build-up within the blower casing that seizes the fan, overloading the motor that drives the fan. A 3-phase motor, with half the power rating, would produce more drive than the current motor, without tripping. Modifying the blower suction pipe, so that it draws air from the top of the plenum, will prevent any further water from entering the cooling system.

Possible replacement of all the plenum vacuum seals could reduce the vacuum losses. Speed control is a problem on the hydraulic pump. Should the unit be kept in use for further testing, routine service intervals should apply. The pump is old and a more accurate and modern motor with accurate speed control is recommended. This entails possibly replacing the hydraulic network with an AC induction motor. The variable speed limitations of the AC induction motor can be solved with adjustable speed drives (ASD's). The most common AC drives are based on pulse-width modulation (PWM). The constant AC line voltage from the supply network is rectified, filtered, and then converted to a variable voltage and variable frequency. When this output from the frequency converter is connected to an AC motor, it becomes possible to adjust the motor speed. These and other experimental equipment maintenance requirements, impose obvious concern regarding the future use of the rig for accurate and modern research purposes. The rig's foundation is certainly laid; and with the associated equipment being upgraded, its use in the turbo machinery research field will be most valuable. It is evident that careful consideration into the project budget and the allocation of funds will be required.

The numerical solution from FLUENT produced very satisfying results. FLUENT showed an excellent ability to predict the flow trends and the characteristic boundary layer phenomena for the SMR-95 blade. A comprehensive analysis of these phenomena has been concluded in Chapter 6, considering the boundary layer thickness, velocity and pressure gradients as well as the Mach number contour. The suction surface certainly showed more vulnerability to small fluctuations in flow as compared to the pressure surface. On the

pressure surface, no significant change in heat transfer level was seen with a change in turbulence intensity. The velocity distribution can be concluded to be of prime importance to the heat transfer distribution. Both the SA and RKE turbulence models produced an average error of approximately 3% with the pressure distribution. The SA and RKE models produced an average error of 12% and 16%, respectively, for the isothermal heat transfer coefficient distribution. The experimental values certainly show good validation for the use of FLUENT as an alternative, faster and cheaper means with which to acquire turbine blade heat transfer distributions. The new results show remarkable improvements over the previous average error of 29% achieved by de Villiers [2002]. These final solutions followed the investigation of the varying levels of turbulence intensity at the inlet, which are generated by the cascade inlet probes. The influential findings prompt further investigation into a 3-D numerical model. Further investigation into this finding by the author could lead to even more accurate results and provide conclusions to the SMR-95 heat transfer analysis. A 3-D model will provide accurate modelling of the probe induced turbulent intensity. In addition, 3-D modelling will aid further in resolving the complex secondary flows of the passage vortices that are associated with the complex cascade geometry. These vortex flows, unresolved in the 2-D model, are understood to be a possible cause of error on the suction surface.

This dissertation includes a detailed explanation of all experimental equipment associated with the experimental cascade testing at the University of KwaZulu-Natal. This will serve as an operational manual for further researchers in the ongoing project.

Faults with the experimental equipment have been identified to improve the quality and accuracy of the experimental facility. This experimental literature source, the numerical and experimental results, and the comprehensive and conclusive characterisation of the boundary layer phenomenon, form an excellent base with which to develop to the next level of modern turbo machinery research.

APPENDIX 1

SMR-95 BLADE COORDINATES

Suction Surface		Pressure Surface	
X-Coordinate (mm)	Y-Coordinate (mm)	X-Coordinate (mm)	Y-Coordinate (mm)
9.383	2	97.861	31.162
9.262	2.003	97.77	30.997
9.136	2.009	97.655	30.864
9	2.019	97.518	30.764
8.859	2.033	97.361	30.699
8.717	2.051	97.186	30.669
8.583	2.072	96.995	30.675
8.454	2.095	94.849	31.137
8.334	2.12	92.7	31.587
8.216	2.146	90.548	32.026
8.094	2.177	88.395	32.456
7.964	2.213	86.24	32.876
7.827	2.255	84.082	33.278
7.69	2.301	83.6	33.364
7.561	2.348	83.112	33.45
7.44	2.396	82.549	33.547
7.327	2.443	81.918	33.653
7.217	2.492	81.328	33.751
7.102	2.546	80.804	33.836
6.981	2.607	80.263	33.922
6.854	2.675	79.75	34.002
6.724	2.749	79.24	34.08
6.604	2.822	78.711	34.159
6.497	2.89	78.163	34.24
6.397	2.957	77.579	34.324
6.299	3.026	76.998	34.406
6.192	3.105	76.434	34.484
6.085	3.188	75.909	34.555
5.971	3.282	75.403	34.621
5.86	3.378	74.895	34.686
5.756	3.474	74.372	34.751
5.664	3.564	73.782	34.823
5.58	3.649	73.224	34.889
5.499	3.737	72.708	34.949
5.411	3.836	72.18	35.008
5.318	3.947	71.602	35.072
5.228	4.061	71.042	35.132
5.142	4.177	70.605	35.177
5.068	4.283	70.053	35.233
4.999	4.388	69.484	35.289
4.937	4.486	68.857	35.348
4.871	4.596	68.401	35.389
4.807	4.709	67.858	35.435

Suction Surface cont.		Pressure Surface cont.	
X-Coordinate (mm)	Y-Coordinate (mm)	X-Coordinate (mm)	Y-Coordinate (mm)
4.745	4.824	67.266	35.483
4.678	4.955	66.668	35.528
4.629	5.057	66.251	35.557
4.558	5.215	65.761	35.589
4.481	5.399	65.1	35.628
4.435	5.523	64.477	35.661
4.403	5.624	64.143	35.677
4.387	5.685	63.659	35.697
4.362	5.792	63.233	35.713
4.34	5.889	62.283	35.742
4.279	6.167	61.192	35.766
4.264	6.237	60.066	35.775
4.25	6.302	58.941	35.768
4.218	6.451	57.891	35.748
4.21	6.488	56.984	35.722
4.16	6.726	56.566	35.708
4.072	7.173	56.027	35.687
4.003	7.583	55.697	35.672
3.958	7.924	55.2	35.647
3.932	8.197	54.564	35.612
3.909	8.517	54.027	35.58
3.891	8.77	53.505	35.546
3.86	9.224	53.05	35.513
3.829	9.677	52.463	35.467
3.761	10.563	51.918	35.421
3.693	11.449	51.317	35.364
3.634	12.238	50.829	35.314
3.596	12.745	50.3	35.254
3.574	13.077	49.743	35.186
3.537	13.8	49.136	35.106
3.501	14.682	48.59	35.028
3.469	15.819	48.071	34.95
3.453	16.607	47.528	34.862
3.445	17.268	46.967	34.766
3.441	18.056	46.41	34.665
3.446	18.896	45.872	34.562
3.457	19.552	45.334	34.454
3.477	20.32	44.812	34.344
3.507	21.099	44.282	34.227
3.553	21.972	43.755	34.105
3.6	22.695	43.196	33.971
3.659	23.442	42.675	33.841
3.732	24.224	42.19	33.715
3.821	25.037	41.672	33.576
3.911	25.764	41.12	33.424
4.011	26.486	40.556	33.262
4.133	27.291	40.09	33.124
4.266	28.081	39.553	32.959

Suction Surface cont.		Pressure Surface cont.	
X-Coordinate (mm)	Y-Coordinate (mm)	X-Coordinate (mm)	Y-Coordinate (mm)
4.392	28.773	39.029	32.792
4.536	29.506	38.461	32.604
4.7	30.285	37.998	32.445
4.883	31.097	37.491	32.262
5.045	31.764	36.967	32.066
5.24	32.518	36.401	31.845
5.447	33.263	35.906	31.644
5.687	34.066	35.421	31.439
5.9	34.731	34.911	31.214
6.143	35.441	34.385	30.974
6.415	36.181	33.89	30.74
6.723	36.965	33.406	30.501
7.012	37.655	32.913	30.251
7.312	38.332	32.421	29.991
7.647	39.045	31.947	29.732
8.005	39.764	31.473	29.464
8.351	40.422	30.995	29.185
8.717	41.082	30.517	28.897
9.11	41.756	30.059	28.611
9.529	42.436	29.599	28.315
9.931	43.056	29.139	28.009
10.362	43.689	28.68	27.694
10.811	44.315	28.244	27.385
11.296	44.957	27.803	27.062
11.767	45.549	27.361	26.729
12.259	46.136	26.918	26.383
12.769	46.713	26.5	26.046
13.307	47.29	26.08	25.698
13.846	47.838	25.66	25.338
14.391	48.365	25.24	24.966
14.962	48.888	24.844	24.604
15.548	49.395	24.448	24.23
16.754	50.368	24.054	23.846
17.37	50.827	23.656	23.445
17.994	51.267	23.277	23.05
18.637	51.697	22.904	22.649
19.291	52.11	22.539	22.243
19.94	52.497	22.175	21.823
20.618	52.88	21.82	21.399
21.333	53.26	21.476	20.975
22.034	53.608	21.138	20.543
22.709	53.923	20.807	20.105
23.388	54.218	20.476	19.652
24.149	54.527	20.161	19.204
24.871	54.798	19.853	18.752
25.599	55.051	19.556	18.3
26.281	55.272	19.255	17.825
27.079	55.511	18.966	17.353

Suction Surface cont.		Pressure Surface cont.	
X-Coordinate (mm)	Y-Coordinate (mm)	X-Coordinate (mm)	Y-Coordinate (mm)
27.827	55.718	18.688	16.883
28.569	55.908	18.424	16.419
29.254	56.07	18.158	15.934
30.042	56.241	17.9	15.447
30.827	56.396	17.652	14.958
31.56	56.542	17.412	14.469
33.064	56.754	17.173	13.962
33.852	56.85	16.944	13.457
34.583	56.926	16.714	12.926
35.335	56.991	16.521	12.462
36.194	57.05	15.754	10.405
36.982	57.088	15.11	8.305
37.732	57.111	14.891	7.231
38.41	57.12	14.741	6.648
39.254	57.118	14.592	6.171
40.023	57.104	14.406	5.626
40.813	57.08	14.238	5.155
41.485	57.051	14.21	5.086
42.33	57.005	14.161	4.98
43.135	56.951	14.092	4.845
43.872	56.886	13.985	4.659
45.333	56.76	13.896	4.512
46.149	56.671	13.845	4.431
46.871	56.584	13.779	4.331
47.612	56.487	13.715	4.238
48.426	56.371	13.64	4.133
49.203	56.25	13.551	4.017
49.935	56.127	13.465	3.909
50.65	55.999	13.379	3.807
51.521	55.834	13.298	3.715
52.283	55.681	13.214	3.625
53.037	55.522	13.129	3.537
53.665	55.384	13.053	3.444
54.504	55.193	12.937	3.353
55.272	55.011	12.833	3.26
56.026	54.828	12.723	3.168
56.658	54.671	12.617	3.084
57.45	54.469	12.517	3.009
58.253	54.258	12.42	2.939
58.959	54.069	12.32	2.871
59.632	53.885	12.207	2.798
60.359	53.681	12.087	2.724
61.132	53.459	11.958	2.65
61.843	53.249	11.827	2.58
62.587	53.025	11.704	2.518
63.386	52.779	11.59	2.464
64.13	52.544	11.481	2.417
64.837	52.315	11.37	2.371

Suction Surface cont.	
X-Coordinate (mm)	Y-Coordinate (mm)
65.518	52.091
66.334	51.817
67.065	51.566
67.798	51.31
68.426	51.088
69.227	50.8
69.969	50.53
70.693	50.263
71.316	50.031
72.05	49.755
72.813	49.464
73.513	49.194
74.189	48.931
74.876	48.661
75.612	48.367
76.308	48.087
77.045	47.787
77.787	47.481
78.505	47.182
79.176	46.898
79.882	46.597
80.694	46.247
81.408	45.934
82.095	45.631
82.7	45.361
83.512	44.995
84.221	44.673
84.947	44.341
85.5	44.087
86.273	43.729
87.013	43.385
87.693	43.067
88.289	42.787
88.981	42.461
89.745	42.098
90.403	41.784
91.067	41.466
93.834	40.12
96.589	38.75
99.332	37.358
99.483	37.244
99.599	37.112
99.68	36.964
99.724	36.802
99.731	36.628
99.699	36.444
98.78	33.803

Pressure Surface cont.	
X-Coordinate (mm)	Y-Coordinate (mm)
11.244	2.322
11.108	2.274
10.964	2.227
10.821	2.185
10.687	2.15
10.559	2.12
10.442	2.096
10.323	2.074
10.196	2.054
10.058	2.036
9.913	2.021
9.771	2.01
9.636	2.003
9.506	2

APPENDIX 2

CALIBRATION CURVES FOR THE ROSEMOUNT AND KULITE PRESSURE TRANSDUCERS

A2.1 Rosemount calibration data and curve

Time (s)	Mercury Height (mm)	Differential Pressure (Pa)	Plenum Pressure (Pa)	Corresponding Voltage (V)
0	0	0	101325	1.88
20	59	7871.544	93453.456	3.302
40	101	13475.016	87849.984	4.32
60	136	18144.576	83180.424	5.187
80	168	22413.888	78911.112	5.937
100	195	26016.12	75308.88	6.65
120	219	29218.104	72106.896	7.214
140	242	32286.672	69038.328	7.792
160	260	34688.16	66636.84	8.264
180	279	37223.064	64101.936	8.669
200	294	39224.304	62100.696	9.038
220	308	41092.128	60232.872	9.39

Table A2-1: Rosemount transducer calibration data used to plot the calibration curve

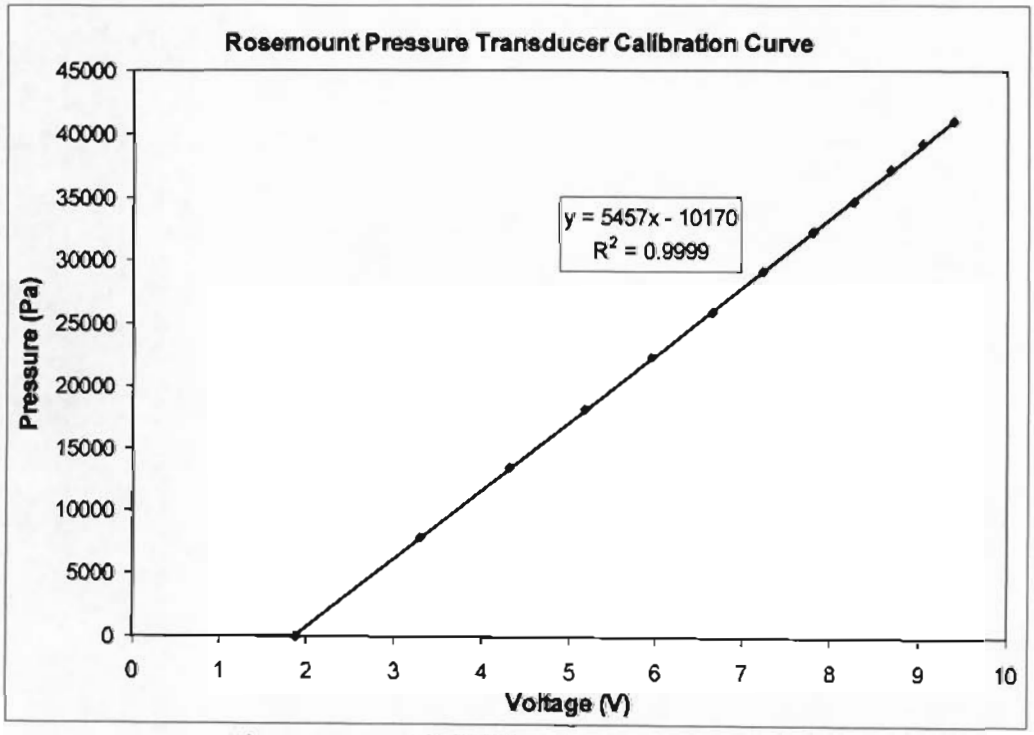

Figure A2-1: Rosemount transducer calibration curve

A2.2 Kulite calibration data and curve

Time (s)	Manometer Height (m)	Differential Pressure (Pa)	Plenum Pressure (Pa)	Kulite (V)
0	0	0	101325	0.098
10	0.015	4002.48	97322.52	0.0942
20	0.02	5336.64	95988.36	0.0907
30	0.04	10673.28	90651.72	0.0876
40	0.052	13875.264	87449.736	0.085
50	0.062	16543.584	84781.416	0.0825
60	0.071	18945.072	82379.928	0.0802
70	0.08	21346.56	79978.44	0.078
80	0.087	23214.384	78110.616	0.0761
90	0.095	25349.04	75975.96	0.0741
100	0.102	27216.864	74108.136	0.0723
110	0.109	29084.688	72240.312	0.0706
120	0.116	30952.512	70372.488	0.069
130	0.122	32553.504	68771.496	0.0674
140	0.127	33887.664	67437.336	0.066
150	0.133	35488.656	65836.344	0.0646
170	0.142	37890.144	63434.856	0.062
180	0.148	39491.136	61833.864	0.0608
200	0.155	41358.96	59966.04	0.0586
220	0.163	43493.616	57831.384	0.0566
240	0.17	45361.44	55963.56	0.0548

Table A2-2: Kulite transducer calibration data (Reproduced from de Villiers)

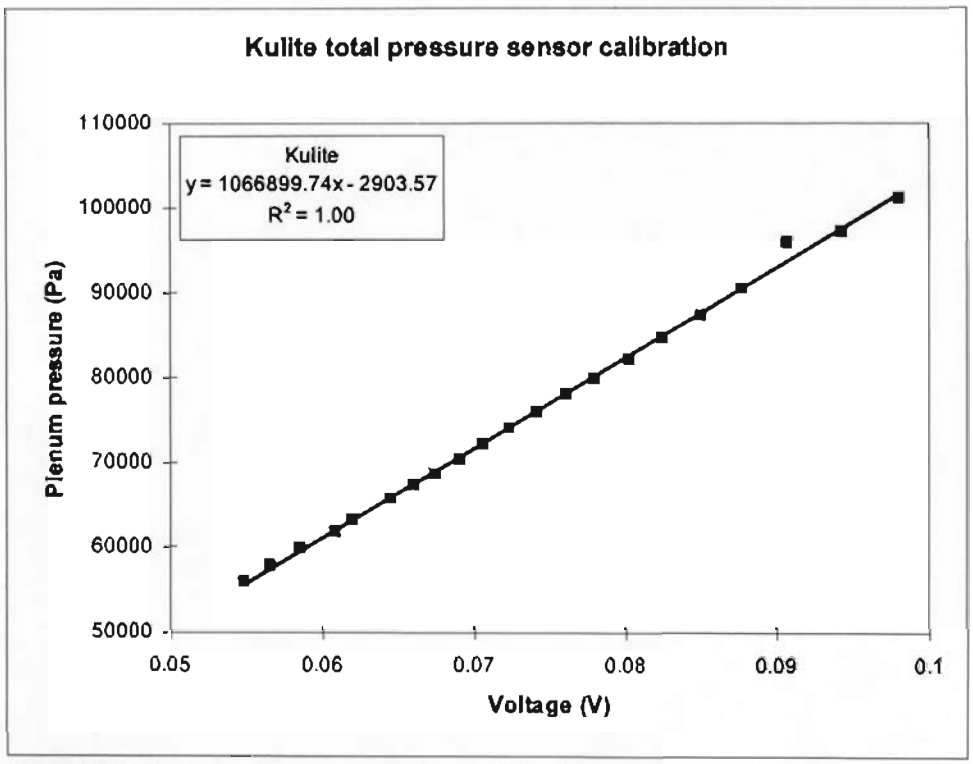

Figure A2-2: Kulite total pressure transducer calibration curve (Reproduced from de Villiers)

APPENDIX 3

EXPERIMENTAL RIG OPERATING PROCEDURE

1 Check that the plenum is completely sealed at all locations to allow a vacuum to be achieved in the plenum.

2 Switch on the oil heater in order to preheat the gearbox lubrication oil.

3 Turn on the main workshop compressor to supply air to the air motor in order to pump the gearbox lubrication oil. For the heat transfer measurements, open the valve for the pneumatic ram.

4 Turn on the safety control box, display box and the pressure control box. All interlocks will be shown as active and all displays will indicate readings. The pressure controller will open the solenoid valve.

5 Switch on the vacuum pump.

6 Open the main cooling water supply. This water supplies the heat exchanger that cools the gearbox lubrication oil, as well as the water that supplies the radiator for control of the cascade temperature. A small valve on the heat exchanger can be opened to check that the water supply is working. This is important since the water comes from the workshop tank, which is known to have run dry. This water also supplies the heat exchangers responsible for cooling the blade in the heat transfer measurements (see section 5.4). The cooling water on the main Uchida hydraulic pump must also be opened.

7 Start the air pump. The oil flow, oil pressure and air pressure interlocks should at this stage deactivate and all illuminate green.

8 At a plenum pressure of 0.55 bar, the vacuum pressure interlock should deactivate. On the hydraulic pump control circuitry, the switch must be turned to "sonic"; all interlock LED's should now be off. An active LED indicates a safety compromise. Check the hydraulic oil level nevertheless. A fault free system should now be indicated allowing for start-up of the pump.

9 Ensure the hydraulic level on the pump is neutral, if not, adjust it by turning the power screw. Start the primer pump and then the main pump.

10 Allow the motor to run at a speed between 500 and 1000 rpm for approximately 5 minutes, increasing the speed steadily to 2500 rpm thereafter. This appears to prevent vibration in the rig. For the heat transfer measurements, turn the blower on and open the blade cooling water valve fully to cool the blade.

11 Adjust the pressure control setting on the pressure controller such that the Kulite total pressure transducer outputs 40.2 mV corresponding to the required 40 kPa plenum pressure (see section 3-3).

12 Adjust the radiator cooling water valve to maintain a cascade temperature of $100°C$.

13 Conduct experiments whilst monitoring motor speed and cascade inlet temperature. Heat transfer experiments involve initial sensor voltage and resistance measurements. The blower must be turned off immediately prior to plunging the blade.

14 For the heat transfer experiments, plunge and retract the blade now.

15 Shut down the rig in reverse order.

Various obstacles were encountered with equipment during the carrying out of experiments. The following are brief explanations of the problems encountered followed by a suggested solution:

- The oil flow interlock does not deactivate – Twisting the oil flow meter should solve the problem of possible loose wiring
- Air motor is not supplying gearbox with oil – Check the air motor bearings are receiving lubricating oil from the air supply. This oil is enclosed within the clear container on the air supply hose.
- The rig suddenly shuts down after start up because of a loss in vacuum pressure – This means the mechanical seal on the compressor shaft is possibly not sealing effectively and requires either replacement or cleaning after standing for long periods (see section A5.1 in Appendix 5).
- Difficulty in locating a leak in the plenum – An effective technique of locating a leak is by using a long thin plastic pipe and holding one end in one ear, and focusing the free end on places with possible leaks. This technique focuses any leakage noises into the ear for an effective and time saving solution.

APPENDIX 4

MAINTENANCE PERFORMED ON THE RIG

A4.1 Maintenance performed prior to the rig start-up

A4.1.1 Mechanical seal

In the early stages of the project, initial attempts to start the experimental rig were returned with dismal results. The experimental procedure, as outlined by de Villiers, was followed. Once the safety interlock criteria, outlined in section 3.7, were satisfied, an attempt was made to start the compressor. The hydraulic pump started and the compressor rotation was initiated. However, the entire system shut down only moments later. It could immediately be seen that the fault lay with the vacuum pressure interlock. This indicated that once the compressor was started, the plenum vacuum pressure was being lost. This would activate the interlock, and override the entire operating system.

To investigate the problem at hand, all seals on the plenum were checked for possible leaks. Subsequent to sealing any potential leakage points using silicon, further attempts were made to get the compressor to run continuously. The same results were seen time and time again. It was clear that further investigation of the problem was required.

Review of literature documented by past researchers using the rig, it was seen that a mechanical carbon seal lay at the shaft-plenum interface. This seal served to provide a vacuum seal between the rotating shaft and the plenum. Consulting mechanics with experience and knowledge of the rig's service history, revealed that this seal had given rise to vacuum loss problems in the past. It had been replaced approximately seven years prior. With this in mind, it was justifiable to perform a check on the seal to ascertain its working condition.

The location of the seal, meant that the task of removing it was time consuming and difficult. All the hydraulic piping from the hydraulic pump was removed from the motor. The entire motor and gearbox section at the rear end of the plenum was removed so that the plenum end plate could be removed. Observation of the seal revealed that the seal in fact was not broken. The leak was however, being caused by corrosion that had built up on the surface of the shaft at the junction of the seal. This corrosion affected the tolerance of the mechanical

seal and when the shaft rotated, the vacuum was being lost from the plenum. Sanding the shaft down using fine sand paper, solved the problem. In addition to this, a new gasket was installed on the rear plate to replace the older fibrous gasket. When the seal was replaced, the rig start-up was now successful.

A4.1.2 Air motor

During the early stages of experimental testing, the air motor ceased to operate. This meant that no lubrication oil was being supplied to the gearbox, and the interlock subsequently shut the rig down. The air pressure supply to the air motor was sufficient, meaning that the problem lay with the air motor itself.

Close investigation of the air motor revealed that the shaft was not turning, indicative of a possible cease in the bearings. On the air line, there is a transparent cylinder, which turned out to be the lubrication oil for the air motor. This cylinder is specially designed to collect small amounts of oil in the air line, thereby lubricating the air motor. This cylinder was empty and upon filling it with pneumatic oil, the air motor worked appropriately. Figure A5-1 below illustrates the air motor with the lubrication oil cylinder shown.

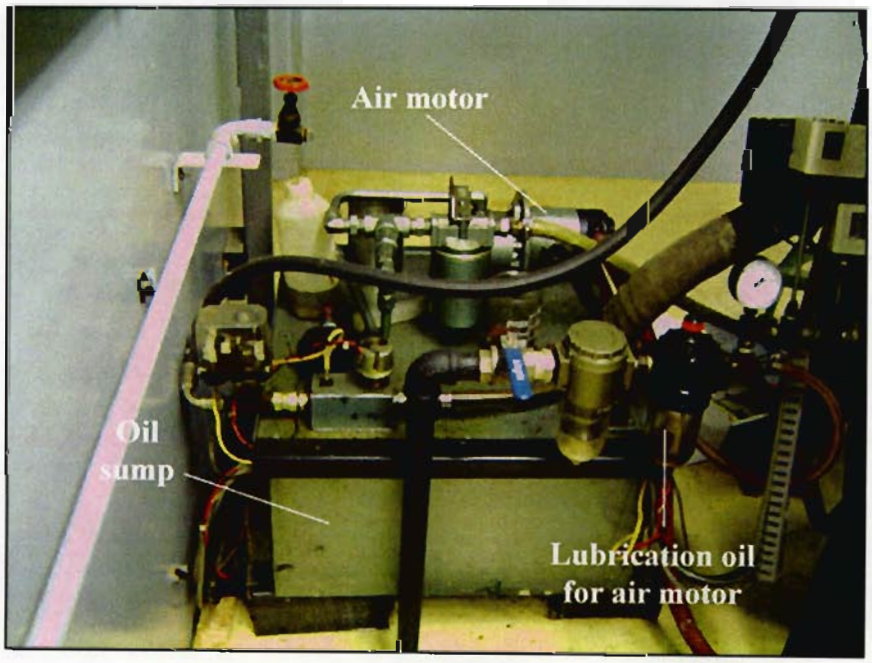

Figure A4-1: Air motor with associated components

A4.2 The blower fan

The plenum was opened to help with the diagnosis of the blower fault. A significant and concerning amount of water was seen in the plenum and clearly the radiator leak was deteriorating. The cooling pipes were removed from the cooling box and the blower switched on. The blower started up and a large flow rate of water exited the cooling pipes. This is a serious problem since the blade, heat flux sensors and contact boards within the blade, should not get wet, to avoid short circuits and damage to the electrical equipment.

The main cause of the problem was identified as the leaking radiator. The blower sucks air from the bottom of the plenum. This means that any water leaking from the radiator simply flows down this pipe and enters the cooling system flow. The blower was switched on to try and blow the water out of the system. This caused the motor to trip on every occasion. Feeling the motor housing, it was extremely warm, indicative of current overloading. The motor has a maximum current loading of 9 A. An ammeter was connected to the mains switch and the motor started again. The ammeter read 20 A, followed by the motor tripping again. The motor was hence being overloaded. The belts driving the blower were not too tight and the problem appeared to lie with the blower fan.

The blower was stripped, and the fan removed. This proved to be a very difficult task since the casing was extremely tight fitting and was difficult to remove. Once finally removed, a large volume of water drained from the housing and the problem was clearly visible. The water in the cooling system from the radiator was causing a corrosive build-up on the fan edges. The tolerance between the fan and the outer casing is extremely small. Therefore the corrosion was causing friction and overworking the motor. Furthermore, with the fan designed for airflow, water in the system would undoubtedly cause significant extra loading on the fan and hence the motor. The fan was sanded down and polished before being replaced. Following this, the motor was started and run for some length of time to drain the water from the system.

A4.3 Hydraulic pump seal

During the heat transfer experimental testing, the rig experienced violent vibration and loud pulsating noises were evident from the hydraulic pump. The emergency shut-down switch was immediately activated. The problem was immediately evident since a very large volume of hydraulic oil had collected beneath the hydraulic pump. By starting the primer pump, the origin of the oil could be distinguished. The seal on the pump shaft had clearly failed,

releasing large volumes of the extremely high pressure hydraulic oil. The pump was stripped, and the seal removed, which revealed the seal to be badly cracked from age and drying out. The seal was consequently replaced with a new one, and the pump was filled with new hydraulic oil, which allowed for the testing to commence.

A4.4 Repair of the annular cooling radiator

The water leak from the radiator had serious implications on the blade cooling system equipment. No further testing could commence until the radiator was repaired. Removal of the radiator required that the plenum be unbolted at its mid section. The one half of the plenum could then be lifted with the use of a chain block. The hoses and connecting elbows were also removed for cleaning and replacement. Figure A5-2 below illustrates the radiator having just been installed.

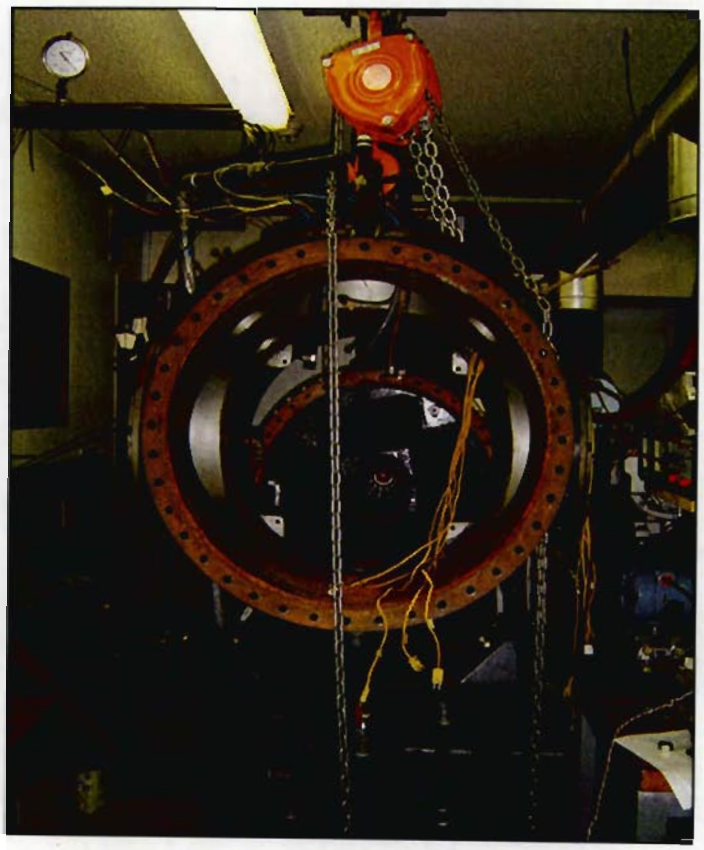

Figure A4-2: Plenum suspended from chain block during the radiator instalment

APPENDIX 5

HEAT TRANSFER SENSOR CALIBRATION DATA

P1

Sensor 1							
Thermocouple 1	Thermocouple 2	Average Temp	Ave temp (K)	Resistance	T0 (40C)	Gradient	0.030026226
25.5		25.5	298.65	74.1	313.15	Y-intercept	65.11699807
35.1	34.9	35	308.15	74.3	313.15	R0 (40C)	74.51971063
59.8	59.7	59.75	332.9	75.2	313.15		
79.1	79.3	79.2	352.35	75.7	313.15	Alpha R*R0	0.030026226
93.8	93.9	93.85	387	76.1	313.15	AlphaR	0.00040293

Sensor 2							
Thermocouple 1	Thermocouple 2	Average Temp	Ave temp (K)	Resistance	T0 (40C)	Gradient	0.03434061
25.5		25.5	298.65	80.1	313.15	Y-intercept	69.82578569
35.1	34.9	35	308.15	80.4	313.15	R0 (40C)	80.57954763
59.7	59.7	59.7	332.85	81.2	313.15		
79	79.3	79.15	352.3	82	313.15	Alpha R*R0	0.03434061
93.8	94	93.9	387.05	82.4	313.15	AlphaR	0.00042617

Sensor 3							
Thermocouple 1	Thermocouple 2	Average Temp	Ave temp (K)	Resistance	T0 (40C)	Gradient	#DIV/0!
BROKEN					313.15	Y-intercept	#DIV/0!
					313.15	R0 (40C)	#DIV/0!
					313.15		
					313.15	Alpha R*R0	#DIV/0!
					313.15	AlphaR	#DIV/0!

Sensor 4							
Thermocouple 1	Thermocouple 2	Average Temp	Ave temp (K)	Resistance	T0 (40C)	Gradient	0.031412841
25.6	25.6	25.6	298.75	69.1	313.15	Y-intercept	59.77627695
35.1	35	35.05	308.2	69.5	313.15	R0 (40C)	69.61320813
59.7	59.7	59.7	332.85	70.3	313.15		
79.1	79.3	79.2	352.35	70.8	313.15	Alpha R*R0	0.031412841
93.7	94	93.85	387	71.3	313.15	AlphaR	0.000451248

Sensor 5							
Thermocouple 1	Thermocouple 2	Average Temp	Ave temp (K)	Resistance	T0 (40C)	Gradient	0.032176526
26.1	26	26.05	299.2	68	313.15	Y-intercept	58.42125471
35.1	35	35.05	308.2	68.4	313.15	R0 (40C)	68.49733368
59.6	59.6	59.6	332.75	69.1	313.15		
79.1	79.3	79.2	352.35	69.8	313.15	Alpha R*R0	0.032176526
93.6	93.9	93.75	366.9	70.2	313.15	AlphaR	0.000469749

Sensor 6							
Thermocouple 1	Thermocouple 2	Average Temp	Ave temp (K)	Resistance	T0 (40C)	Gradient	0.027749362
25.6		25.6	298.75	70	313.15	Y-intercept	61.65276176
35.3	35.2	35.25	308.4	70.2	313.15	R0 (40C)	70.3424744
59.5	59.5	59.5	332.65	70.8	313.15		
79	79.2	79.1	352.25	71.4	313.15	Alpha R*R0	0.027749362
93.6	94	93.8	366.95	71.9	313.15	AlphaR	0.000394489

Sensor 7							
Thermocouple 1	Thermocouple 2	Average Temp	Ave temp (K)	Resistance	T0 (40C)	Gradient	0.033264163
26	26	26	299.15	70.6	313.15	Y-intercept	60.69962419
35.2	35.1	35.15	308.3	71	313.15	R0 (40C)	71.11629694
59.6	59.6	59.6	332.75	71.8	313.15		
79.1	79.3	79.2	352.35	72.4	313.15	Alpha R*R0	0.033264163
93.6	94	93.8	366.95	72.9	313.15	AlphaR	0.000467743

Sensor 8							
Thermocouple 1	Thermocouple 2	Average Temp	Ave temp (K)	Resistance	T0 (40C)	Gradient	0.035805426
26	26	26	299.15	69.6	313.15	Y-intercept	58.94146048
35.1	34.8	34.95	308.1	69.9	313.15	R0 (40C)	70.09129982
					313.15		
79.1	79.3	79.2	352.35	71.5	313.15	Alpha R*R0	0.035805426
93.7	94	93.85	387	72	313.15	AlphaR	0.000507986

Table A5-1:Heat flux sensor sensor calabration data (D-type connnector P1)

P2

Sensor 9							
Thermocouple 1	Thermocouple 2	Average Temp	Ave temp (K)	Resistance	T0 (40C)	Gradient	0.032328987
26.2		26.2	299.35	69.5	313.15	Y-intercept	59.82871593
35.3	35	35.15	308.3	69.8	313.15	R0 (40C)	69.95253833
59.6	59.6	59.6	332.75	70.6	313.15		
79.2	79.2	79.2	352.35	71.2	313.15	Alpha R*R0	0.032328987
93.7	93.9	93.8	366.95	71.7	313.15	AlphaR	0.000462156

Sensor 10							
Thermocouple 1	Thermocouple 2	Average Temp	Ave temp (K)	Resistance	T0 (40C)	Gradient	0.033150688
26.2		26.2	299.35	71.9	313.15	Y-intercept	62.07562917
35.2	35	35.1	308.25	72.4	313.15	R0 (40C)	72.45676707
59.5	59.5	59.5	332.65	73.1	313.15		
79.2	79.3	79.25	352.4	73.8	313.15	Alpha R*R0	0.033150688
93.9	94	93.95	367.1	74.2	313.15	AlphaR	0.000457524

Sensor 11							
Thermocouple 1	Thermocouple 2	Average Temp	Ave temp (K)	Resistance	T0 (40C)	Gradient	0.034047094
26.3		26.3	299.45	77.5	313.15	Y-intercept	67.29772671
35.3	35.1	35.2	308.35	77.8	313.15	R0 (40C)	77.95957416
59.4	59.5	59.45	332.6	78.6	313.15		
79.2	79.3	79.25	352.4	79.3	313.15	Alpha R*R0	0.034047094
93.8	93.9	93.85	367	79.8	313.15	AlphaR	0.000436728

Sensor 12							
Thermocouple 1	Thermocouple 2	Average Temp	Ave temp (K)	Resistance	T0 (40C)	Gradient	0.035150513
26.3		26.3	299.45	86.5	313.15	Y-intercept	75.95178708
35.3	35.1	35.2	308.35	86.8	313.15	R0 (40C)	86.95917035
59.5	59.5	59.5	332.65	87.6	313.15		
79.2	79.2	79.2	352.35	88.3	313.15	Alpha R*R0	0.035150513
93.6	94	93.8	366.95	88.9	313.15	AlphaR	0.000404219

Sensor 13							
Thermocouple 1	Thermocouple 2	Average Temp	Ave temp (K)	Resistance	T0 (40C)	Gradient	0.033331052
26.3		26.3	299.45	75.2	313.15	Y-intercept	65.25642396
35.2	35	35.1	308.25	75.6	313.15	R0 (40C)	75.69404285
59.5	59.5	59.5	332.65	76.3	313.15		
79.2	79.3	79.25	352.4	77	313.15	Alpha R*R0	0.033331052
93.6	93.9	93.75	366.9	77.5	313.15	AlphaR	0.000440339

Sensor 14							
Thermocouple 1	Thermocouple 2	Average Temp	Ave temp (K)	Resistance	T0 (40C)	Gradient	0.031500222
26.3		26.3	299.45	75.3	313.15	Y-intercept	65.85686265
35.2	35	35.1			313.15	R0 (40C)	75.72115702
59.6	59.6	59.6	332.75	76.3	313.15		
79.2	79.3	79.25	352.4	77	313.15	Alpha R*R0	0.031500222
93.6	93.9	93.75	366.9	77.4	313.15	AlphaR	0.000416003

Sensor 15							
Thermocouple 1	Thermocouple 2	Average Temp	Ave temp (K)	Resistance	T0 (40C)	Gradient	0.039844704
26.3		26.3	299.45	85.8	313.15	Y-intercept	73.85394882
35.2	35	35.1	308.25	86.1	313.15	R0 (40C)	86.331318
59.6	59.6	59.6	332.75	87.1	313.15		
79.2	79.2	79.2	352.35	88	313.15	Alpha R*R0	0.039844704
93.6	93.9	93.75	366.9	88.4	313.15	AlphaR	0.000461532

Sensor 16							
Thermocouple 1	Thermocouple 2	Average Temp	Ave temp (K)	Resistance	T0 (40C)	Gradient	0.033981067
26.3		26.3	299.45	77.4	313.15	Y-intercept	67.2799849
35.2	35	35.1	308.25	77.8	313.15	R0 (40C)	77.92115595
59.6	59.6	59.6	332.75	78.6	313.15		
79.2	79.3	79.25	352.4	79.3	313.15	Alpha R*R0	0.033981067
93.6	93.9	93.75	366.9	79.7	313.15	AlphaR	0.000436096

Table A5-2:Heat flux sensor_sensor calabration data (D-type connnector P2)

P3							
Sensor							
17							
Thermocouple 1	Thermocouple 2	Average Temp	Ave temp (K)	Resistance	T0 (40C)	Gradient	0.036041985
26.1		26.1	299.25	74.5	313.15	Y-Intercept	63.73730484
35.2	35	35.1	308.25	74.9	313.15	R0 (40C)	75.02385237
59.6	59.6	59.6	332.75	75.7	313.15		
79.1	79.2	79.15	352.3	76.4	313.15	Alpha R*R0	0.036041985
93.7	94	93.85	367	77	313.15	AlphaR	0.000480407

Sensor							
18							
Thermocouple 1	Thermocouple 2	Average Temp	Ave temp (K)	Resistance	T0 (40C)	Gradient	0.037344995
26.1	26.1	26.1	299.25	73.5	313.15	Y-Intercept	62.30370232
35.2	35	35.1	308.25	73.8	313.15	R0 (40C)	73.99828754
59.6	59.6	59.6	332.75	74.7	313.15		
79.2	79.3	79.25	352.4	75.5	313.15	Alpha R*R0	0.037344995
93.7	94.1	93.9	367.05	76	313.15	AlphaR	0.000504674

Sensor							
19							
Thermocouple 1	Thermocouple 2	Average Temp	Ave temp (K)	Resistance	T0 (40C)	Gradient	0.034599505
26.1		26.1	299.25	73.2	313.15	Y-Intercept	62.83573243
35.3	35	35.15	308.3	73.5	313.15	R0 (40C)	73.6705673
59.6	59.5	59.55	332.7	74.3	313.15		
79.1	79.3	79.2	352.35	75.1	313.15	Alpha R*R0	0.034599505
93.7	94	93.85	367	75.5	313.15	AlphaR	0.000469652

Sensor							
20							
Thermocouple 1	Thermocouple 2	Average Temp	Ave temp (K)	Resistance	T0 (40C)	Gradient	0.029572452
26.2		26.2	299.35	69.6	313.15	Y-Intercept	60.70342462
35.2	35	35.1	308.25	69.8	313.15	R0 (40C)	69.96403791
59.6	59.6	59.6	332.75	70.5	313.15		
79.2	79.3	79.25	352.4	71.1	313.15	Alpha R*R0	0.029572452
93.7	94	93.85	367	71.6	313.15	AlphaR	0.000422681

Sensor							
21							
Thermocouple 1	Thermocouple 2	Average Temp	Ave temp (K)	Resistance	T0 (40C)	Gradient	0.028466012
26.2		26.2	299.35	67.5	313.15	Y-Intercept	58.95099194
35.1	34.9	35	308.15	67.7	313.15	R0 (40C)	67.86512363
59.6	59.6	59.6	332.75	68.4	313.15		
79.2	79.3	79.25	352.4	69	313.15	Alpha R*R0	0.028466012
93.8	94	93.9	367.05	69.4	313.15	AlphaR	0.00041945

Sensor							
22							
Thermocouple 1	Thermocouple 2	Average Temp	Ave temp (K)	Resistance	T0 (40C)	Gradient	0.030476041
					313.15	Y-Intercept	60.58471743
35.2	35	35.1	308.25	70	313.15	R0 (40C)	70.12828974
59.6	59.6	59.6	332.75	70.7	313.15		
79.2	79.3	79.25	352.4	71.3	313.15	Alpha R*R0	0.030476041
93.8	94	93.9	367.05	71.8	313.15	AlphaR	0.000434576

Sensor							
23							
Thermocouple 1	Thermocouple 2	Average Temp	Ave temp (K)	Resistance	T0 (40C)	Gradient	0.029367627
26.2		26.2	299.35	70.4	313.15	Y-Intercept	61.57777999
					313.15	R0 (40C)	70.77425251
59.6	59.6	59.6	332.75	71.3	313.15		
79.2	79.3	79.25	352.4	71.9	313.15	Alpha R*R0	0.029367627
93.7	93.9	93.8	366.95	72.4	313.15	AlphaR	0.000414948

Sensor							
24							
Thermocouple 1	Thermocouple 2	Average Temp	Ave temp (K)	Resistance	T0 (40C)	Gradient	0.030569576
26.2		26.2	299.35	69.7	313.15	Y-Intercept	60.55273509
35.2	35	35.1	308.25	70	313.15	R0 (40C)	70.12559768
59.5	59.6	59.55	332.7	70.7	313.15		
79.2	79.3	79.25	352.4	71.3	313.15	Alpha R*R0	0.030569576
93.7	94	93.85	367	71.8	313.15	AlphaR	0.000435926

Table A5-3:Heat flux sensor sensor calabration data (D-type connector P3)

P4

Sensor							
25							
Thermocouple 1	Thermocouple 2	Average Temp	Ave temp (K)	Resistance	T0 (40C)	Gradient	0.031586595
26.2		26.2	299.35	74.6	313.15	Y-Intercept	65.19609321
35.2	35	35.1	308.25	75	313.15	R0 (40C)	75.08743548
59.5	59.5	59.5	332.65	75.7	313.15		
79.1	79.2	79.15	352.3	76.3	313.15	Alpha R*R0	0.031586595
93.7	94	93.85	367	76.8	313.15	AlphaR	0.000420664

Sensor							
26							
Thermocouple 1	Thermocouple 2	Average Temp	Ave temp (K)	Resistance	T0 (40C)	Gradient	0.033957334
26.2		26.2	299.35	73.3	313.15	Y-Intercept	63.1271839
35.2	35	35.1	308.25	73.6	313.15	R0 (40C)	73.76092298
59.6	59.6	59.6	332.75	74.4	313.15		
79.3	79.3	79.3	352.45	75.1	313.15	Alpha R*R0	0.033957334
93.7	94.1	93.9	367.05	75.6	313.15	AlphaR	0.00046037

Sensor							
27							
Thermocouple 1	Thermocouple 2	Average Temp	Ave temp (K)	Resistance	T0 (40C)	Gradient	0.031963869
26.3		26.3	299.45	77.7	313.15	Y-Intercept	68.08799543
35.3	35.1	35.2	308.35	77.9	313.15	R0 (40C)	78.09748107
59.6	59.6	59.6	332.75	78.7	313.15		
79.3	79.3	79.3	352.45	79.4	313.15	Alpha R*R0	0.031963869
93.7	94	93.85	367	79.8	313.15	AlphaR	0.000409282

Sensor							
28							
Thermocouple 1	Thermocouple 2	Average Temp	Ave temp (K)	Resistance	T0 (40C)	Gradient	0.079102633
26.3		26.3	299.45	183.3	313.15	Y-Intercept	159.6595078
35.3	35.1	35.2	308.35	184.1	313.15	R0 (40C)	184.4304974
59.5	59.6	59.55	332.7	186	313.15		
79.1	79.4	79.25	352.4	187.5	313.15	Alpha R*R0	0.079102633
93.7	94	93.85	367	188.7	313.15	AlphaR	0.000428902

Sensor							
29							
Thermocouple 1	Thermocouple 2	Average Temp	Ave temp (K)	Resistance	T0 (40C)	Gradient	0
BROKEN		26.2	299.35		313.15	Y-Intercept	0
		0	273.15		313.15	R0 (40C)	0
		0	273.15		313.15		
		0	273.15		313.15	Alpha R*R0	0
		0	273.15		313.15	AlphaR	#DIV/0!

Sensor							
30							
Thermocouple 1	Thermocouple 2	Average Temp	Ave temp (K)	Resistance	T0 (40C)	Gradient	0.035777274
					313.15	Y-Intercept	69.98393802
35.2	34.9	35.05	308.2	81	313.15	R0 (40C)	81.18759133
59.5	59.6	59.55	332.7	81.9	313.15		
79.1	79.2	79.15	352.3	82.6	313.15	Alpha R*R0	0.035777274
93.7	94	93.85	367	83.1	313.15	AlphaR	0.000440674

Sensor							
31							
Thermocouple 1	Thermocouple 2	Average Temp	Ave temp (K)	Resistance	T0 (40C)	Gradient	0.033897455
26.3		26.3	299.45	72.6	313.15	Y-Intercept	62.44435017
35	34.9	34.95	308.1	72.9	313.15	R0 (40C)	73.05933811
60	59.6	59.8	332.95	73.7	313.15		
79.9	79.2	79.55	352.7	74.4	313.15	Alpha R*R0	0.033897455
93.8	94	93.9	367.05	74.9	313.15	AlphaR	0.000463972

Sensor							
32							
Thermocouple 1	Thermocouple 2	Average Temp	Ave temp (K)	Resistance	T0 (40C)	Gradient	0.035728658
26.2	26.2	26.2	299.35	74.2	313.15	Y-Intercept	63.50058657
35.2	35	35.1	308.25	74.5	313.15	R0 (40C)	74.6890158
59.6	59.6	59.6	332.75	75.4	313.15		
79.1	79.2	79.15	352.3	76.1	313.15	Alpha R*R0	0.035728658
93.7	94	93.85	367	76.6	313.15	AlphaR	0.000478366

Table A5-4:Heat flux sensor sensor calabration data (D-type connector P4)

P5

Sensor							
33							
Thermocouple 1	Thermocouple 2	Average Temp	Ave temp (K)	Resistance	T0 (40C)	Gradient	0.035109076
26.3		26.3	299.45	76	313.15	Y-intercept	65.4862443
35.2	34.9	35.05	308.2	76.3	313.15	R0 (40C)	76.48065155
59.5	59.5	59.5	332.65	77.2	313.15		
79.1	79.2	79.15	352.3	77.8	313.15	Alpha R*R0	0.035109076
93.7	94.1	93.9	367.05	78.4	313.15	AlphaR	0.000459058

Sensor							
34							
Thermocouple 1	Thermocouple 2	Average Temp	Ave temp (K)	Resistance	T0 (40C)	Gradient	0.035004124
26.2	26.2	26.2	299.35	73.6	313.15	Y-intercept	63.18143105
35.2	34.9	35.05	308.2	74	313.15	R0 (40C)	74.14297259
59.5	59.6	59.55	332.7	74.9	313.15		
79.1	79.3	79.2	352.35	75.5	313.15	Alpha R*R0	0.035004124
93.7	94	93.85	367	76	313.15	AlphaR	0.000472117

Sensor							
35							
Thermocouple 1	Thermocouple 2	Average Temp	Ave temp (K)	Resistance	T0 (40C)	Gradient	0.03398944
26.3		26.3	299.45	74	313.15	Y-intercept	63.81652545
35.2	34.9	35.05	308.2	74.3	313.15	R0 (40C)	74.46031873
59.6	59.6	59.6	332.75	75.1	313.15		
79.2	79.3	79.25	352.4	75.8	313.15	Alpha R*R0	0.03398944
93.7	94.1	93.9	367.05	76.3	313.15	AlphaR	0.000456477

Sensor							
36							
Thermocouple 1	Thermocouple 2	Average Temp	Ave temp (K)	Resistance	T0 (40C)	Gradient	0.034950079
26.2	26.2	26.2	299.35	71.2	313.15	Y-intercept	60.77832129
35.2	34.9	35.05	308.2	71.6	313.15	R0 (40C)	71.72293852
59.6	59.6	59.6	332.75	72.4	313.15		
79.2	79.3	79.25	352.4	73.1	313.15	Alpha R*R0	0.034950079
93.7	94.1	93.9	367.05	73.6	313.15	AlphaR	0.000487293

Sensor							
37							
Thermocouple 1	Thermocouple 2	Average Temp	Ave temp (K)	Resistance	T0 (40C)	Gradient	0.034020814
26.3		26.3	299.45	72.4	313.15	Y-intercept	62.20645059
35.2	35	35.1	308.25	72.7	313.15	R0 (40C)	72.86006849
59.6	59.5	59.55	332.7	73.5	313.15		
79.2	79.3	79.25	352.4	74.2	313.15	Alpha R*R0	0.034020814
93.7	94	93.85	367	74.7	313.15	AlphaR	0.000466934

Sensor							
38							
Thermocouple 1	Thermocouple 2	Average Temp	Ave temp (K)	Resistance	T0 (40C)	Gradient	0.03498334
26.2	26.2	26.2	299.35	73.4	313.15	Y-intercept	62.9679799
35.2	35	35.1	308.25	73.8	313.15	R0 (40C)	73.92301287
59.5	59.5	59.5	332.65	74.6	313.15		
79.2	79.3	79.25	352.4	75.3	313.15	Alpha R*R0	0.03498334
93.7	94	93.85	367	75.8	313.15	AlphaR	0.00047324

Sensor							
39							
Thermocouple 1	Thermocouple 2	Average Temp	Ave temp (K)	Resistance	T0 (40C)	Gradient	0.032947681
26.3		26.3	299.45	73	313.15	Y-intercept	63.14268768
35.2	35	35.1	308.25	73.3	313.15	R0 (40C)	73.46025411
59.5	59.6	59.55	332.7	74.1	313.15		
79.2	79.3	79.25	352.4	74.8	313.15	Alpha R*R0	0.032947681
93.7	94	93.85	367	75.2	313.15	AlphaR	0.00044851

Sensor							
40							
Thermocouple 1	Thermocouple 2	Average Temp	Ave temp (K)	Resistance	T0 (40C)	Gradient	0.035729992
26.3		26.3	299.45	75.4	313.15	Y-intercept	64.69978635
35.2	34.9	35.05	308.2	75.7	313.15	R0 (40C)	75.88863344
59.5	59.5	59.5	332.65	76.6	313.15		
79.2	79.3	79.25	352.4	77.3	313.15	Alpha R*R0	0.035729992
93.7	94	93.85	367	77.8	313.15	AlphaR	0.000470821

Table A5-5:Heat flux sensor sensor calabration data (D-type connector P5)

P6

Sensor							
41							
Thermocouple 1	Thermocouple 2	Average Temp	Ave temp (K)	Resistance	T0 (40C)	Gradient	0.034895458
26.4		26.4	299.55	75.1	313.15	Y-intercept	64.53540571
35.3	35	35.15	308.3	75.2	313.15	R0 (40C)	75.46291852
59.6	59.6	59.6	332.75	76.1	313.15		
79.1	79.2	79.15	352.3	76.8	313.15	Alpha R*R0	0.034895458
93.7	94	93.85	367	77.4	313.15	AlphaR	0.000462419

Sensor							
42							
Thermocouple 1	Thermocouple 2	Average Temp	Ave temp (K)	Resistance	T0 (40C)	Gradient	0.034119301
26.4		26.4	299.55	72.3	313.15	Y-intercept	62.07341576
35.3	35.1	35.2	308.35	72.6	313.15	R0 (40C)	72.75787476
59.5	59.6	59.55	332.7	73.4	313.15		
79.1	79.2	79.15	352.3	74.1	313.15	Alpha R*R0	0.034119301
93.6	94	93.8	366.95	74.6	313.15	AlphaR	0.000468943

Sensor							
43							
Thermocouple 1	Thermocouple 2	Average Temp	Ave temp (K)	Resistance	T0 (40C)	Gradient	0.037630662
26.4		26.4	299.55	77.9	313.15	Y-intercept	66.56737296
35.3	35.1	35.2	308.35	78.1	313.15	R0 (40C)	78.35141464
59.5	59.6	59.55	332.7	79.1	313.15		
79.1	79.2	79.15	352.3	79.8	313.15	Alpha R*R0	0.037630662
93.7	94	93.85	367	80.4	313.15	AlphaR	0.000480281

Sensor							
44							
Thermocouple 1	Thermocouple 2	Average Temp	Ave temp (K)	Resistance	T0 (40C)	Gradient	0.041278377
26.4		26.4	299.55	85.6	313.15	Y-intercept	73.25557872
35.3	35	35.15	308.3	86	313.15	R0 (40C)	86.18190259
59.6	59.6	59.6	332.75	87	313.15		
79.2	79.2	79.2	352.35	87.8	313.15	Alpha R*R0	0.041278377
93.7	94.1	93.9	367.05	88.4	313.15	AlphaR	0.000478968

Sensor							
45							
Thermocouple 1	Thermocouple 2	Average Temp	Ave temp (K)	Resistance	T0 (40C)	Gradient	0.034191043
26.4		26.4	299.55	71.4	313.15	Y-intercept	61.10925748
35.3	35	35.15	308.3	71.6	313.15	R0 (40C)	71.81618266
59.6	59.6	59.6	332.75	72.5	313.15		
79.1	79.2	79.15	352.3	73.1	313.15	Alpha R*R0	0.034191043
93.7	94	93.85	367	73.7	313.15	AlphaR	0.000476091

Sensor							
46							
Thermocouple 1	Thermocouple 2	Average Temp	Ave temp (K)	Resistance	T0 (40C)	Gradient	0.033998455
26.1	26.1	26.1	299.25	68.2	313.15	Y-intercept	58.03557273
35.2	35	35.1	308.25	68.5	313.15	R0 (40C)	68.68218898
59.6	59.6	59.6	332.75	69.4	313.15		
79.1	79.2	79.15	352.3	70	313.15	Alpha R*R0	0.033998455
93.7	94	93.85	367	70.5	313.15	AlphaR	0.000495011

Sensor							
47							
Thermocouple 1	Thermocouple 2	Average Temp	Ave temp (K)	Resistance	T0 (40C)	Gradient	0.038348886
26.1	26.1	26.1	299.25	75.6	313.15	Y-intercept	64.1720046
35.1	34.9	35	308.15	76	313.15	R0 (40C)	76.18095838
59.5	59.6	59.55	332.7	77	313.15		
79.2	79.2	79.2	352.35	77.7	313.15	Alpha R*R0	0.038348886
93.7	94.1	93.9	367.05	78.2	313.15	AlphaR	0.000503392

Sensor							
48							
Thermocouple 1	Thermocouple 2	Average Temp	Ave temp (K)	Resistance	T0 (40C)	Gradient	0.037460687
26.4		26.4	299.55	78.6	313.15	Y-intercept	67.38267723
35.2	35	35.1	308.25	78.9	313.15	R0 (40C)	79.11349144
59.6	59.6	59.6	332.75	79.9	313.15		
79.2	79.3	79.25	352.4	80.6	313.15	Alpha R*R0	0.037460687
93.8	94.1	93.95	367.1	81.1	313.15	AlphaR	0.000473506

Table A5-6:Heat flux sensor sensor calabration data (D-type connector P6)

APPENDIX 6

MEASURED EXPERIMENTAL DATA SPREADSHEET

The following spreadsheet was used to record the variables that were monitored during the experimental heat transfer tests.

Sensor #	Pin #'s	Res for 40C	Initial Res	Initial Volt	alphaR	Plenum Var	Values
P1/1	1&2	**74.519711**				Motor RPM	
2	3&4	**80.579548**				Inlet Temp	
3	5&6	**BROKEN**				Pstat In (V)	
4	7&8	**69.613208**				Pstat Out (V)	
5	9&10	**68.497334**					
6	11&12	**70.342474**					
7	14&15	**71.116297**					
8	16&17	**70.0913**					
P2/9	1&2	**69.952538**				Motor RPM	
10	3&4	**72.456767**				Inlet Temp	
11	5&6	**77.959574**				Pstat In (V)	
12	7&8	**86.95917**				Pstat Out (V)	
13	9&10	**75.694043**					
14	11&12	**75.721157**					
15	14&15	**86.331318**					
16	16&17	**77.921156**					
P3/17	1&2	**75.023852**				Motor RPM	
18	3&4	**73.998288**				Inlet Temp	
19	5&6	**73.670567**				Pstat In (V)	
20	7&8	**69.964038**				Pstat Out (V)	
21	9&10	**67.865124**					
22	11&12	**70.12829**					
23	14&15	**70.774253**					
24	16&17	**70.125598**					
P4/25	1&2	**75.087435**				Motor RPM	
26	3&4	**73.760923**				Inlet Temp	
27	5&6	**78.097481**				Pstat In (V)	
28	7&8	**184.4305**				Pstat Out (V)	
29	9&10	**BROKEN**					
30	11&12	**81.187591**					
31	14&15	**73.059338**					
32	16&17	**74.689016**					
P5/33	1&2	**76.480652**				Motor RPM	
34	3&4	**74.142973**				Inlet Temp	
35	5&6	**74.460319**				Pstat In (V)	
36	7&8	**71.722939**				Pstat Out (V)	
37	9&10	**72.860068**					
38	11&12	**73.923013**					
39	14&15	**73.460254**					
40	16&17	**75.888633**					
P6/41	1&2	**75.462919**				Motor RPM	
42	3&4	**72.757875**				Inlet Temp	
43	5&6	**78.351415**				Pstat In (V)	
44	7&8	**86.181903**				Pstat Out (V)	
45	9&10	**71.816183**					
46	11&12	**68.682189**					
47	14&15	**76.180958**					
48	16&17	**79.113491**					

Table 6.1: Measured experimental data spreadsheet

APPENDIX 7

QUANTIFYING ERROR ASSOCIATED THIN-FILM CALIBRATION CONSTANTS

Sensor#	Gradient	Y-Intercept	Ro @ 298	alphaR @298	q' @ 298	h' @ 298	Ro @ 313	alphaR @313	q" @ 313	h" @ 313	h"/h'
			298.150				313.150				
1	0.029	54.439	62.966	0.000454	2276.608	30.355	63.395	0.000451	2276.608	37.943	**1.250**
2	0.029	57.145	65.881	0.000445	2323.498	30.980	66.320	0.000442	2323.498	38.725	**1.250**
3	0.030	54.015	62.870	0.000472	2191.847	29.225	63.316	0.000469	2191.847	36.531	**1.250**
4	0.031	54.425	63.519	0.000480	2157.586	28.768	63.976	0.000477	2157.586	35.960	**1.250**
5	0.031	54.462	63.645	0.000484	2141.387	28.552	64.107	0.000480	2141.387	35.690	**1.250**
6	0.031	56.410	65.622	0.000471	2198.700	29.316	66.086	0.000468	2198.700	36.645	**1.250**
7	0.029	55.151	63.768	0.000453	2281.493	30.420	64.201	0.000450	2281.493	38.025	**1.250**
8	0.031	55.735	64.918	0.000474	2182.715	29.103	65.380	0.000471	2182.715	36.379	**1.250**
9	0.032	55.687	65.079	0.000484	2140.994	28.547	65.551	0.000481	2140.994	35.683	**1.250**
10	0.032	56.500	65.981	0.000482	2149.873	28.665	66.458	0.000478	2149.873	35.831	**1.250**
11	0.032	57.723	67.234	0.000474	2182.648	29.102	67.712	0.000471	2182.648	36.377	**1.250**
12	0.031	56.739	65.892	0.000466	2221.323	29.618	66.353	0.000463	2221.323	37.022	**1.250**
13	0.031	57.003	66.335	0.000472	2194.345	29.258	66.805	0.000469	2194.345	36.572	**1.250**
14	0.033	58.574	68.353	0.000480	2158.934	28.786	68.845	0.000476	2158.934	35.982	**1.250**
15	0.037	66.417	77.508	0.000480	2158.542	28.781	78.066	0.000477	2158.542	35.976	**1.250**
16	0.032	60.424	70.084	0.000462	2238.098	29.841	70.570	0.000459	2238.098	37.302	**1.250**
17	0.035	57.255	67.601	0.000513	2023.150	26.975	68.121	0.000509	2023.150	33.719	**1.250**
18	0.033	57.960	67.769	0.000485	2134.858	28.465	68.263	0.000482	2134.858	35.581	**1.250**
19	0.034	57.707	67.695	0.000495	2095.750	27.943	68.198	0.000491	2095.750	34.929	**1.250**
20	0.031	56.382	65.565	0.000470	2203.731	29.383	66.027	0.000466	2203.731	36.729	**1.250**
21	0.031	55.147	64.241	0.000475	2181.261	29.083	64.698	0.000471	2181.261	36.354	**1.250**
22	0.032	56.943	66.364	0.000476	2175.141	29.002	66.838	0.000473	2175.141	36.252	**1.250**
23	0.031	57.109	66.262	0.000463	2233.371	29.778	66.723	0.000460	2233.371	37.223	**1.250**
24	0.031	56.896	66.228	0.000473	2190.910	29.212	66.697	0.000469	2190.910	36.515	**1.250**

Table A7.1: Table illustrating calculations for quantifying thin-film gauge calibration constant errors

APPENDIX 8

ILLUSTRATIONS OF THE FINAL CFD MESH

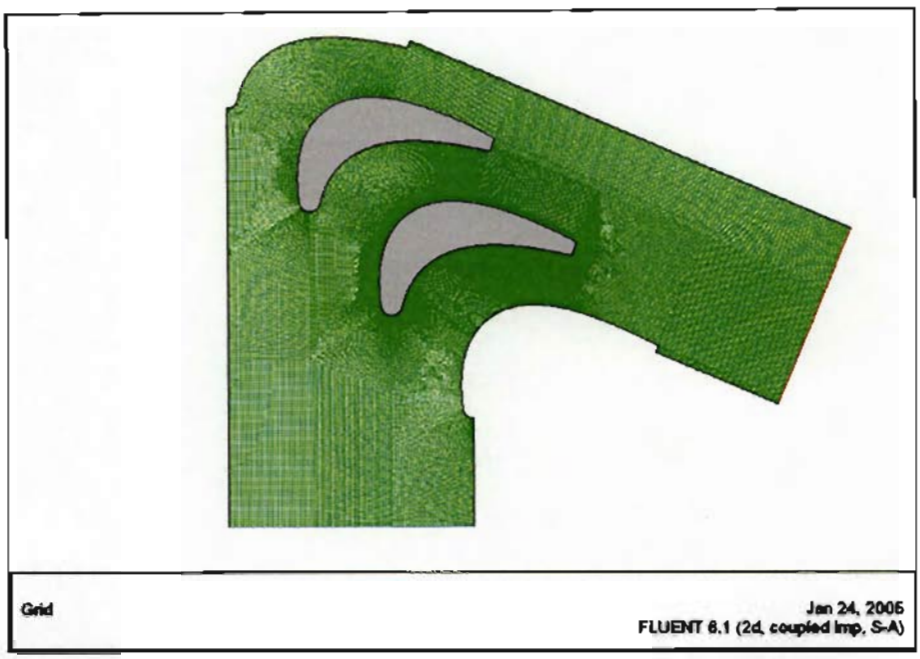

Figure A8-1: The final CFD mesh used, consisting of structured and unstructured regions

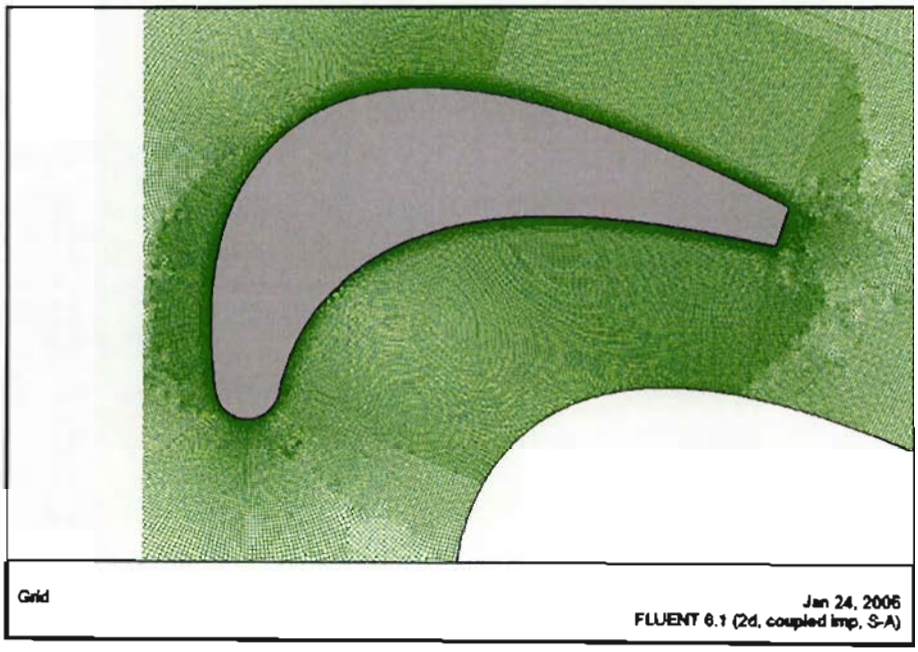

Figure A8-2: Close up on the test blade, illustrating the extremely fine mesh

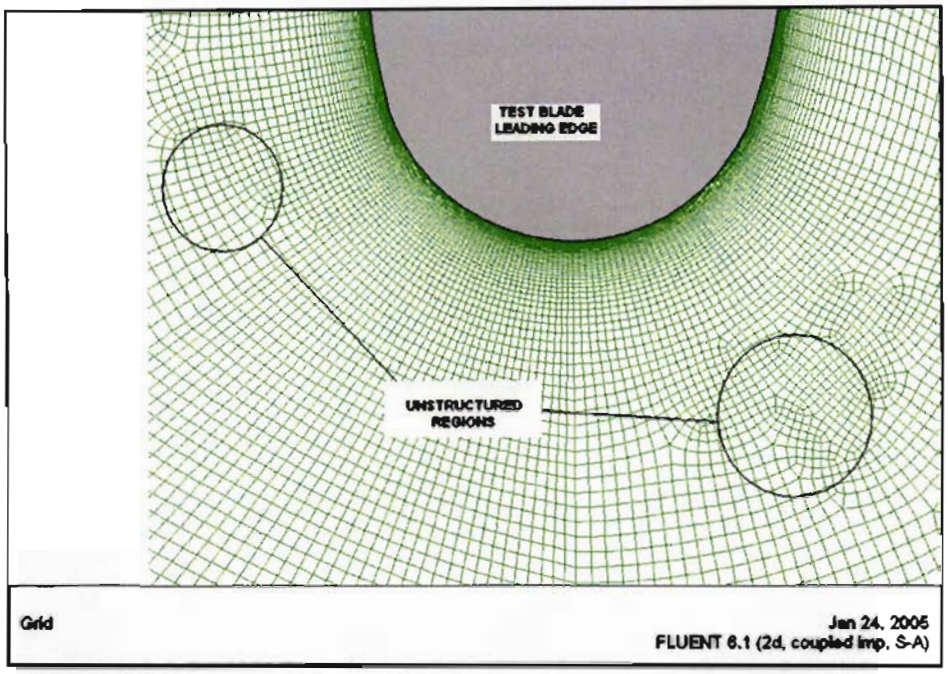

Figure A8-3: Close up on the test blade leading edge, illustrating the unstructured regions

REFERENCES

Bellows, W.J. and Mayle, R.E., 'Heat Transfer Downstream of a Leading Edge Separation Bubble', Journal of Engineering for Gas Turbines and Power, 86-GT-59. 1986.

Bradshaw, P., and Unsworth, K., 'An Improved FORTRAN Program for the Bradshaw-Ferris-Atwell Method of Calculating Turbulent Shear Layers', Imperial College, London, Aero Dept., Report No. 74-02, 1974.

Brown, A., Burton, R.C., 'The Effects of Free-Steam Turbulence Intensity and Velocity Distribution on Heat Transfer to Curved Surfaces', Journal of Engineering for Power, Vol. 100, Jan 1978.

Camci, C. and Arts, T., 'Experimental Heat Transfer Investigation Around the Film-Cooled Leading Edge of a High-Pressure Gas Turbine Rotor Blade', Journal of Engineering for Gas Turbines and Power, Vol. 107, pp 1017-1021, October 1985.

Camci, C. and Arts, T., 'An Experimental Convective Heat Transfer Investigation Around a Film-Cooled Gas Turbine Blade', Journal of Turbomachinery, May 1989.

Cassie, K.B., 'External Aerothermodynamics on a Transonic Turbine Blade', Masters Thesis, School of Mechanical Engineering, University of Kwa-Zulu Natal, Durban, South Africa, 2007.

Consigny, H., Richards, B.E. and Ville J.P., 'Short Duration Measurements of Heating to Cooled Gas Turbine Surfaces', Journal of Engineering for Power, Vol. 100, pp 439-443, July 1978.

Consigny, H. and Richards, B.E., 'Short Duration Measurements of Heat-Transfer Rate to a Gas Turbine Rotor Blade', Journal of Engineering for Power, Vol. 104, pp 542-551, July 1982.

Crawford, M.E., Kays, W.M., 'STAN5 – A Program for Numerical Computation of Two-Dimensional Internal and External Boundary Layer Flows', NASA CR-2742, Dec 1976.

de Villiers, J.E., 'Experimental and numerical validation of the flow and heat transfer on a transonic turbine blade', Masters thesis, School of Mechanical Engineering, University of Natal, Durban, South Africa. 2002.

Doorley, J.E. and Oldfield, M.L.G., 'New Heat Transfer Gauges for Use on Multilayered Substrates', ASME Paper Mo. 86-GT-96. 1986.

Doorley, J.E. and Oldfield, M.L.G., 'The Theory of Advance Multi-Layer Thin Film Heat Transfer Gauges,' International Journal of Heat and Mass Transfer, pp. 1159-1168.

Doorley, J.E., 'Procedures for Determining Surface Heat Flux Using Thin Film Gauges on a Coated Metal Model in a Transient Test Facility,' ASME Paper No. 87-GT-85. 1987.

Dunn, M.G., 'The Thin Film Gauge, von Karman Institute for Fluid Dynamics', Lecture series 1995-01, January 30 – February 3 1995.

Dunn M.G. 'Convective Heat Transfer and Aerodynamics in Axial Flow Turbines', ASME Turbo Expo, New Orleans, Louisiana, 4-7 June 2001.

Eagle Technology, 'Data Acquisition Catalogue', Eagle Appliances SA Pty. (Ltd) 2004.

Fluent Inc., 'Fluent Inc. Product Documentation', 2003.
Root:\Fluent.inc\documentation\Fluent.inc\manuals\index.html.

Glezer, B, McLean, C., Camci, C., 'Mainstream Aerodynamic Effects Due to Wheelspace Coolant Injection in a High Pressure Turbine Stage Part 1: Aerodynamic Measurements in the Stationary Frame', Journal of Turbomachinery, Vol. 123, October 2001.

Gostelow, J.P., 'Cascade Aerodynamics', Pergamon Press, 1984.

Graziani, R.A., Blair, M.F., Taylor, J.R. and Mayle, R.E., 'An Experimental Study of Endwall and Airfoil Surface Heat Transfer in a Large Scale Turbine Blade Cascade', Journal of Engineering for Power, Vol.102, pp 257-267, April 1980.

Harasgama, S.P. and Wedlake, E.T., 'Heat Transfer and aerodynamics of a High Rim Speed Turbine Nozzle Guide Vane Tested in the RAE Isentropic Light Piston Cascade (ILPC)',

Presented at the Gas Turbine and Aeroengine Congress and Exposition, June 11-14, 1990, Brussels, Belgium.

Hodson, H.P., 'Boundary-Layer and Loss Measurements on the rotor of an axial_Flow Turbine,' ASME Journal of Engineering for Gas Turbines and Power, Vol. 106, pp. 391-399, 1984.

Hodson, H.P., 'Boundary-Layer Transition and Separation Near the Leading Edge of a High-Speed Turbine Blade', Journal of Engineering for Gas Turbines and Power, Vol. 107, pp 127-134, January 1985.

Hylton, L. D., Mihelc, M.S., Turner, E.R., Nealy D.A., York, R.E.,' Analytical and Experimental Evaluation of the Heat Transfer Distribution Over the Surfaces of Turbine Vanes', NASA CR 168015, May 1983.

Incropera, F.P., DeWitt D.P., 'Fundamentals of Heat and Mass Transfer', John Wiley and Sons Inc., 4th Edition, 1996.

Jones, W.P., Launder, B.E., 'The Prediction of Laminarisation With a Two-Equation Model of Turbulence', International Journal of Heat and Mass Transfer, Vol. 15, pp. 301, 1972.

Jones, W.P., Launder, B.E., 'The Calculation of Low Reynolds Number Phenomena With a Two-Equation Model of Turbulence', International Journal of Heat and Mass Transfer, Vol. 16, pp. 1119-1130. 1973.

Kundu, P.K., Cohen, I.M., 'Fluid Mechanics', Third Edition, Elsevier Inc., 2004.

Langston, L.S., Nice, M.L., Hooper, R.M., 'Three-Dimensional Flow Within a Turbine Cascade Passage', ASME Journal of Engineering for Power, Vol. 99, No.1, Jan 1977.

Larsson, J., 'Numerical Simulation of Turbulent Flows for Turbine Heat Transfer Applications', Doctorate Thesis, School of Mechanical and Vehicular Engineering, Chalmers University of Technology, Goteborg, Sweden. 1998.

Ligrani, P.M., C. Camci and M.S. Grady., 'Thin film heat transfer gage construction and measurement details', Technical Memorandum 33, von Karman Institute for Fluid Dynamics. 1982.

Maya, T., Katsumata I., Itoh M., 'A Study of Thermal fatigue Life Prediction of Air-Cooled Turbine Blades', ASME Paper No. 78-GT-158. 1978.

Mayle, R.E., 'The Role of Laminar-Turbulent Transition in Gas Turbine Engines,' Journal of Turbomachinery, Vol. 113, pp. 509-537, October 1991.

Oldfield, M.L.G., Schultz, D.L. and T.V. Jones., 'On-line computer for transient turbine cascade instrumentation', IEEE Transactions on aerospace and Electronic Systems, AES-14 (5), 738-749.

Oldfield, M.L.G., H.J. Burd and N.G. Doe., 'Design of Wide-Bandwidth Analogue Circuits for Heat Transfer Instrumentation in Transient Tunnels', Department of Engineering Science, University of Oxford. 1982.

Nicholson, J.E., Forest, A.E., Oldfield, M.L.G. and Schultz, D.L., 'Heat Transfer Optimised Turbine Rotor Blades – An experimental Study Using Transient Techniques', Journal Of Engineering for Gas Turbines and Power, Vol 106, January 1984, pp 173-181.

Patankar, S.V., Spalding, D.B., 'Heat and Mass Transfer in Boundary Layers', 1st Edition, Morgan-Grampian, London, 1967.

Patel, V.C., Rodi, W., Scheuerer, G., 'A Review an Evaluation of Turbulence models for Near Wall and Low Reynolds Number Flows', AIAA Journal, Vol. 23, p 1308, 1985.

Radomsky, R.W. and Thole, K.A., 'Effects of High Free-stream Turbulence Levels and Length Scales on Stator Vane Heat Transfer', ASME Paper 89-GT-236. Presented at the 43rd ASME Turbo Expo in Stockholm, 1998.

Schmidt, R.C., Patankar, S.V., 'Simulating Boundary Layer Transition With Low-Reynolds-Number k-e Turbulence models: Part 1 – An Evaluation of Prediction Characteristics', Journal of Turbomachinery, Vol. 113, pp 10-17, Jan 1991.

Schultz, D.L. and T.V. Jones., 'Heat transfer measurements in short duration hypersonic facilities', AGARD, AG-165. 1973.

Schultz, D.L., Jones, T.V. and Hendley, A.D., 'On the Flow in an Isentropic Light Piston Tunnel', Aero Research Council R and M No. 3731, Jan 1973.

Schultz, D.L., Jones, T.V, Oldfield, M.L.G., Daniels, L.C., 'A New Transient Cascade Facility for the Measurement of Heat Transfer Rates', AGARD Conference Proceedings No. 229, High Temperature Problems in Gas Turbine Engines, 1977.

Schultz, D.L., Jones, T.V, Oldfield, M.L.G., 'Heat Transfer Rate and Film Cooling Effectiveness Measurements in a Transient Cascade', AGARD-CPP-281, 1981.

Snedden, G.C., 'SMR-95 Cascade Aerodynamic Characterisation and Heat Transfer Measurement', IZMAR 6, CSIR, AEROTEK, Pretoria, South Africa. 1998.

Snedden, G.C., 'Transient measurement of heat transfer in steady state turbine cascades', Masters thesis, School of Mechanical Engineering, University of Natal, Durban, South Africa. 1995.

Spalding, D.B., and Chi, S.W., 'The Drag of Compressible Turbulent Boundary Layer ona smooth Flat plate With and Without Heat Transfer', Journal of Fluid Mechanics, Vol. 18, p. 117. 1964.

Stepka, F.S., 'Uncertainties in Predicting Turbine Blade Metal Temperatures', ASME Paper 80-HT-25, July 1980.

Stieger, R., 'Experimental evaluation of heat transfer distribution on a turbine blade', Masters thesis, School of Mechanical Engineering, University of Natal, Durban, South Africa. 1998.

Tinga, T., Hagmeijer, R., de Boer, A., ten Hoeve, H.J., Huisman, H.N., Kok, J.C., Kool, G.A., Kooloos, M.F.J., Visser, W.P.J., Woldendorp, S., de wolf, W.P., 'Towards Integrated Analysis of Gas Turbine Components for Life Prediction', National Aerospace Laboratory NLR, NLR-TP-2000-196. 2000.

Turner, A.B., 'Local Heat Transfer Measurements on a Gas Turbine Blade', Journal of Mechanical Engineering Sciences', Vol. 13, pp 1 -12, 1971.

VKI web site, 'http://www.vki.ac.be/tu-dept/index.html', Internet.

Van der Steege, A.W., 'Experimental Investigations of Special Turbine Blade Cooling Configurations', Masters thesis, Department of Mechanical Engineering, University of Natal, Durban, RSA, 1990.

Vidal, R.J., 'Model Instrumentation Techniques for Heat Transfer and Force Measurements in a Hypersonic Shock tunnel', Cornell Aeronautical Laboratory Report AD-917-A-1, 1956.

Walsh, P., Fletcher, P., 'Gas Turbine Performance', Oxford, Blackwell Science, 2004.

Wang, J.H., Jen, H.F., Hartel, E.O., 'Airfoil Heat Transfer Calculation Using a Low Reynolds Number Version of a Two-Equation Turbulence Model', Journal of Engineering for Gas Turbines and Power, Vol. 107, pp 61 - 67, 1985.